Control of Large Offshore Wind Turbines

by

Xin Tong

Thesis

Submitted to the University of Warwick in partial

fulfilment of the requirements for the degree of

Doctor of Philosophy

School of Engineering

September 2017

THE UNIVERSITY OF
WARWICK

Contents

List of Tables

List of Figures

Acknowledgments

I am forever beholden to my supervisor, Dr. Xiaowei Zhao. His patient guidance, strong academic abilities, and great kindness have profoundly encouraged me all the way along my PhD journey. I feel really fortunate to have him as my PhD supervisor. I also would like to express my gratitude to Dr. Shi Zhao and Mr. Aris Karcanias for their help.

Declarations

This thesis is submitted to the University of Warwick in support of my application for the degree of Doctor of Philosophy. It has been composed by myself and has not been submitted in any previous application for any degree.

Parts of this thesis have been published by the author:

Journal (Peer Reviewed)

a. X. Tong and X. Zhao, "Power generation control of a monopile hydrostatic wind turbine using an $\mathcal{H}_\infty$ loop-shaping torque controller and an LPV pitch controller," *IEEE Transactions on Control Systems Technology*, 2017, DOI: 10.1109/TCST.2017.2749562.

b. X. Tong, X. Zhao, and S. Zhao, "Load reduction of a monopile wind turbine tower using optimal tuned mass dampers," *International Journal of Control*, vol. 90, no. 7, pp. 1283–1298, 2017.

c. X. Tong, X. Zhao, and A. Karcanias, "Passive vibration control of an offshore floating hydrostatic wind turbine," *Wind Energy*, accepted subject to revision.

d. X. Tong and X. Zhao, "Passive vibration control of the SCOLE beam system," *Structural Control and Health Monitoring*, accepted subject to revision.

Conference (Peer Reviewed)

a. X. Tong and X. Zhao, "LPV pitch control of a hydrostatic wind turbine based on LIDAR preview," in *2017 American Control Conference*, WA, USA, May 2017.

b. X. Tong and X. Zhao, "Vibration suppression of the finite-dimensional approximation of the non-uniform SCOLE model using multiple tuned mass dampers," in *55th IEEE Conference on Decision and Control*, NV, USA, December 2016.

c. X. Tong, X. Zhao, and S. Zhao, "Passive structural vibration control of a monopile wind turbine tower," in *54th IEEE Conference on Decision and Control*, Osaka, Japan, December 2015.

d. X. Tong and X. Zhao, "Platform-pitch response mitigation of a floating hydrostatic wind turbine," submitted.

Abstract

Several control strategies are proposed to improve overall performances of conventional (geared equipped) and hydrostatic offshore wind turbines.

Firstly, to maximise energy capture of a conventional turbine, an adaptive torque control technique is proposed through simplifying the conventional extremum seeking control algorithm. Simulations are conducted on the popular National Renewable Energy Laboratory (NREL) monopile 5-MW baseline turbine. The results demonstrate that the simplified ESC algorithms are quite effective in maximising power generation.

Secondly, a TMD (tuned mass damper) system is configured to mitigate loads on a monopile turbine tower whose vibrations are typically dominated by its first mode. TMD parameters are obtained via $\mathcal{H}_2$ optimisation based on a spatially discretised tower-TMD model. The optimal TMDs are assessed through simulations using the NREL monopile 5-MW baseline model and achieve substantial tower load reductions. In some cases it is necessary to damp tower vibrations induced by multiple modes and it is well-known that a single TMD is lack of robustness. Thus a control strategy is developed to suppress wind turbine's vibrations (due to multiple modes) using multiple groups of TMDs. The simulation studies demonstrate the superiority of the proposed methods over traditional ones.

Thirdly, the NREL 5-MW baseline turbine model is transformed into a hydrostatic wind turbine (HWT). An $\mathcal{H}_\infty$ loop-shaping torque controller and a light detection and ranging-based linear-parameter-varying anti-windup pitch controller are designed for the HWT. The tests on a monopile HWT model indicate good tracking behaviours of the torque controller and much improved performances of the

linear-parameter-varying pitch controller over a gain-scheduled PI pitch controller. Finally, the hydraulic reservoir of a barge HWT is made into a bidirectional-tuned-liquid-column-damper (BTLCD) to suppress barge pitch and roll motions. The simulation results validate the effectiveness of the optimal BTLCD reservoir in reducing the tower loads and power fluctuations.

Abbreviations

ADAMS Automatic Dynamic Analysis of Mechanical Systems

AW anti-windup

BTLCD bidirectional tuned liquid column damper

CAE computer-aided-engineering

COM centre of mass

CW continuous wave

DD Digital Displacement

DEQL damage equivalent load

DFIG doubly fed induction generator

DLL dynamic-link-library

DOF degree of freedom

EOM equation of motion

ESC extremum seeking control

ETM extreme turbulence model

EWEA European Wind Energy Association

FAST Fatigue, Aerodynamics, Structures, and Turbulence

FEM finite element method

FRC fully rated converter

HAWT horizontal-axis wind turbine

HPF high-pass filter

HSS high-speed shaft

HST hydrostatic transmission

HWT hydrostatic wind turbine

IEC International Electrotechnical Commission

IMU inertial measurement unit

LDA Laser Doppler Anemometry

LDV Laser Doppler Velocimetry

LIDAR Light Detection and Ranging

LOS line-of-sight

LPF low-pass filter

LPV linear parameter varying

LSS low-speed shaft

MHI Mitsubishi Heavy Industries

MSESC more simplified extremum seeking control

MSL mean sea level

NREL National Renewable Energy Laboratory

NTM normal turbulence model

NWP normal wind profile

O&M operation & maintenance

OC3 Offshore Code Comparison Collaboration

PDE partial differential equation

PIV Particle Imaging Velocimetry

PMG permanent magnet generator

PRC partial rated converter

PSD power spectral density

RMS root-mean-square

RNA rotor nacelle assembly

SCOLE Spacecraft Control Laboratory Experiment

SD standard deviation

SESC simplified extremum seeking control

SH sample-and-hold

SODAR SOnic Detection And Ranging

SQP sequential quadratic programming

TLCD tuned liquid column damper

TLCSD tuned liquid column and sloshing damper

TLSD tuned liquid sloshing damper

TMD tuned mass damper

TSR tip-speed ratio

TTD tower-top displacement

ULF ultimate load factor

VAWT vertical-axis wind turbine

WAMIT Wave Analysis at MIT

Chapter 1

Introduction

1.1 Wind Energy

Wind power has been used as a clean source of renewable energy with sustainable growth in penetration and investments. By 2015, the global installed wind power capacity had reached 432.9 GW [10], surging from only 74 GW in 2006 [11]. The United States aims to install 100,000 MW of wind power by 2020 [3]. By the same year, the EU is estimated to install 230 GW of capacity which will meet 15–17% of EU electricity demand. This will save Europe about €8.5 billion of CO_2 cost per year [12]. Electricity generated from wind is predicted to make up 9.1% of world electricity generation in 2020 [13].

The first offshore wind farm became operational in Denmark in 1991 [14]. Since then, offshore wind capacity installed worldwide has been growing drastically. By January 2016, the UK had the worlds highest offshore wind installed capacity (5,017 MW). It currently possesses the 630 MW London Array which is the world's largest offshore wind farm and is on the trajectory to deploy 10 GW of offshore wind by 2020 [15]. By 2012, the total offshore wind capacity installed by Europe had reached 4,995 MW. The European Wind Energy Association (EWEA) has projected installation of 40 GW of offshore wind by 2020 and 150 GW by 2030. EWEA predicts that by 2030 electricity generated by EU offshore wind will meet 14% of EU electricity demand [12]. By May 2014 the total installed offshore wind capacity in China was 565 MW [16], while it installed 636 MW of offshore wind in 2016 alone. This is driven by the Chinese target of installing 30 GW of offshore wind capacity by 2020. Until 2015, the United States had no offshore wind farms. However, it had launched 21 projects by then to achieve its goals of having 3 GW of offshore wind capacity by 2020, 22 GW by 2030, and 86 GW by 2050 [17]. By 2020, global

installed offshore wind capacity is expected to reach 75 GW [18].

The motivations for the significantly increasing offshore wind installation are as follows:

a. The global offshore wind resource is abundant. For instance, the UK's total available offshore wind capacity is estimated to be 675 GW which is more than 6 times the present UK electricity demand [19].
b. The wind tends to blow faster offshore than on land. A small increase in wind speed induces a considerable growth in energy generation, e.g., a turbine in a 15-mph wind can produce twice as much electricity as it does in a 12-mph wind [20]. Hence, much more energy can be generated offshore.
c. Offshore wind is less turbulent than on land and thus is a more reliable energy source.
d. Offshore wind farms cause no noise effect or visual impact if located sufficiently off the coast.
e. The huge area of offshore zones enables turbine installations without hindering other land utilisations [4].

1.2 Wind Turbine System

Wind turbines are designed to convert the kinetic energy of local wind into electricity. They can rotate about either a horizontal axis or a vertical axis, the former and the latter being named horizontal-axis wind turbines (HAWTs) and vertical-axis wind turbines (VAWTs) respectively. Since HAWTs are able to produce more electricity from a given amount of wind than VAWTs, they dominate the wind industry. Figure 1.1 shows the tower and RNA (rotor nacelle assembly) of a modern typical conventional HAWT. The RNA is located at the top of the tower. The rotor comprises the blades and hub. The nacelle supports the generator and drivetrain. The drivetrain of a conventional HAWT is a series of mechanical components including the low-speed shaft (LSS), the gearbox, and the high-speed shaft (HSS). When wind blows past the blades, it lifts and rotates them, causing the rotor shaft to spin, thus capturing wind energy. This process triggers the LSS connected to the gearbox to spin. The gearbox increases the LSS speed into the HSS speed. The HSS drives the generator to produce electricity. In Figure 1.1, the rotor is in upwind position (facing the wind) and has three blades. This design is generally adopted by HAWT rotors mainly due to the following factors:

a. An upwind design avoids the wind shade behind the tower.
b. Each blade root bears a cyclic load as a consequence of wind shear (the variation

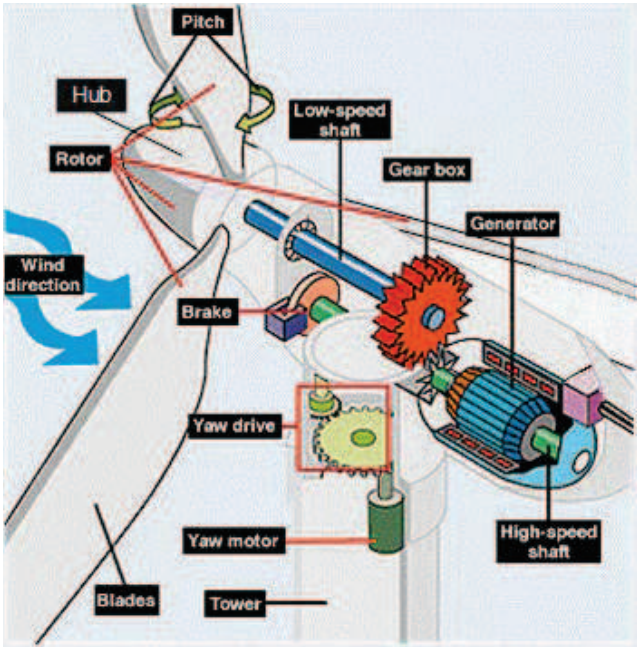

Figure 1.1: Tower and RNA of a modern typical conventional HAWT. This figure is taken from the paper [3].

in wind speed with altitude), yawing, etc. For three-bladed turbines, these cyclic loads are symmetrically balanced when combined together at the LSS, producing a constant load at the drivetrain. However, for one- and two-bladed wind turbines, they combine into a fluctuating load which leads to unnecessary wear on the drivetrain. Hence, one- and two-bladed wind turbines require teetering hubs to reduce this load, which adds complexity to the turbine design.

c. More than three blades are rarely used primarily because of the higher costs associated with the additional blades.

For offshore turbines, towers are installed on substructures with a variety of designs. Monopiles (see the left-hand diagram in Figure 1.2) are the most commonly used substructure and have been largely installed in water up to 30 m deep [2]. A monopile is made of a cylindrical steel tube with one end driven into the seabed and the other end connected to the tower through a transition piece. In many countries (e.g., the United States, China, Norway, and Japan), rich offshore wind resource is available in water deeper than 30 m where monopiles are economically infeasible due to technical difficulty in driving them into deepwater seabed [4]. Hence, fixed-bottom substructures including tripods, quadpods, and jackets have been used in water of 30–60 m deep. In water up to 60–900 m deep, floating substructures will

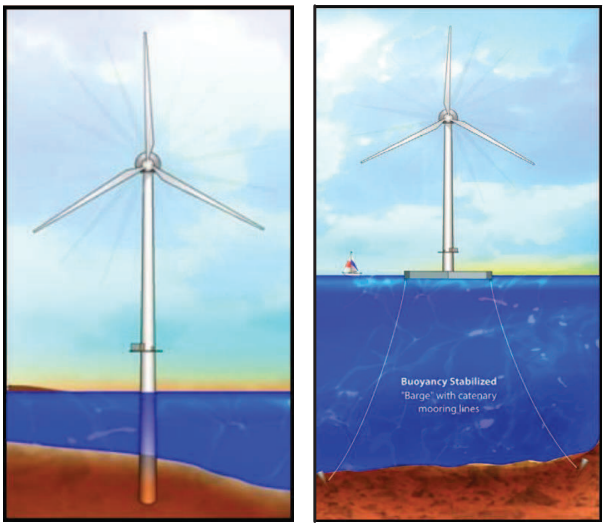

Figure 1.2: Monopile (left) and barge (right) substructures of offshore wind turbines [4].

be the most economical [21]. The National Renewable Energy Laboratory (NREL) has proposed a floating substructure concept—a barge with barge-fastened mooring lines anchored to the seabed to hold the barge in position against winds and waves (see the right-hand diagram in Figure 1.2). This substructure is simple in its design, fabrication, and installation [4].

Wind turbines keep growing in size and rating, especially in the offshore case where the rotor diameter rises from 35 m for the first offshore turbine (450 kW) to 190 m for the currently largest one (10 MW). The average hub height of offshore turbines was 100 m in 2015 and is predicted to reach 125 m in 2027 [22]. These are driven by the fact that larger turbines are more cost-efficient in terms of per unit of electricity [23]. Larger turbines with taller towers and larger swept area of blades can capture more energy without a corresponding increase in turbine mass owing to advances in materials. They even save materials and assembly cost since the number of total turbines needed to produce the same amount of power is reduced. Furthermore, wind energy deployments further off the coast are less restricted by land planning, noise effect, and visual impact, which facilitates the installations of larger turbines.

1.3 Hydrostatic Wind Turbine

The gearbox of a conventional offshore turbine (see Figure 1.1) is one of the largest contributors to the turbine's overall operation & maintenance (O&M) cost [24, 25] due to several reasons:

a. Gearboxes suffer high failure rates principally resulting from underestimation of actual operating loads, impact loads on bearings (under unexpected operating conditions, e.g., grid loss, grid faults, wind gusts, etc.), and misalignment between the gearbox output shaft and the HSS [26]. Their failure rates grow as turbines are built offshore with increasingly large sizes. This is mainly due to three reasons. First, turbines with larger sizes tend to fail more frequently [27, 28]. Second, gearbox bearings have to bear higher loads caused by higher wind speeds and harsher weather offshore. Finally, it is difficult to access offshore turbines, and unfavourable offshore weather conditions hamper maintenance services. According to the paper [25] which investigated about 350 European offshore turbines (2–4 MW) over 5 years, the gearbox is the largest contributor making up 59% of the turbine failures which require major component replacements.
b. The gearbox repair cost is high predominantly because of expensive crane services required. The paper [25] showed that the average replacement cost of the gearbox is €230,000.
c. The gearbox also causes the longest downtime per failure among all the turbine components [29]. One reason is that its complex repair procedures incur high repair time per failure. The average repair time for a major gearbox replacement can be as long as 10 days [25]. Travel time and probably delayed maintenance due to unfavourable offshore weather also contribute to the long downtime. As calculated by Ran et al. [30], the daily average revenue loss during the downtime of a 4-MW offshore turbine is as high as £6,720.
d. The gearbox is one of the components requiring the most technicians after failing, resulting in high labour costs per failure. The paper [25] recorded an average of 17.2 technicians needed for a major gearbox replacement.

To address the gearbox issue, direct-drive turbines are designed with a permanent magnet generator (PMG) directly coupled to the rotor (without a gearbox). In the past, the low-speed high-torque direct-drive PMG was massive, resulting in a heavy nacelle and thus high costs for sufficiently stiff supporting structures. Accordingly, Siemens has developed innovative technologies which have remarkably reduced the nacelle mass of a 6-MW direct-drive turbine to a level even less than

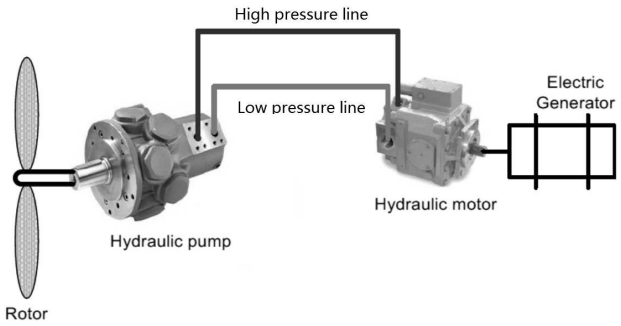

Figure 1.3: Main components of a typical HST drivetrain in the HWT and their connections [5].

that of its geared equipped counterpart [31]. However, direct-drive PMGs still have the following downsides:

a. The manufacturing cost of a PMG is nearly 40% higher than that of a doubly fed induction generator (DFIG, normally used in a geared equipped turbine) with the same rated power [32].
b. A direct-drive PMG necessitates a fully rated converter (FRC) to synchronise its output frequency with the grid frequency while a DFIG is connected to the grid via a partial rated converter (PRC). The cost of an FRC is 60% higher than that of a PRC with the same rating [32]. Besides, Carroll et al. [33] indicated that the failure rate of an FRC is about 5.6 times that of its PRC counterpart.

Another solution is to replace the gearbox drivetrain with a more reliable hydrostatic transmission (HST) one. A turbine with an HST drivetrain is called a hydrostatic wind turbine (HWT). Figure 1.3 represents a typical HST drivetrain [5]. The rotor is directly coupled to a hydraulic pump in the nacelle, driving the high pressurised fluid to operate a hydraulic motor which is coupled to a generator to produce electric power. The low pressure line transports the low pressure fluid back to the pump from the motor. An HST generally needs a hydraulic reservoir as an auxiliary device. A portion of the hydraulic fluid provided by the motor is imported to the reservoir for heat dissipation, contaminant settling and deaeration [24, 34]. Meanwhile, an equivalent amount of fluid is charged into the low pressure line from the reservoir for circulation. When the pump and/or the motor have variable displacements, through controlling the displacement(s), the HST offers continuously variable transmission from the rotor/pump shaft speed to the motor/generator shaft speed. This allows the utilisation of a synchronous generator without the need for power electronics to match the grid frequency [24], which

lowers the turbine capital cost and reduces power losses (due to the inefficiency in the switching operation of power electronics) [35].

The motor & generator of an HST drivetrain can be either configured at the tower base or in the nacelle. The tower-base HST configuration can reduce the nacelle mass of a conventional 5-MW turbine by about 2/3 [36], which saves the costs in the supporting structures and transportation & installation of turbine components, thus reduces the turbine capital cost. The report [24] demonstrated that the O&M cost of a conventional 5-MW offshore turbine can reduce by over 60% when using the tower-base HST drivetrain based on the following facts:

a. The mean time between repairs of the HST can be more than 50% longer than the gearbox.
b. The pump/motor is composed of modular lightweight components which, when configured in the nacelle, can be repaired/replaced using the turbine's internal hoist without the need for a costly external crane.
c. The tower-base HST configuration enables easier access to the motor and generator.
d. The HWT does not need power electronics that is one of the turbine components which are most likely to fail.

According to [24], the in-nacelle HST configuration has even less O&M cost than its tower-base counterpart mainly because it has significantly shorter hydraulic lines filled with much less fluid and thus lower cost in regular fluid replacements. But the in-nacelle configuration has a higher capital cost than its tower-base counterpart because of the substantial reduction of the nacelle mass in the tower-base configuration. Having said that, the overall costs (including capital cost and O&M cost) are similar between the two HST configurations [24].

A disadvantage of a conventional HST was its low partial-load efficiency [37, 34]. This problem was solved in 2011 by Artemis Intelligent which invented the Digital Displacement (DD) technology for HST systems. Artemis tested a DD HST drivetrain designed for a 1.6-MW turbine, which showed high efficiencies over the drivetrain's entire operating range [37]. In 2013, Artemis and its parent company Mitsubishi Heavy Industries (MHI) first installed a DD HST in a 2.4-MW in-house wind turbine in Yokohama, Japan. Soon after that, the excellence of DD technology has been demonstrated on a 7-MW HWT installed at the Hunterston offshore turbine test facility in Scotland. A DD HST drivetrain has also been installed in the world's biggest floating turbine (7 MW) which has been moored (and under operation) 20 km off the coast of Fukushima in Japan since 2015 [38]. These show that the DD HST is a quite promising alternative to the gearbox of a conventional

offshore turbine.

1.4 Wind Turbine Control

Both a conventional turbine and an HWT have 2 control levels [3]. The upper level is accomplished by a supervisory controller which starts and stops the turbine depending on the detected turbine and wind conditions. On the lower level is closed-loop control including torque control, blade pitch control, yaw control, and structural control. The torque controller regulates the rotor reaction torque and thus the rotor speed, through controlling the generator torque for a conventional turbine or the displacement of the hydraulic machine for an HWT. The blade pitch controller generates the blade pitch command following which the pitch actuator turns the blade to keep the rotor speed within its operating limits as the wind speed varies. The yaw control system (including the brake, the yaw drive, and the yaw motor as shown in Figure 1.1) rotates the rotor to face into the wind, ensuring maximal electric power to be extracted as the wind direction changes. Since yaw control is slow, it interests control engineers less than torque and pitch control [3]. Structural control [39] is initially used in civil engineering to protect structures from dynamic loadings due to earthquakes, strong winds, waves, etc. It has been employed to suppress vibrations in wind turbines [40, 41, 42, 43, 44, 45]. Structural control is divided into three major categories: passive, semi-active and active control [46]. Passive structural control is the simplest among them since it needs no external power and uses structural motions to generate control forces. A semi-active structural control device requires power from a small external source and uses structural motions to develop control forces which are regulated by the power source. An active structural control system requires a large power source to produce control forces based on the measurements of external excitations and/or structural responses [47]. In this thesis, only closed-loop control (more specifically, torque, pitch, and passive structural control) is considered.

Both a conventional turbine and an HWT have 3 main operating regions as shown in Figure 1.4 which illustrates the steady-state relationship between the captured power and the wind speed. Region 1 means that the wind speed is below its cut-in value where the turbine does not work or just starts up, and extracts no power from the wind. Region 1 operation is addressed by the supervisory controller and thus not considered in this thesis. As the wind speed increases above the cut-in value but below the rated value, the wind turbine operates in Region 2 where the extracted power from the wind needs to be maximised by optimising the turbine's

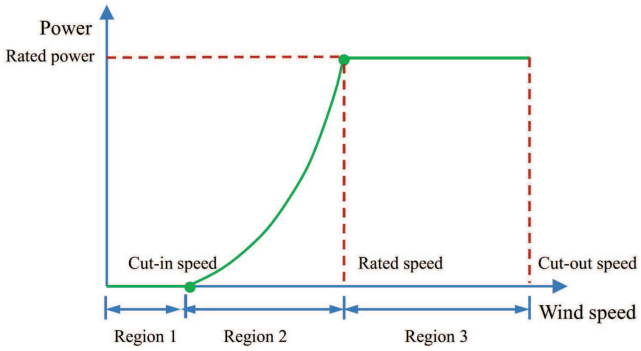

Figure 1.4: Steady-state power-versus-wind-speed curve of turbines.

power coefficient C_p defined as the ratio of the rotor power p_r to the available power from the wind p_{wind}:

$$C_p = \frac{p_r}{p_{wind}} \tag{1.1}$$

where

$$p_r = \tau_{aero}\omega_r, \qquad p_{wind} = \frac{1}{2}\rho_a \pi R^2 V^3. \tag{1.2}$$

τ_{aero} is the aerodynamic torque extracted by the rotor from the wind, ω_r is the rotor shaft speed, ρ_a is the air density, R is the rotor radius, and V is the rotor effective wind speed. The tip-speed ratio (TSR) is

$$\lambda = \frac{\omega_r R}{V}. \tag{1.3}$$

C_p is a function of λ and the blade pitch angle β, and it has a unique global maximum C_p^* at $\lambda = \lambda^*$ and $\beta = \beta^*$ (the superscript star denotes an optimal value) [3]. In Region 2, the blade pitch controller does not work and saturates the pitch angle at its lower limit which is set to be β^*. Thus, maximising wind power extraction means maintaining C_p at its maximum C_p^* through regulating the rotor speed to make λ track λ^*, which is achieved by torque control. In Region 3 the wind is above the rated speed where there is more power available from the wind than actually needed. To avoid electrical and mechanical overloads, the torque and pitch controllers work together to keep the turbine output power and rotor speed around their respective rated values [3]. The passive structural control device operates whenever the main structure to which it is attached vibrates, regardless of the turbine's operating region.

1.5 Motivations and Research Contributions

The focus of this thesis is performance improvements of both conventional (geared equipped) and hydrostatic offshore wind turbines in the following aspects:

a. According to the paper [3], if the US achieves its goal of 100,000 MW of wind power installation by 2020, a 3% loss in wind energy capture would cause a loss of $300 million per year. Hence, the development of a torque controller to effectively maximise the power capture in Region 2 is of great necessity. An adaptive torque control technique is proposed through simplifying the conventional extremum seeking control (ESC) algorithm. The simulations on the popular NREL 5-MW baseline monopile turbine model show that the proposed method enhances the turbine's energy capture over a standard control law.

b. As offshore turbines are getting larger and deployed further offshore, towers are required to be stronger and heavier in order to support heavier tower-top masses, and stand against more severe weather, turbulence, and wave conditions. This incurs expensive structural supporting materials and high transportation & installation costs for turbine components. A feasible solution to this issue is to develop control techniques to mitigate vibration loads acting on turbine towers, which enables the construction of lighter and cheaper towers, and increases the towers' life expectancy. The load reduction of a monopile-tower assembly (also referred to as a monopile tower) is investigated. Because the first tower bending mode dominates the dynamic response of a typical monopile tower [48], tower loads can be significantly reduced by only damping vibrations caused by the first tower mode. For this purpose a tuned mass damper (TMD) system is configured on the nacelle floor. The monopile turbine is modelled using a non-uniform NASA SCOLE (Spacecraft Control Laboratory Experiment) system. Based on it tower dynamics can be accurately simulated, and optimal TMD parameters can be derived through $\mathcal{H}_2$ optimisation. The optimal TMD system is validated to considerably mitigate the tower loads through simulations using the NREL 5-MW baseline monopile turbine model (see also [49, 50]). This work also demonstrates how to optimally tune a TMD to reduce vibrations of a flexible structure described by partial differential equations (PDEs).

c. Although the first bending mode dominates monopile tower vibrations, the second bending mode can play a non-negligible part in tower fatigue damage in some cases [51, 52]. Besides, real monopiles are not ideally fixed into the seabed due to soil-pile interactions, which causes variations of modal frequencies over time [53]. This will not only deteriorate effectiveness of the TMD tuned for

the original first tower mode (because the first tower modal frequency deviates from its original value used for the TMD design), but also possibly cause increased coupling between higher tower modal frequencies and rotor harmonic frequencies. The latter phenomenon was observed by [54] where the second tower bending modal frequency coincided with the 6P (with 1P being the rotor rotational frequency) rotor harmonic frequency (resulting in higher loads and larger fatigue damage to the monopile tower). Therefore, it is worth developing a control scheme to suppress multiple tower vibration modes simultaneously and at the same time improve robustness of the TMD system. Accordingly, the preceding TMD optimisation scheme is extended to the design of multiple TMDs for the vibration reduction of the non-uniform SCOLE beam system (used above to model monopile turbine towers) with multiple dominant vibration modes. Note that the SCOLE model rather than the NREL monopile tower is used as the illustrative application, because the former can be parameterised to have multiple dominant modes while the latter has only one dominant mode. The extended control method takes into account the trade-off between effectiveness and robustness when optimising multiple TMDs. Through simulation studies, the optimal multiple TMDs are shown to be quite effective in damping multiple vibration modes simultaneously and are robust against variations of modal frequencies of the SCOLE model (see also [55, 56]).

d. As discussed in Section 1.3, the HST drivetrain is a quite promising alternative to its conventional gearbox counterpart. However, there has been lack of research on the development of advanced torque and pitch control strategies to achieve satisfactory performances on a detailed HWT simulation model (coupling aerodynamics, hydrodynamics, control and servo dynamics, and structural dynamics). Hence, the NREL offshore 5-MW baseline wind turbine model within the FAST (Fatigue, Aerodynamics, Structures, and Turbulence) code is transformed into a detailed HWT model by replacing its drivetrain with an HST one. Then an $\mathcal{H}_\infty$ loop-shaping torque controller and a linear parameter varying (LPV) blade pitch controller are designed for the HWT. To enhance performances of the pitch control system during the transition around the rated wind speed, an anti-windup (AW) compensator is added to the LPV controller (which would otherwise have had undesirable system responses due to pitch saturation). The LPV AW pitch controller uses the steady rotor effective wind speed as the scheduling parameter which is estimated by LIDAR (Light Detection and Ranging) preview. The simulations based on the transformed HWT model with a monopile substructure show that the torque controller achieves

very good tracking behaviour while the LPV pitch controller (no matter with or without AW) gets much improved overall performances over a gain-scheduled PI pitch controller (see also [57, 58]).

e. The barge (see Figure 1.2) is a quite promising substructure for a floating turbine. However, its rotational motions can not only cause large fluctuations in the rotor speed and generator power, but also cause considerable load variations on the turbine, especially on the tower base [4]. For a barge HWT with a tower-base HST configuration where the reservoir can be placed on the barge, a spin-off application of the reservoir is proposed to suppress pitch and roll motions of the barge. More specifically, the reservoir is made into a shape of an annular rectangular to serve as a bidirectional tuned liquid column damper (BTLCD). This means a barge-motion damper is configured with negligible extra costs as an HST needs a reservoir anyway. The coupled dynamics of the barge-reservoir system are incorporated into the transformed HWT model (mentioned above) with the NREL barge substructure by using Lagrange's equations. Two simplified turbine-reservoir models are used to optimise the parameters of the BTLCD reservoir, which describe the pitch and roll motions of the turbine-reservoir system respectively. Simulation results based on the barge HWT model show that the optimal BTLCD reservoir is very effective in mitigating pitch and roll motions of the barge under realistic wind and wave excitations, which reduces the tower load and improves the power quality (see also [59, 60]).

1.6 Thesis Outline

This thesis is organised as follows. Chapter 2 introduces several NREL computer-aided-engineering (CAE) tools (TurbSim, FAST, and MLife) and the NREL offshore 5-MW baseline (geared equipped) wind turbine model. Chapter 3 investigates maximum power capture of a conventional wind turbine operating in Region 2 using the conventional ESC algorithm and its two simplified versions. Chapter 4 first studies the load reduction of a monopile wind turbine tower using a TMD system derived through $\mathcal{H}_2$ optimisation. Then it extends this research to suppress vibrations of the non-uniform SCOLE beam system (used to model monopile turbine towers) with multiple dominant modes by employing multiple TMDs. Chapter 5 transforms the NREL 5-MW baseline turbine model into an HWT by replacing its gearbox drivetrain with the typical HST one illustrated in Figure 1.3. Then it designs torque and blade pitch controllers for the transformed HWT (with a monopile substructure) working in its entire operating range. Chapter 6 proposes to take advantage of the

HST reservoir to suppress barge pitch and roll motions by making it into a BTLCD configuration for a barge HWT (with a tower-base HST configuration). It modifies the FAST code to incorporate coupled dynamics of the barge-reservoir system into the transformed HWT model with the NREL barge substructure. It also develops a scheme to optimise parameters of the BTLCD reservoir. Finally Chapter 7 concludes this thesis.

Chapter 2

NREL Computer-Aided Engineering Tools and NREL Offshore 5-MW Baseline Wind Turbine Model

This chapter introduces NREL computer-aided-engineering (CAE) tools TurbSim, FAST, and MLife, as well as the NREL offshore 5-MW baseline (geared equipped) wind turbine model. In this thesis, they are used for the design of controllers and simulation studies.

2.1 Stochastic Inflow Turbulence Simulator—TurbSim

NREL TurbSim is utilised to simulate stochastic, full-field, and turbulent wind flows. TurbSim generates a time series of wind speed vectors at points in a two-dimensional vertical rectangular grid fixed in space [61]. Each wind speed vector has three components: u (longitudinal—along the direction of the mean wind velocity), v (crosswise—perpendicular to u and horizontal), and w (vertical—perpendicular to u and v). The height and width of the grid, and the numbers of vertical and crosswise grid points can be specified in the TurbSim input file. The grid points are uniformly distributed in both the crosswise and vertical directions. The grid top is aligned with the rotor disk top, and the grid bottom must be above the mean sea level (MSL). The rotor is crosswise centred on the grid.

The IEC (International Electrotechnical Commission) normal wind profile (NWP) model in TurbSim is used to determine the mean value of u-component

wind speeds at the grid points with the same height. The IEC Kaimal spectral model (giving a good description of atmospheric turbulence [62]) with either the IEC normal turbulence model (NTM) or the IEC extreme turbulence model (ETM) is utilised to determine wind data. The data contain spectra of the three wind components and the spatial coherence between wind speed vectors at any two different grid points in the frequency domain. With these data, TurbSim uses an inverse Fourier transform to create the time series.

2.1.1 Normal Wind Profile Model

The IEC NWP model gives the mean value of u-component wind speeds at the gird points with the same height z as

$$\bar{u}(z) = \bar{u}_{hub}\left(\frac{z}{z_{hub}}\right)^{\alpha_{pl}} \tag{2.1}$$

where $\bar{u}_{hub}$ is the mean u-component wind speed at the hub height, z_{hub} is the hub height, and α_{pl} is the power law exponent whose default value is 0.14 for offshore wind turbines [62]. The mean $v-$ and $w-$component wind speeds are zero at all the grid points.

2.1.2 IEC Kaimal Spectral Model with NTM/ETM

The IEC Kaimal spectral model describes the relationships among standard deviations of the three wind components (σ_K where $K = u, v, w$) at each grid point as

$$\sigma_v = 0.8\sigma_u,\ \sigma_w = 0.5\sigma_u. \tag{2.2}$$

Then the spectra of the three wind components at each grid point are

$$S_K(f) = \frac{4\sigma_K^2 L_K/\bar{u}_{hub}}{\left(1 + 6fL_K/\bar{u}_{hub}\right)^{5/3}} \tag{2.3}$$

where f is the frequency in Hz. L_K is the integral scale parameter:

$$L_K = \begin{cases} 8.10\Lambda_u, & K = u \\ 2.70\Lambda_u, & K = v \\ 0.66\Lambda_u, & K = w \end{cases}. \tag{2.4}$$

Λ_u is the turbulence scale parameter:

$$\Lambda_u = 0.7 \min\left(60\,m,\, z_{hub}\right). \tag{2.5}$$

If using the standard IEC turbulence category A, B, or C (with A being the most turbulent) to specify the turbulence intensity I_{turb}, the IEC NTM determines σ_u as below to derive (2.2) and (2.3):

$$\sigma_u = I_{turb}\left(0.75\bar{u}_{hub} + 5.6\right) \tag{2.6}$$

where

$$I_{turb} = \begin{cases} 0.16, & \text{category A} \\ 0.14, & \text{category B} \\ 0.12, & \text{category C} \end{cases}. \tag{2.7}$$

If specifying I_{turb} in percent, the IEC NTM determines σ_u as

$$\sigma_u = \frac{I_{turb}}{100}\bar{u}_{hub}. \tag{2.8}$$

The IEC ETM only accepts I_{turb} specified using the standard IEC turbulence category. The IEC ETM has three classes: 1, 2, and 3. It calculates σ_u as

$$\sigma_u = 2I_{turb}\left(0.072\left(0.1V_{ref} + 3\right)\left(\frac{\bar{u}_{hub}}{2} - 4\right) + 10\right). \tag{2.9}$$

V_{ref} is the reference wind speed:

$$V_{ref} = \begin{cases} 50\,\text{m/s}, & \text{Class 1} \\ 42.5\,\text{m/s}, & \text{Class 2} \\ 37.5\,\text{m/s}, & \text{Class 3} \end{cases}. \tag{2.10}$$

The IEC Kaimal model defines the spatial coherence between the u-components at grid points i and j as

$$Coh_{i,j}(f) = exp\left(-12\sqrt{\left(\frac{fr}{\bar{u}_{hub}}\right)^2 + \left(0.12\frac{r}{L_c}\right)^2}\right) \tag{2.11}$$

where r is the distance between points i and j. L_c is the coherence scale parameter:

$$L_c = 5.67 \min(60\,m,\ z_{hub}). \tag{2.12}$$

The spatial coherence between the $v-/w-$components at points i and j is

$$Coh_{i,j}(f) = \begin{cases} 1, & i = j \\ 0, & i \neq j \end{cases}. \tag{2.13}$$

2.2 Simulator of Wind Turbine Dynamics—FAST

The NREL FAST code is widely employed for simulating aerodynamics, hydrodynamics, control and electrical (servo) dynamics, and structural (elastic) dynamics of offshore turbines. In FAST, equations of motion are set up using Kane's method and solved by numerical integrations [4]. Before running FAST, properties of a turbine composed of rigid and flexible bodies must be specified in its input files to construct a wind turbine model. The rigid bodies include the earth, nacelle, hub, and substructure of a floating turbine while the flexible bodies include the tower, blades, drive shaft, and substructure of a fixed-bottom turbine. These bodies are coupled using several degrees of freedom (DOFs) including the tower bending, blade bending, rotor speed, and drive shaft torsional DOFs. FAST has 6 DOFs for the floating rigid substructure: translational surge, sway, & heave DOFs, and rotational roll, pitch, & yaw DOFs. All the DOFs can be switched on or off in FAST input files.

FAST utilises several coordinate systems for input and output parameters. Its inertial coordinate system $\mathcal{I}$ has the origin O and the set of orthogonal axes $\mathbf{x}_\mathcal{I}, \mathbf{y}_\mathcal{I}, \mathbf{z}_\mathcal{I}$. O is the substructure reference point. The 6 floating substructure motion DOFs are defined about it on which the external loads act [4]. The $\mathbf{x}_\mathcal{I}$-axis points in the nominal downwind direction, the $\mathbf{x}_\mathcal{I}\mathbf{y}_\mathcal{I}$-plane designates the mean sea level (MSL), and the $\mathbf{z}_\mathcal{I}$-axis points upward opposite to gravity along the undeflected tower's centreline when the substructure is undisplaced. FAST has a nacelle inertial measurement unit (IMU) whose location is user-prescribed. FAST can output the displacement, velocity, and acceleration of the nacelle IMU relative to $\mathcal{I}$. u, v, w components of the wind speed vector generated by TurbSim are defined in $\mathcal{I}$ [61]. The nacelle coordinate system in FAST is denoted as $\mathcal{N}$ which is fixed on the tower top and moves with the nacelle. It has the origin O_s (the intersection of the tower's centreline and the tower top connection to the nacelle) and the set of orthogonal

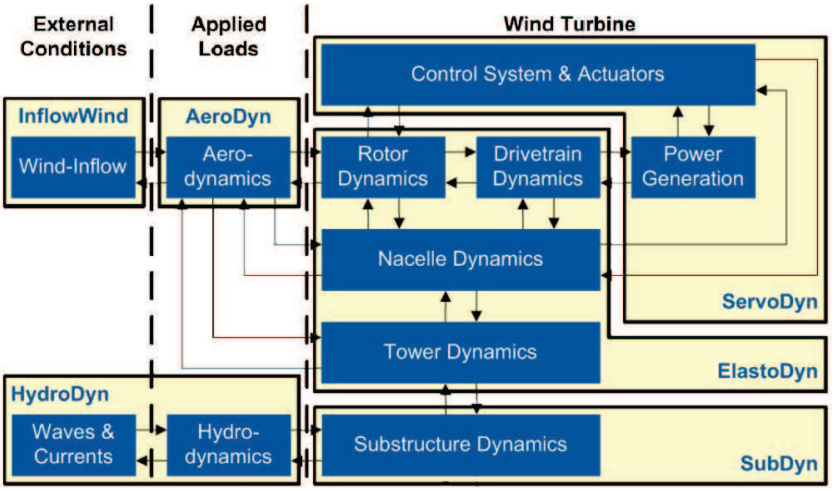

Figure 2.1: Schematic of FAST modules for a fixed-bottom turbine [6].

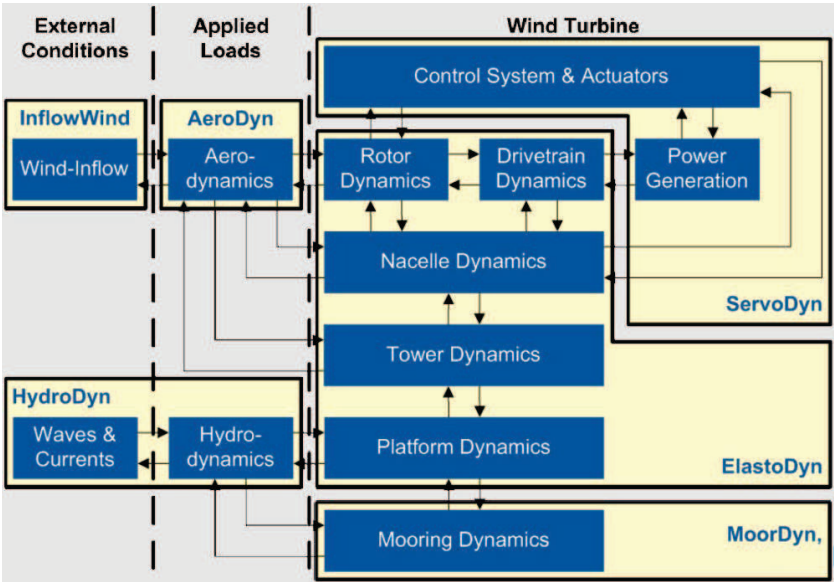

Figure 2.2: Schematic of FAST modules for a floating turbine [6].

axes $\mathbf{x}_{\mathcal{N}}, \mathbf{y}_{\mathcal{N}}, \mathbf{z}_{\mathcal{N}}$ which is parallel with $\mathbf{x}_{\mathcal{I}}, \mathbf{y}_{\mathcal{I}}, \mathbf{z}_{\mathcal{I}}$ when the turbine is undisplaced.

FAST includes InflowWind, AeroDyn, ElastoDyn, ServoDyn, HydroDyn, SubDyn, and MoorDyn modules. Figures 2.1 and 2.2 show the schematics of FAST modules for a fixed-bottom turbine and a floating turbine respectively [6]. InflowWind receives coordinates of various tower and blade nodes from AeroDyn. It computes undisturbed wind velocities (without interactions with the turbine)

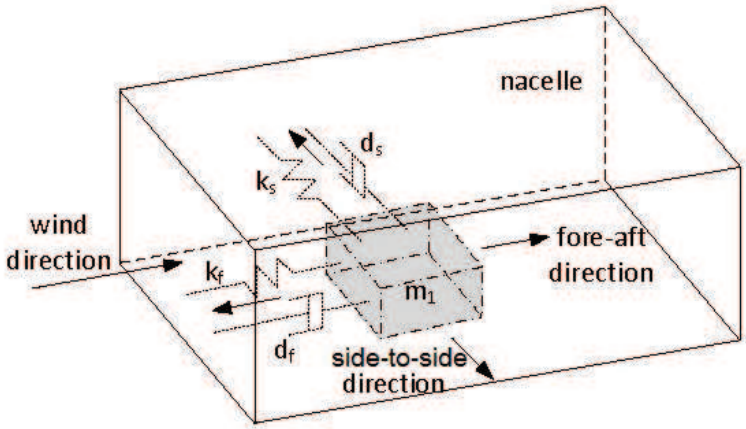

Figure 2.3: Configuration of the in-nacelle TMD system in ServoDyn.

at these nodes through interpolating the time series from TurbSim in time and space based on Taylor's frozen turbulence hypothesis (assuming that the turbulent wind field moves with the mean hub-height wind speed $\bar{u}_{hub}$), and outputs them to AeroDyn [63]. AeroDyn computes aerodynamic loads along blades and tower, and outputs them to ElastoDyn. ElastoDyn is a structural-dynamic model which outputs displacements, velocities, accelerations, and reaction loads to AeroDyn and ServoDyn. For a fixed-bottom turbine, it also outputs tower motion & load data to SubDyn which models the flexible substructure. While for a floating turbine, ElastoDyn simulates dynamics of the 6-DOF rigid substructure, and outputs substructure motion & load data to MoorDyn which models the mooring system. ServoDyn includes control & actuator models for blade pitch, generator torque, nacelle yaw, etc. It also incorporates a TMD system in the nacelle and/or tower for structural control. The TMD system contains two TMDs, one acting in the fore-aft direction and the other in the side-to-side direction. Both TMDs share the same mass component but can have different spring and damping constants. Figure 2.3 shows the configuration of the TMD system in the nacelle. HydroDyn receives substructure motion data from SubDyn (for a fixed-bottom turbine) or ElastoDyn & MoorDyn (for a floating turbine), and calculates hydrodynamic loads on the substructure and returns them back to SubDyn or ElastoDyn & MoorDyn. It allows for three approaches to calculate hydrodynamic loads, based on the potential-flow theory, the strip theory, and the combination of the two respectively. For slender vertical cylindrical substructures extending to the seabed (e.g., monopiles), the strip theory is preferable [4]. It splits the substructure into a number of transverse two-

dimensional slices and calculates hydrodynamic loads by integrating the loads acting on each slice over the substructure length. Strip-theory hydrodynamic loads include added mass and incident-wave inertia loads, and viscous drag associated with the relative velocity between the seawater and the substructure [4]. For the NREL barge, the combination of strip and potential-flow theories is used. The potential-flow theory provides hydrodynamic loads including excitation loads from incident waves, hydrostatic restoring loads, and added mass & damping loads associated with wave radiation. The strip theory produces viscous drag. The potential-flow method necessitates hydrodynamic coefficients which must be supplied by a separate numerical-panel code, e.g., WAMIT (Wave Analysis at MIT) used by FAST [64]. HydroDyn incorporates several incident wave kinematics model to describe wave elevations (closely related to wave-excitation loads). The JONSWAP spectrum is chosen to model irregular waves with no currents. This model depends on two user-prescribed parameters—the significant wave height and peak-spectral period of waves [4].

FAST can be interfaced with MATLAB/Simulink through a Simulink S-Function block. During simulations, this block calls the FAST Dynamic Library which is compiled as a dynamic-link-library (DLL) integrating all the FAST modules [65]. This enables flexible turbine modelling and control design in the Simulink environment. Besides, FAST can conduct linearisation analyses. Before linearisation, an operating point is specified as a set of steady values of the enabled DOF displacements, velocities, & accelerations, and control & wind inputs. FAST numerically linearises the non-linear turbine model at this point by perturbing system variables about their respective steady values, which results in a linear state-space model. In addition, FAST can work as an ADAMS (Automatic Dynamic Analysis of Mechanical Systems) preprocessor. It can generate an ADAMS dataset of a complete aero-hydro-servo-elastic wind turbine model [65] which can be input to the ADAMS Aggregate Mass tool to derive the values of some useful turbine parameters [66].

2.3 Estimator of Fatigue Life—MLife

NREL MLife is employed to compute the short-term damage equivalent load (DEQL) which is usually regarded as a measurement of the fatigue load. MLife break downs the load time series from the FAST simulation into a set of cycles, and computes the load mean and load range of each cycle, using rainflow counting [67, 68]. Then it transforms the ith cycle's load range L_i^R with a load mean L_i^M to a load range

L_i^{RF} with a load mean L^{MF}:

$$L_i^{RF} = L_i^R \left(\frac{L^{ult} - \left| L^{MF} \right|}{L^{ult} - \left| L_i^M \right|} \right). \tag{2.14}$$

L^{MF} is the mean of the load time series and is the same for all the cycles. L^{ult} represents the ultimate design load obtained by multiplying the maximum of the time series with an ultimate load factor (ULF) which is set to be 20 according to the report [69]. Then MLife bins each cycle. The number of load-range bins is set to be 60 following Sutherland [70]. The width of each bin is

$$\Delta^R = \frac{L_{max}^R}{60} \tag{2.15}$$

where L_{max}^R is the maximum L_i^{RF}. The bin index k for the load range L_i^{RF} is

$$k = \left\lceil \left(\frac{L_i^{RF}}{\Delta^R} \right) \right\rceil \tag{2.16}$$

where $\lceil x \rceil$ is the smallest integer not less than x. Then the load-range value L_k^R for the kth bin is

$$L_k^R = \left(k - \frac{1}{2} \right) \Delta^R. \tag{2.17}$$

The short-term DEQL $DEQL^{STF}$ is defined as a constant-amplitude load applied over the elapsed time of the time series T_{et} which produces the same damage as caused by the loads from the FAST simulation over T_{et} [67]:

$$DEQL^{STF} = \left(\frac{\sum_k \left(n_k^F \left(L_k^R \right)^m \right)}{f^{eq} T_{et}} \right)^{\frac{1}{m}} \tag{2.18}$$

where n_k^F is the total number of cycles whose transformed load ranges L_i^{RF} fall into the kth load-range bin, f^{eq} is the DEQL frequency set to be 1 Hz, and m is the material-dependent Wholer exponent ($m = 3$ is commonly used for steel [69]).

Table 2.1: Selected gross properties of the NREL offshore 5-MW baseline wind turbine model.

Rated generator power	5 MW
Rated rotor power p_{rr}	5.2966e6 W
Rated generator torque τ_{gr}	43,093.55 N·m
Rotor, hub radius	62.94 m, 1.5 m
Hub height above the mean sea level (MSL) L_{hh}	90 m
Tower-top height above the MSL	87.6 m
Tower-base diameter, thickness	6 m, 0.027 m
Tower-top diameter, thickness	3.87 m, 0.019 m
Cut-in, rated, cut-out wind speed	3 m/s, 11.4 m/s, 25 m/s
Cut-in, rated rotor speed	6.9 rpm, 12.1 rpm
Gearbox ratio N_g	97
Rated generator speed ω_{gr}	1,173.7 rpm
Rotor mass	110,000 kg
Nacelle mass	240,000 kg
Rotor inertia J_r	38,759,236 kg·m^2
Generator inertia about the HSS J_g	534.116 kg·m^2
Corner frequency of the generator-speed low-pass filter	0.25 Hz
Maximum power coefficient C_p^*	0.482
Optimal TSR λ^*	7.55
Optimal torque gain K	0.025576386 N·m/rpm^2

2.4 NREL Offshore 5-MW Baseline Wind Turbine Model

The well-known NREL offshore 5-MW baseline (geared equipped) wind turbine is a representative utility-scale large offshore turbine model whose dynamic responses can be simulated by FAST (see Section 2.2). Table 2.1 lists some gross properties of this turbine model [4]. The diameter and thickness of the steel tower linearly decrease from the tower base to top.

The substructures used in this thesis are the NREL OC3 (Offshore Code Comparison Collaboration) monopile and NREL ITI Energy barge. Tables 2.2 and 2.3 summarise undistributed and distributed properties of the NREL OC3 monopile 5-MW wind turbine tower [1]. In Table 2.3, Elevation is the vertical position along the tower centreline relative to the mudline, HtFract is the fractional height from

Table 2.2: Undistributed properties of the NREL OC3 monopile 5-MW wind turbine tower.

Monopile diameter, thickness	6 m, 0.06 m
Tower-base height above the MSL	10 m
Water depth (from the MSL down to the mudline)	20 m
Overall mass	522,617 kg

Table 2.3: Distributed properties of the NREL OC3 monopile 5-MW wind turbine tower [1].

Elevation (m)	HtFract (-)	TMassDen (kg/m)	TwFAStif (Nm^2)	TwSSStif (Nm^2)
0.00	0.00000	9,517.14	1,037.13e9	1,037.13e9
30.00	0.27881	9,517.14	1,037.13e9	1,037.13e9
30.00	0.27882	4,306.51	474.49e9	474.49e9
37.76	0.35094	4,030.44	413.08e9	413.08e9
45.52	0.42306	3,763.45	357.83e9	357.83e9
53.28	0.49517	3,505.52	308.30e9	308.30e9
61.04	0.56729	3,256.66	264.08e9	264.08e9
68.80	0.63941	3,016.86	224.80e9	224.80e9
76.56	0.71153	2,786.13	190.06e9	190.06e9
84.32	0.78365	2,564.46	159.49e9	159.49e9
92.08	0.85576	2,351.87	132.77e9	132.77e9
99.84	0.92788	2,148.34	109.54e9	109.54e9
107.60	1.00000	1,953.87	89.49e9	89.49e9

the mudline (0) to the tower top (1) along the tower centreline, TMassDen is the tower section mass per unit length, TwFAStif is the tower section fore-aft stiffness, and TwSSStif is the tower section side-to-side stiffness. The NREL ITI Energy barge is rigid, square, and moored by 8 catenary lines as illustrated in Figure 2.4 [4]. Each corner of the barge is linked to 2 lines which are 45° apart at the corner when the barge is undisplaced. Table 2.4 lists some tower and barge properties of the NREL ITI Energy barge 5-MW turbine model [4].

The standard control system for the NREL 5-MW baseline turbine includes a generator torque controller and a full-span rotor-collective blade pitch controller [7]. They regulate the turbine output power following the steady-state power curve

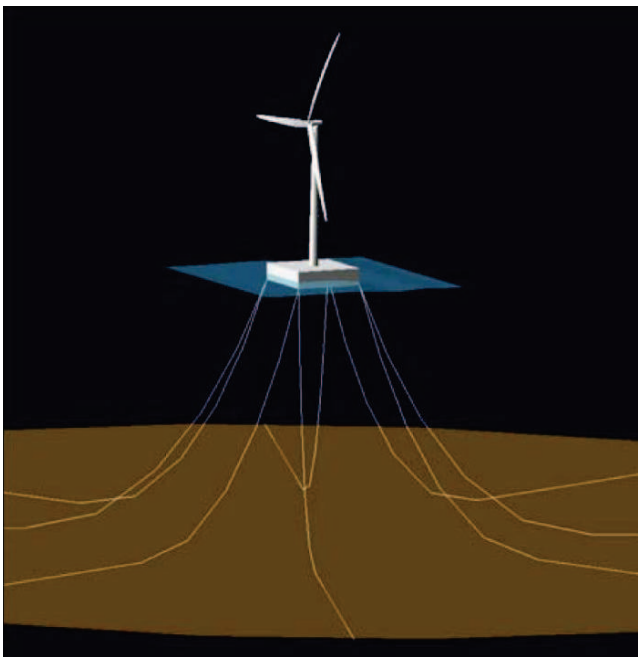

Figure 2.4: NREL ITI Energy barge 5-MW wind turbine [4].

Table 2.4: Selected tower and barge properties of the NREL ITI Energy barge 5-MW wind turbine model.

Barge size (width×length×height)	40 m×40 m×10 m
Tower-base height above the MSL	0 m
Water (anchor) depth (from the MSL down to the mudline)	150 m
Distance from the mass centre of the undeflected tower & RNA to O (L_t)	63.97 m
Distance from the mass centre of the barge to O (L_p)	0.28 m
Barge mass m_p	5,452,000 kg
Tower mass	347,460 kg
Barge pitch inertia about O (I_{bp})	7.27e8 kg·m^2

shown in Figure 1.4 where the cut-in, rated, and cut-out wind speeds are given in Table 2.1. There are 5 control regions 1, 1.5, 2, 2.5, and 3 as illustrated in Figure 2.5, based on the measurement of the generator speed (filtered by a low-pass filter to reduce the impact of high-frequency generator speed components on control system behaviours). Region 1 is below the filtered generator speed of 670 rpm (corresponding to the cut-in rotor speed of 6.9 rpm), where the generator torque

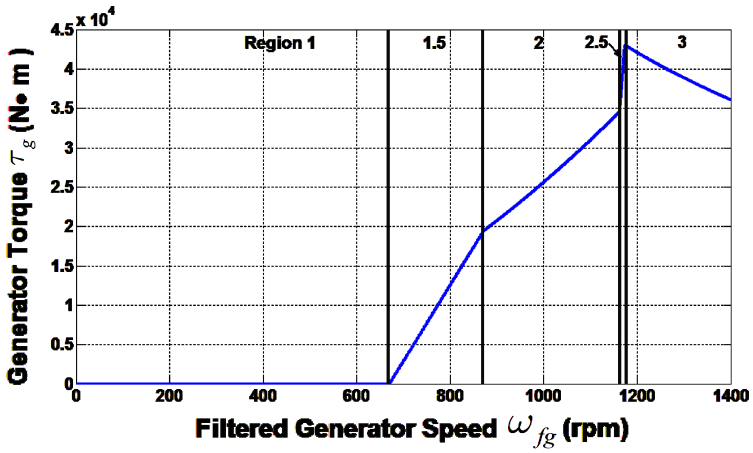

Figure 2.5: Torque-versus-speed curve of the NREL offshore 5-MW baseline model [7].

is zero, and the turbine extracts no power from the wind. Region 1.5 is a linear transition between Regions 1 and 2 where the filtered generator speed is between 670 rpm and 871 rpm (30% above 670 rpm). As the filtered generator speed increases to above 871 rpm but below 1,161.96 rpm (99% of the rated speed of 1,173.7 rpm), the turbine works in Region 2 where the control aim is to maximise power capture. A so-called standard control law is applied to set the generator torque τ_g to be proportional to the square of the filtered generator speed ω_{fg}:

$$\tau_g = K\omega_{fg}^2 \tag{2.19}$$

where the value of the gain K (see Table 2.1) is obtained from

$$K = \frac{1}{2}\rho_a \pi R^5 \frac{C_p^*}{(\lambda^*)^3 N_g^3}. \tag{2.20}$$

Assuming there is no torsional motion between the rotor and generator, the rotational motion of the rotor shaft is then described by

$$\dot{\omega}_r = \frac{1}{J_r + N_g^2 J_g}\left(\tau_{aero} - N_g \tau_g\right). \tag{2.21}$$

From (1.1) and (1.2), one can derive

$$\tau_{aero} = \frac{1}{2}\frac{\rho_a \pi R^2 V^3 C_p}{\omega_r}. \tag{2.22}$$

Combining (2.19), (2.20), (2.21), & (2.22), and assuming that $\omega_{fg} = N_g \omega_r$ (neglecting the high-frequency noise of the rotor speed), one can derive

$$\dot{\omega}_r = \frac{\rho \pi R^5 \omega_r^2}{2\left(J_r + N_g^2 J_g\right)} \left[\frac{C_p}{\lambda^3} - \frac{C_p^*}{(\lambda^*)^3}\right]. \tag{2.23}$$

Clearly, if $C_p < \left(C_p^*/(\lambda^*)^3\right)\lambda^3$, then $\dot{\omega}_r < 0$, and vice versa. It means that the standard control law given by (2.19) and (2.20) drives λ towards the optimum λ^* whenever the rotor speed ω_r is too slow or too fast [71]. Region 2.5 is a linear transition between Regions 2 and 3. This region is required to limit the blade tip speed around the rated power and therefore to reduce noise. Below the rated generator speed (1,173.7 rpm), the blade pitch controller does not work and saturates the pitch angle at its lower limit of 0°. In Region 3 above the rated generator speed, the control goal is to maintain the turbine output power and generator speed around their respective rated values. Accordingly, the generator torque is set to be inversely proportional to the filtered generator speed:

$$\tau_g = \frac{p_{rr}}{\omega_{fg}}. \tag{2.24}$$

Note that whenever the blade pitch angle is 1° or greater, the generator torque is calculated following (2.24) to reduce power dips and thus improve output power quality. This may incur short-term drivetrain overloads which can be avoided by setting the maximum allowable torque to be 47,402.91 N·m (10% above the rated value of 43,093.55 N·m). The torque rate is also limited within ±15,000 N·m/s. A gain-scheduled proportional-integral (PI) blade pitch control on the error between ω_{fg} and ω_{gr} is implemented, with the gains of proportional and integral terms K_P and K_I scheduled by the pitch angle β:

$$K_P(\beta) = -\frac{2\left(J_r + N_g^2 J_g\right)\omega_{rr}\zeta_p f_p}{N_g\left[\frac{\partial P_r}{\partial \beta}(\beta = 0°)\right]\left(1 + \frac{\beta}{\beta_K}\right)}, \quad K_I(\beta) = -\frac{\left(J_r + N_g^2 J_g\right)\omega_{rr} f_p^2}{N_g\left[\frac{\partial P_r}{\partial \beta}(\beta = 0°)\right]\left(1 + \frac{\beta}{\beta_K}\right)}, \tag{2.25}$$

where $\omega_{rr} = 12.1$ rpm is the rated rotor speed, $\partial p_r/\partial\beta\,(\beta = 0°)$ =-25.52e6 W/rad is the sensitivity of the rotor power to the pitch angle at $\beta = 0°$, and $\beta_K = 6.302336°$ is the pitch angle at which $\partial p_r/\partial\beta$ doubles its value at $\beta = 0°$ [7]. This scheduling implies that the idealised response of the generator speed error will be like that of a second-order system with the natural frequency of f_p and damping ratio of ζ_p. f_p and ζ_p are 0.6 rad/s and 0.7 for the NREL OC3 monopile 5-MW turbine as

recommended by the report [7], while they are advised to be 0.4 rad/s and 0.7 for the NREL ITI Energy barge 5-MW turbine [4]. The blade pitch rate is restricted within $\pm 8^{\circ}/s$. The upper limit of the blade pitch angle is 90°.

2.5 Conclusions

Several NREL CAE tools which are used for the control design and simulation studies in the following chapters are introduced. TurbSim is used to generate wind speed time series which are passed to FAST for simulating time-domain dynamics of wind turbines. FAST modules integrate aerodynamics models, hydrodynamics models, control and servo dynamics models, and structural dynamics models. FAST can be interfaced with MATLAB/Simulink, which enables simulations, turbine modelling and control design in the Simulink environment. Besides, FAST can provide linearisation analyses and work as the ADAMS preprocessor. To quantify fatigue loads, MLife is used to calculate short-term DEQLs through processing load time series from FAST simulations.

The conventional (geared equipped) wind turbine simulation model utilised throughout this thesis is the NREL offshore 5-MW baseline turbine model within FAST. Monopile and barge substructures are considered. The former is the most widely installed offshore substructure while the latter is a quite promising floating substructure for deepwater deployment. The gross properties of the NREL 5-MW model, properties of the NREL OC3 monopile tower, and properties of the tower and barge of the NREL ITI Energy barge turbine are presented. The standard torque and pitch controllers of the NREL 5-MW baseline turbine are also introduced.

Chapter 3

Maximising Wind Power Capture and Generation Based on Extremum Seeking Control

This chapter investigates the maximum power capture for a conventional (geared equipped) wind turbine operating in Region 2 using extremum seeking control (ESC). Via ESC, the optimal torque gain is obtained with the rotor power as the optimisation objective. The conventional ESC algorithm can be simplified by omitting the low-pass filter (LPF) in the ESC loop and adding a sample-and-hold (SH) block. One advantage of this simplified ESC (SESC) method is that the implementation of the SH is easier than the LPF because the selection of the LPF corner frequency needs not be considered. SESC also removes the influence of the LPF on the dynamics of the control system. Furthermore, even the high-pass filter (HPF) can be abandoned in the SESC loop, resulting in more simplified ESC (MSESC). Simulations are carried out using the NREL OC3 monopile 5-MW baseline wind turbine model within FAST. The simulation results demonstrate the effectiveness of the proposed SESC and MSESC schemes.

3.1 Introduction

To maximise wind power capture for conventional turbines operating in Region 2, Johnson et al. [72] proposed a standard control law for the NREL offshore 5-MW baseline turbine model, as explained in Section 2.4. It is noticeable from (2.20) that to derive the accurate K, some turbine properties (e.g., the maximum power coefficient C_p^* and optimal TSR λ^*) are required accurately, which is usually

impossible. Besides, C_p^* and λ^* change over time due to debris buildup and blade erosion, implying actually varying K [3]. Accordingly, Johnson et al. [72] designed an adaptive torque controller which updated the torque gain every 3 hours without requiring the information of turbine properties. However, it took an extremely long time (about 40 hours) for the torque gain to converge to its optimum. According to (1.3), the maximum power capture can also be achieved through tracking the optimal TSR λ^* by regulating ω_r around $\frac{\lambda^* V}{R}$, which requires the measurement of V. Based on this idea, Cutululis et al. [73] developed a generator torque controller and tested it on a simplified turbine drivetrain simulation model. However, the controller could not keep the TSR around its optimum under turbulent winds. Creaby et al. [74] employed the conventional extremum seeking control (ESC) algorithm developed in [75] for torque control and evaluated it on a two-bladed 600-kW onshore turbine. It showed that the conventional ESC scheme can find the optimal torque gain quickly under turbulent winds without requiring turbine properties. In this chapter, this area is further studied. More specifically, the conventional ESC method [75] is simplified by replacing its low-pass filter (LPF) with a sample-and-hold (SH) block so that the LPF corner frequency needs not be selected. This also removes the influence of the LPF on dynamics of the whole control system. Moreover, even the high-pass filter (HPF) can be omitted.

The structure of this chapter is as follows. In Section 3.2, turbine torque controllers are designed based on ESC to maximise wind power capture in Region 2. First, the mechanism of the conventional ESC algorithm for torque control is analysed. Then this algorithm is simplified by replacing its LPF with an SH block, called simplified ESC (SESC). After that, SESC is further simplified by removing its HPF, called more simplified ESC (MSESC). In Section 3.3, simulation studies are carried out. First, some modifications are made to the NREL offshore 5-MW baseline turbine model (introduced in Section 2.4) to make it applicable to the simulation studies. Subsequently, simulations are conducted to verify the effectiveness of SESC and MSESC in finding the optimal torque gain under several typical wind inputs along with a same irregular wave input.

3.2 Torque Control Based on ESC

Figure 3.1 is the block diagram for torque control using conventional ESC where the torque gain K is not a constant (for standard torque control) but a variable signal tuned by ESC to maximise the rotor power p_r. In Figure 3.1, v_w is the wind speed, ω_g is the generator speed, $\hat{K}$ is the estimate of the torque gain, ΔK is the amplitude

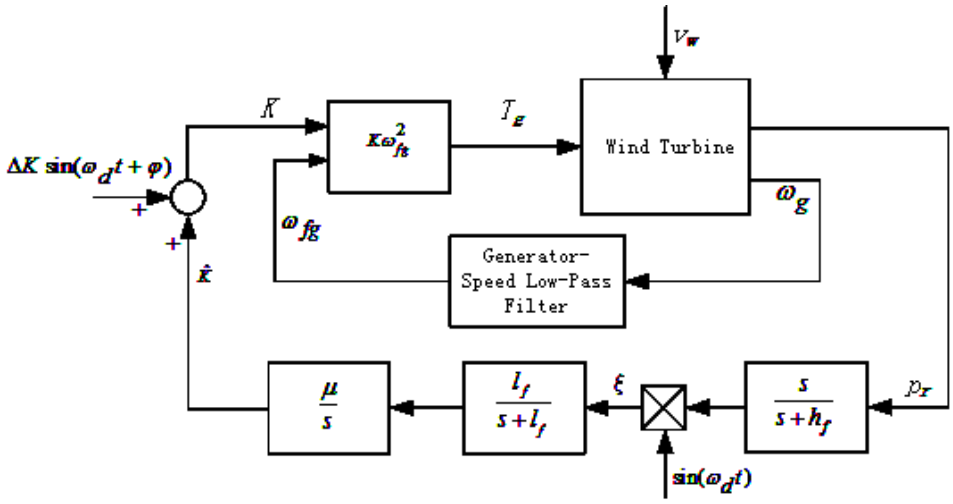

Figure 3.1: Block diagram of a conventional wind turbine (operating in Region 2) with a torque controller using conventional ESC.

of the sinusoidal search signal $\Delta K \sin(\omega_d t + \varphi)$ and needs to be very small [75], ω_d is the angular frequency of the search signal and needs to be less than the corner frequency of the generator-speed LPF [75], h_f and l_f are the corner frequencies of the HPF and LPF respectively.

Now the mechanism of torque control using the conventional ESC algorithm [75] (see Figure 3.1) is analysed. Assume that there is no wind turbulence, the relationship between the torque gain K and the rotor power p_r is a static map $p_r(K)$, and the added sinusoidal search signal $\Delta K \sin(\omega_d t + \varphi)$ varies much faster than $\hat{K}$. Using the Taylor series expansion, one can derive

$$\begin{aligned} p_r(K) &= p_r\left(\hat{K} + \Delta K \sin(\omega_d t + \varphi)\right) \\ &\approx p_r\left(\hat{K}\right) + \frac{\partial p_r}{\partial K}\left(\hat{K}\right) \Delta K \sin(\omega_d t + \varphi). \end{aligned} \tag{3.1}$$

The HPF corner frequency is set to be less than ω_d in order to eliminate the DC component and pass the ω_d frequency component of the HPF input (3.1). Then

$$\begin{aligned} \xi &\approx \frac{\partial p_r}{\partial K}\left(\hat{K}\right) \Delta K \sin(\omega_d t + \varphi + \varphi_h) \sin(\omega_d t) \\ &= \frac{1}{2}\frac{\partial p_r}{\partial K}\left(\hat{K}\right) \Delta K \left[\cos(\varphi + \varphi_h) - \cos(2\omega_d t + \varphi + \varphi_h)\right] \end{aligned} \tag{3.2}$$

where φ_h is the phase shift induced by the HPF. The LPF corner frequency is set to be less than ω_d with the aim of passing the DC component and largely reducing

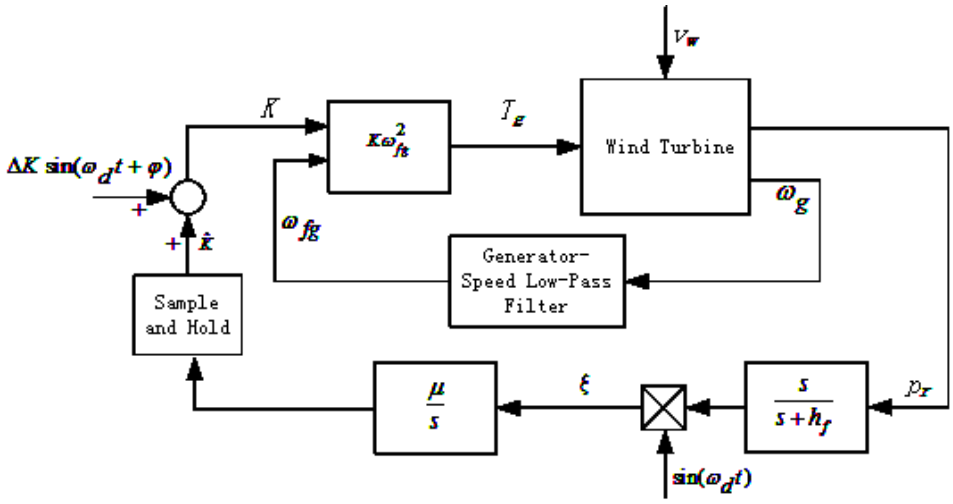

Figure 3.2: Block diagram of a conventional wind turbine (operating in Region 2) with a torque controller using SESC.

the oscillation components of ξ. Thus the integrator input is approximately

$$\frac{1}{2}\frac{\partial p_r}{\partial K}\left(\hat{K}\right)\Delta K\cos\left(\varphi+\varphi_h\right). \tag{3.3}$$

Note that the actual integrator input still has small $2\omega_d$, $3\omega_d$, $4\omega_d\ldots$ frequency components because the LPF cannot remove them thoroughly. To guarantee correct optimum search direction, it is necessary that $\cos(\varphi+\varphi_h)>0$, implying

$$-\frac{\pi}{2}<\varphi+\varphi_h<\frac{\pi}{2}. \tag{3.4}$$

Therefore, when $\hat{K}$ is larger than its optimum, the integrator input (3.3) is negative, which drives the integrator output $\hat{K}$ down, and vice versa. If all the loop parameters are properly selected, the ESC loop in Figure 3.1 is stable [75]. Once the system is stable, the integrator input (3.3) is approximately 0, and thus $\frac{\partial p_r}{\partial K}(\hat{K})\approx 0$, which means the optimal $\hat{K}$ (estimate of the torque gain) that maximises p_r is acquired.

The conventional ESC loop can be simplified by replacing the LPF with a sample-and-hold (SH) block, resulting in simplified ESC (SESC) as shown in Figure 3.2. The transfer function of the SH and its magnitude are

$$H(s)=\frac{1-e^{-sT}}{s},\quad \left|H(j\omega)\right|=T\frac{\left|\sin\left(\omega T/2\right)\right|}{\left|\omega T/2\right|}, \tag{3.5}$$

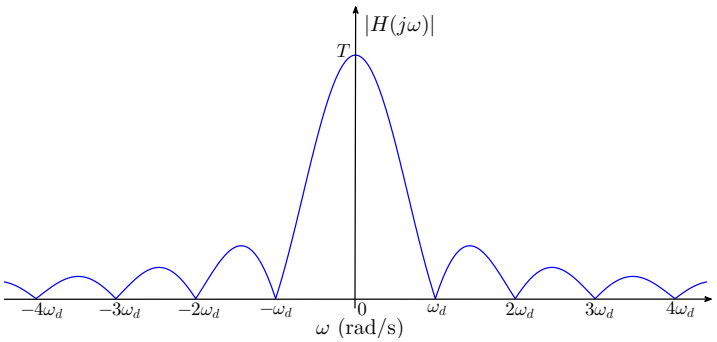

Figure 3.3: Magnitude frequency response of the sample-and-hold.

where $T = 2\pi/\omega_d$ is the sample period. The magnitude frequency response of the SH is illustrated in Figure 3.3. In the SESC loop, ξ is the same as in (3.2). The integral of the $2\omega_d$ frequency component of ξ over each sample period is approximately 0, thus the useful component of the integrator input is the same as the integrator input in the conventional ESC loop (3.3). This validates the SESC algorithm. Besides, as illustrated in Figure 3.3, the SH can attenuate high-frequency components like an LPF and removes the signals whose frequencies are integer multiples of ω_d.

Considering removing both the HPF and LPF, and keeping the SH (called MSESC as seen in Figure 3.4), the integrator input becomes

$$\xi \approx p_r\left(\hat{K}\right)\sin\left(\omega_d t\right) + \frac{1}{2}\frac{\partial p_r}{\partial K}\left(\hat{K}\right)\Delta K\left[\cos\left(\varphi\right) - \cos\left(2\omega_d t + \varphi\right)\right]. \tag{3.6}$$

The integrals of both ω_d and $2\omega_d$ frequency components in (3.6) over each sample period $(2\pi/\omega_d)$ are 0. Thus, the useful component of the integrator input is approximately

$$\frac{1}{2}\frac{\partial p_r}{\partial K}\left(\hat{K}\right)\Delta K\cos\left(\varphi\right) \tag{3.7}$$

which is almost the same as (3.3) except the absence of φ_h (the phase shift caused by the HPF).

However, the real mapping between K and p_r is not static as illustrated in Figure 3.5: when the torque gain suddenly changes, the rotor power will not instantly reach the corresponding steady value because of the transient response of the rotor speed. Hence, the integrals of the ω_d and $2\omega_d$ frequency components of the integrator inputs (3.3) and (3.7) over each sample period will deviate from 0 for SESC and MSESC. The resulting deviation is larger in the MSESC case due to the additional large-amplitude component $p_r(\hat{K})\sin\left(\omega_d t\right)$ in the integrator input. To

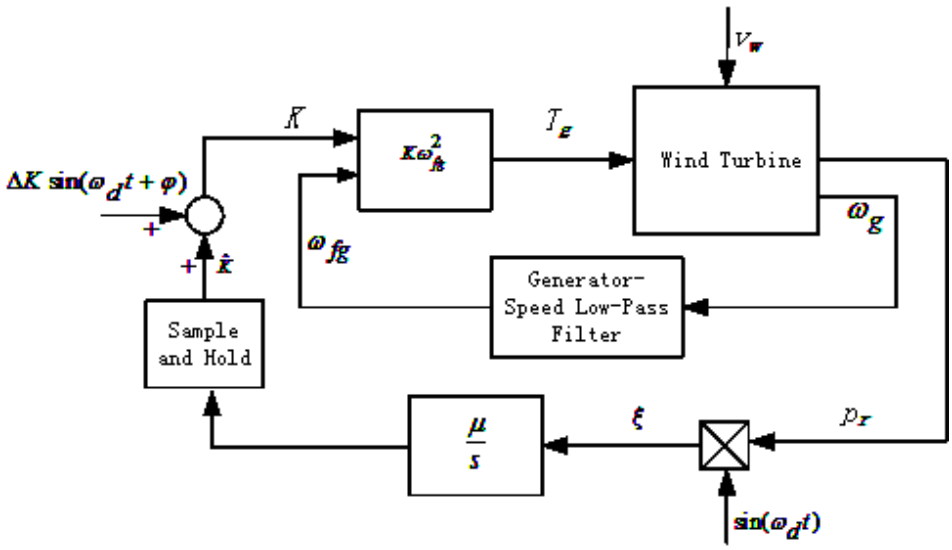

Figure 3.4: Block diagram of a conventional wind turbine (operating in Region 2) with a torque controller using MSESC.

avoid loop instability caused by the deviation, the loop gain μ for MSESC must be less than the one for conventional ESC and SESC.

For the above three ESC schemes, in the case that there exists wind turbulence, it is required to increase ΔK to augment the weight of the useful component of the integrator input ((3.3) or (3.7)) relative to the turbulence component, and correspondingly decrease the loop gain μ to ensure loop stability. Note that the torque gain will converge more slowly with MSESC than with conventional ESC & SESC under wind turbulence. This is because with MSESC, the turbulence will cause the amplitude $p_r(\hat{K})$ of the component $p_r(\hat{K})\sin(\omega_d t)$ in the integrator input (3.6) to change drastically during each sample period, which will strongly affect optimum seeking.

3.3 Simulation Study

In this section, simulations are conducted to test performances of the torque controllers designed based on the conventional ESC, SESC, and MSESC algorithms described in Section 3.2, using the NREL OC3 monopile 5-MW baseline turbine model introduced in Section 2.4.

Following Figures 3.1, 3.2 and 3.4, torque controllers are developed based on the ESC algorithms in MATLAB/Simulink, and incorporated into the baseline

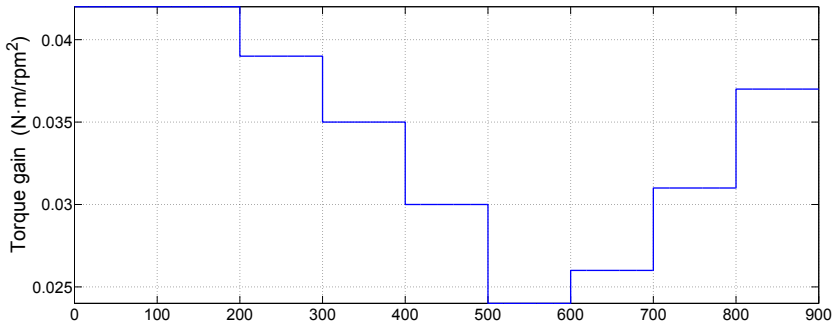

(a)

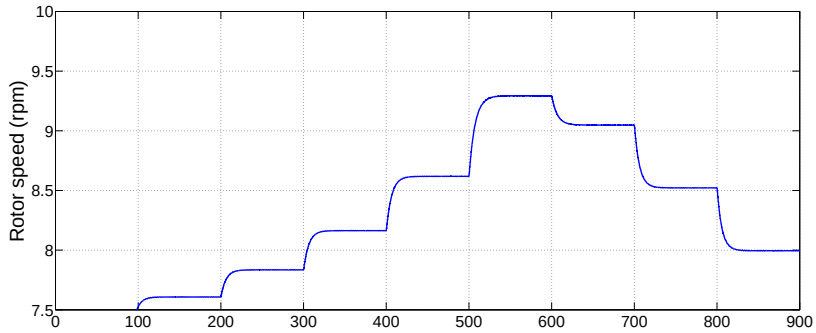

(b)

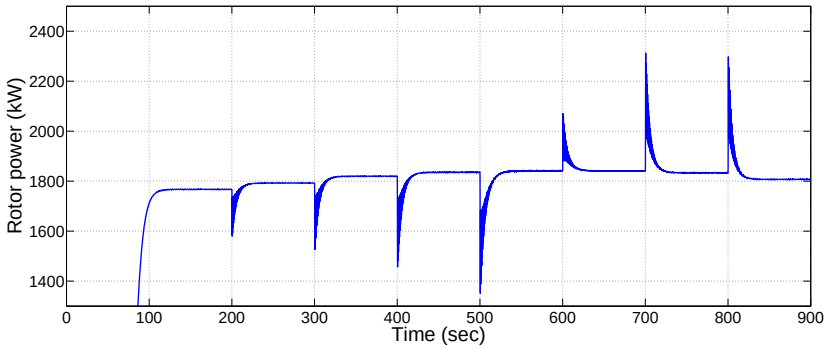

(c)

Figure 3.5: Responses of the rotor speed and rotor power under step torque gains for the NREL offshore 5-MW baseline wind turbine model.

model through the interface between FAST and Simulink. The controller computes the generator torque following the description for the baseline torque control design in Section 2.4. To make the baseline model fit for simulation studies, Region 2 is enlarged from 871–1,161.96 rpm (see Figure 2.5) to 400–1,161.96 rpm, and Region 1.5 is shrinked to the range of 370–400 rpm. Besides, the torque gain K is not

a constant but a variable signal tuned by ESC, so the torque-versus-speed curve is no longer fixed as in Figure 2.5 but keeps varying. The initial estimate of the torque gain $\hat{K}$ is set to be 0.042 N·m/rpm^2 which is about 64.2% above the optimal value 0.025576386 N·m/rpm^2 (see Table 2.1). Following the rules for the ESC loop parameter selection in Section 3.2, ω_d is set to be $(2\pi/25.1375)$ rad/s. For SESC and MSESC, the sample period of the SH is set to be 25.1375 seconds which is the same as the period of the sinusoidal search signal. The transfer functions of the HPF and LPF for conventional ESC and SESC are respectively

$$G_{hp} = \frac{s}{s+0.2}, \quad G_{lp} = \frac{0.01}{s+0.01}. \tag{3.8}$$

The phase angle φ is set to be 0.116π for conventional ESC and SESC while it is set to be 0.3308π (obtained by adding the phase shift caused by the HPF at the angular frequency of 25.1375 rad/s to $\varphi = 0.116\pi$) for MSESC.

Several types of wind inputs (a constant wind, step winds, and turbulent winds) along with a same irregular wave input are used during the simulations. The wind turbulence is generated by TurbSim using the IEC Kaimal spectral model with NTM (introduced in Section 2.1.2). The waves are irregularly generated based on the JONSWAP spectrum by FAST HydroDyn (see Section 2.2). The peak-spectral period and significant wave height of the incident waves are 10 seconds and 6 m, respectively.

3.3.1 Simulation Results under A Constant Wind

For a constant wind of 8 m/s, the amplitude of the search signal ΔK is set to be 0.0008 N·m/rpm^2. The loop gain μ is set to be 7.8e-6 for conventional ESC and SESC while for MSESC, it is set to be 3.8e-6. As shown in Figure 3.6, with the three ESC controllers, the torque gain converges to 0.0259 N·m/rpm^2 (only 1.27% above the optimal value of 0.025576386 N·m/rpm^2), and the average rotor power increases by about 4.15% compared with standard control using $K = 0.042$ N·m/rpm^2 and is almost the same as that with standard control using the optimal torque gain. The torque gain converges within 3,000 seconds in the conventional ESC and MSESC cases, while it converges 500 seconds faster in the SESC case.

3.3.2 Simulation Results under Step Winds with/without 2% Turbulence

When a sudden change of wind speed occurs, the adaptive torque gain will shift dramatically from its optimum and spend a long time converging to a new optimum,

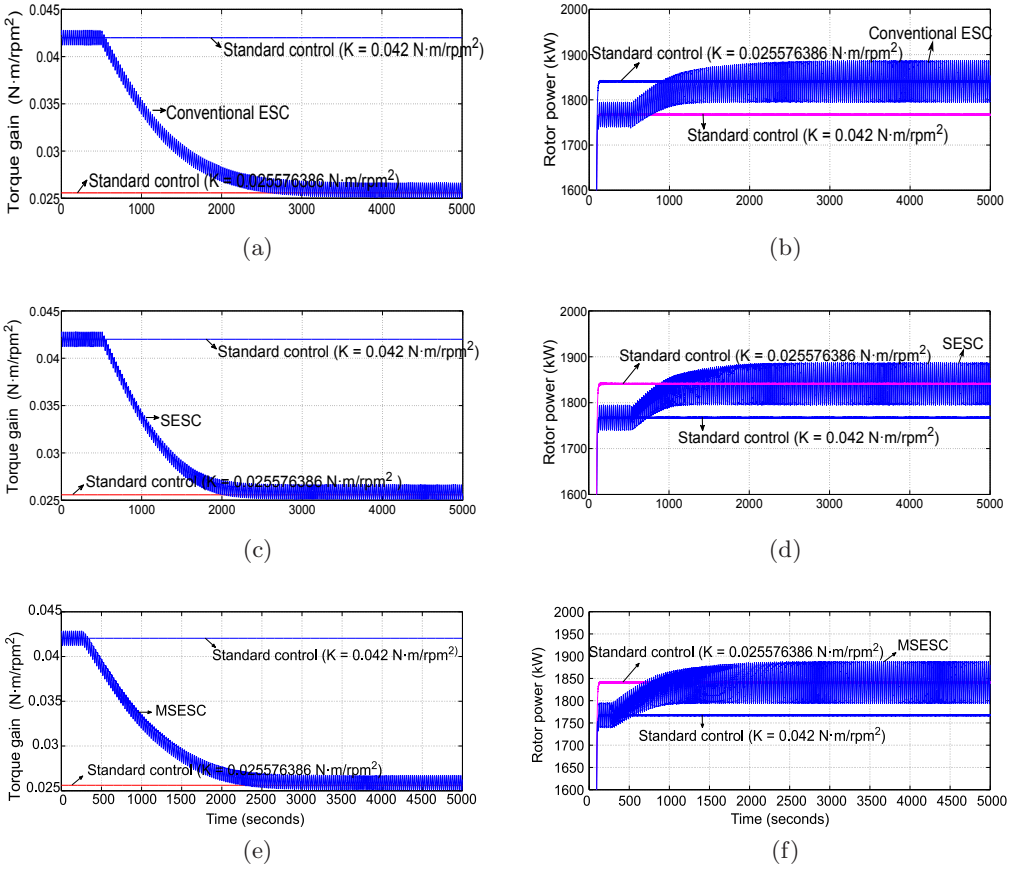

Figure 3.6: Simulation results under a constant wind of 8 m/s along with a wave input.

or even worse, the estimate $\hat{K}$ may drop below 0, which leads to the failure of the algorithm. For conventional ESC and SESC, this happens because an abrupt wind speed change will cause a sudden change of the rotor power and thus a big change of the integrator input. To address this issue, the integrator reset mechanism proposed by Creaby et al. [74] is used: once the integrator input exceeds a certain threshold, it is reset to 0 which is held for some time. Here the threshold is set to be 3.1e-5 for conventional ESC and 2.2e-4 for SESC, and the hold time is set to be 120 seconds. However, the integrator reset does not work for MSESC because the integrator input in this case is dominated by the component $p_{rs}(\hat{K})\sin(\omega_d t)$ (see (3.6)) whose amplitude $p_{rs}(\hat{K})$ is quite large. Thus the step size of $\hat{K}$ is restricted to be within ± 0.0006 N·m/rpm^2 instead. Figures 3.7 and 3.8 show that the integrator reset and step-size limit can accelerate the reconvergence of the torque gain after the wind speed changes abruptly.

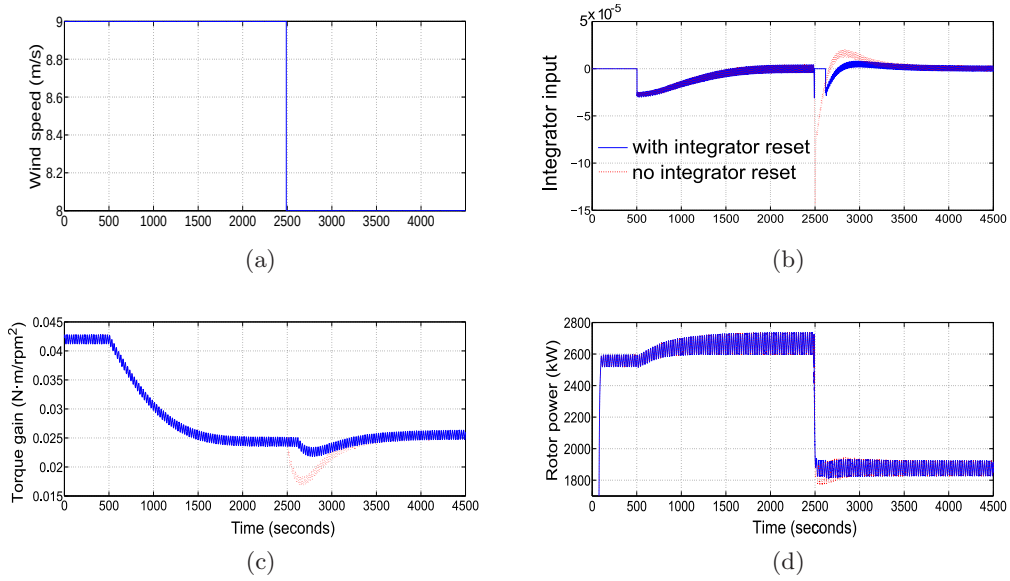

Figure 3.7: Simulation results with conventional ESC under a step wind along with a wave input.

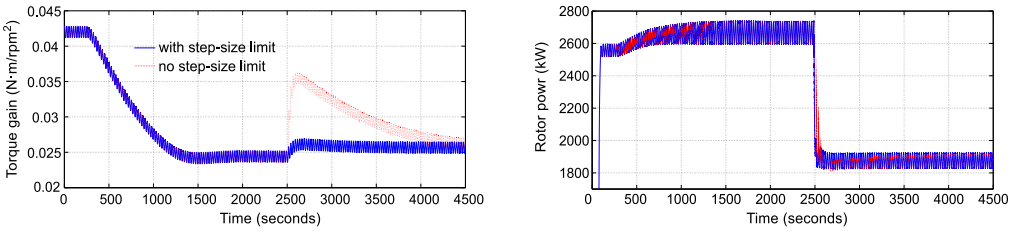

Figure 3.8: Simulation results with MSESC under a step wind (see Figure 3.7a) along with a wave input.

Figure 3.9 illustrates the simulation results under the step winds with the mean hub-height longitudinal wind speed varying between 7 m/s and 9 m/s (without turbulence). With any of the 3 ESC controllers, the torque gain converges to the range of 0.0244–0.0274 N·m/rpm^2 within 2,000 seconds. The improvement of the average rotor power is 4.28% compared with standard control using $K = 0.042$ N·m/rpm^2. Then simulations are conducted under step winds with 2% turbulence. In this case, ΔK is increased to 0.002 N·m/rpm^2, and the loop gain μ is decreased to 2.2e-6 for conventional ESC & SESC and to 9.4e-7 for MSESC. Figure 3.10 shows that the torque gain converges to the optimum approximately in 2,500 seconds with conventional ESC & SESC, while this process takes 4,000 seconds with MSESC.

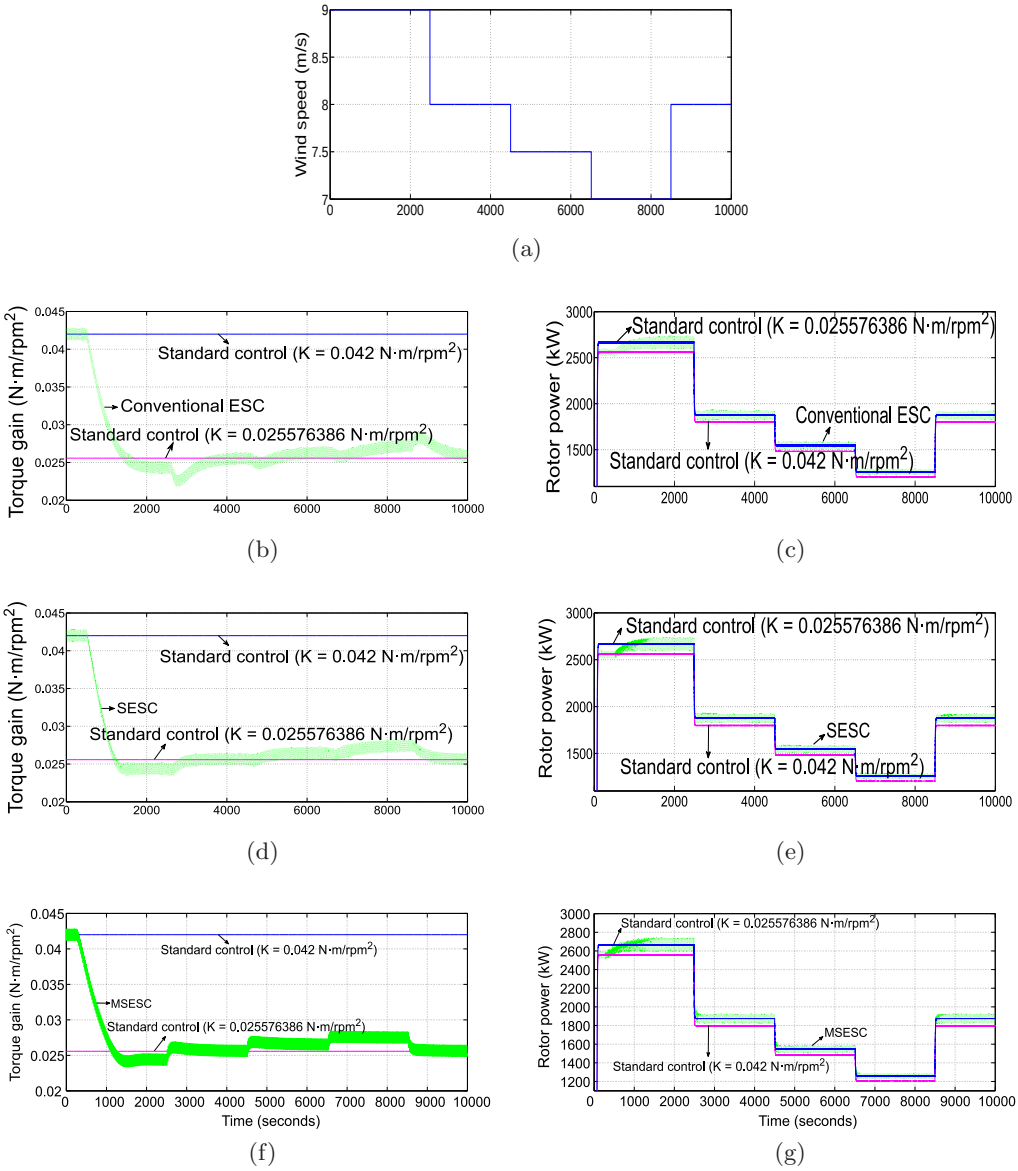

Figure 3.9: Simulation results under step winds (without turbulence) along with a wave input.

The rotor power increases by 4.4% compared with standard control using $K = 0.042$ N·m/rpm^2 with any of the 3 ESC controllers. Under either wind input, the mean rotor powers obtained by standard control using the optimal torque gain and obtained by the 3 ESC schemes are approximately the same.

3.3.3 Simulation Results under 15% Wind Turbulence

In this case, the mean hub-height longitudinal wind speed is set to be 7 m/s, and the turbulence intensity is set to be 15%. The amplitude of the search signal ΔK is increased to 0.006 N·m/rpm^2, and the loop gain μ is decreased to 6e-7 for conventional ESC & SESC and 2.8e-7 for MSESC. Clearly, from Figure 3.11, the torque gain converges within 0.024–0.03 N·m/rpm^2 in about 2,000 seconds with conventional ESC and SESC. Both algorithms achieve an improvement of about 4.95% for the average rotor power compared with standard control using $K = 0.042$ N·m/rpm^2. The torque gain converges within 0.023–0.028 N·m/rpm^2 in about 4,200 seconds with MSESC, achieving an improvement of about 4.59% for the average rotor power compared with standard control using $K = 0.042$ N·m/rpm^2. Besides, the mean rotor powers obtained by standard control using the optimal torque gain of 0.025576386 N·m/rpm^2 and obtained by the 3 ESC schemes are approximately the same.

3.4 Conclusions

To optimise power capture of a conventional (geared equipped) turbine, the SESC and MSESC mechanisms for torque control were proposed based on the conventional ESC algorithm [75]. The standard torque control method (described in Section 2.4) relies on the knowledge of accurate turbine properties (usually unavailable) for the calculation of a constant torque gain. However, the SESC and MSESC schemes can quickly find the optimal torque gain without requiring turbine properties. The SESC algorithm is developed by replacing the LPF in the conventional ESC loop with an SH block. This avoids the selection of the LPF corner frequency and the impact of the LPF on system dynamics. SESC can be further simplified by omitting the HPF (together with the omission of the LPF), called more simplified ESC (MSESC). The simulations were carried out on the NREL OC3 monopile 5-MW baseline turbine model. The performances of the torque controllers designed based on conventional ESC, SESC, and MSESC were compared with the standard torque controller. It was shown that SESC and MSESC algorithms were almost as effective as the conventional ESC algorithm in finding the optimal torque gain (but with simpler control configurations) except that MSESC converged more slowly than the other two under wind turbulence (explained in Section 3.2).The controllers using ESC increased the average rotor power by more than 4% over the standard controller in all the simulation cases. This improvement is significant considering the fact that for 100 GW of installed wind power capacity, 1% of energy improvement will make $100 million profit annually [3].

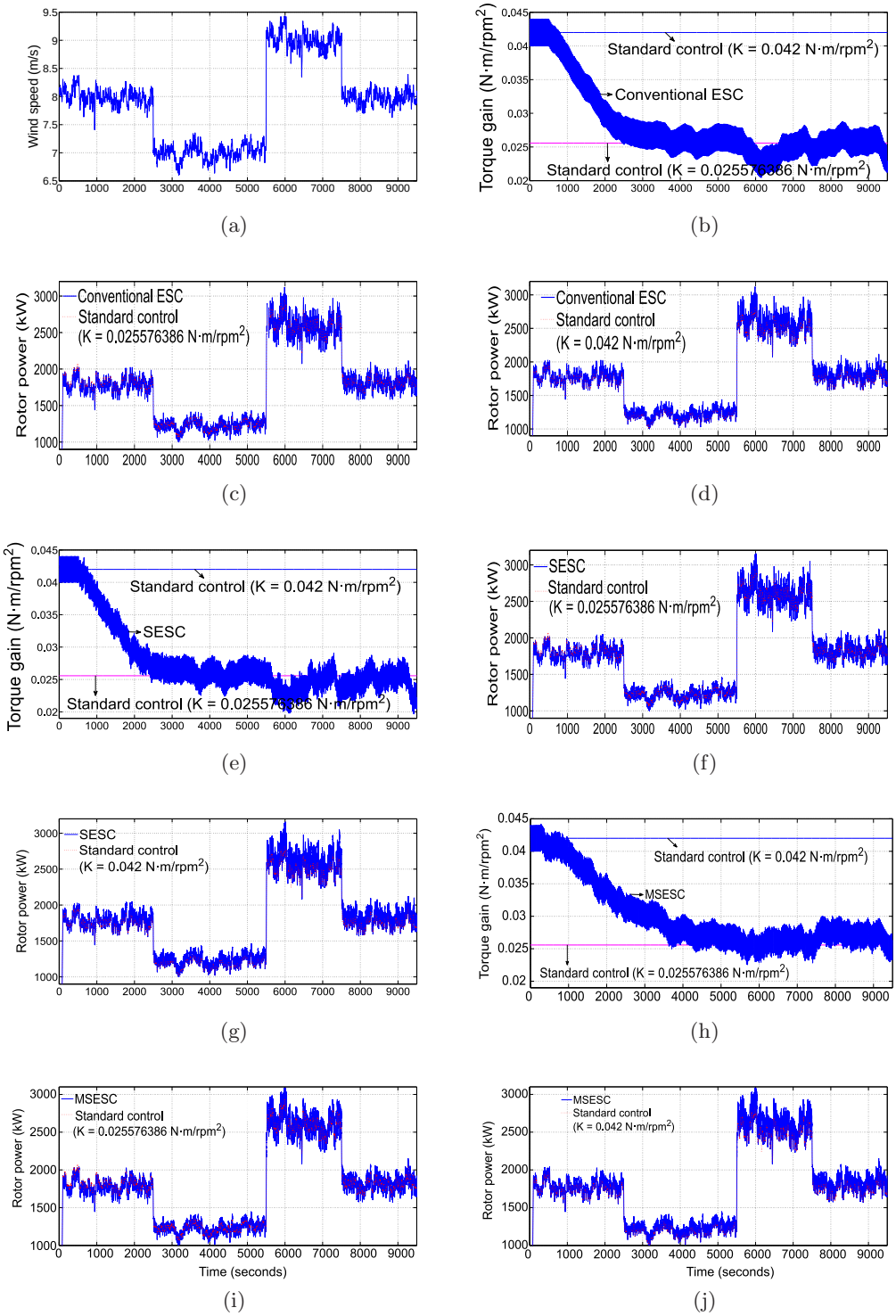

Figure 3.10: Simulation results under step winds (with 2% turbulence) along with a wave input.

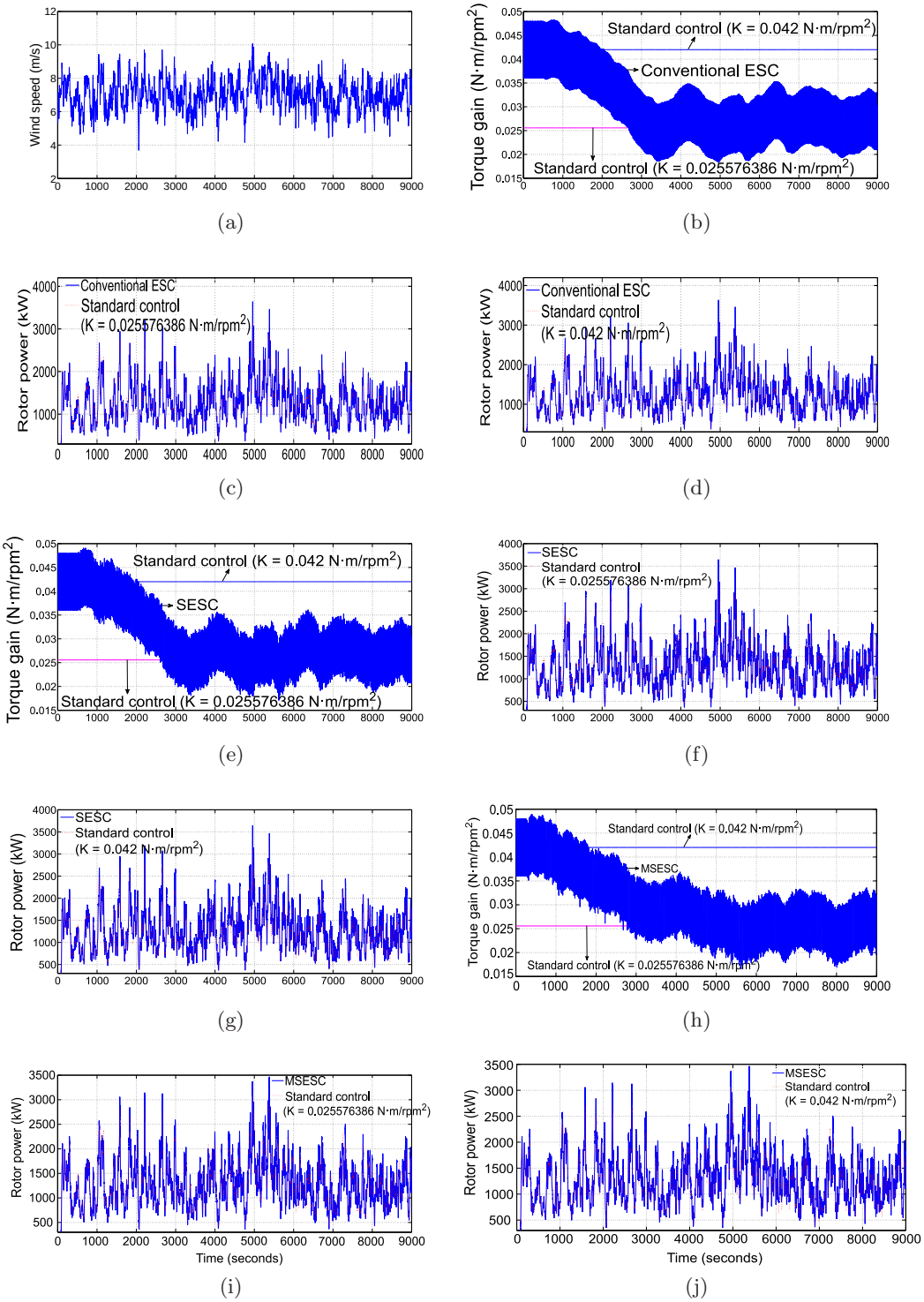

Figure 3.11: Simulation results under a wind input with a mean speed of 7 m/s and 15% turbulence along with a wave input.

Chapter 4

Load Reduction of Monopile Wind Turbine Towers

The application of tuned mass dampers (TMDs) (one in the fore-aft direction, one in the side-to-side direction) to suppress vibrations of a monopile wind turbine tower is investigated in this chapter. Using the spectral element method, a finite-dimensional state space model Σ_d is derived from an infinite-dimensional model Σ of a monopile wind turbine tower stabilised by a TMD located in the nacelle. Σ and Σ_d can be used to represent the dynamics of the tower and TMD in either the fore-aft direction or the side-to-side direction. The wind turbine tower subsystem of Σ is modelled as a non-uniform SCOLE (NASA Spacecraft Control Laboratory Experiment) system consisting of an Euler-Bernoulli beam equation describing the dynamics of the flexible tower and the Newton-Euler rigid body equations describing the dynamics of the heavy rotor-nacelle assembly (RNA) by neglecting any coupling with blade motions. Σ_d can be used for fast & accurate simulation for the dynamics of the wind turbine tower as well as for optimal TMD design. It is shown that Σ_d agrees very well with the FAST (Fatigue, Aerodynamics, Structures, and Turbulence) simulation of the NREL OC3 monopile 5-MW baseline wind turbine model. The TMD parameters are optimised by minimising the frequency-limited $\mathcal{H}_2$-norm of the transfer function matrix of Σ_d which has the input of force and torque acting on the RNA, and the output of tower-top displacement. The optimal TMD system is tested through FAST simulations and achieves substantial fatigue load reductions.

Although the first bending mode dominates monopile tower vibrations, the second bending mode can play a non-negligible part in tower fatigue damage in some cases [51, 52]. Besides, modal frequencies of real monopiles vary over time [53]. This will not only deteriorate effectiveness of the TMD tuned for the original first

tower mode, but also possibly cause increased coupling between higher tower modal frequencies and rotor harmonic frequencies [54]. Hence, it is important to develop a control scheme to suppress multiple tower vibration modes simultaneously and at the same time improve robustness of the TMD system. In Section 4.2, the research in Section 4.1 is extended to the optimisation of multiple TMDs to reduce vibrations of flexible structures described by partial differential equations, using the non-uniform SCOLE beam system with multiple dominant modes as an illustrative application. Multiple groups of TMDs with each group being placed at the antinode of the mode shape of a dominant mode of the SCOLE beam are used. Frequency-limited $\mathcal{H}_\infty$ and $\mathcal{H}_2$ optimisations are employed for harmonic and random excitations respectively to determine the parameters of the TMDs. The optimisation scheme takes into account the trade-off between effectiveness and robustness of multiple TMDs to suppress multiple dominant modes of the SCOLE beam. Simulation studies show that the proposed scheme achieves substantial improvements over traditional methods in terms of both effectiveness and robustness and that with equal total mass, TMD systems with each group having multiple TMDs are more effective and more robust than the ones with each group having a single TMD.

4.1 Load Reduction of Monopile Wind Turbine Towers Using Optimal Tuned Mass Dampers

4.1.1 Introduction

A conventional method for damping fore-aft vibrations of the turbine tower is blade pitch control. For this purpose, Bossanyi [76] and Darrow [77] added a tower-top-acceleration feedback loop and a tower-top-velocity feedback loop respectively to the collective blade pitch control. However, such methods increase blade pitch actuator activities. Soltani et. al [78] employed receding horizon control to calculate collective pitch angles based on the estimated wind speed from LIDAR (Light Detection and Ranging), which significantly reduced the tower loads and power fluctuations. The papers [40, 79, 80] suppressed the side-to-side vibrations of turbine towers by modulating the generator torque at the expense of interfering with the power generation.

The tuned mass damper (TMD), a simple and widely-used passive structural control device, has been verified to offer a good alternative solution to effectively suppress turbine tower vibrations [48, 2]. Besides, it works in the entire operating range of the turbine while blade pitch control is effective only in Region 3. A TMD

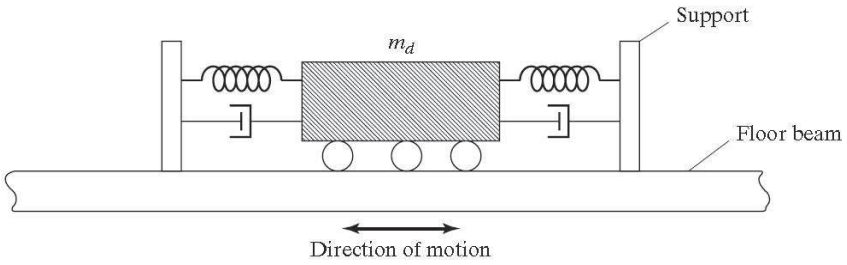

Figure 4.1: Schematic diagram of the TMD systems used in the John Hancock Tower in Boston and the Citicorp Center in Manhattan [8].

comprises a mass, springs and dampers. The mass is linked to the main structure to be stabilised via springs and dampers. The mechanism is that the TMD is tuned to a particular structural frequency, and thus will resonate and dissipate input energy via the dampers when the structure is excited at that particular frequency. It has been successfully configured in building structures to reduce vibrations due to environmental excitations such as strong winds and earthquakes. For example the John Hancock Tower in Boston and Citicorp Center in Manhattan have employed TMD systems where mass components are put on the high floor of the building through wheels (see Figure 4.1) to combat wind's effects [81]. These TMDs reduce about 50% of worst-case wind-induced motions. The Taipei 101 skyscraper contains the world's largest and heaviest TMD whose mass component is hung above the floor through cables [82]. This TMD reduces up to 40% of the tower's motion caused by strong winds.

In terms of the design of a single TMD, Den Hartog derived formulae for the optimal parameters of a TMD system to suppress harmonic excitations [83] while the research [84, 85, 86] provided formulae for the case of random excitations. Younesian et al. [87] proposed a TMD optimisation scheme through minimising the root mean square of system displacements to suppress vibrations of Timoshenko beams subject to random excitations with peaked power spectral densities. Leung et al. [88] applied the particle swarm algorithm to optimise TMD parameters for the structure under non-stationary excitations. All these studies deal with the case of suppressing a single dominant vibration mode of the main structure using a single TMD. A dominant mode means the mode which contributes significantly to structural vibrations. For main structures with one dominant vibration mode, multiple TMDs with natural frequencies distributed around the dominant modal frequency are more effective and more robust than a single TMD with equal total mass [89, 90, 91, 92]. Robustness of a TMD system is usually tested by mistun-

ing where modal frequencies of the main structure deviate from their corresponding frequencies utilised in the design of TMDs [92]. Mistuning may be caused by estimation errors of modal frequencies of the main structure, changes of modal frequencies due to external loadings, and/or manufacturing errors of TMDs [93, 94]. For main structures with several dominant vibration modes that all respond to seismic loads, Clark [95] designed multiple TMDs in such a way that each TMD was tuned for a dominant mode based on Den Hartog's formulae [83]. Bergman et al. [96] placed TMDs on several floors of a building. The TMD tuned for the first mode played the most part in damping vibrations of the building while other dampers tuned for higher modes further improved the damping performances. Lewandowski and Grzymisawska [97] employed multiple TMDs with each TMD tuned for a selected vibration mode to reduce vibrations of a building, using Warburton's formulae [86].

Lackner and Rotea [48] placed two independent TMDs (translating in the fore-aft and side-to-side directions) into the nacelle of a wind turbine as shown in Figure 2.3. The TMD translating in the fore-aft direction was tuned to reduce tower vibrations induced by the first tower fore-aft bending mode. The mass of the TMD was set to be about 2% of the total turbine mass. The spring constant of the TMD was chosen such that the natural frequency of the TMD equalled the first tower fore-aft modal frequency. The damping constant was determined by trial and error to minimise the standard deviation of tower-top fore-aft translational deflections. The NREL OC3 monopile 5-MW baseline turbine model within FAST was used for testing performances of the tuned TMD system. The results commentated the effectiveness of the TMD in mitigating the monopile tower's fore-aft loads. Stewart and Lackner [2] advanced the research in [48] with a similar TMD setup but an improved tuning method based on limited DOF control design models (for four types of turbine substructures) which were obtained by only considering the specific DOFs that affect tower motions most. In Stewart and Lackner [2], the limited DOF model of the monopile wind turbine tower with a TMD system in the nacelle was a TMD-stabilised rigid inverted pendulum with the base stiffness and damping modelled as rotational spring and damper. The spring and damping constants of the rigid inverted pendulum were obtained through a non-linear least square algorithm based on a FAST simulation. Then the authors conducted simulations using the TMD-stabilised rigid inverted pendulum model with different combinations of TMD spring and damping constants, under the combination of a top-displacement step input and a constant thrust moment (obtained from a FAST simulation at the rated wind speed). The optimal TMD was the one which minimised the standard deviation of the top displacement of the inverted pendulum (equivalent to the turbine tower-top

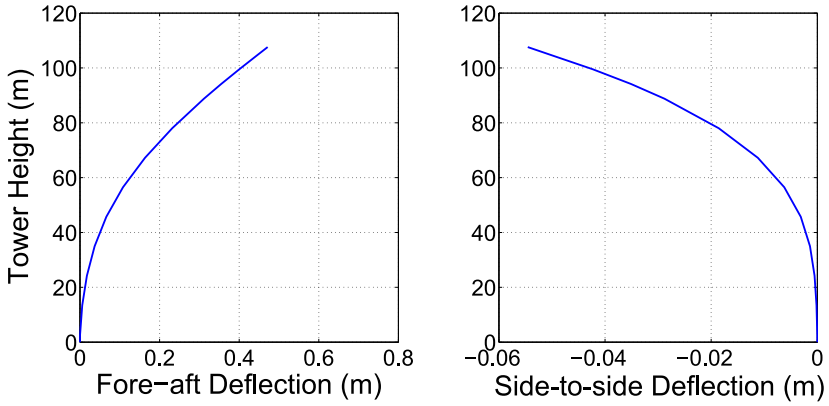

Figure 4.2: Deflections of the NREL monopile 5-MW baseline turbine tower at a certain time instant by a FAST simulation.

displacement). Finally, they conducted FAST simulations using the optimal TMD, which showed substantial fatigue load reductions.

A simulation was done for the fore-aft and side-to-side deflections of the NREL monopile 5-MW baseline turbine tower at a certain time instant using FAST, which was shown in Figure 4.2. Clearly, the wind turbine tower is not a rigid inverted pendulum as in the paper [2] but a flexible beam. Because the first tower bending mode dominates the dynamic response of a typical monopile wind turbine tower subject to wind and wave excitations, and the largest deflection for this mode occurs at the tower top [48], it is acceptable to use an inverted pendulum as the control design model to only control the first mode. But apparently, the inverted pendulum cannot be used to simulate dynamics of a wind turbine tower. Stewart and Lackner [2] mentioned that desirably the parameter optimisation of the TMD should be based on the FAST simulation which was unfortunately an overkill because a 10-min simulation time approximately took a computation of 10–30 minutes. So a rigid rod was used to model the turbine tower (with a big mass at its top as the heavy rotor-nacelle assembly (RNA)) in the paper [2] because fortunately there was usually only one DOF accounting for the most fatigue load for a typical monopile tower. But a rigid rod might not be able to model other types of wind turbine towers or more generally other flexible beams (which have more modes dominating their vibrations) even only for control design purpose. Thus it is more sensible to use a type of beam equations to model the wind turbine tower. This tower model can be used to conduct both control design and fast & accurate simulation. Furthermore, the optimisation of the TMD system in the paper [2] was conducted based on a specific loading excitation obtained from a FAST simulation. It will

be nice to have a proper mathematical formulation and systematic design method for the optimisation procedure, which can take account of more general wind and wave excitations and can be extended to vibration control of other types of flexible structures.

The literature [40, 41] used a non-uniform NASA SCOLE system to model the monopile wind turbine tower in either the fore-aft plane or the side-to-side plane. The SCOLE system is a well known model for a flexible beam with one end clamped and the other end connected to a rigid body. Originally it has been developed to model a flexible mast carrying an antenna on a satellite [98, 99]. For more details about the SCOLE model, these four papers and the literature [100, 101] which contain many references for previous work (controllability, observability, stabilisation by static feedback, etc.) in the framework of infinite-dimensional systems described by partial differential equations (PDEs) are referred to. As seen in Section 4.1.2, the flexible beam in the SCOLE model is described by a PDE. This SCOLE system is very suitable to model the monopile wind turbine tower, which has the bottom end clamped in the ocean floor and the upper end linked to the RNA.

Zhao and Weiss [102, 103] incorporated a TMD into the SCOLE model denoted by Σ, and showed its strong stability. The mass component of the TMD can be either put on the floor of the nacelle through wheels/racks (reducing friction) or hanged above the floor through cables. In the present chapter, this infinite-dimensional SCOLE-TMD system Σ is discretised into a finite-dimensional model Σ_d using the spectral element method, and then Σ_d is verified against the FAST simulation of the NREL 5-MW baseline monople wind turbine model. Σ_d is able to describe dynamics of the tower and TMD in either the fore-aft direction or the side-to-side direction. Finally the fore-aft and side-to-side optimal TMDs are derived by minimising the $\mathcal{H}_2$-norm of Σ_d with external force and torque as input and the tower-top displacement as output, which means to minimise the standard deviation of the tower-top displacement under external excitation. Similar vibration suppression performances are obtained as the paper [2]. But the SCOLE model is more realistic because it contains more vibration modes and thus can simulate dynamics of the tower more precisely than a rigid inverted pendulum model with only one mode. Besides, the optimisation scheme can be extended to the design of multiple TMDs to reduce vibrations of general flexible structures described by PDEs, for which the non-uniform SCOLE beam system with multiple dominant modes is used as an illustrative application in the subsequent research. More specifically, an optimisation scheme for multiple TMDs is proposed to suppress multiple vibration modes of a general SCOLE beam and to increase the system robustness against mis-

tuning effects, under harmonic and random excitations. Note that either the $\mathcal{H}_\infty$ optimisation or the $\mathcal{H}_2$ optimisation can handle both types of excitations. But $\mathcal{H}_\infty$ optimisation can get better suppression performance for harmonic excitations than $\mathcal{H}_2$ optimisation while $\mathcal{H}_2$ optimisation can get better suppression performance for random excitations than $\mathcal{H}_\infty$ optimisation. So in practice the optimisation method should be chosen based on the spectra of excitation signals.

The structure of this chapter is as follows. In Section 4.1.2, the infinite-dimensional model Σ of a monopile wind turbine tower stabilised by a TMD system located in the nacelle is introduced. It is then reformulated to the state space format. Subsequently, Σ is discretised along the tower span using the spectral element method to derive its finite-dimensional version Σ_d. Finally, Σ_d is verified against the FAST simulation of the NREL monopile 5-MW baseline wind turbine model. In Section 4.1.3, optimal design for the TMD system is conducted based on Σ_d. The spring and damping constants of the TMD are the design parameters while the mass of the TMD is fixed to be 2% of the total turbine mass. The design parameters are obtained by minimising the $\mathcal{H}_2$-norm of the transfer function matrix of Σ_d with force and torque input and tower-top displacement output. Here the frequency-limited version of the $\mathcal{H}_2$-norm is used, which means to compute the $\mathcal{H}_2$-norm over a small interval around the first modal frequency of the monopile wind turbine tower. Finally, an optimal fore-aft TMD and an optimal side-to-side TMD are obtained. In Section 4.1.4, simulations are carried out using the NREL monopile 5-MW baseline wind turbine model within FAST to test the effectiveness of the optimal TMD system. In Section 4.2, first multiple TMDs are incorporated into a non-uniform SCOLE model. Then the infinite-dimensional SCOLE-TMD system Σ_e is spatially discretised into a finite-dimensional model Σ_{ed} using the finite element method (FEM). After that, a scheme is proposed for the optimisation of the parameters of the multiple TMDs in Σ_{ed} based on the $\mathcal{H}_\infty$ and $\mathcal{H}_2$ optimisations to suppress vibrations of the non-uniform SCOLE model with several dominant modes under harmonic and random excitations respectively. Finally, the performances of different TMD systems designed by the proposed scheme are compared with traditional methods.

4.1.2 System Modelling

An Infinite-dimensional Model of the Monopile Wind Turbine Tower Stabilised by A TMD Located in the Nacelle

The SCOLE system is a well known model for a flexible beam with one end clamped and the other end connected to a rigid body. Like Zhao and Weiss [40, 41], here it is used to model a monopile wind turbine tower that has the bottom end clamped in the ocean floor and the upper end linked to the heavy rigid RNA by neglecting any coupling with blade motions. The SCOLE system can be used to represent the tower dynamics in the fore-aft plane and in the side-to-side plane respectively with corresponding parameters. In this chapter, a TMD is designed in either plane to reduce vibration loads of the whole monopile wind turbine tower because all vibrations can be decomposed into these two orthogonal planes. The two TMDs share the same mass component, but have different springs and dampers as shown in Figure 2.3. The spring and damper components of the TMD system in each plane connect at one end to the nacelle and link at the other end to its mass component in parallel. The mass component of the TMD is put on the floor of the nacelle through wheels/racks or hanged above the floor through cables. The mathematical model Σ of the monopile wind turbine tower stabilised by a TMD, in either the fore-aft plane or the side-to-side plane, is shown below [102].

$$\rho(x)w_{tt}(x,t) + (EI(x)w_{xx}(x,t))_{xx} = 0, \quad (x,t) \in (0,l) \times [0,\infty), \tag{4.1}$$

$$w(0,t) = 0,\ w_x(0,t) = 0, \tag{4.2}$$

$$mw_{tt}(l,t) - (EIw_{xx})_x(l,t) = F_{aero}(t) + k_1(p(t) - w(l,t)) + d_1(p_t(t) - w_t(l,t)), \tag{4.3}$$

$$Jw_{xtt}(l,t) + EI(l)w_{xx}(l,t) = T_{aero}(t), \tag{4.4}$$

$$m_1 p_{tt}(t) = k_1(w(l,t) - p(t)) + d_1(w_t(l,t) - p_t(t)), \tag{4.5}$$

where the subscripts t and x denote derivatives with respect to the time t and the position x. The equations (4.1)–(4.4) are the non-uniform monopile wind turbine tower subsystem while the equation (4.5) is the TMD subsystem. The tower subsystem (4.1)–(4.4) is introduced first. (4.1) is Euler-Bernoulli beam equation which represents the dynamics of the flexible tower while (4.2) means that the tower is clamped. (4.3)–(4.4) are the Newton-Euler rigid body equations which represent the dynamics of the RNA. l, ρ and EI denote the tower's height, mass density function and flexural rigidity function while w denotes the translational displacement of the tower. $\rho, EI \in C^4[0,l]$ are assumed to be strictly positive functions. The

parameters $m > 0$ and $J > 0$ are the mass and the moment of inertia of the RNA. F_{aero} and T_{aero} denote the aerodynamic force and the aerodynamic torque acting on the RNA. In the TMD system (4.5), $m_1 > 0$, $k_1 > 0$ and $d_1 > 0$ are the mass, spring constant and damping coefficient of the TMD. Both subsystems are interconnected through the translational velocity of the RNA (tower-top translational velocity) $w_t(l,t)$ and the force $\big(k_1(p(t) - w(l,t)) + d_1(p_t(t) - w_t(l,t))\big)$ generated by the TMD system.

The state of Σ at the time t is

$$z(t) = \begin{bmatrix} z_1(t) \\ z_2(t) \\ z_3(t) \\ z_4(t) \\ z_5(t) \\ z_6(t) \end{bmatrix} = \begin{bmatrix} w(\cdot,t) \\ w_t(\cdot,t) \\ w_t(l,t) \\ w_{xt}(l,t) \\ p(t) - w(l,t) \\ p_t(t) \end{bmatrix}, \tag{4.6}$$

where z_1 and z_2 are the translational displacement and velocity of the tower. z_3 and z_4 are the translational velocity and angular velocity of the nacelle. z_5 and z_6 are the position and translational velocity of the mass component of the TMD. The natural energy state space of Σ is

$$X = \mathcal{H}_l^2(0,l) \times L^2[0,l] \times \mathbb{C}^4, \tag{4.7}$$

where

$$\mathcal{H}_l^2(0,l) = \{h \in \mathcal{H}^2(0,l) \mid h(0) = 0,\ h_x(0) = 0\}. \tag{4.8}$$

Here $\mathcal{H}^n$ ($n \in \mathbb{N}$) denotes the usual Sobolev spaces. Zhao and Weiss [102, 103] proved that Σ is strongly stable on X.

Discretising the TMD-stabilised Monopile Wind Turbine Tower Model Σ

In this section, the spectral element method is used to discretise the infinite-dimensional TMD-stabilised monopile wind turbine tower model Σ (4.1)–(4.5) in the spatial domain for fast simulation and TMD optimisation. For discretisation, the spatial domain $x \in (0,l)$ of Σ is normalised to the standard domain $x \in (-1,1)$.

The first step is to obtain the weak form of the governing equation. Multiplying both sides of the equation (4.1) with a weight function $u(x)$ and integrating

over the domain $x \in (-1, 1)$ yield

$$\int_{-1}^{1} \{\rho w_{tt} u + (EIw_{xx})_{xx} u\} \mathrm{d}x = 0. \tag{4.9}$$

Using integration by parts, one has

$$\int_{-1}^{1} \{\rho w_{tt} u + EIw_{xx} u_{xx}\} \mathrm{d}x + \left[(EIw_{xx})_x u - EIw_{xx} u_x\right]_{x=-1}^{x=1} = 0. \tag{4.10}$$

As in the finite element method, the weight function here is required to satisfy the essential boundary conditions (4.2), that is

$$u(x = -1) = u_x(x = -1) = 0. \tag{4.11}$$

Substituting equations (4.3)-(4.4) and (4.11) into (4.10), one gets the weak form

$$\begin{aligned} \int_{-1}^{1} \{\rho w_{tt} u + EIw_{xx} u_{xx}\} \mathrm{d}x = \quad & \left[-mw_{tt} + F_{aero} + k_1(p - w) + d_1(p_t - w_t)\right] u \Big|_{x=1} \\ & + \left(T_{aero} - Jw_{xtt}\right) u_x \big|_{x=1}. \end{aligned} \tag{4.12}$$

Moving all the terms containing time derivatives to the left-hand side of the equation and all other terms to the right-hand side, one has

$$\begin{aligned} \int_{-1}^{1} \{\rho w_{tt} u\} \mathrm{d}x + \quad & \left[mw_{tt} u - d_1(p_t - w_t) u\right]_{x=1} + \left[Jw_{xtt} u_x\right]_{x=1} = -\int_{-1}^{1} \{EIw_{xx} u_{xx}\} \mathrm{d}x \\ & + \left[F_{aero} u + k_1(p - w) u\right]_{x=1} + T_{aero} u_x|_{x=1}. \end{aligned} \tag{4.13}$$

Now introduce

$$v(x, t) = w_t(x, t), \tag{4.14}$$

and

$$r(t) = p_t(t) \tag{4.15}$$

which represents the translational velocity of the mass component of the TMD. Then equation (4.13) can be written as

$$\begin{aligned} \int_{-1}^{1} \{\rho v_t u\} \mathrm{d}x + \quad & \left[mv_t u - d_1(r - v) u\right]_{x=1} + \left[Jv_{xt} u_x\right]_{x=1} = -\int_{-1}^{1} \{EIw_{xx} u_{xx}\} \mathrm{d}x \\ & + \left[F_{aero} u + k_1(p - w) u\right]_{x=1} + T_{aero} u_x|_{x=1}. \end{aligned} \tag{4.16}$$

The second step is to approximate the solution using high-order basis func-

tions. Specifically, $w(x,t)$ is approximated by

$$w(x,t) = \sum_{n=0}^{N} \hat{w}_n(t)\psi_n(x), \tag{4.17}$$

where the basis function $\psi_n(x)$ needs to satisfy the essential boundary conditions

$$\psi_n(x=-1) = \frac{\mathrm{d}\psi_n}{\mathrm{d}x}(x=-1) = 0. \tag{4.18}$$

A convenient choice is

$$\psi_n(x) = (1+x)^2 T_n(x) \tag{4.19}$$

where $T_n(x)$ is the n_{th} Chebyshev polynomial of the first kind [104]. Similarly,

$$v(x,t) = \sum_{n=0}^{N} \hat{v}_n(t)\psi_n(x) \tag{4.20}$$

and it is obvious that

$$\hat{v}_n = \frac{\mathrm{d}\hat{w}_n}{\mathrm{d}t} \quad \forall\ n \in \{0,1,\cdots,N\}\,. \tag{4.21}$$

Substitute (4.20) for $v(x,t)$, (4.17) for $w(x,t)$ and $\psi_n(x)$ for $u(x)$ into (4.16) for $n \in \{0,1,\cdots,N\}$. The resulting $N+1$ linear equations can be written in matrix form

$$\mathbf{E}\dot{\hat{\mathbf{v}}} = \mathbf{A_{21}}\hat{\mathbf{w}} + \mathbf{A_{22}}\hat{\mathbf{v}} + \mathbf{A_{23}}p + \mathbf{A_{24}}r + \mathbf{B_{21}}F_{aero} + \mathbf{B_{22}}T_{aero} \tag{4.22}$$

where

$$\hat{\mathbf{w}} = [\hat{w}_0, \hat{w}_1, \cdots, \hat{w}_N]^T \tag{4.23}$$

$$\hat{\mathbf{v}} = [\hat{v}_0, \hat{v}_1, \cdots, \hat{v}_N]^T \tag{4.24}$$

and each element of the matrices is given by

$$\begin{aligned}
\mathbf{E}(i,j) &= \int_{-1}^{1} \rho\psi_i\psi_j \mathrm{d}x + \left[m\psi_i\psi_j + J\frac{\mathrm{d}\psi_i}{\mathrm{d}x}\frac{\mathrm{d}\psi_j}{\mathrm{d}x} \right]_{x=1} && (4.25)\\
\mathbf{A_{21}}(i,j) &= -\int_{-1}^{1} EI\frac{\mathrm{d}^2\psi_i}{\mathrm{d}x^2}\frac{\mathrm{d}^2\psi_j}{\mathrm{d}x^2}\mathrm{d}x - [k_1\psi_i\psi_j]_{x=1} && (4.26)\\
\mathbf{A_{22}}(i,j) &= -[d_1\psi_i\psi_j]_{x=1} && (4.27)\\
\mathbf{A_{23}}(i) &= k_1\psi_i|_{x=1} && (4.28)\\
\mathbf{A_{24}}(i) &= d_1\psi_i|_{x=1} && (4.29)\\
\mathbf{B_{21}}(i) &= \psi_i|_{x=1} && (4.30)\\
\mathbf{B_{22}}(i) &= \left.\frac{\mathrm{d}\psi_i}{\mathrm{d}x}\right|_{x=1}. && (4.31)
\end{aligned}$$

Note that $\mathbf{E}, \mathbf{A_{21}}, \mathbf{A_{22}} \in \mathbb{R}^{(N+1)\times(N+1)}$ and $\mathbf{A_{23}}, \mathbf{A_{24}}, \mathbf{B_{21}}, \mathbf{B_{22}} \in \mathbb{R}^{(N+1)\times 1}$.

Equation (4.5) can be written as

$$m_1 r_t(t) = k_1(w(1,t) - p(t)) + d_1(v(1,t) - r(t)). \tag{4.32}$$

Substituting (4.20) for $v(x,t)$ and (4.17) for $w(x,t)$ into (4.32), one gets

$$m_1 r_t = \mathbf{A_{41}}\hat{\mathbf{w}} + \mathbf{A_{42}}\hat{\mathbf{v}} - k_1 p - d_1 r \tag{4.33}$$

where $\mathbf{A_{41}}, \mathbf{A_{42}} \in \mathbb{R}^{1\times(N+1)}$ and

$$\begin{aligned}
\mathbf{A_{41}}(j) &= k_1\psi_j|_{x=1}, && (4.34)\\
\mathbf{A_{42}}(j) &= d_1\psi_j|_{x=1}. && (4.35)
\end{aligned}$$

By the relations (4.15) and (4.21), the finite-dimensional model can be formulated as

$$\mathbf{M_1}\begin{bmatrix} \dot{\hat{\mathbf{w}}} \\ \dot{\hat{\mathbf{v}}} \\ \dot{p} \\ \dot{r} \end{bmatrix} = \mathbf{M_2}\begin{bmatrix} \hat{\mathbf{w}} \\ \hat{\mathbf{v}} \\ p \\ r \end{bmatrix} + \mathbf{M_3}\begin{bmatrix} F_{aero} \\ T_{aero} \end{bmatrix} \tag{4.36}$$

where

$$\mathbf{M_1} = \begin{bmatrix} \mathbf{I} & \mathbf{0} & \mathbf{0} & \mathbf{0} \\ \mathbf{0} & \mathbf{E} & \mathbf{0} & \mathbf{0} \\ \mathbf{0} & \mathbf{0} & 1 & 0 \\ \mathbf{0} & \mathbf{0} & 0 & m_1 \end{bmatrix}, \tag{4.37}$$

$$\mathbf{M_2} = \begin{bmatrix} \mathbf{0} & \mathbf{I} & \mathbf{0} & \mathbf{0} \\ \mathbf{A_{21}} & \mathbf{A_{22}} & \mathbf{A_{23}} & \mathbf{A_{24}} \\ \mathbf{0} & \mathbf{0} & 0 & 1 \\ \mathbf{A_{41}} & \mathbf{A_{42}} & -k_1 & -d_1 \end{bmatrix}, \tag{4.38}$$

$$\mathbf{M_3} = \begin{bmatrix} \mathbf{0} & \mathbf{0} \\ \mathbf{B_{21}} & \mathbf{B_{22}} \\ 0 & 0 \\ 0 & 0 \end{bmatrix} \tag{4.39}$$

and $\mathbf{I}$ is the identity matrix of appropriate size.

Note that the states $\hat{\mathbf{w}}$ and $\hat{\mathbf{v}}$ are spectral coefficients, rather than the values of $w(x,t)$ and $v(x,t)$ in the physical space. Thus transformation is needed between the spectral space and the physical space. For example, to simulate tower movements and derive the tower deflection $w(x,t)$, initial conditions need specifying first. The initial conditions $w(x,0)$ and $v(x,0)$ cannot be assigned to the ODE solver directly. Instead, the corresponding $\hat{\mathbf{w}}(0)$ and $\hat{\mathbf{v}}(0)$ need calculating. It follows from (4.17) that

$$\begin{bmatrix} w(x_0,0) \\ \vdots \\ w(x_N,0) \end{bmatrix} = \mathbf{T}\hat{\mathbf{w}}(0) \tag{4.40}$$

where the matrix $\mathbf{T} \in \mathbb{R}^{(N+1)\times(N+1)}$ is given by

$$\mathbf{T}(i,j) = \psi_j|_{x=x_i} \tag{4.41}$$

and $x_i, i = 0, 1, \ldots, N$ are the collocation points

$$x_i = \begin{cases} \cos(\frac{i\pi}{N}), & i = 0, 1, \ldots, N-1 \\ \cos(\frac{(N-0.5)\pi}{N}), & i = N \end{cases} . \tag{4.42}$$

Note that the last collocation point is $x_N = \cos(\frac{(N-0.5)\pi}{N})$ instead of $x_N = \cos\pi = -1$. That is because $\psi_j(x=-1) = 0$ (see equation (4.18)), the last row of $\mathbf{T}$ would be a zero vector if $x_N = -1$. Such a $\mathbf{T}$ is guaranteed to be nonsingular. Now it is evident that

$$\hat{\mathbf{w}}(0) = \mathbf{T}^{-1} \begin{bmatrix} w(x_0, 0) \\ \vdots \\ w(x_N, 0) \end{bmatrix} \tag{4.43}$$

and $\hat{\mathbf{v}}(0)$ can be obtained in the same manner.

With the initial conditions, the model can be simulated easily, whose outputs $\hat{\mathbf{w}}(t)$ and $\hat{\mathbf{v}}(t)$ can be transformed to physical domain variables

$$\mathbf{w}(x,t) = \mathbf{T}\hat{\mathbf{w}}(t), \tag{4.44}$$

$$\mathbf{v}(x,t) = \mathbf{T}\hat{\mathbf{v}}(t), \tag{4.45}$$

where

$$\mathbf{w}(x,t) = [w(x_0,t), \ldots, w(x_N,t)]^T, \tag{4.46}$$

$$\mathbf{v}(x,t) = [v(x_0,t), \ldots, v(x_N,t)]^T. \tag{4.47}$$

Thus the state space formulation of the spatially discretised monopile wind turbine tower-TMD system Σ_d is

$$\begin{cases} \dot{\mathbf{X}} = \mathbf{A}\mathbf{X} + \mathbf{B}\mathbf{u} & (4.48) \\ \mathbf{Y} = \mathbf{C}\mathbf{X} & (4.49) \end{cases}$$

where the state $\mathbf{X} = [\hat{\mathbf{w}}, \hat{\mathbf{v}}, p, r]^T$, input $\mathbf{u} = [F_{aero}, T_{aero}]^T$, state matrix $\mathbf{A} = \mathbf{M_1}^{-1}\mathbf{M_2}$, input matrix $\mathbf{B} = \mathbf{M_1}^{-1}\mathbf{M_3}$. If $\mathbf{Y} = \mathbf{w}(x,t)$ (the whole tower deflection), output matrix $\mathbf{C} = [\mathbf{T}\ \mathbf{0}\ 0\ 0]$ while if $\mathbf{Y} = w(l,t)$ (tower-top translational displacement), $\mathbf{C} = \big[\mathbf{T}(\mathbf{1},:)\ \mathbf{0}\ 0\ 0\big]$. Based on Σ_d, not only can the TMD design be conducted using $\mathcal{H}_2$ optimisation, but also can tower dynamics be simulated (for example using the MATLAB built-in function *lsim*).

Model Verification

Now the monopile wind turbine tower model Σ_d (4.48)–(4.49) is verified against the NREL monopile 5-MW baseline wind turbine tower model within FAST. Σ_d can be used to represent the dynamics of the tower and TMD in the fore-aft direction and in the side-to-side direction respectively with corresponding parameter choices.

The mass of the TMD m_1 is chosen to be 20,000 kg because it is about 2% of the total structural mass of the turbine, which is a mass percentage normally used in civil structures [2]. The spring and damping constants of the TMDs are chosen to be 51,320.72 N/m and 5,427.46 N·s/m respectively in the fore-aft direction, and to be 51,136.47 N/m and 5,220.53 N·s/m respectively in the side-to-side direction. The tower parameters in Σ_d (4.48)–(4.49) can be obtained directly or through simple computations from the distributed properties of the monopile tower, which are available in Table 2.3. According to Tables 2.1 and 2.2, the height l of the monopile wind turbine tower above the mudline is 107.6 m, and the RNA mass is 350,000 kg. The rigid RNA moment of inertia is 4.5050443961e7 kg·m^2 in the side-to-side plane and is 2.4940615741e7 kg·m^2 in the fore-aft plane, both of which are obtained using the Aggregate Mass tool in ADAMS based on the ADAMS wind turbine dataset generated by the FAST-to-ADAMS preprocessor (see Section 2.2). The transition piece between the tower and monopile is not continuous, so a 1-meter smooth transition region is set at the position $x \in$ [29.5 m, 30.5 m] (half from the monopile region and the other half from the tower region) because Σ (4.1)–(4.5) requires that the mass density function $\rho \in C^4(0, l)$ and the flexural rigidity function $EI \in C^4(0, l)$. When $x \leq$29.5 m, i.e, at the monopile region, $\rho =$9,517.14 kg/m; when $x >$30.5 m, i.e., at the tower region, a 2nd-order polynomial is used to fit the discrete density data of the monopile wind turbine tower (from Table 2.3) using the least squares method. Then the transition region $x \in$ [29.5 m, 30.5 m] is fitted with a 9th-order polynomial to make $\rho \in C^4(0, l)$ for the whole monopile wind turbine tower. The flexural rigidity function EI is fitted in the same way. The fitted curves of ρ and EI are shown in Figure 4.3.

The same loading data are used for Σ_d (4.48)–(4.49) (i.e. the force F_{aero} and torque T_{aero}) and the FAST model. The loading data are obtained from a FAST simulation under a wind input with a mean hub-height longitudinal speed of 10 m/s and 15% turbulence generated by TurbSim IEC Kaimal spectral model with NTM (introduced in Section 2.1.2). The whole tower deflections and tower-top displacements computed from Σ_d (4.48)–(4.49) are compared with FAST simulations, as shown in Figures 4.4–4.7. These figures clearly indicate that the dynamic outputs of Σ_d (4.48)–(4.49) are extremely close to those of the FAST simulations, which verifies the SCOLE-TMD model. Simulations are also conducted for the case of a sole wind turbine tower using Σ_d (4.48)–(4.49) (excluding TMD) and FAST, which got similar agreements as Figures 4.4–4.7, thus is omitted.

Finally, the power spectral densities (PSDs) of the tower-top displacements for the case of a sole NREL monopile 5-MW baseline turbine tower and the case

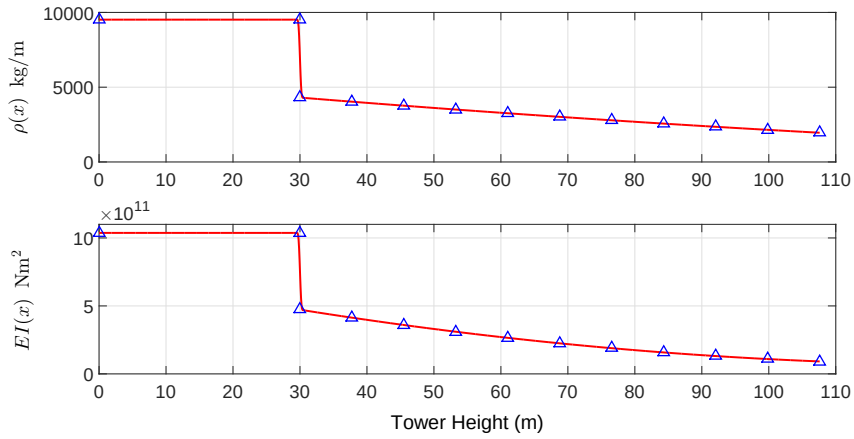

Figure 4.3: Comparisons between the distributed properties of the mass density & flexural rigidity of the NREL monopile 5-MW baseline wind turbine tower and their corresponding fitted functions $\rho(x)$ & $EI(x)$. The blue triangles represent distributed tower properties given in Table 2.3 while the red solid lines are their corresponding fitted functions.

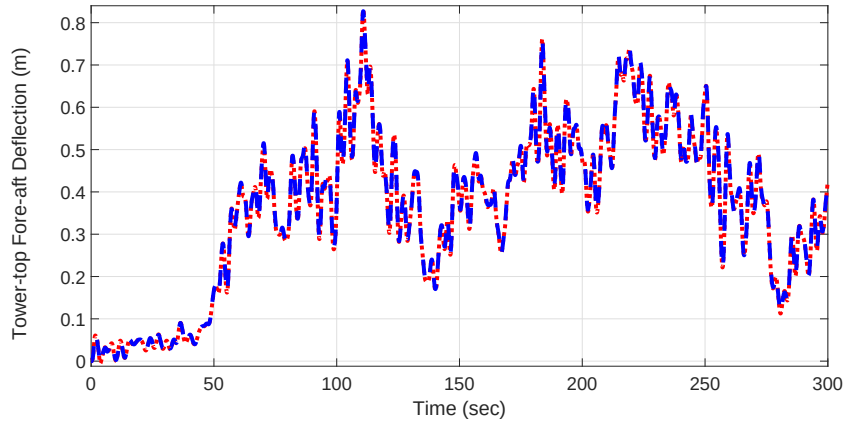

Figure 4.4: Time simulation (in seconds) of the fore-aft tower-top translational displacement (in meters) of the NREL monopile 5-MW baseline turbine tower stabilised by a fore-aft TMD under a wind input with a mean speed of 10 m/s and turbulence intensity of 15%, obtained from Σ_d (4.48)–(4.49) (red dotted line) and FAST (blue dash line) respectively.

of the tower stabilised by a TMD, computed from Σ_d (4.48)–(4.49), are compared with FAST simulations. As shown in Figures 4.8 and 4.9, the results obtained by Σ_d agree perfectly with the ones obtained using the FAST simulations in both cases with and without TMD.

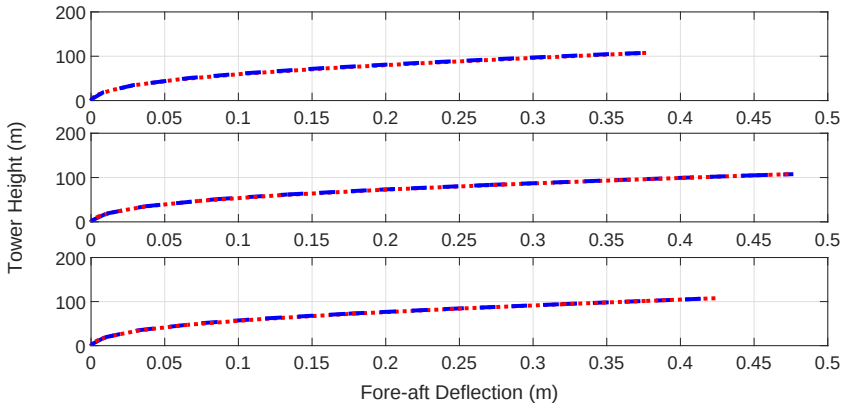

Figure 4.5: Simulation of the fore-aft translational deflections of the NREL monopile 5-MW baseline turbine tower stabilised by a fore-aft TMD under a wind input with a mean speed of 10 m/s and turbulence intensity of 15%, obtained from Σ_d (4.48)–(4.49) (red dotted lines) and FAST (blue dash lines) respectively. The upper, middle and lower diagrams show results at 100 s, 200 s and 300 s, respectively. The horizontal axis denotes the translational tower deflections (in meters) with positive value meaning 'right' and negative value meaning 'left', while the vertical axis describes the height of the tower (in meters).

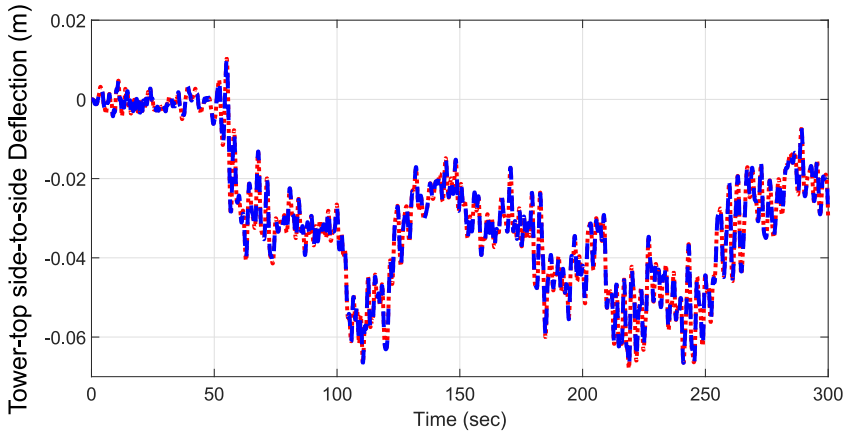

Figure 4.6: Time simulation (in seconds) of the side-to-side tower-top translational displacement (in meters) of the NREL monopile 5-MW baseline turbine tower stabilised by a side-to-side TMD under a wind input with a mean speed of 10 m/s and turbulence intensity of 15%, obtained from Σ_d (4.48)–(4.49) (red dotted line) and FAST (blue dash line) respectively.

4.1.3 Optimisation of TMDs for Load Reduction of A Monopile Wind Turbine Tower

In this section, optimal TMDs are designed to reduce vibrations of the monopile wind turbine tower-TMD model Σ_d (4.48)–(4.49). For the system under harmonic

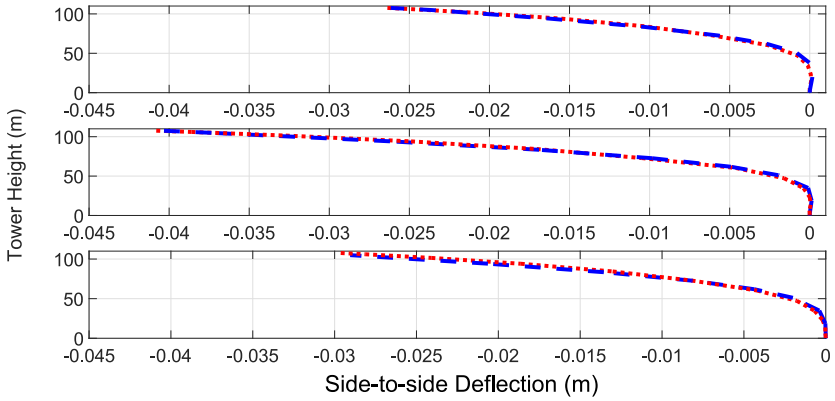

Figure 4.7: Simulation of the side-to-side translational deflections of the NREL monopile 5-MW baseline turbine tower stabilised by a side-to-side TMD under a wind input with a mean speed of 10 m/s and turbulence intensity of 15%, obtained from Σ_d (4.48)–(4.49) (red dotted lines) and FAST (blue dash lines) respectively. The upper, middle and lower diagrams show results at 100 s, 200 s and 300 s, respectively. The horizontal axis denotes the translational tower deflections (in meters) with positive value meaning 'right' and negative value meaning 'left', while the vertical axis describes the height of the tower (in meters).

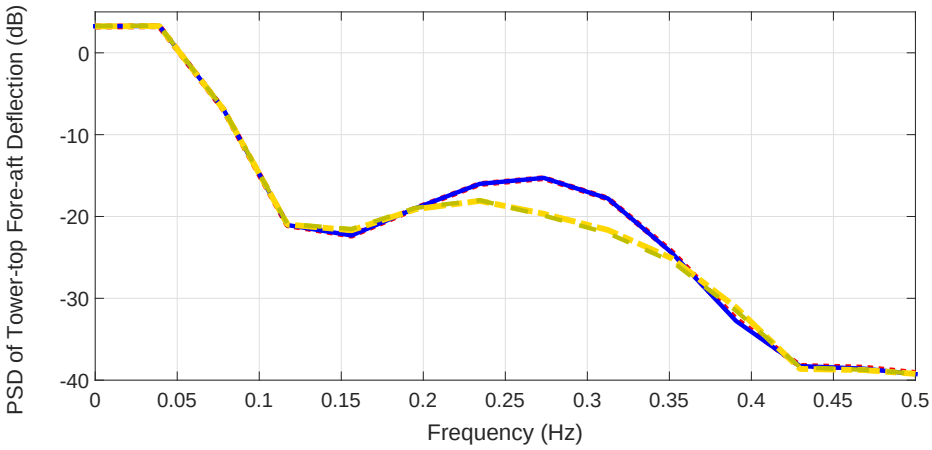

Figure 4.8: Power spectral density (PSD) of tower-top fore-aft translational displacement of the NREL monopile 5-MW baseline turbine tower under a wind input with a mean speed of 10 m/s and turbulence intensity of 15%, obtained from Σ_d (4.48)–(4.49) (red dotted and yellow dash-dotted lines denoting cases of sole tower and tower stabilised by a fore-aft TMD, respectively) and FAST (blue solid and green dash lines denoting cases of sole tower and tower stabilised by a fore-aft TMD, respectively).

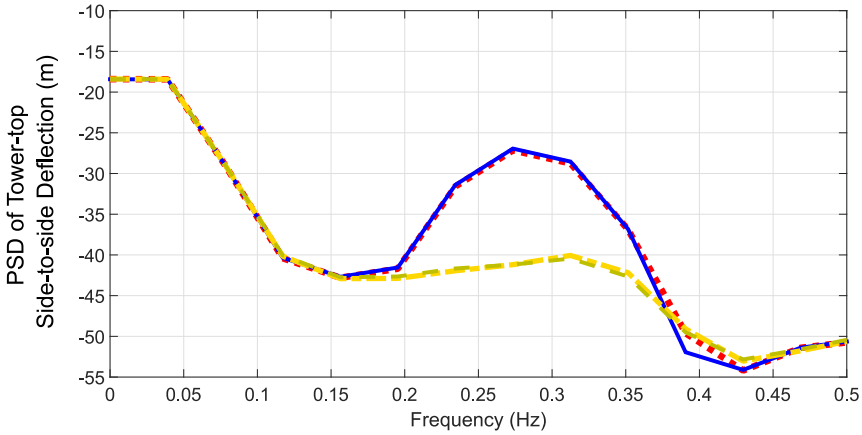

Figure 4.9: Power spectral density (PSD) of tower-top side-to-side translational displacement of the NREL monopile 5-MW baseline turbine tower under a wind input with a mean speed of 10 m/s and turbulence intensity of 15%, obtained from Σ_d (4.48)–(4.49) (red dotted and yellow dash-dotted lines denoting cases of sole tower and tower stabilised by a side-to-side TMD, respectively) and FAST (blue solid and green dash lines denoting cases of sole tower and tower stabilised by a side-to-side TMD, respectively).

excitations, it is desirable to develop a control mechanism to minimise the peak magnitude of the system frequency response, which is associated with $\mathcal{H}_\infty$ optimisation. If the system is subject to random excitations (like winds), it is more appropriate to take the RMS (root-mean-square) value of the system response as the performance index for optimisation design, which is linked with the system's $\mathcal{H}_2$ optimisation [105, 106]. In terms of vibration control, some frequencies are of particular interest since the excitations in the real world usually have limited frequency bands and mainly affect narrow bands around dominant modal frequencies of the systems with little or no damping. Therefore, the frequency-limited version of the $\mathcal{H}_2$-norm is utilised in the optimisation of TMD parameters, i.e., computing the $\mathcal{H}_2$-norm over a limited frequency range around the first (dominant) modal frequency of the monopile tower, which is numerically cheaper. As mentioned earlier, the largest deflection occurs at the tower top when the first mode is excited. Hence, to achieve optimal vibration suppression of the monopile wind turbine tower, optimal TMD

parameters are chosen to minimise the frequency-limited $\mathcal{H}_2$-norm (4.50) of $\mathbf{H}(s)$:

$$\|\mathbf{H}\|_{2,[\omega_1,\omega_2]} = \frac{1}{\sqrt{2\pi}} \left(\int_{-\omega_2}^{-\omega_1} trace\left[\mathbf{H}^*\left(\mathrm{j}\nu\right)\mathbf{H}\left(\mathrm{j}\nu\right)\right] d\nu + \int_{\omega_1}^{\omega_2} trace\left[\mathbf{H}^*\left(\mathrm{j}\nu\right)\mathbf{H}\left(\mathrm{j}\nu\right)\right] d\nu \right)^{\frac{1}{2}} \tag{4.50}$$

where $\omega_2 > \omega_1 \in \mathbb{R}^+$, and the superscript $*$ denotes complex conjugate transpose. $\mathbf{H}(s) = \mathbf{C}\left(s\mathbf{I} - \mathbf{A}\right)^{-1}\mathbf{B}$ is the transfer function matrix of Σ_d (4.48)–(4.49) with the external force & torque $[F_{aero}, T_{aero}]^T$ as the input (excitation sources) and the translational displacement $w(l,\cdot)$ of the tower top as the output.

The numerical integrations for the frequency-limited $\mathcal{H}_2$-norm defined in (4.50) can become problematic for high-order systems. Since Σ_d is stable, the Gramian-based formulation can be employed to avoid the calculation of integrations [107]:

$$\begin{aligned} \|\mathbf{H}\|_{2,[\omega_1,\omega_2]} &= \left(trace\left(\mathbf{B}^T\mathbf{Q}_{\omega_2}\mathbf{B}\right) - trace\left(\mathbf{B}^T\mathbf{Q}_{\omega_1}\mathbf{B}\right)\right)^{\frac{1}{2}} \\ &= \left(trace\left(\mathbf{C}\mathbf{P}_{\omega_2}\mathbf{C}^T\right) - trace\left(\mathbf{C}\mathbf{P}_{\omega_1}\mathbf{C}^T\right)\right)^{\frac{1}{2}}, \end{aligned} \tag{4.51}$$

where $\mathbf{P}_{\omega_1}$, $\mathbf{P}_{\omega_2}$ and $\mathbf{Q}_{\omega_1}$, $\mathbf{Q}_{\omega_2}$ are the frequency-limited reachability and observability Gramians, respectively [108]. $\mathbf{P}_{\omega_1}$ and $\mathbf{Q}_{\omega_1}$ can be derived by solving two Lyapunov equations:

$$\begin{aligned} \mathbf{A}\mathbf{P}_{\omega_1} + \mathbf{P}_{\omega_1}\mathbf{A}^T + \mathbf{W}_c(\omega_1) = 0, \\ \mathbf{A}^T\mathbf{Q}_{\omega_1} + \mathbf{Q}_{\omega_1}\mathbf{A} + \mathbf{W}_o(\omega_1) = 0, \end{aligned} \tag{4.52}$$

where

$$\begin{aligned} \mathbf{W}_c(\omega_1) = \mathbf{S}(\omega_1)\mathbf{B}\mathbf{B}^T + \mathbf{B}\mathbf{B}^T\mathbf{S}^{'}(\omega_1), \\ \mathbf{W}_o(\omega_1) = \mathbf{S}^{'}(\omega_1)\mathbf{C}^T\mathbf{C} + \mathbf{C}^T\mathbf{C}\mathbf{S}(\omega_1), \end{aligned} \tag{4.53}$$

and

$$\mathbf{S}(\omega_1) = \frac{\mathrm{j}}{2\pi}\mathbf{logm}\left[\left(\mathbf{A} + \mathrm{j}\omega_1\mathbf{I}\right)\left(\mathbf{A} - \mathrm{j}\omega_1\mathbf{I}\right)^{-1}\right], \tag{4.54}$$

where $\mathbf{logm}(\cdot)$ denotes the matrix logarithm. $\mathbf{P}_{\omega_2}$ and $\mathbf{Q}_{\omega_2}$ are obtained in the same way.

To determine the frequency interval $[\omega_1, \omega_2]$, the first modal frequency of the monopile wind turbine tower is needed. It is the smallest absolute value of the imaginary parts of eigenvalues of $\mathbf{A}$ in Σ_d (4.48)–(4.49) excluding TMD. Through simple computations, one gets that the first tower fore-aft and side-to-side modal

Table 4.1: Values of the $\mathcal{H}_2$-norm (4.50) of Σ_d with N increasing from 9 to 17.

N	9	10	11	12	13	14	15	16	17
$\mathcal{H}_2$-norm ($\times 10^{-6}$)	1.891	1.890	1.893	1.893	1.892	1.895	1.894	1.895	1.893

frequencies are 0.290 Hz (1.822 rad/s) and 0.287 Hz (1.806 rad/s) respectively, while they are both 0.28 Hz calculated by FAST [109]. Here the frequency intervals [1.458 rad/s, 2.186 rad/s] with the central frequency at 1.822 rad/s and [1.445 rad/s, 2.167 rad/s] with the central frequency at 1.806 rad/s are used for the optimisations of the fore-aft TMD and side-to-side TMD respectively.

The *fmincon* function of MATLAB is employed to minimise the frequency-limited $\mathcal{H}_2$-norm (4.50) with spring and damping constants of TMD as design variables. All the other parameters of Σ_d are explained in Section 4.1.2. Recall that the mass of the TMD is chosen to be 20000 kg (about 2% of the total structural mass of the turbine). The optimal spring and damping constants are derived as 61514.97 N/m and 7518.93 N·s/m respectively in the fore-aft TMD, and 60565.20 N/m and 7405.66 N·s/m respectively in the side-to-side TMD. It is noticeable that the natural frequencies of the fore-aft TMD (0.279 Hz) and side-to-side TMD (0.277 Hz) are both approximately equal to their corresponding first modal frequencies of the monopile wind turbine tower.

Note that the discretisation resolution (i.e., the number of collocation points) used for conducting model verification in Section 4.1.2 as well as for optimising TMD above is $N = 13$. Ideally, the value of N should be independent of the $\mathcal{H}_2$-norm (4.50), which implies that as N increases, the $\mathcal{H}_2$-norm of $\mathbf{H}$ should converge to a small range. Table 4.1 lists its values in the fore-aft direction with N increasing from 9 to 17. Clearly, it converges to a small narrow range between 1.890×10^{-6} and 1.895×10^{-6}, which means that the relative error is less than 0.27%. The result for the $\mathcal{H}_2$-norm of $\mathbf{H}$ in the side-to-side direction is similar, thus omitted.

4.1.4 Simulation Tests

Now the optimal TMD system is tested based on the simulations of the NREL OC3 monopile 5-MW baseline wind turbine model within FAST. First, average damage equivalent loads (DEQLs) at the monopile base are compared between the cases with and without TMD(s) under wind and wave excitations. Note that the monopile base of the monopile wind turbine tower has the largest bending moment (maximum stress) [110]. The results are verified against the paper [2]. As obtained in Section 4.1.3, the optimal spring and damping constants are 61,514.97 N/m and 7,518.93

N·s/m respectively in the fore-aft TMD, and are 60,565.20 N/m and 7,405.66 N·s/m respectively in the side-to-side TMD. In the paper [2] the optimal spring and damping constants of the TMDs in the fore-aft and the side-to-side directions are the same, i.e., 54,274 N/m and 7,414 N·s/m respectively. The mass of the TMD is chosen to be 20,000 kg in all the cases.

The wind inputs are generated by TurbSim using the IEC Kaimal spectral model with NTM (introduced in Section 2.1.2). The turbulence intensity is 15%. The waves are irregularly (stochastically) generated by HydroDyn based on the JONSWAP spectrum (see Section 2.2). The peak spectral period of incident waves is set to be 12.4 seconds. Four types of wind and wave inputs are generated for simulations. Two inputs are generated by different random seeds based on a same mean hub-height longitudinal speed of 10 m/s (below the rated value 11.4 m/s, in Region 2) and a same significant wave height of 2 m. The DEQLs with these two types of inputs are averaged. The other two inputs are also generated by different random seeds based on a same mean hub-height longitudinal speed of 18 m/s (above-rated, in Region 3) and a same significant wave height of 3.5 m. The DEQLs with these two types of inputs are averaged as well. Three cases are simulated: the sole tower case (i.e., without TMDs), the case using the optimal TMDs obtained in Section 4.1.3, and the case using TMDs designed in the paper [2]. For the cases with TMDs, three kinds of TMD configurations are considered: only the fore-aft TMD, only the side-to-side TMD, and both (the fore-aft and side-to-side) TMDs.

The NREL MLife code (introduced in Section 2.3) is used to compute DEQL. The Wohler exponent is set to be 3 because the monopile wind turbine tower is made of steel. Table 4.2 lists the DEQLs at the monopile base of the NREL monopile 5-MW baseline turbine model and load reduction ratios with the TMD system designed in Section 4.1.3 and the paper [2] under the wind and wave inputs mentioned above. It is noticeable from Table 4.2 that the vibration control results are similar as the paper [2]. But the proposed control design model can also simulate the dynamics of the wind turbine tower very accurately as shown in Figures 4.4–4.7.

Finally the PSDs of the tower-top translational deflections of the sole tower are compared with the tower stabilised by the optimal fore-aft and side-to-side TMDs based on FAST simulations under a wind input with a mean hub-height longitudinal speed of 18 m/s and turbulence intensity of 15%, and a wave input with the significant wave height of 3.5 m. As shown in Figures 4.10 and 4.11, the optimal TMDs have achieved substantial vibration reductions.

Table 4.2: Average damage equivalent loads (DEQLs) at the monopile base of the NREL monopile 5-MW baseline turbine model for the simulation cases of the sole tower (no TMD), tower stabilised by a fore-aft TMD, tower stabilised by a side-to-side TMD, and tower stabilised by both (the fore-aft and side-to-side) TMDs. The data outside the brackets are obtained using the optimal TMD(s) while the data in the brackets are obtained using the TMD(s) designed in the paper [2]. 'Load A' denotes a wind input with a mean speed of 10 m/s and a turbulence intensity of 15%, together with a wave input with a significant wave height of 2 m. It is generated twice by two different random seeds. The DEQL is the averaged value of the DEQLs under both excitations. 'Load B' denotes a wind input with a mean speed of 18 m/s and a turbulence intensity of 15%, together with a wave input with a significant wave height of 3.5 m. It is generated twice by two different random seeds. The DEQL is the averaged value of the DEQLs under both excitations.

	No TMD	Fore-aft TMD	Side-to-side TMD	Both TMDs
Fore-aft DEQL (kN·m), load A	15,275	12,628 (12,442)	15,507 (15,496)	12,948 (12,737)
Reduction from no TMD case	N/A	17.3% (18.5%)	-1.52% (-1.45%)	15.2% (16.6%)
side-to-side DEQL (kN·m), load A	3,871	3,831 (3,752)	1,214 (1,205)	1,182 (1,150)
Reduction from no TMD case	N/A	1.03% (3.07%)	68.6% (68.9%)	69.5% (70.3%)
Fore-aft DEQL (kN·m), load B	28,011	22,272 (22,368)	28,402 (28,396)	22,140 (22,448)
Reduction from no TMD case	N/A	20.5% (20.1%)	-1.40% (-1.37%)	21.0% (19.9%)
side-to-side DEQL (kN·m), load B	7,263	7,090 (6,806)	2,271 (2,249)	2,199 (1,946)
Reduction from no TMD case	N/A	2.38% (6.29%)	68.7% (69.0%)	69.7% (73.2%)

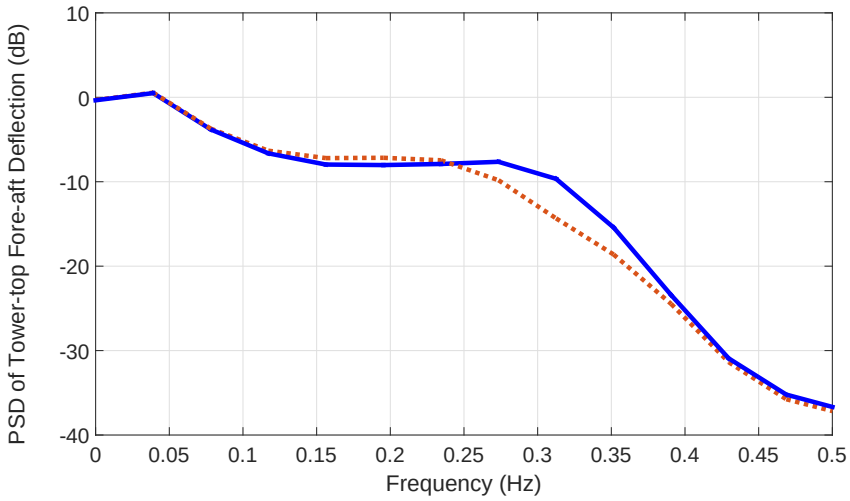

Figure 4.10: Power spectral density (PSD) of the tower-top fore-aft translational deflections of the NREL 5-MW monopile wind turbine tower based on FAST simulations under a wind input with a mean speed of 18 m/s and turbulence intensity of 15%, and a wave input with the significant wave height of 3.5 m. Blue solid and red dotted lines denote cases of sole tower and tower stabilised by optimal fore-aft and side-to-side TMDs designed in Section 4.1.3, respectively.

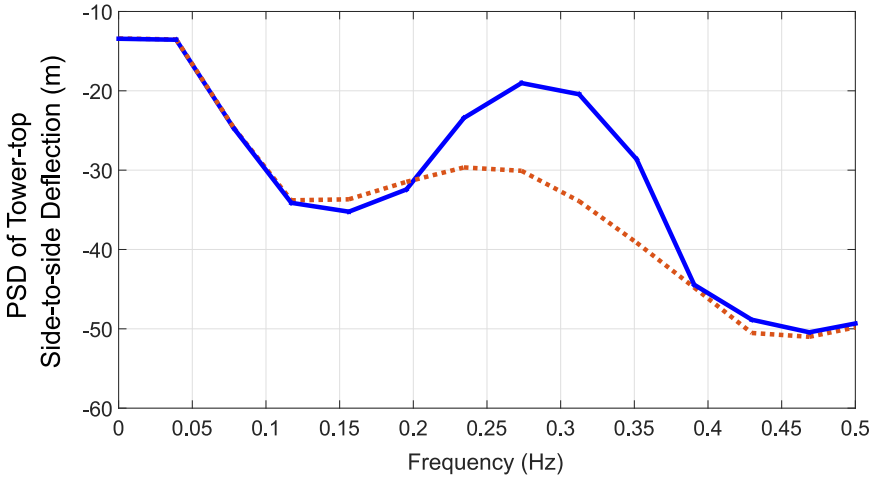

Figure 4.11: Power spectral density (PSD) of the tower-top side-to-side translational deflections of the NREL 5-MW monopile wind turbine tower based on FAST simulations under a wind input with a mean speed of 18 m/s and turbulence intensity of 15%, and a wave input with the significant wave height of 3.5 m. Blue solid and red dotted lines denote cases of sole tower and tower stabilised by optimal fore-aft and side-to-side TMDs designed in Section 4.1.3, respectively.

4.2 Passive Vibration Control of the SCOLE Beam System with Multiple Dominant Modes Using Multiple TMDs

Although the first bending mode dominates monopile tower vibrations, the second bending mode can play a non-negligible part in tower fatigue damage in some cases [51, 52]. Besides, real monopiles are not ideally fixed into the seabed due to soil-pile interactions, which causes variations of modal frequencies over time [53]. This will not only deteriorate effectiveness of the TMD tuned for the original first tower mode (because the first tower modal frequency deviates from its original value used for the TMD design), but possibly cause increased coupling between higher tower modal frequencies and rotor harmonic frequencies. The latter phenomenon was observed by [54] where the second tower bending modal frequency coincided with the 6P (with 1P being the rotor rotational frequency) rotor harmonic frequency (resulting in higher loads and larger fatigue damage to the monopile tower). Therefore, it is worth developing a control scheme to suppress multiple tower vibration modes simultaneously and at the same time improve robustness of the TMD system. In this section, the preceding TMD optimisation scheme is extended to the design of multiple TMDs for the vibration reduction of the non-uniform SCOLE beam system (used in Section 4.1 to model monopile turbine towers) with multiple dominant vibration modes. Note that the SCOLE model rather than the NREL monopile tower is used as the illustrative application here, because the former can be parameterised to have multiple dominant modes while the latter has only one dominant mode.

4.2.1 System Modelling

In this section, multiple groups of TMDs are designed to reduce vibrations of the non-uniform SCOLE model which has multiple dominant vibration modes. The number of TMD groups is equal to the number of dominant vibration modes of the SCOLE model. Each group of TMDs is used to control a dominant mode of the SCOLE model, placed at the antinode of the corresponding mode shape [95, 111, 112, 113]. So the TMD groups are distributed along the beam, as in Figure 4.12. Each TMD group contains the same number of TMDs. The TMDs in each TMD group have equal spring and damping constants but different masses with natural frequencies uniformly distributed around a central frequency which is close to the frequency of the corresponding mode to be controlled [89]. If the mode shape of a dominant mode has several antinodes, the corresponding TMD group is divided

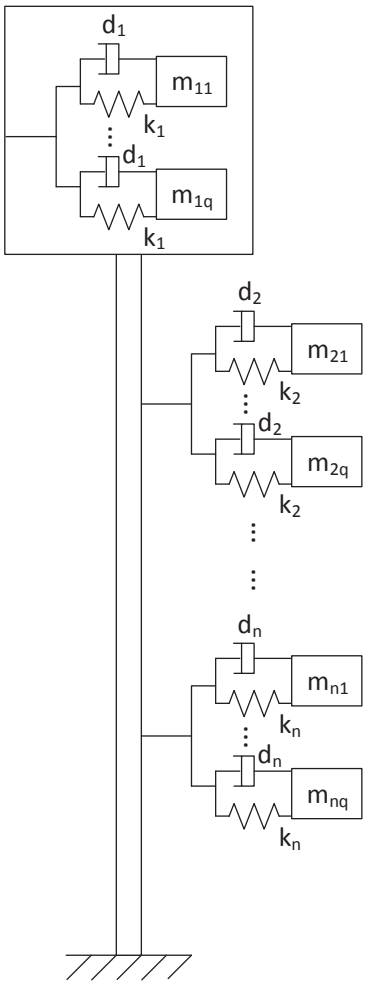

Figure 4.12: An SCOLE beam system stabilised by multiple groups of TMDs.

into sub-groups whose number is the same as the antinode number [114]. Other design procedures for this TMD group remain the same. For the sake of simplicity (but without loss of generality), the mode shape of each dominant mode of the SCOLE beam has a single antinode here.

For a non-uniform SCOLE model with n dominant vibration modes controlled by n groups of TMDs as shown in Figure 4.12 (assuming that the antinode of the mode shape of the first dominant mode is at the beam top), properties of the

ith ($i = 1, 2, \cdots, n$) TMD group tuned to suppress the ith mode are

$$\omega_{ij} = \omega_T^i \left[1 + \left(j - \tfrac{q+1}{2}\right) \tfrac{B_W^i}{q-1}\right], \tag{4.55}$$

$$k_i = m_T^i \left(\textstyle\sum_{j=1}^{q} \frac{1}{\omega_{ij}^2}\right)^{-1}, \tag{4.56}$$

$$d_i = 2\zeta_i k_i (\omega_T^i)^{-1}, \tag{4.57}$$

$$m_{ij} = \tfrac{k_i}{\omega_{ij}^2}, \tag{4.58}$$

where ω_{ij} and m_{ij} are the natural frequency and the mass of the jth ($j = 1, 2, \cdots, q$) TMD in the ith TMD group, respectively. k_i and d_i are the spring and damping constants of all the TMDs in the ith TMD group. q is the number of TMDs in each TMD group, so the total number of TMDs is $N_T = nq$. One can choose a practical value for q according to actual situation. ω_T^i, B_W^i, $m_T^i (= \sum_{j=1}^{q} m_{ij})$, ζ_i are the central frequency, the non-dimensional frequency bandwidth (w.r.t ω_T^i), the total mass, and the average damping ratio of the ith TMD group respectively, which are design variables to be optimised. A special case is that if $q = 1$ then $B_W^i = 0$.

The mathematical model Σ_e of the non-uniform SCOLE model coupled with n TMD groups with each group having q TMDs located at the antinode of the mode shape of a dominant mode as shown in Figure 4.12 is given below:

$$\begin{cases}
\rho(x) w_{tt}(x,t) + (EI(x) w_{xx}(x,t))_{xx} = f_1, & (4.59)\\
(x,t) \in (0,l) \times [0,\infty), & \\
f_1 = \displaystyle\sum_{i=2}^{n} \delta(x - x_T^i) \sum_{j=1}^{q} \{k_i [p^{ij}(t) - w(x_T^i, t)] & \\
\qquad + d_i [p_t^{ij}(t) - w_t(x_T^i, t)]\}, & (4.60)\\
w(0,t) = 0,\ w_x(0,t) = 0, & (4.61)\\
m w_{tt}(l,t) - (EI w_{xx})_x(l,t) = F_e(t) + f_2, & (4.62)\\
f_2 = \displaystyle\sum_{j=1}^{q} \{k_1 [p^{1j}(t) - w(l,t)] & \\
\qquad + d_1 [p_t^{1j}(t) - w_t(l,t)]\}, & (4.63)\\
J w_{xtt}(l,t) + EI(l) w_{xx}(l,t) = T_e(t), & (4.64)\\
m_{ij} p_{tt}^{ij}(t) = -k_i [p^{ij}(t) - w(x_T^i, t)] & \\
\qquad\qquad - d_i [p_t^{ij}(t) - w_t(x_T^i, t)], & (4.65)
\end{cases}$$

where the subscripts t and x denote derivatives with respect to the time t and the position x. The equations (4.59)-(4.64) are the non-uniform SCOLE subsystem while

the equation (4.65) describes the dynamics of each TMD of the TMD subsystem. l, ρ and EI denote the beam's height, the mass density function and the flexural rigidity function while w denotes the translational displacement of the beam. ρ and EI are assumed to be strictly positive functions. The parameters $m > 0$ and $J > 0$ are the mass and the moment of inertia of the rigid body. F_e and T_e denote the external force and torque excitations acting on the rigid body. $p^{ij}(t)$ ($i = 1, 2, \cdots, n$ and $j = 1, 2, \cdots, q$) represents the translational displacement of the mass component of the jth TMD in the ith TMD group. x_T^i denotes the antinode location of the mode shape of the ith dominant mode with $0 < x_T^n \leqslant x_T^{n-1} \leqslant \cdots \leqslant x_T^1 = l$, thus the location of the ith TMD group. δ is the Dirac delta function defined as

$$\delta(x - x_T^i) = \begin{cases} \infty, x = x_T^i \\ 0, x \neq x_T^i \end{cases}, \tag{4.66}$$

$$\int_{-\infty}^{+\infty} \delta(x - x_T^i) f(x) \mathrm{d}x = f(x_T^i) \tag{4.67}$$

for a continuous compactly supported function f. Both subsystems are interconnected through the translational velocity $w_t(x_T^i, t)$ of the SCOLE beam at $x = x_T^i$ and the force generated by the ith TMD group.

In order to simulate the dynamics of the infinite-dimensional SCOLE-TMD model Σ_e (4.59)-(4.65) and to optimise TMDs, finite element method (FEM) is used to spatially discretise Σ_e to a finite-dimensional model Σ_{ed}. The first step is to approximate the solution using a set of high-order basis functions as below

$$w(x, t) = \sum_{k=1}^{N} W_k(t) u_k(x), \tag{4.68}$$

where $u_k(x)$ ($k = 1, 2, \ldots N$) is the basis function, which satisfies the essential boundary conditions (4.61), i.e.,

$$u_k(x = 0) = \frac{\mathrm{d}u_k}{\mathrm{d}x}(x = 0) = 0. \tag{4.69}$$

The coefficients of (4.68) are denoted by

$$\mathbf{W} = \begin{bmatrix} W_1 & W_2 & \cdots & W_N \end{bmatrix}^T \tag{4.70}$$

where the superscript T denotes the nonconjugate transpose. A convenient choice for $u_k(x)$ is the Hermite interpolating polynomials [115], which have been successfully

applied to the discretisation of the Euler-Bernoulli beam and the Timoshenko beam [116]. Assuming there are $(P+1)$ collocation points along the beam $0 = x_0 < x_1 < \cdots < x_P = l$, one can derive $N = 2P$ piecewise cubic Hermite polynomials u_k satisfying

$$u_{2r-1}(x_c) = \begin{cases} 1, r = c \\ 0, r \neq c \end{cases}, (u_{2r-1})_x(x_c) = 0, \tag{4.71}$$

$$(u_{2r})_x(x_c) = \begin{cases} 1, r = c \\ 0, r \neq c \end{cases}, u_{2r}(x_c) = 0, \tag{4.72}$$

where $r = 1, 2, \cdots, P$ and $c = 0, 1, \cdots, P$. The MATLAB function *pwch* is employed to produce polynomials u_k which are continuous and have compact supports satisfying the property of the function f in (2.13). It is obvious that in (4.70),

$$W_{2r-1} = w(x_r, t), W_{2r} = w_x(x_r, t). \tag{4.73}$$

Now the weak form of the governing equation is determined. Multiply both sides of the equation (4.59) with $u_k(x)$ $(k = 1, 2, \cdots, N)$, integrate the resulting equation over the domain $x \in (0, l)$, employ the definition (4.67), and then derive N equations each of which has the form

$$\begin{aligned} &\int_0^l \{\rho w_{tt} u_k + (EIw_{xx})_{xx} u_k\} \mathrm{d}x \\ &= \sum_{i=2}^{n} u_k(x_T^i) \sum_{j=1}^{q} \{k_i[p^{ij}(t) - w(x_T^i, t)] \\ &+ d_i[p_t^{ij}(t) - w_t(x_T^i, t)]\}. \end{aligned} \tag{4.74}$$

Using integration by parts, one has

$$\begin{aligned} &\int_0^l \{\rho w_{tt} u_k + EIw_{xx}(u_k)_{xx}\} \mathrm{d}x + \big[(EIw_{xx})_x u_k \\ &- EIw_{xx}(u_k)_x\big]_{x=0}^{x=l} = \sum_{i=2}^{n} u_k(x_T^i) \sum_{j=1}^{q} \{k_i[p^{ij}(t) \\ &- w(x_T^i, t)] + d_i[p_t^{ij}(t) - w_t(x_T^i, t)]\}. \end{aligned} \tag{4.75}$$

Substituting equations (4.62)-(4.64) and (4.69) into (4.75), one gets the weak form

$$\int_0^l \{\rho w_{tt} u_k + EI w_{xx} (u_k)_{xx}\} \mathrm{d}x = \left[\left(-m w_{tt} + F_e\right) u_k \right.$$
$$\left. + \left(T_e - J w_{xtt}\right) (u_k)_x \right] \Big|_{x=l} + \sum_{i=1}^{n} u_k(x_T^i) \sum_{j=1}^{q} \{k_i [p^{ij}(t)$$
$$- w(x_T^i, t)] + d_i [p_t^{ij}(t) - w_t(x_T^i, t)]\}. \tag{4.76}$$

Now introduce

$$\mathbf{h} = \begin{bmatrix} h^{11} & h^{12} & \cdots & h^{1q} & \cdots & h^{n1} & h^{n2} & \cdots & h^{nq} \end{bmatrix}^T, \tag{4.77}$$

$$\mathbf{p} = \begin{bmatrix} p^{11} & p^{12} & \cdots & p^{1q} & \cdots & p^{n1} & p^{n2} & \cdots & p^{nq} \end{bmatrix}^T, \tag{4.78}$$

in which

$$h^{ij}(t) = p^{ij}(t) - w(x_T^i, t). \tag{4.79}$$

Substituting (4.68), (4.77), and (4.78) to (4.76), N equations of motion are derived as

$$\mathbf{M}_p \ddot{\mathbf{W}} + \mathbf{C}_p \dot{\mathbf{W}} + \mathbf{K}_p \mathbf{W} + \mathbf{K}_d \mathbf{h} + \mathbf{C}_d \dot{\mathbf{p}} = \mathbf{E}_F F_e + \mathbf{E}_T T_e \tag{4.80}$$

where

$$\mathbf{M}_p = \int_0^l \rho \mathbf{u}_m \mathbf{u}_m^T \mathrm{d}x + \left[m \mathbf{u}_m \mathbf{u}_m^T + J (\mathbf{u}_m)_x (\mathbf{u}_m)_x^T \right]_{x=l} \tag{4.81}$$

$$\mathbf{C}_p = q \sum_{i=1}^{n} d_i \mathbf{u}_m(x_T^i) \mathbf{u}_m(x_T^i)^T \tag{4.82}$$

$$\mathbf{K}_p = \int_0^l EI (\mathbf{u}_m)_{xx} (\mathbf{u}_m)_{xx}^T \mathrm{dx} \tag{4.83}$$

$$\mathbf{K}_d(:, b) = -k_i \mathbf{u}_m(x_T^i) \tag{4.84}$$

$$\mathbf{C}_d(:, b) = -d_i \mathbf{u}_m(x_T^i) \tag{4.85}$$

$$\mathbf{E}_F = \mathbf{u}_m(l) \tag{4.86}$$

$$\mathbf{E}_T = (\mathbf{u}_m)_x(l). \tag{4.87}$$

$\mathbf{u}_m = \begin{bmatrix} u_1 & u_2 & \cdots & u_N \end{bmatrix}^T$, $b = 1, 2, \ldots N_T$ (recall that N_T is the total number of TMDs) and $i = \lceil (b/q) \rceil$ where $\lceil x \rceil$ denotes the smallest integer not less than x.

Besides, the following equations of motion for the TMDs can be easily derived:

$$\dot{\mathbf{h}} = \mathbf{h}_W\dot{\mathbf{W}} + \dot{\mathbf{p}}, \tag{4.88}$$

$$\ddot{\mathbf{p}} = \mathbf{p}_W\dot{\mathbf{W}} + \mathbf{K}_T\mathbf{h} + \mathbf{C}_T\dot{\mathbf{p}}, \tag{4.89}$$

where

$$\mathbf{h}_W(b,:) = -\mathbf{u}_m(x_T^i)^T, \tag{4.90}$$

$$\mathbf{p}_W(b,:) = \frac{d_i}{m_{ij}}\mathbf{u}_m(x_T^i)^T, \tag{4.91}$$

$$\mathbf{K}_T(b,b) = -\frac{k_i}{m_{ij}}, \tag{4.92}$$

$$\mathbf{C}_T(b,b) = -\frac{d_i}{m_{ij}}. \tag{4.93}$$

Here $i = \lceil (b/q) \rceil$ and $j = b - (i-1)q$. $\mathbf{K}_T$ and $\mathbf{C}_T$ are diagonal matrices.

Now the state space formulation of the spatially discretised SCOLE-TMD model Σ_{ed} is get from (4.80), (4.88) and (4.89):

$$\begin{cases} \dot{\mathbf{X}} = \mathbf{A}\mathbf{X} + \mathbf{B}\mathbf{u} & (4.94) \\ \mathbf{Y} = \mathbf{C}\mathbf{X}, & (4.95) \end{cases}$$

where the state $\mathbf{X} = \begin{bmatrix} \mathbf{W} & \dot{\mathbf{W}} & \mathbf{h} & \dot{\mathbf{p}} \end{bmatrix}^T$ and the input $\mathbf{u} = [F_e, T_e]^T$. The system matrix $\mathbf{A}$ and the input matrix $\mathbf{B}$ are

$$\mathbf{A} = \begin{bmatrix} \mathbf{0} & \mathbf{I} & \mathbf{0} & \mathbf{0} \\ -\mathbf{M}_p^{-1}\mathbf{K}_p & -\mathbf{M}_p^{-1}\mathbf{C}_p & -\mathbf{M}_p^{-1}\mathbf{K}_d & -\mathbf{M}_p^{-1}\mathbf{C}_d \\ \mathbf{0} & \mathbf{h}_W & \mathbf{0} & \mathbf{I} \\ \mathbf{0} & \mathbf{p}_W & \mathbf{K}_T & \mathbf{C}_T \end{bmatrix},$$

$$\mathbf{B} = \begin{bmatrix} \mathbf{0} & \mathbf{0} \\ \mathbf{M}_p^{-1}\mathbf{E}_F & \mathbf{M}_p^{-1}\mathbf{E}_T \\ \mathbf{0} & \mathbf{0} \\ \mathbf{0} & \mathbf{0} \end{bmatrix}, \tag{4.96}$$

where $\mathbf{I}$ is the identity matrix. Note that $\mathbf{A} \in \mathbb{R}^{n_d \times n_d}$, $\mathbf{B} \in \mathbb{R}^{n_d \times 2}$ and $n_d = 2N + 2N_T$. If $\mathbf{Y} = \begin{bmatrix} w(x_1,t) & w(x_2,t) & \cdots & w(x_P,t) \end{bmatrix}^T$ (beam displacements at the collocation points), the output matrix is $\mathbf{C} = [\mathbf{T}\ \mathbf{0}\ \mathbf{0}\ \mathbf{0}]$ where $\mathbf{T}(r, 2r-1) = 1$ and $\mathbf{T} \in \mathbb{R}^{P \times N}$. If $\mathbf{Y} = \begin{bmatrix} w(x_T^1,t)\ w(x_T^2,t)\ \cdots w(x_T^n,t) \end{bmatrix}^T$ (beam displacements at the

locations of TMD groups), the output matrix is

$$\mathbf{C} = \begin{bmatrix} \mathbf{C}_W & \mathbf{0} & \mathbf{0} & \mathbf{0} \end{bmatrix}, \tag{4.97}$$

$$\mathbf{C}_W(i,:) = \mathbf{u}_m(x_T^i)^T, \mathbf{C}_W \in \mathbb{R}^{n \times N}. \tag{4.98}$$

The transfer function matrix of Σ_{ed} is

$$\mathbf{H}(s) = \mathbf{C}\left(s\mathbf{I} - \mathbf{A}\right)^{-1}\mathbf{B}. \tag{4.99}$$

Based on Σ_{ed}, not only can the design of optimal multiple TMDs be conducted using $\mathcal{H}_\infty$ and $\mathcal{H}_2$ optimisations, but also can the dynamics of the SCOLE beam system be simulated (for example using the MATLAB built-in function *lsim*).

4.2.2 Optimisation of TMDs for Vibration Suppression of the Non-Uniform SCOLE model

In this section, $\mathcal{H}_\infty$ and $\mathcal{H}_2$ optimisations are employed to derive the parameters of multiple TMDs in the spatially discretised SCOLE-TMD model Σ_{ed} (4.94)–(4.95) to achieve optimal vibration reduction. As explained in Section 4.1.3, frequency-limited versions of $\mathcal{H}_\infty$- and $\mathcal{H}_2$-norms are utilised in the optimisation of TMD parameters, i.e., computing the $\mathcal{H}_\infty$- and $\mathcal{H}_2$-norms over bounded frequency intervals around dominant modal frequencies of the SCOLE model. Note that the modal frequencies of the SCOLE model are absolute values of the imaginary parts of the eigenvalues of $\mathbf{A}$ in Σ_{ed} (4.94)–(4.95) excluding TMDs. Mode shapes can be derived by pre-multiplying eigenvectors of $\mathbf{A}$ by $\mathbf{T}_v = \begin{bmatrix} \mathbf{T} & \mathbf{0} \end{bmatrix} \in \mathbb{R}^{P \times 2N}$.

The external force and torque $\begin{bmatrix} F_e & T_e \end{bmatrix}^T$ are considered as the excitations (inputs). The beam displacements at the locations of TMD groups $[w(x_T^1, t)\ w(x_T^2, t)\ \cdots\ w(x_T^n, t)]^T$ (i.e., antinode positions of the mode shapes of the dominant modes) are regarded as the outputs. $\|\mathbf{H}\|_{\infty,[\omega_l^i,\omega_r^i]}$ and $\|\mathbf{H}\|_{2,[\omega_l^i,\omega_r^i]}$ are used to denote the frequency-limited $\mathcal{H}_\infty$- and $\mathcal{H}_2$-norms of the transfer function matrix $\mathbf{H}$ (4.99) of Σ_{ed} (4.94)–(4.95) over the frequency range $[\omega_l^i, \omega_r^i]$ (in rad/s, $\omega_l^i, \omega_r^i \in \mathbb{R}^+$, $\omega_l^i < \omega_r^i$) around the ith dominant modal frequency ω_i, respectively. $\|\mathbf{H}\|_{2,[\omega_l^i,\omega_r^i]}$ is derived based on (4.51)–(4.54). $\|\mathbf{H}\|_{\infty,[\omega_l^i,\omega_r^i]}$ is calculated using

$$\|\mathbf{H}\|_{\mathcal{H}_{\infty,[\omega_{il},\omega_{ir}]}} = \sup_{\omega \in [\omega_{il},\omega_{ir}]} \bar{\sigma}\left(\mathbf{H}(\mathrm{j}\omega)\right) \tag{4.100}$$

where $\bar{\sigma}(\cdot)$ denotes the maximum singular value of the matrix.

Now the proposed optimisation scheme is described, starting with the simple

case of n TMD groups with each group having a single TMD (i.e., $q = 1$). They are tuned to suppress the n dominant modes of the SCOLE model. If the control purpose is only to improve effectiveness of TMDs without considering robustness against mistuning effects, the objective functions to minimise the response of the SCOLE-TMD system Σ_{ed} under harmonic and random excitations are

$$f_{hc}(\mathbf{x}) = \max(\|\mathbf{H}\|_{\infty,[\omega_l^1,\omega_r^1]}, \|\mathbf{H}\|_{\infty,[\omega_l^2,\omega_r^2]}, \cdots, \|\mathbf{H}\|_{\infty,[\omega_l^n,\omega_r^n]}), \tag{4.101}$$

$$f_{rc}(\mathbf{x}) = \sqrt{\sum_{i=1}^{n} \|\mathbf{H}\|^2_{2,[\omega_l^i,\omega_r^i]}}, \tag{4.102}$$

respectively. Here $\mathbf{x}$ is the vector of design variables with

$$\mathbf{x} = \left[\mathbf{m}_T \ \boldsymbol{\omega}_T \ \boldsymbol{\zeta}\right]^T, \tag{4.103}$$

among which

$$\begin{aligned} \mathbf{m}_T &= \left[m_T^1 \ m_T^2 \ \cdots \ m_T^n\right], \\ \boldsymbol{\omega}_T &= \left[\omega_T^1 \ \omega_T^2 \ \cdots \ \omega_T^n\right], \\ \boldsymbol{\zeta} &= \left[\zeta_1 \ \zeta_2 \ \cdots \ \zeta_n\right], \end{aligned} \tag{4.104}$$

whose elements have been explained after equation (4.58).

Considering only the robustness of TMDs against mistuning effects under harmonic excitations, the objective function is defined as

$$f_h(\mathbf{x}) = f_{hc}(\mathbf{x}_s) + f_{hc}(\mathbf{x}) + f_{hc}(\mathbf{x}_b), \tag{4.105}$$

where

$$\mathbf{x}_s = \begin{bmatrix} \mathbf{I} & \mathbf{0} & \mathbf{0} \\ \mathbf{0} & 0.9\mathbf{I} & \mathbf{0} \\ \mathbf{0} & \mathbf{0} & \mathbf{I} \end{bmatrix} \mathbf{x}, \tag{4.106}$$

$$\mathbf{x}_b = \begin{bmatrix} \mathbf{I} & \mathbf{0} & \mathbf{0} \\ \mathbf{0} & 1.1\mathbf{I} & \mathbf{0} \\ \mathbf{0} & \mathbf{0} & \mathbf{I} \end{bmatrix} \mathbf{x}, \tag{4.107}$$

and $\mathbf{I}$ is the identity matrix of size n. This means that (4.105) takes into account $\pm 10\%$ deviations of the central frequencies of all TMD groups to include mistuning effects for robust control design. Similarly, for random excitations, the robustness

objective function is

$$f_r(\mathbf{x}) = f_{rc}(\mathbf{x}_s) + f_{rc}(\mathbf{x}) + f_{rc}(\mathbf{x}_b). \tag{4.108}$$

In view of the trade-off between effectiveness and robustness, the following constraints are enforced for (4.105) and (4.108) respectively:

$$f_{hc}(\mathbf{x}) \leq \theta_h, \tag{4.109}$$

$$f_{rc}(\mathbf{x}) \leq \theta_r. \tag{4.110}$$

In (4.109), the value of θ_h can be selected between $f_{hc}(\mathbf{x}_e^*)$ and $f_{hc}(\mathbf{x}_r^*)$ where $\mathbf{x}_e^*$ and $\mathbf{x}_r^*$ are the minimisers of objective functions (4.101) (which only considers effectiveness) and (4.105) (which only considers robustness), respectively. Through increasing the value of θ_h, the effectiveness of the TMD system decreases while its robustness against mistuning effects grows, and vice versa. The value of θ_r in (4.110) is set using the same idea. For optimisation of the TMD system with each TMD group having multiple TMDs ($q > 1$) to control a dominant mode, a design variable $\mathbf{B}_W = \begin{bmatrix} B_W^1 & B_W^2 & \cdots & B_W^n \end{bmatrix}$ is added to those in the vector (4.103), which contains the non-dimensional frequency bandwidths of the n TMD groups as shown in (4.55). The optimisation mechanism is the same as the case of $q = 1$, thus omitted.

The MATLAB sequential quadratic programming (SQP) algorithm *fmincon* is used as a tool to derive the optimal parameters of the TMD system. In practice, the ratio between the total mass of the TMD system and the mass of the main structure is usually chosen between 1% and 2% [92, 93]. During the optimisation procedure, it is set as a constant. Besides, to ensure stability of the finite-dimensional SCOLE-TMD model Σ_{ed} (4.94)–(4.95), the real parts of all the eigenvalues of the system matrix $\mathbf{A}$ are constrained to be negative.

4.2.3 Simulation Study

In this section, the optimisation scheme proposed in Section 4.2.2 is tested against the traditional methods for the TMD design through simulation studies on the SCOLE-TMD model under harmonic and random excitations. The model has following properties: $l = 1$ m, $\rho(x) = EI(x) = -0.1x + 0.2$, $m = 0.05$ kg and $J = 0.1$ kg·m^2. The total mass of the SCOLE beam system is therefore 0.2 kg. The collocation points are uniformly distributed along the beam: $x_r = rh$, $r = 1, 2, \cdots, P$, where $h = l/P$. Without loss of generality, the torque excitation T_e is assumed to be very small and negligible, and the force F_e is regarded as the only excitation source.

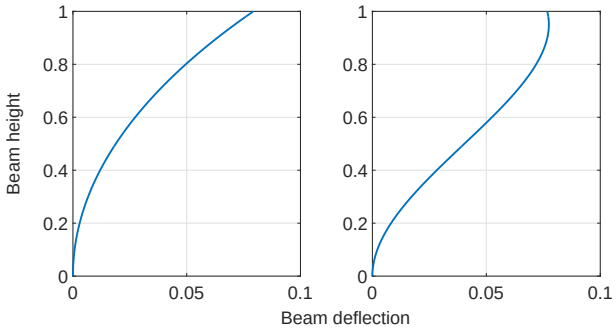

Figure 4.13: Mode shapes of the first two modes of the SCOLE model. The left-hand diagram shows the mode shape of the first mode while the right-hand one is the mode shape of the second mode.

The modal mass M_i for the ith mode of the SCOLE model is

$$M_i = \frac{\left[\int_0^l \rho(x) Y_i(x) \mathrm{d}x + m Y_i(l)\right]^2}{\int_0^l \rho(x) Y_i^2(x) \mathrm{d}x + m Y_i^2(l)}, \tag{4.111}$$

where $Y_i(x)$ denotes the mode shape of the ith mode. According to the description at the beginning of Section 4.2.2, the first two modal frequencies are derived as

$$\omega_1 = 1.1203\,\mathrm{rad/s} \quad \text{and} \quad \omega_2 = 4.6184\,\mathrm{rad/s} \tag{4.112}$$

with their corresponding mode shapes in Figure 4.13. The antinode of the first mode shape is located at $x = 1$ m (the beam top) while the antinode of the second mode shape is at $x = 0.95$ m. The modal masses for the first two modes are

$$M_1 = 0.08095\,\mathrm{kg} \quad \text{and} \quad M_2 = 0.09988\,\mathrm{kg}, \tag{4.113}$$

respectively. In total they make up 90.41% of the mass of the SCOLE beam, which implies that the first two modes play dominant roles in the dynamic response of the SCOLE beam. Hence, only these two modes are taken into account for vibration control, for which two TMD groups are placed at locations $x_T^1 = 1$ m and $x_T^2 = 0.95$ m. The frequency interval $\left[\omega_l^i, \omega_r^i\right]$ $(i = 1, 2)$ around each modal frequency ω_i for frequency-limited $\mathcal{H}_\infty$ and $\mathcal{H}_2$ optimisations is chosen to be $[0.7\omega_i, 1.3\omega_i]$. Note that only the simulation results at $x = 1$ m are shown while the conclusion on results at $x = 0.95$ m are similar, thus omitted.

The number of collocation points is selected to be $P = 10$ in the optimisation of TMD parameters and dynamic simulation of the SCOLE-TMD model. Ideally,

the value of P should be independent of $\mathcal{H}_\infty$- and $\mathcal{H}_2$-norms, which implies that as P increases, the $\mathcal{H}_\infty$- and $\mathcal{H}_2$-norms of the SCOLE-TMD system should converge within a small range. $P = 10$ satisfies this rule with a relative error of the order of 10^{-4} for both norms when P is chosen from $7, 8, \cdots, 13$.

Simulation Studies under Harmonic Excitations

In this section, various TMD systems are designed for the case of the SCOLE beam subject to harmonic excitations using Den Hartog's formulae [83] and the scheme proposed in Section 4.2.2 respectively, and their performances are compared. For the TMD system with $q = 1$ (each TMD group has a single TMD), first the optimal parameters of TMDs by Den Hartog's formulae are determined:

$$\frac{(\omega_T^i)^2}{\omega_i^2} = \frac{1}{(1+\mu_i)^2}, \tag{4.114}$$

$$\zeta_i = \sqrt{\frac{3\mu_i}{8(1+\mu_i)}}, \tag{4.115}$$

where $i = 1, 2$. ω_T^i and ζ_i are the optimal central frequency and the optimal average damping ratio of the ith TMD group, respectively. ω_i is the ith modal frequency of the SCOLE beam. $\mu_i = \frac{m_T^i}{M_i}$ is the mass ratio of the ith TMD group where m_T^i and M_i are the total mass of the ith TMD group and the modal mass of the ith mode as in (4.111), respectively. μ_i should be specified according to the realistic situation. All the other parameters of the TMD system can be obtained through equations (4.55)–(4.58). μ_1 and μ_2 are set to be 0.02, which means that the total mass of each TMD group is 2% of the corresponding modal mass. Together with the values of ω_i and M_i from (4.112) and (4.113), the TMD system T_D is obtained using the above Den Hartog's formulae, whose parameters are listed in Table 4.3. The total mass of the TMD system is 0.003617 kg. The same total mass for TMDs is used in the frequency-limited $\mathcal{H}_\infty$ optimisations under harmonic excitations, which derive all the other TMD systems in Table 4.3. Table 4.3 also lists the values of objective functions f_{hc} (4.101) and f_h (4.105) for these optimal TMD systems, and the values of the constraint θ_h in (4.109) for the trade-off between effectiveness and robustness of some TMD systems.

In Table 4.3, T_{hs}^1–T_{hs}^4 have a single TMD in each of the two TMD groups (i.e, $q = 1$). First T_{hs}^1 and T_{hs}^4 are designed by only considering effectiveness with the objective function (4.101) and by only considering robustness against mistuning effects with the objective function (4.105), respectively. Then T_{hs}^2 and T_{hs}^3 are

Table 4.3: The optimal parameters of 9 TMD systems and the values of corresponding objective functions f_{hc} (4.101) and f_h (4.105) at these optimal parameters (all denoted by superscript $*$) for the SCOLE-TMD system under harmonic excitations. q is the number of TMDs in each TMD group. θ_h in constraint (4.109) is set for the trade-off between effectiveness and robustness. In the notation of TMD systems, the subscript D/h means that the TMD system is designed by Den Hartog's formulae/$\mathcal{H}_\infty$ optimisation to suppress harmonic excitations; the subscript s/m means that each TMD group has a single/multiple TMDs; the superscript 1-4 is the TMD system's index (with its increase, a TMD system's effectiveness decreases and robustness increases).

TMD system	q	m_T^{1*} (kg)	m_T^{2*} (kg)	ω_T^{1*} (rad/s)	ω_T^{2*} (rad/s)	ζ_1^*	ζ_2^*	B_W^{1*}	B_W^{2*}	θ_h	f_{hc}^*	f_h^*
T_D	1	0.001619	0.001998	1.098	4.528	0.08575	0.08575	-	-	-	108.6	608.5
T_{hs}^1	1	0.003415	2.02e-4	1.112	4.528	0.04880	0.04268	-	-	-	35.67	419.3
T_{hs}^2	1	0.003466	1.51e-4	1.112	4.637	0.06453	0.04887	-	-	40	40.00	355.9
T_{hs}^3	1	0.003467	1.50e-4	1.108	4.625	0.08074	0.06531	-	-	50	50.00	332.7
T_{hs}^4	1	0.003483	1.34e-4	1.103	4.628	0.09748	0.07287	-	-	-	60.26	326.4
T_{hm}^1	11	0.003420	1.97e-4	1.115	4.773	0.01275	0.009135	0.1113	0.09364	-	28.32	1,301
T_{hm}^2	11	0.003460	1.57e-4	1.112	4.640	0.06412	0.03936	0.01324	0.07917	40	40.00	357.1
T_{hm}^3	11	0.003380	2.37e-4	1.123	4.460	0.02826	0.08340	0.1882	0.004000	50	50.00	309.4
T_{hm}^4	11	0.003341	2.76e-4	1.141	4.725	0.01608	0.07034	0.2538	0.2424	-	61.77	202.4

designed by taking into account the trade-off between effectiveness and robustness with the objective function (4.105) and the constraint (4.109) through changing the value of θ_h in (4.109) in a range between the lower bound 35.67 (the value of the effectiveness objective function (4.101) f_{hc}^* for T_{hs}^1) and the upper bound 60.26 (the value of (4.101) f_{hc}^* for T_{hs}^4). T_{hm}^1–T_{hm}^4 have 11 TMDs in each of the two TMD groups (i.e., $q = 11$). They are designed similarly as the case that each TMD group has a single TMD. Please refer the caption of Table 4.3 for further information contained in the notation of each TMD system.

Figure 4.14 shows the displacement root-mean-square (RMS) of the SCOLE model at $x = 1$ m, stabilised by T_D, T_{hs}^1 and T_{hm}^1 of Table 4.3 respectively, under harmonic excitations

$$F_e = 0.0001 \sin(\omega_e t), \tag{4.116}$$

where the excitation frequency ω_e ranges from $0.8\omega_1$ to $1.2\omega_1$ and from $0.8\omega_2$ to $1.2\omega_2$. In Figure 4.14, T_{hs}^1 reduces the peak displacement RMS by 61.34% from the case with T_D designed using Den Hartog's formulae, which demonstrates that

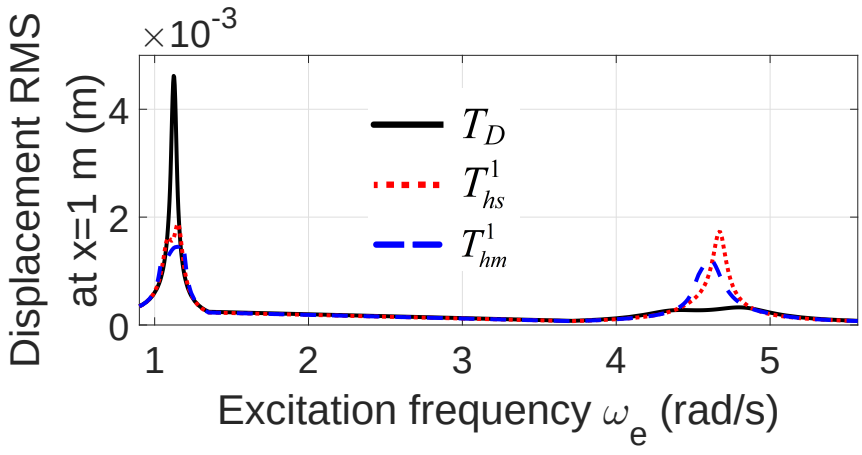

Figure 4.14: Beam-top displacement RMS values of the SCOLE model stabilised by T_D, T^1_{hs} and T^1_{hm} in Table 4.3 versus the excitation frequency ω_e.

the proposed optimisation scheme achieves a better performance than Den Hartog's formulae. Recall that, in both cases, a single TMD is tuned for each dominant mode. Besides, T^1_{hm} reduces the peak displacement RMS by 17.93% from the case with T^1_{hs}, which shows that the TMD system with each TMD group having multiple TMDs to suppress a dominant mode is more effective than the TMD system with each TMD group having a single TMD. The improved effectiveness achieved by T^1_{hs} over T_D and by T^1_{hm} over T^1_{hs} agree with Table 4.3, where the value of the effectiveness objective function f^*_{hc} (the smaller, the more effective) drops by 67.15% from T_D to T^1_{hs} and by 20.51% from T^1_{hs} to T^1_{hm}.

The trade-off between effectiveness and robustness is evaluated through mistuning by multiplying the flexural rigidity function EI by a coefficient α which is varied between 0.81 and 1.21 so the modal frequencies of the SCOLE beam vary by $\pm 10\%$. Figure 4.15 shows the peak displacement RMS of the SCOLE model (for a range of α) stabilised by the TMD systems in Table 4.3. For each α, the peak displacement RMS is the maximal displacement RMS over the excitation frequencies $\left\{\omega_e : \bigcup_{i=1}^{2} \omega_e/\omega_i \in [0.8,\, 1.2]\right\}$. Thus, Figure 4.15 can be used to assess the robustness of each TMD system against mistuning effects.

Table 4.4 lists the maximum of the peak displacement RMS values over α, along with the peak displacement RMS at $\alpha = 1$, for each of the TMD systems in Table 4.3, as well as their percent changes from the case with T_D. The peak displacement RMS for the original model (at $\alpha = 1$) in Figure 4.15 and Table 4.4 is used to evaluate the effectiveness of each TMD system, where it is clear that effectiveness from T^1_{hs} to T^4_{hs} and from T^1_{hm} to T^4_{hm} decrease. Such trends are expected

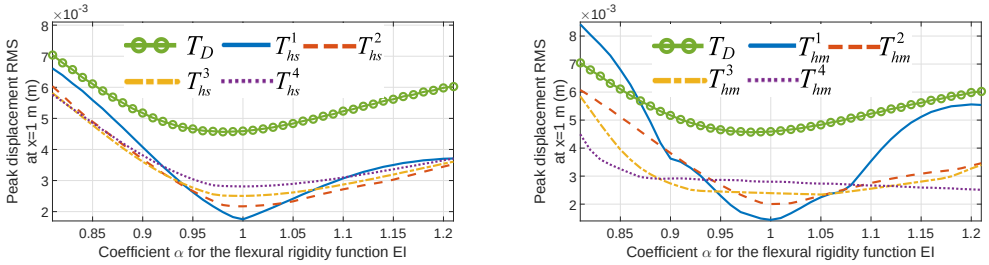

(a) (b)

Figure 4.15: Peak beam-top displacement RMS values of the SCOLE model stabilised by the TMD systems in Table 4.3 versus the coefficient α for the flexural rigidity function EI under harmonic excitations.

Table 4.4: Maximum of the peak beam-top displacement RMS values over α (the coefficient for the flexural rigidity function EI), along with the peak beam-top displacement RMS at $\alpha = 1$, for each of the TMD systems in Table 4.3, as well as their percent changes from the case with T_D. In the notation of TMD systems, the subscript D/h means that the TMD system is designed by Den Hartog's formulae/$\mathcal{H}_\infty$ optimisation to suppress harmonic excitations; the subscript s/m means that each TMD group has a single/multiple TMDs; the superscript 1-4 is the TMD system's index (with its increase, a TMD system's effectiveness decreases and robustness increases).

TMD system	Maximum of the peak displacement RMS values over α ($\times 10^{-3}$ m)	Percent change	Peak displacement RMS at $\alpha = 1$ ($\times 10^{-3}$ m)	Percent change
T_D	7.041	-	4.622	-
T_{hs}^1	6.609	-6.137%	1.871	-59.52%
T_{hs}^2	6.034	-14.30%	2.182	-52.79%
T_{hs}^3	5.815	-17.41%	2.513	-45.63%
T_{hs}^4	5.762	-18.16%	2.815	-39.10%
T_{hm}^1	8.419	19.57%	1.504	-67.46%
T_{hm}^2	6.074	-13.74%	2.012	-56.47%
T_{hm}^3	5.851	-16.90%	2.382	-48.46%
T_{hm}^4	4.494	-36.18%	2.799	-39.45%

from the value of the effectiveness objective function f_{hc}^* (the smaller, the more effective) in Table 4.3. Meanwhile, these TMD systems become increasingly robust with the decreasing of effectiveness as shown in Figure 4.15 where the sensitivity of

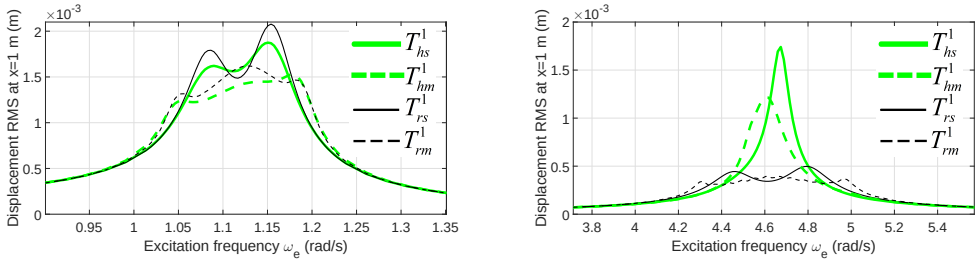

(a) (b)

Figure 4.16: Beam-top displacement RMS values of the SCOLE model stabilised by T_{hs1} & T_{hm1} in Table 4.3 and T_{rs1} & T_{rm1} in Table 4.5 versus the excitation frequency ω_e.

the TMD systems to variations of α reduces, and also as shown in Table 4.4 where the maximum of the peak displacement RMS values over α dwindles from T^1_{hs} to T^4_{hs} and from T^1_{hm} to T^4_{hm}. This is expected from the value of the robustness objective function f^*_h (the smaller, the more robust) in Table 4.3.

From Table 4.3, as the constraint θ_h in (4.109) increases, the value of the effectiveness objective function f^*_{hc} increases while the value of the robustness objective function f^*_h decreases. This shows that the trade-off between effectiveness and robustness is achieved by adjusting the value of θ_h in (4.109) when optimising TMD parameters. Moreover, with a same value of θ_h, TMD systems with $q = 11$ are generally more effective and more robust than those with $q = 1$. T^1_{hm} is the most effective among all the TMD systems for the original model ($\alpha = 1$), but is the least robust against variations of modal frequencies induced by the varying α. Clearly from Figure 4.15, except T^1_{hm}, all the other TMD systems optimised by the proposed scheme are more effective than T_D derived by Den Hartog's formulae over the whole range of α.

Now the performances of T_{hs1} and T_{hm1} in Table 4.3 (designed by $\mathcal{H}_\infty$ optimisation) are compared against T_{rs1} and T_{rm1} in Table 4.5 (designed by $\mathcal{H}_2$ optimisation), as shown in Figure 4.16. These 4 TMD systems are designed by only considering effectiveness. As expected, the peak displacement RMS values of the SCOLE model stabilised by TMD systems based on $\mathcal{H}_\infty$ optimisation are lower than their counterparts designed by $\mathcal{H}_2$ optimisation. In addition, the performances of T_{hs4} and T_{hm4} in Table 4.3 (designed by $\mathcal{H}_\infty$ optimisation) are compared against T_{rs4} and T_{rm4} in Table 4.5 (designed by $\mathcal{H}_2$ optimisation). All these four TMD systems are designed by only considering robustness. As shown in Figure 4.17, over the range of α, TMD systems designed based on $\mathcal{H}_\infty$ optimisation are generally more effective than their counterparts designed by $\mathcal{H}_2$ optimisation. These results

Table 4.5: The optimal parameters of 9 TMD systems and the values of corresponding objective functions f_{rc} (4.102) and f_r (4.108) at these optimal parameters (all denoted by superscript $*$) for the SCOLE-TMD system under random excitations. q is the number of TMDs in each TMD group. θ_r in constraint (4.110) is set for the trade-off between effectiveness and robustness. In the notation of TMD systems, the subscript W/r means that the TMD system is designed by Warburton's formulae/$\mathcal{H}_2$ optimisation to suppress random excitations; the subscript s/m means that each TMD group has a single/multiple TMDs; the superscript 1-4 is the TMD system's index (with its increase, a TMD system's effectiveness decreases and robustness increases).

TMD system	q	m_T^{1*} (kg)	m_T^{2*} (kg)	ω_T^{1*} (rad/s)	ω_T^{2*} (rad/s)	ζ_1^*	ζ_2^*	B_W^{1*}	B_W^{2*}	θ_r	f_{rc}^*	f_r^*
T_W	1	0.001619	0.001998	1.104	4.550	0.07019	0.07019	-	-	-	11.25	46.84
T_{rs}^1	1	0.002783	8.34e-4	1.114	4.600	0.03637	0.04422	-	-	-	8.844	46.34
T_{rs}^2	1	0.002820	7.97e-4	1.112	4.596	0.05480	0.06379	-	-	9.2	9.200	41.74
T_{rs}^3	1	0.002815	8.02e-4	1.111	4.592	0.07078	0.08590	-	-	9.8	9.800	40.26
T_{rs}^4	1	0.002794	8.23e-4	1.111	4.593	0.08514	0.1140	-	-	-	10.44	39.93
T_{rm}^1	11	0.002804	8.13e-4	1.119	4.636	0.006741	0.008196	0.1123	0.1302	-	8.262	77.36
T_{rm}^2	11	0.002849	7.68e-4	1.121	4.613	0.03319	0.04817	0.1409	0.08988	9.2	9.200	41.27
T_{rm}^3	11	0.002846	7.71e-4	1.131	4.672	0.01190	0.01414	0.2197	0.2220	9.8	9.800	35.11
T_{rm}^4	11	0.002846	7.71e-4	1.135	4.693	0.01137	0.01257	0.2493	0.2586	-	10.34	33.20

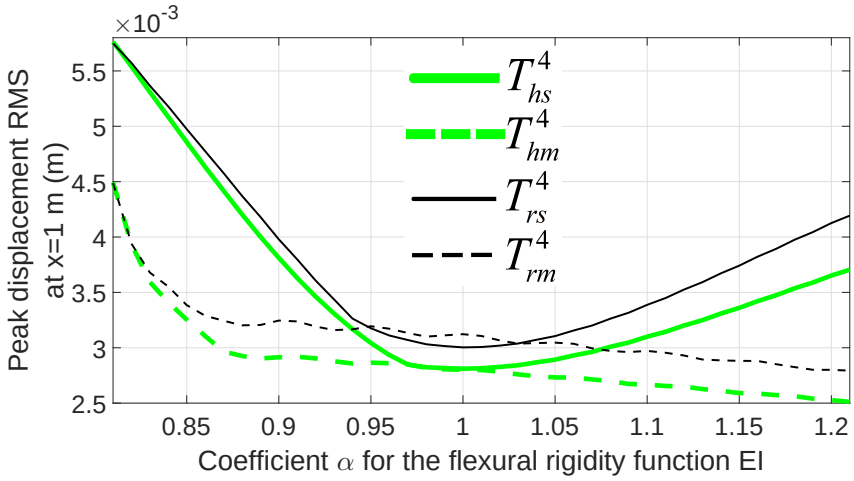

Figure 4.17: Peak beam-top displacement RMS values of the SCOLE model stabilised by T_{hs4} & T_{hm4} in Table 4.3 and T_{rs4} & T_{rm4} in Table 4.5 versus the coefficient α for the flexural rigidity function EI under harmonic excitations.

demonstrate that $\mathcal{H}_\infty$ optimisation is more suitable than $\mathcal{H}_2$ optimisation for the design of TMD systems to suppress vibrations due to harmonic excitations.

Simulation Studies under Random Excitations

Now various TMD systems are designed for the case of the SCOLE beam subject to random excitations using Warburton's formulae [86] and the scheme proposed in Section 4.2.2, and their performances are compared. For the TMD system with $q = 1$ (each TMD group has a single TMD), first the optimal parameters of TMDs by Warburton's formulae are determined:

$$\frac{(\omega_T^i)^2}{\omega_i^2} = \frac{2+\mu_i}{2(1+\mu_i)^2}, \tag{4.117}$$

$$\zeta_i = \sqrt{\frac{\mu_i(4+3\mu_i)}{8(1+\mu_i)(2+\mu_i)}}. \tag{4.118}$$

Similarly as the case for harmonic excitations, with $\mu_1 = \mu_2 = 0.02$ and the values of ω_i and M_i from (4.112) and (4.113), the TMD system T_W is obtained using the above Warburton's formulae, whose parameters are listed in Table 4.5. All the other TMD systems of Table 4.5 are derived using the frequency-limited $\mathcal{H}_2$ optimisations under random excitations. The procedures are similar as those in Section 4.2.3, thus omitted. All these TMD systems have the same total mass of 0.003617 kg. Table 4.5 also lists the values of corresponding objective functions f_{rc} (4.102) and f_r (4.108), and the trade-off constraint θ_r in (4.110) between effectiveness and robustness, during optimisation.

Figure 4.18 shows the power spectral densities (PSDs) of displacements of the SCOLE model stabilised by TMD systems T_W, T_{rs}^1 and T_{rm}^1 in Table 4.5 (see the caption of Table 4.5 for the meaning of the TMD system's notation), under a random excitation. The excitation is generated by passing a white Gaussian noise with the power of 0.001 Watts through a low-pass filter whose passband and stopband frequencies are 1 Hz and 1.2 Hz respectively to covers the first and second modal frequencies of the SCOLE model. It is clear from Figure 4.18 that TMD system T_{rs}^1 has better vibration reduction performances around the first modal frequency than T_W designed using Warburton's formulae, but is not as good as T_W around the second modal frequency. However, the later result shown in Figure 4.19a validates that the overall effectiveness of T_{rs}^1 is better than T_W. In addition, performances of T_{rm}^1 are slightly better than T_{rs}^1 around both modal frequencies. These agree with Table 4.5, where the value of the effectiveness objective function f_{rc}^* (the smaller, the

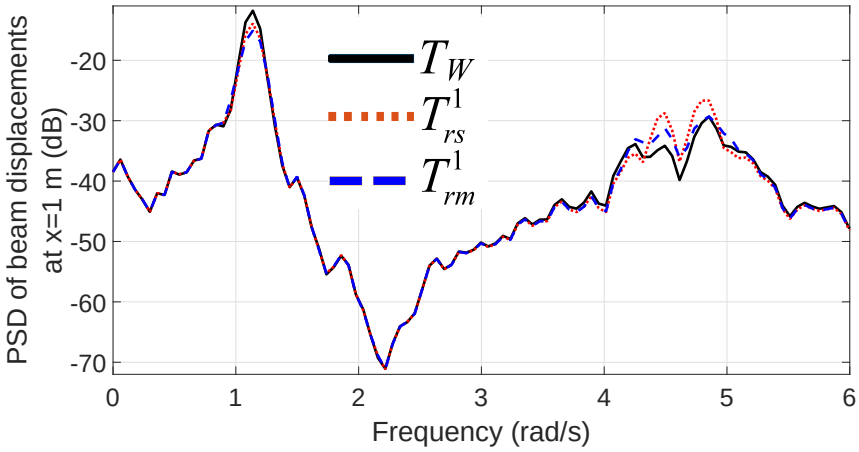

Figure 4.18: PSD of beam-top displacements of the SCOLE model stabilised by T_W, T_{rs}^1 and T_{rm}^1 in Table 4.5.

more effective) drops by 21.39% from T_W to T_{rs}^1 and drops by 6.58% from T_{rs}^1 to T_{rm}^1. To conclude, the proposed optimisation scheme achieves better performance than Warburton's formulae, and the TMD system with each TMD group having multiple TMDs to suppress a dominant mode is more effective than the TMD system with each TMD group having a single TMD.

Like Section 4.2.3, a varied coefficient α is introduced for the flexural rigidity function EI to evaluate the trade-off between effectiveness and robustness. 50 different realisations of the excitation characterised above are generated using 50 different random seeds. For the SCOLE model at a certain value of α stabilised by each TMD system, the standard deviation (SD) of beam-top displacements is computed for each excitation; these 50 SDs are then averaged to form a mean SD. Figure 4.19 shows these mean SDs for the TMD systems in Table 4.5 as functions of the coefficient α, which can be used to assess the robustness of these TMD systems against mistuning effects. Table 4.6 lists the maximum of the mean SDs over α, along with the mean SD at $\alpha = 1$, for each of the TMD systems in Table 4.5, as well as their percent changes from the case with T_W. Table 4.5, Figure 4.19 and Table 4.6 have similar trends as Table 4.3, Figure 4.15 and Table 4.4 of Section 4.2.3. According to Table 4.5, the trade-off between effectiveness and robustness can be made by adjusting the value of θ_r in the constraint (4.110) when optimising TMD parameters. T_{rm}^1 is the most effective among all the TMD systems for the original model ($\alpha = 1$), but is the least robust against mistuning effects. From Figure 4.19, except T_{rm}^1, the TMD systems optimised by the proposed scheme are more effective than T_W derived by Warburton's formulae over most of the range of α considered.

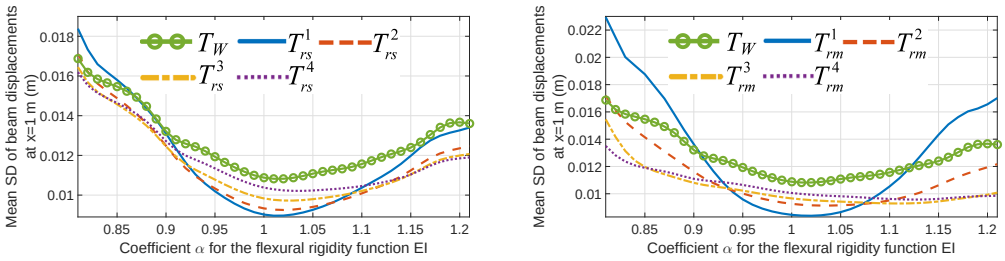

(a) (b)

Figure 4.19: Mean SDs of beam-top displacements of the SCOLE model stabilised by the TMD systems in Table 4.5 versus the coefficient α for the flexural rigidity function EI under random excitations.

Table 4.6: Maximum of the mean SDs of beam-top displacements over α (the coefficient for the flexural rigidity function EI), along with the mean SD at $\alpha = 1$, for each of the TMD systems in Table 4.5, as well as their percent changes from the case with T_W. In the notation of TMD systems, the subscript W/r means that the TMD system is designed by Warburton's formulae/$\mathcal{H}_2$ optimisation to suppress random excitations; the subscript s/m means that each TMD group has a single/multiple TMDs; the superscript 1-4 is the TMD system's index (with its increase, a TMD system's effectiveness decreases and robustness increases).

TMD system	Maximum of the mean SDs of displacements over α ($\times 10^{-3}$ m)	Percent change	Mean SD of displacements at $\alpha = 1$ ($\times 10^{-3}$ m)	Percent change
T_W	16.87	-	10.82	-
T_{rs}^1	18.38	8.974%	8.964	-17.16%
T_{rs}^2	17.11	1.438%	9.268	-14.34%
T_{rs}^3	16.45	-2.501%	9.761	-9.787%
T_{rs}^4	16.19	-4.029%	10.29	-4.888%
T_{rm}^1	22.95	36.02%	8.399	-22.37%
T_{rm}^2	17.18	1.829%	9.193	-15.03%
T_{rm}^3	15.45	-8.402%	9.588	-11.39%
T_{rm}^4	13.50	-19.96%	9.987	-7.698%

Then the performances of the TMD systems in Table 4.3 (designed by $\mathcal{H}_\infty$ optimisation) are compared against the ones in Table 4.5 (designed by $\mathcal{H}_2$ optimisation) under random excitations. The mean SD of displacements of the SCOLE model (at $\alpha = 1$) with T_{hs1} (T_{hm1}) is 14.64% (15.09%) larger than the case with T_{rs1}

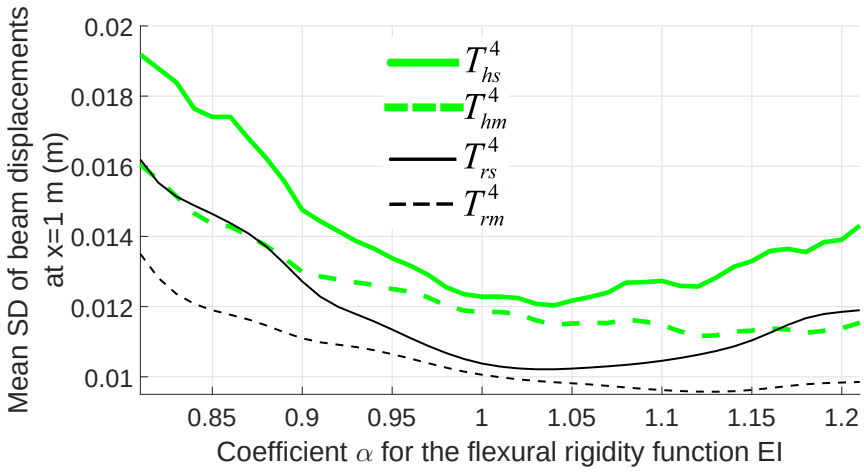

Figure 4.20: Mean SDs of beam-top displacements of the SCOLE model stabilised by T_{rs}^4 & T_{rm}^4 in Table 4.5 and T_{hs}^4 & T_{hm}^4 in Table 4.3 versus the coefficient α for the flexural rigidity function EI under random excitations.

(T_{rm1}). From these results, along with Figure 4.20, it is clear that $\mathcal{H}_2$ optimisation is more suitable for the design of optimal TMD systems for the SCOLE model subject to random excitations than $\mathcal{H}_\infty$ optimisation.

4.3 Conclusions

A TMD system was used to suppress the vibrations of a monopile wind turbine tower effectively. The TMD system comprises two TMDs (sharing the same mass component), one moving in the fore-aft direction while the other in the side-to-side direction. The mass component of the TMDs is put on the floor of the nacelle through wheels/racks (reducing friction). The spring and damper components of each TMD are connected at one end to the nacelle and linked at the other end to the mass component in parallel. Similar TMD systems have been used in the John Hancock Tower in Boston and the Citicorp Center in Manhattan, and have reduced the worst-case wind-induced motion up to 50%. The TMD can also be hanged above the floor through cables like the case of Taipei 101 skyscraper. For the optimisation of the in-nacelle TMD system, first an infinite-dimensional model Σ (4.1)–(4.5) of the turbine tower-TMD system was derived. Then Σ was discretised along the tower's span to derive its finite-dimensional version Σ_d (4.48)–(4.49) using the spectral element method. The responses of Σ_d were compared against those of the NREL monopile 5-MW baseline turbine model within FAST, and Σ_d was verified to accurately simulate the dynamics of the tower and TMD in both fore-aft and side-

to-side directions. Then the transfer function matrix of Σ_d (with the force & torque acting on the RNA as the input, and the tower-top translational displacement as the output) was derived, based on which the $\mathcal{H}_2$ optimisation was performed. Since the motion of the monopile wind turbine tower is dominated by its first mode, the frequency-limited $\mathcal{H}_2$ optimisation was used to obtain optimal fore-aft and side-to-side TMDs. The performances of the optimal TMD(s) were compared against the TMD(s) designed by Stewart and Lackner [2] and similar results were obtained. But the SCOLE model is more realistic (because it contains many vibration modes) and thus can simulate the tower dynamics more precisely than a rigid inverted pendulum tower model with only one mode (used by Stewart and Lackner [2]). In addition, $\mathcal{H}_2$ optimisation is more systematic than the optimisation requiring a number of simulations under a specific loading excitation (employed by Stewart and Lackner [2]). Furthermore, the work successfully demonstrated how to optimally tune a TMD to reduce vibrations of flexible structures described by PDEs.

As an extension of the above research, a method for the design of multiple TMDs was then proposed to suppress vibrations of the non-uniform SCOLE model with multiple dominant vibration modes (representing the monopile wind turbine tower with multiple modes needed to be controlled). Multiple groups of TMDs were configured. Each group was placed at the antinode of the mode shape of a dominant mode of the SCOLE model. Then finite element method was employed to discretise this infinite-dimensional SCOLE-TMD model into a finite-dimensional model Σ_{ed}, which was used for control design based on frequency-limited versions of $\mathcal{H}_\infty$ and $\mathcal{H}_2$ optimisations. TMD systems derived by the proposed scheme are able to suppress multiple dominant vibration modes simultaneously. The simulation tests showed that the performances of the TMD systems with a single TMD tuned for each dominant mode designed by the proposed methods were superior to the ones derived by the traditional methods (Den Hartog's formulae and Warburton's formulae). In addition, the presented methods can specify the trade-off between effectiveness and robustness. The TMD systems with multiple TMDs tuned for each dominant mode were demonstrated to be more effective and robust than the TMD systems with a single TMD tuned for each dominant mode. Furthermore, it was verified that $\mathcal{H}_\infty$ optimisation is more suitable to design TMD systems for the case under excitations dominated by harmonic signals while $\mathcal{H}_2$ optimisation is more suitable for the case under excitations dominated by random signals.

Chapter 5

Power Generation Control of A Monopile Hydrostatic Wind Turbine

In this chapter, the NREL offshore 5-MW baseline turbine model (see Section 2.4) is transformed into a hydrostatic wind turbine (HWT) by replacing its gearbox drivetrain with a hydrostatic transmission (HST) one. Then an $\mathcal{H}_\infty$ loop-shaping torque controller (to regulate the motor displacement) and a linear parameter varying (LPV) blade pitch controller are designed for the transformed HWT with a monopile substructure. To enhance performances of the pitch control system during the transition region around the rated wind speed, an anti-windup (AW) compensator is added to the LPV controller, which would otherwise have had undesirable system responses due to pitch saturation. The LPV AW pitch controller uses the steady rotor effective wind speed as the scheduling parameter which is estimated by LIDAR (Light Detection and Ranging) preview. The simulations based on the transformed HWT model with the NREL OC3 monopile substructure (introduced in Section 2.4) show that the torque controller achieves very good tracking behaviour while the LPV pitch controller (no matter with or without AW) gets much improved overall performances over a gain-scheduled PI pitch controller.

5.1 Introduction

Recall from Section 1.4 that like a conventional geared equipped turbine, an HWT has two controllers (a torque controller and a blade pitch controller) to regulate the power capture in Regions 2 and 3 following the curve in Figure 1.4. In Region 2,

torque control works to capture as much power as possible through regulating the motor displacement. In Region 3, the torque and pitch controllers work together to keep the turbine output power at its rated value and regulate the rotor speed around its rated value.

Now a brief overview of HWT torque control in the existing literature is given. Dutta [5] proposed to calculate the pressure difference (across the hydraulic pump) command for a PI motor displacement controller based on the standard torque control law employed by the NREL offshore 5-MW baseline turbine model (see Section 2.4). The PI controller was derived based on a simplified HWT model (consisting of controller actuator and HST drivetrain dynamics) linearised at an operating point (i.e., one specific wind speed). However, the PI controller did not track the command well under turbulent winds. Wang and Stelson [117] applied model predictive torque control to track the optimal TSR using the predicted future wind speed and did comparisons with the PI controller employing standard control. Both controllers were tested under two kinds of step changes of wind speeds (1 and 2 m/s) in Region 2. Under the step change of 1 m/s, the MPC (model predictive control) controller tracked the optimal TSR faster than the PI controller, but had much larger overshoots in the rotor speed response. Under the step change of 2 m/s, the MPC controller failed while the PI controller was still able to work. Rapp and Turesson [34] compared four torque control strategies: the standard control law, a direct TSR tracking method, and both methods with feedforward. All of them utilised PI/PID motor displacement controllers whose parameters were optimised by the generic algorithm. The simulation results indicated that the standard control law performed better than the direct TSR tracking method, and the feedforward did not make the control performances better under real wind conditions. Regarding pitch control, the literature [5, 118, 119] designed pitch controllers using a single-DOF (i.e., the angular rotation of the rotor/pump shaft) model of the HWT. The papers [5, 119] adopted PI control on the error between the filtered rotor speed and its rated value. The PI controller designed by Dutta [5] had constant gains and was derived based on the single-DOF model linearised at an operating point. Laguna [119] employed a gain-scheduled PI controller with the pitch angle as the scheduling parameter. This control method was adapted from the pitch control of the NREL offshore 5-MW baseline turbine model (see Section 2.4). Skaare et al. [118] proposed gain-scheduled integral control on the error between the aerodynamic power and its command with the pitch angle as the scheduling parameter, based on an aerodynamic power estimator. All the above pitch controllers did not consider the undesirable responses during the transition between Region 2 and 3 (due to

pitch saturation). Besides, all the controllers were tested on simplified HWT models neglecting tower dynamics, blade flexibility, etc. A more detailed HWT simulation model is needed to test the control design.

To solve the above challenges, an $\mathcal{H}_\infty$ loop-shaping torque controller and a linear parameter varying (LPV) pitch controller with an anti-windup (AW) compensator are designed for a monopile HWT. The LPV AW controller is scheduled by the steady rotor effective wind speed estimated by a LIDAR (Light Detection and Ranging) simulator. Both controllers are assessed based on a detailed aero-hydro-servo-elastic monopile HWT simulation model. This model is transformed from the NREL offshore 5-MW baseline turbine model within FAST (introduced in Sections 2.2 and 2.4), through replacing its gearbox drivetrain with the HST one shown in Figure 1.3. The simulation results demonstrate that the torque controller achieves very good tracking behaviours, and the LPV pitch controller obtains much better overall performances (in regulating the rotor speed & generator power and reducing the loads on the blade bearings & tower) than the gain-scheduled PI pitch controller developed in the paper [119].

The structure of the chapter is as follows. In Section 5.2, the NREL offshore 5-MW baseline wind turbine model within FAST is transformed into a detailed HWT. In Sections 5.3 and 5.4, an $\mathcal{H}_\infty$ loop-shaping torque controller and an LPV AW blade pitch controller are designed for the transformed HWT with a monopile substructure. In Section 5.5, performances of the developed torque and pitch controllers are tested through simulation studies using the transformed HWT model with the NREL OC3 monopile substructure.

5.2 Transformation of the NREL Offshore 5-MW Baseline Turbine Model within FAST into An Offshore Hydrostatic Turbine Model

In this section, the NREL offshore 5-MW baseline wind turbine model within FAST is transformed into a detailed aero-hydro-servo-elastic hydrostatic wind turbine (HWT) model for simulation studies, by replacing its gearbox drivetrain system with the HST drivetrain shown in Figure 1.3.

The HST mathematical model (5.1)–(5.3) from Laguna [119] was employed, along with the parameters therein which were tailored for a simplified HWT comprising only the HST drivetrain shown in Figure 1.3 (using the rotor of the NREL offshore 5-MW baseline wind turbine model). The values of other turbine parame-

ters in the equations below are given in Table 2.1.

$$\dot{\omega}_r = \frac{1}{J_r + J_p}(\tau_{aero}(\omega_r, V, \beta)) - \tau_p), \tag{5.1}$$

$$\dot{D}_m = \frac{1}{T_m}(D_{md} - D_m), \tag{5.2}$$

$$\dot{\mathbf{x}}_l = \mathbf{A}_l \mathbf{x}_l + \begin{bmatrix} \mathbf{B}_{l1} & \mathbf{B}_{l2} \end{bmatrix} \begin{bmatrix} Q_p \\ Q_m \end{bmatrix}, \begin{bmatrix} P_p \\ P_m \end{bmatrix} = \begin{bmatrix} \mathbf{C}_{l1} \\ \mathbf{C}_{l2} \end{bmatrix} \mathbf{x}_l. \tag{5.3}$$

(5.1) represents the rotational motion of the rotor/pump shaft, where $J_p = 3,680$ kg·m^2 is the moment of inertia of the pump. τ_{aero} is the aerodynamic torque which depends nonlinearly on the rotor/pump shaft speed ω_r, rotor effective wind speed V, and blade pitch angle β. τ_p is the pump torque described by

$$\tau_p = D_p P_p + B_p \omega_r + C_{fp} D_p P_p \tag{5.4}$$

where $D_p = 0.13$ m^3/rad and P_p are the pump displacement and the pressure difference across the pump, respectively. $B_p = 50,000$ N·m·s and $C_{fp} = 0.02$ are the viscous damping and Coulomb friction coefficients of the pump, respectively. The equation (5.2) describes the displacement actuator dynamics of the variable displacement motor, where D_m and D_{md} are the motor displacement and its command, respectively. $T_m = 0.1$ seconds is the time constant. HST systems normally use highly viscous hydraulic fluid to minimise volumetric losses [24]. Thus, fluid inertia effects, and compressibility & pressure losses due to frequency-dependent friction need to be considered when modelling the hydraulic line [120]. These effects are included in (5.3) which represents the dynamics of the high pressure hydraulic line (assuming the low pressure line has constant pressure), with the flow rates of the pump and motor (Q_p and Q_m) as the inputs and the pressure differences across the pump and motor (P_p and P_m) as the outputs [121, 119]. Laguna [119] derived $\mathbf{A}_l$, $\mathbf{B}_{l1}$, $\mathbf{B}_{l2}$, $\mathbf{C}_{l1}$, and $\mathbf{C}_{l2}$ in (5.3). Q_p and Q_m are given by

$$Q_p = D_p \omega_r - C_{sp} P_p, \; Q_m = D_m \omega_m + C_{sm} P_m, \tag{5.5}$$

where $C_{sp} = 7.1\text{e}{-11}$ m^3/s/Pa and $C_{sm} = 7.0\text{e}{-11}$ m^3/s/Pa are the laminar leakage coefficients of the pump and motor, respectively. $\omega_m = 125.6637$ rad/s is the fixed rotational speed of the assembly composed of the motor and synchronous generator. According to (5.5), Q_m varies with the change of D_m, which affects P_p in accordance

with (5.3) and thus affects τ_p (5.4). The generator power is

$$p_g = \eta \tau_m \omega_m \tag{5.6}$$

where $\eta = 94.4\%$ is the generator efficiency and τ_m is the motor torque:

$$\tau_m = D_m P_m - B_m \omega_m + C_{fm} D_m P_m \tag{5.7}$$

in which $B_m = 3.5$ N·m·s and $C_{fm} = 0.02$ are the viscous damping and Coulomb friction coefficients of the motor, respectively.

The difference between a geared equipped turbine and an HWT lies in their drivetrain structures. Hence, the input file of FAST ElastoDyn (including structural properties of the turbine) is modified to transform the gearbox drivetrain to the HST one modelled above. In (2.21), if $N_g = 1$ and the generator is regarded as the HST pump, then (2.21) and (5.1) are equivalent. Therefore, to replace the baseline rotor shaft dynamics with HWT rotor/pump shaft dynamics, the drivetrain torsional flexibility DOF is disabled since there is no torsional motion between the rotor and pump, the gearbox ratio is set to be 1, and the generator inertia J_g is set to be the pump inertia J_p in the ElastoDyn input file. Then the mathematical model of the HST drivetrain, and torque & pitch controllers (to be developed in Chapter 5) are incorporated into the NREL 5-MW turbine model to get an HWT, through the interface between FAST and MATLAB/Simulink. Figure 5.1 illustrates how to integrate the HST drivetrain model, torque and pitch controllers (together with their actuators), and FAST in the Simulink environment. The FAST block stands for the FAST/Simulink interface which passes the generator power P_g, pump torque τ_p, & collective blade pitch angle β from Simulink to FAST, and outputs the rotor speed ω_r from FAST to Simulink. The HL block represents the state-space model (5.3) of the hydraulic line. The MG block stands for the motor-generator assembly. It uses the inputs P_m and D_m, and equations (5.5), (5.6), and (5.7) to derive the outputs Q_m and P_g. The TC block represents the torque controller (i.e., the motor displacement controller), together with its actuator dynamics described by (5.2). The torque controller receives ω_r from FAST and P_p from the HL block to output the motor displacement D_m. The PC block represents the pitch controller together with its actuator dynamics. It needs ω_r from FAST as the input, and outputs β to FAST. The PU block represents the hydraulic pump. It utilises the inputs P_p and ω_r, together with equations (5.4) and (5.5), to derive the outputs Q_p and τ_p.

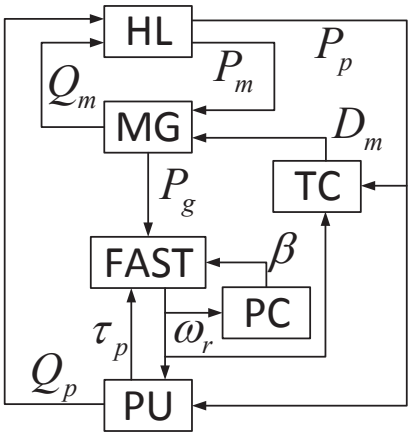

Figure 5.1: Block diagram showing the integration of the HST drivetrain model, torque and pitch controllers (together with their actuators), and FAST in the Simulink environment.

5.3 Torque Control

The NREL baseline torque controller regulates the generator torque to track its command $\tau_g(\omega_{fg})$ which is inversely proportional to the filtered generator speed ω_{fg} in Region 3 and is calculated using the standard control law in Region 2 (see Section 2.4). The same torque control strategy is employed for the transformed NREL 5-MW hydrostatic wind turbine (HWT), but the control variable becomes the pump torque. Regulation of the pump torque is typically fulfilled by adjusting the pressure difference across the pump P_p to track its command $P_{pd}(\omega_{fr})$ (where ω_{fr} is the filtered rotor speed), through controlling the motor displacement D_m. According to (5.1) and (2.21), the desired pump torque is

$$\tau_{pd}(\omega_{fr}) = N_g \tau_g(\omega_{fg}) = N_g \tau_g(N_g \omega_{fr}) \tag{5.8}$$

where $N_g = 97$ (from Table 2.1). Then from (5.4), the pressure command is

$$P_{pd}(\omega_{fr}) = \frac{\tau_{pd} - B_p \omega_{fr}}{(1 + C_{fp}) D_p}. \tag{5.9}$$

The torque controller is designed based on the HST drivetrain model (5.1)–(5.3). Recall that the nonlinear term τ_{aero} in (5.1) depends on ω_r (rotor/pump shaft speed), V (rotor effective wind speed) and β (blade pitch angle). Linearising the model at an operating point $(\bar{\omega}_r, \bar{V}, \bar{\beta})$ (where the bar over a variable denotes its

steady value at the operating point), a state-space model Σ_m is derived as

$$\dot{\hat{\mathbf{x}}}_m = \mathbf{A}_m\hat{\mathbf{x}}_m + \mathbf{B}_m\hat{D}_{md} + \mathbf{B}_{md}\hat{V},\ \hat{P}_p = \mathbf{C}_m\hat{\mathbf{x}}_m, \tag{5.10}$$

in which

$$\mathbf{A}_m = \begin{bmatrix} \frac{f_{\omega_r}-B_p}{J_r+J_p} & 0 & \mathbf{A}_{13} \\ 0 & -\frac{1}{T_m} & \mathbf{0} \\ \mathbf{A}_{31} & \mathbf{A}_{32} & \mathbf{A}_{33} \end{bmatrix},\ \mathbf{B}_m = \begin{bmatrix} 0 & \frac{1}{T_m} & \mathbf{0} \end{bmatrix}^T,$$
$$\mathbf{B}_{md} = \begin{bmatrix} \frac{f_V}{J_r+J_p} & 0 & \mathbf{0} \end{bmatrix}^T,\ \mathbf{C}_m = \begin{bmatrix} 0 & 0 & \mathbf{C}_{l1} \end{bmatrix},$$

where $f_{\omega_r} = \left(\frac{\partial\tau_{aero}}{\partial\omega_r}\right)_{\bar{\omega}_r}$, $\mathbf{A}_{13} = -\frac{(D_p+C_{fp}D_p)\mathbf{C}_{l1}}{J_r+J_p}$, $\mathbf{A}_{31} = D_p\mathbf{B}_{l1}$, $\mathbf{A}_{32} = \omega_m\mathbf{B}_{l2}$, $\mathbf{A}_{33} = \mathbf{A}_l - C_{sp}\mathbf{B}_{l1}\mathbf{C}_{l1} + C_{sm}\mathbf{B}_{l2}\mathbf{C}_{l2}$ and $f_V = \left(\frac{\partial\tau_{aero}}{\partial V}\right)_{\bar{\omega}_r,\bar{V},\bar{\beta}}$. The state variable vector is $\hat{\mathbf{x}}_m = \begin{bmatrix} \hat{\omega}_r & \hat{D}_m & \hat{\mathbf{x}}_l \end{bmatrix}^T$ where $\hat{\mathbf{x}}_m = \mathbf{x}_m - \bar{\mathbf{x}}_m$ in which $\mathbf{x}_m = \begin{bmatrix} \omega_r & D_m & \mathbf{x}_l \end{bmatrix}^T$. The input is $\hat{D}_{md} = D_{md} - \bar{D}_m$. The disturbance is $\hat{V} = V - \bar{V}$. The output is $\hat{P}_p = P_p - P_{pd}$. The values of f_{ω_r} and f_V are derived through a FAST linearisation process (briefly introduced in Section 2.2) at an operating point. The operating point is chosen at $\bar{V} = 9$ m/s in Region 2 where $\bar{\omega}_r = 1.08$ rad/s and the blade pitch controller does not work. So in Σ_m the blade pitch actuator dynamics are neglected, and τ_{aero} only depends on ω_r and V. Before the linearisation of the baseline turbine, steady values of the control inputs (the generator torque and rotor-collective blade-pitch angle) need to be specified. While for the HWT, the steady value of the generator torque is replaced by the desired pump torque which is 2.4828e6 N (calculated from (5.8) with $\omega_{fr} = \bar{\omega}_r = 1.08$ rad/s). The steady value of the blade pitch angle is 0° in Region 2. Only the generator DOF is enabled for the linearisation. The resulting one-DOF linear HWT model is

$$\dot{\hat{\omega}}_r = -2.843\text{e}{-3}\hat{\omega}_r + 1.478\text{e}{-2}\hat{V}. \tag{5.11}$$

If (5.1) is linearised at $\bar{V} = 9$ m/s with τ_p assumed to be constant at its desired value, then

$$\dot{\hat{\omega}}_r = \frac{f_{\omega_r}}{J_r+J_p}\hat{\omega}_r + \frac{f_V}{J_r+J_p}\hat{V}. \tag{5.12}$$

Since (5.11) and (5.12) are equivalent,

$$f_{\omega_r} = -2.843\text{e}{-3}\left(J_r+J_p\right) = -1.1020\text{e}5\ \text{N·m·s}, \tag{5.13}$$
$$f_V = 1.478\text{e}{-2}\left(J_r+J_p\right) = 5.7292\text{e}5\ \text{N·s}. \tag{5.14}$$

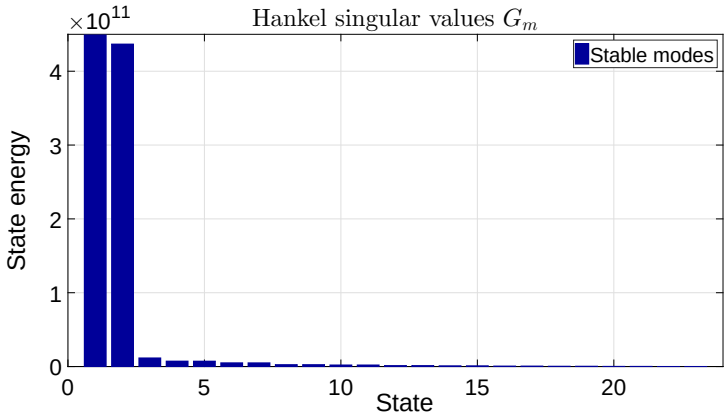

Figure 5.2: Hankel singular values of the 23rd-order plant G_m.

A transfer function G_m from $\hat{D}_{md}$ to $\hat{P}_p$ is finally acquired with the state-space realisation $(\mathbf{A}_m, \mathbf{B}_m, \mathbf{C}_m, 0)$.

The highest natural frequency of the NREL offshore 5-MW baseline turbine model is about 2.5 Hz [109]. Hence, the number of modes for the 10-m hydraulic line is chosen to be 10, so the line's modal frequencies are in a wide range of [0, 93.12] Hz. This results in a stable 23rd-order plant G_m. The singular perturbation approximation method [122] is used to reduce the order of G_m so that the reduced model matches G_m well at low frequencies, which is sufficient for the control design due to slow variations of ω_{fr}. First compute the Hankel singular values of G_m, which are the square roots of the eigenvalues for the product of G_m's controllability Gramian $\mathbf{P}_{Gm}$ and observability Gramian $\mathbf{Q}_{Gm}$, using the Matlab function *hsvd*. $\mathbf{P}_{Gm}$ and $\mathbf{Q}_{Gm}$ are the solutions of the Lyapunov equations

$$\mathbf{A}_m\mathbf{P}_{Gm} + \mathbf{P}_{Gm}\mathbf{A}_m^T + \mathbf{B}_m\mathbf{B}_m^T = \mathbf{0}, \tag{5.15}$$

$$\mathbf{A}_m^T\mathbf{Q}_{Gm} + \mathbf{Q}_{Gm}\mathbf{A}_m + \mathbf{C}_m^T\mathbf{C}_m = \mathbf{0}. \tag{5.16}$$

The Hankel singular values of G_m are illustrated in Figure 5.2. The smaller the Hanker singular value is, the less the associated state contributes to the behaviour of the system. Hence, 14 states with relatively small singular values are discarded. Then a reduced 9th-order model G_{rm} is derived using the following steps (realised by the Matlab function *balred* [123]):

a. Calculate the lower triangular Cholesky factors L_P and L_Q of the Gramians $\mathbf{P}_{Gm}$ and $\mathbf{Q}_{Gm}$:

$$\mathbf{P}_{Gm} = \mathbf{L}_P\mathbf{L}_P^*, \quad \mathbf{Q}_{Gm} = \mathbf{L}_Q\mathbf{L}_Q^*. \tag{5.17}$$

b. Compute the singular value decomposition of $\mathbf{L}_Q^* \mathbf{L}_P$:

$$\mathbf{L}_Q^* \mathbf{L}_P = \mathbf{U}_{Gm} \mathbf{\Lambda} \mathbf{V}_{Gm}^* \tag{5.18}$$

where $\mathbf{U}_{Gm}$ and $\mathbf{V}_{Gm}$ are unitary ($\mathbf{U}_{Gm}\mathbf{U}_{Gm}^* = \mathbf{U}_{Gm}^*\mathbf{U}_{Gm} = \mathbf{I}$, and $\mathbf{V}_{Gm}\mathbf{V}_{Gm}^* = \mathbf{V}_{Gm}^*\mathbf{V}_{Gm} = \mathbf{I}$). $\mathbf{\Lambda}$ is a diagonal matrix with non-negative real elements on the diagonal in the descending order.

c. Derive the balancing transformation $\mathbf{T}_{tr} = \mathbf{L}_P \mathbf{V}_{Gm} \mathbf{\Lambda}^{-\frac{1}{2}}$.

d. Derive a balanced realisation G_{mb} of G_m:

$$G_{mb} \overset{s}{=} \left[\begin{array}{c|c} \mathbf{T}_{tr}\mathbf{A}_m\mathbf{T}_{tr}^{-1} & \mathbf{T}_{tr}\mathbf{B}_m \\ \hline \mathbf{C}_m\mathbf{T}_{tr}^{-1} & 0 \end{array}\right]. \tag{5.19}$$

e. Partition G_{mb} as

$$\begin{bmatrix} \dot{\hat{\mathbf{x}}}_{mb1} \\ \dot{\hat{\mathbf{x}}}_{mb2} \end{bmatrix} = \begin{bmatrix} \mathbf{A}_{m11} & \mathbf{A}_{m12} \\ \mathbf{A}_{m21} & \mathbf{A}_{m22} \end{bmatrix} \begin{bmatrix} \hat{\mathbf{x}}_{mb1} \\ \hat{\mathbf{x}}_{mb2} \end{bmatrix} + \begin{bmatrix} \mathbf{B}_{m1} \\ \mathbf{B}_{m2} \end{bmatrix} \hat{D}_{md}, \tag{5.20}$$

$$\hat{P}_p = \begin{bmatrix} \mathbf{C}_{m1} & \mathbf{C}_{m2} \end{bmatrix} \begin{bmatrix} \hat{\mathbf{x}}_{mb1} \\ \hat{\mathbf{x}}_{mb2} \end{bmatrix}, \tag{5.21}$$

where $\hat{\mathbf{x}}_{mb1}$ is the reduced state vector (with 9 states) to be kept and $\hat{\mathbf{x}}_{mb2}$ is the vector of remaining 14 states to be discarded.

f. Set $\dot{\hat{\mathbf{x}}}_{mb2}$ to 0 and then obtain G_{rm} with the state-space matrices

$$\begin{aligned} \mathbf{A}_{rm} &= \mathbf{A}_{m11} - \mathbf{A}_{m12}\mathbf{A}_{m22}^{-1}\mathbf{A}_{m21}, \\ \mathbf{B}_{rm} &= \mathbf{B}_{m1} - \mathbf{A}_{m12}\mathbf{A}_{m22}^{-1}\mathbf{B}_{m2}, \\ \mathbf{C}_{rm} &= \mathbf{C}_{m1} - \mathbf{C}_{m2}\mathbf{A}_{m22}^{-1}\mathbf{A}_{m21},\ \mathbf{D}_{rm} = -\mathbf{C}_{m2}\mathbf{A}_{m22}^{-1}\mathbf{B}_{m2}. \end{aligned}$$

Figure 5.3 shows the Bode frequency responses of the original model G_m and the reduced-order model G_{rm}. Clearly, G_{rm} matches G_m very well at frequencies below 40 Hz.

Using the $\mathcal{H}_\infty$ loop-shaping approach [124], a torque controller K_m is designed based on G_{rm} to shape the singular values of the open-loop transfer function $G_s = G_{rm}K_m$ to match closely those of a desired transfer function G_{md} and simultaneously stabilise the closed-loop system. The control structure is shown in Figure 5.4, where $r_m = 0$ is the reference, $\hat{D}_{md}$ is the control signal, and $\hat{P}_p$ is the output. Select

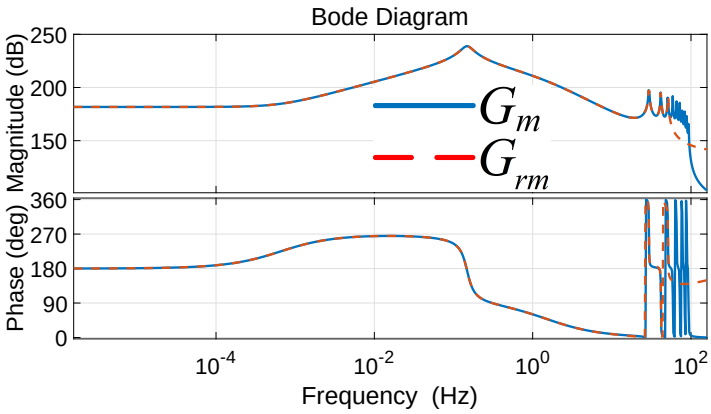

Figure 5.3: Bode frequency responses of the original 23rd-order plant G_m and its reduced 9th-order model G_{rm}.

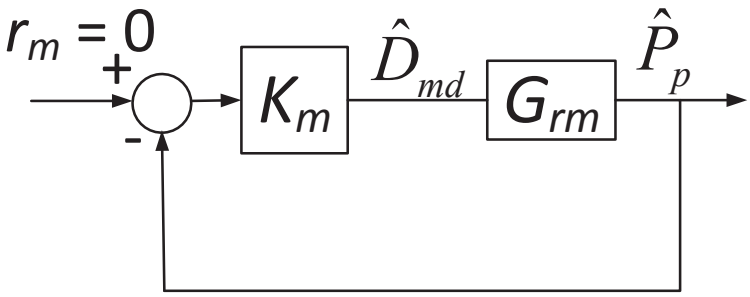

Figure 5.4: Control structure of the motor displacement controller K_m.

$$G_{md}(s) = \frac{930}{(s + 1\text{e}{-7})(s + 50)} \tag{5.22}$$

which has high gains at low frequencies, implying low tracking error in the steady state. Its gain crossover frequency is 17.88 rad/s, and the high-frequency roll-off is about -40 dB/decade, which indicates fast tracking performance and good robustness against unstructured model uncertainties. Subsequently, a pre-compensator W_m is calculated such that the singular values of $G_W = G_{rm}W_m$ are identical to those of G_{md} in the frequency range of $[0, \infty)$, using the algorithm proposed by Doyle [125] as follows:

a. Calculate the inner-outer factorisation of G_{rm}

$$G_{rm} = \theta_{io1} M_{io1} \tag{5.23}$$

where θ_{io1} is stable and unitary, and M_{io1} is minimum-phase.

b. Calculate the inner-outer factorisation of M_{io1}^{-1}:

$$M_{io1}^{-1} = \theta_{io2} M_{io2} \tag{5.24}$$

where θ_{io2} is stable and unitary, and M_{io2} is minimum-phase.

c. Derive $W_m = M_{io2} G_{md}$.

The resulting closed loop is unstable because the original (uncompensated) closed-loop system has right-half-plane poles and zeros [126]. To guarantee a stabilising controller, $\mathcal{H}_\infty$ synthesis [124] is conducted by first calculating the normalised co-prime factorisation of G_W:

$$G_W = M_W^{-1} N_W \tag{5.25}$$

in which $N_W N_W^* + M_W M_W^* = 1$. The perturbed system of G_W is then written as

$$\tilde{G}_W = (M_W + \Delta_1)^{-1} (N_W + \Delta_2) \tag{5.26}$$

where Δ_1, Δ_2 are stable unknown modelling uncertainties. Now consider finding an optimal $\mathcal{H}_\infty$ controller K_s to minimise ν_s such that

$$\left\| \begin{bmatrix} K_s \\ 1 \end{bmatrix} (1 - G_W K_s)^{-1} M_W^{-1} \right\|_\infty \leq \nu_s. \tag{5.27}$$

According to Lemma 3.1 in the paper [124], K_s ensures the closed-loop stability if $\left\| \begin{bmatrix} \Delta_1 & \Delta_2 \end{bmatrix} \right\|_\infty \leq \nu_s^{-1}$. Finally, the torque controller is derived:

$$K_m = W_m K_s \tag{5.28}$$

which can be solved by the Matlab function *loopsyn* [124]. The resulting closed-loop gain is $\nu_s = 1.78$, which means that the modelling uncertainties of less than 0.56 are tolerated. The phase and minimum gain margins of $G_m K_m$ are 73.4 deg and 11.3 dB, respectively. The closed-loop step response has an overshoot of 0 and a settling time of 0.22 s (see Figure 5.5). These results demonstrate that the closed-loop system has good robust stability and tracking performance.

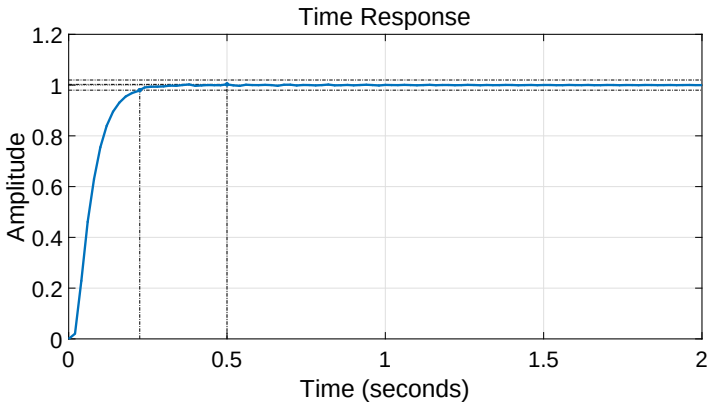

Figure 5.5: Closed-loop step response.

5.4 Pitch Control Using LIDAR Wind Preview

In Region 3, blade pitch control regulates the rotor speed around its rated value. First an LPV pitch controller is designed. Then an AW compensator is added to it for the purpose of system recovery after pitch saturation during the transition between Region 2 and 3. The LPV AW pitch controller uses the steady rotor effective wind speed as the scheduling parameter. A LIDAR simulator is developed to process raw data and obtain estimated steady rotor effective speeds for LPV AW control.

5.4.1 LPV Pitch Controller

The pitch controller is designed by taking the rotor/pump shaft dynamics (5.1) and blade pitch actuator dynamics into account. The latter one is represented by a first-order time delay

$$\dot{\beta} = \frac{1}{T_\beta}(\beta_d - \beta) \tag{5.29}$$

where β and β_d are the pitch angle and its command, respectively. $T_\beta = 0.1$ seconds is the time constant. To maintain the constant rated rotor power in Region 2, the torque controller regulates the pump torque τ_p to be inversely proportional to the rotor speed ω_r. Then (5.1) is rewritten as

$$\dot{\omega}_r = \frac{1}{J_r + J_p}\left(\tau_{aero}(\omega_r, V, \beta) - \frac{p_{rr}}{\omega_r}\right). \tag{5.30}$$

where $p_{rr} = 5.2966\text{e}6$ W is the rated rotor power (see Table 2.1). Combining (5.29) and (5.30), a nonlinear model is derived. By linearising it at an operating point $(\bar{\omega}_r, \bar{V}, \bar{\beta})$, one obtains

$$\dot{\hat{\mathbf{x}}}_p = \mathbf{A}_p\hat{\mathbf{x}}_p + \mathbf{B}_p\hat{\beta}_d + \mathbf{B}_{pd}\hat{V},\ \hat{\omega}_r = \mathbf{C}_p\hat{\mathbf{x}}_p, \tag{5.31}$$

in which

$$\mathbf{A}_p = \begin{bmatrix} \frac{f_{\omega_r} + \frac{p_{rr}}{\bar{\omega}_r^2}}{J_r + J_p} & \frac{f_\beta}{J_r + J_p} \\ 0 & -\frac{1}{T_\beta} \end{bmatrix},\ \mathbf{B}_p = \begin{bmatrix} 0 & \frac{1}{T_\beta} \end{bmatrix}^T, \tag{5.32}$$

$$\mathbf{C}_p = \begin{bmatrix} 1 & 0 \end{bmatrix},\ \mathbf{B}_{pd} = \begin{bmatrix} \frac{f_V}{J_r + J_p} & 0 \end{bmatrix}^T, \tag{5.33}$$

where $f_\beta = \left(\frac{\partial \tau_{aero}}{\partial \beta}\right)_{\bar{\omega}_r, \bar{V}, \bar{\beta}}$. The state variable vector is $\hat{\mathbf{x}}_p = \begin{bmatrix} \hat{\omega}_r & \hat{\beta} \end{bmatrix}^T$ where $\hat{\mathbf{x}}_p = \mathbf{x}_p - \bar{\mathbf{x}}_p$ in which $\mathbf{x}_p = \begin{bmatrix} \omega_r & \beta \end{bmatrix}^T$. The input is $\hat{\beta}_d = \beta_d - \bar{\beta}$. The disturbance is $\hat{V} = V - \bar{V}$. The output is $\hat{\omega}_r = \omega_r - \bar{\omega}_r$. In Region 3, $\bar{\omega}_r = 12.1$ rpm. Since the steady values $\bar{\omega}_r$ and $\bar{\beta}$ depend uniquely on $\bar{V}$ over the entire operating range of the wind turbine, (5.31) can be treated as an LPV model with $\bar{V}$ as the only scheduling parameter.

The design of an LPV pitch controller is to seek a controller $K_p(\bar{V})$ scheduled by $\bar{V}$ such that for the resulting closed-loop system, the induced $\mathcal{L}_2$ norm $\|\mathcal{F}\|_{\mathcal{L}_2}$ from the external signal w to the performance output $\mathbf{z} = \begin{bmatrix} z_1 & z_2 \end{bmatrix}^T$ satisfies a performance level $\gamma > 0$, i.e.,

$$\|\mathcal{F}\|_{\mathcal{L}_2} = \sup_{\substack{w \neq 0 \\ \bar{V} \in \Theta}} \frac{\|\mathbf{z}\|_2}{\|w\|_2} < \gamma \tag{5.34}$$

in which $\|\mathbf{x}\|_2 = \sqrt{\int \mathbf{x}^T\mathbf{x}\mathrm{d}t}$ and

$$\Theta = \left\{ \sum_{j=1}^{2} \alpha_j\theta_j : \alpha_j \geq 0, \sum_{j=1}^{2} \alpha_j = 1 \right\} \tag{5.35}$$

where $\theta_1 = 11.4$ m/s and $\theta_2 = 25$ m/s are the vertices of Θ. Hence, $\bar{V} \in \Theta$ means that $\bar{V}$ varies in Region 3. The control structure is shown in Figure 5.6. The external signal w is the reference value for $\hat{\omega}_r = \omega_r - \bar{\omega}_r$. The performance output $\mathbf{z}$ is the outputs of the weighting functions W_e and W_u. $W_e = \frac{0.5s + 0.25}{s + 5\text{e}{-7}}$ which has high gains at low frequencies to penalise the rotor speed error e and has low gains

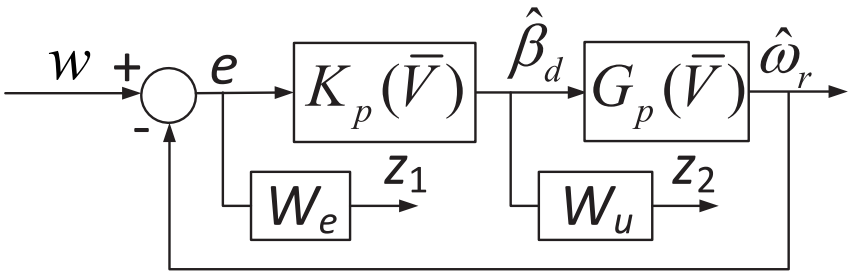

Figure 5.6: Control structure of the LPV blade pitch controller $K_p(\bar{V})$.

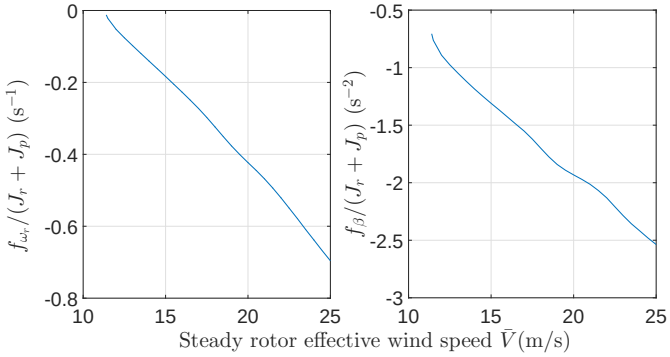

Figure 5.7: $f_{\omega_r}/(J_r + J_p)$ and $f_\beta/(J_r + J_p)$ at $\bar{V} \in \Theta$ ($\bar{V}$ is the steady rotor effective wind speed).

at high frequencies to limit overshoot. $W_u = 1.3\frac{0.1s+0.5}{0.02s+1}$ which limits the control bandwidth and to avoid fast pitch angle variations. $G_p(\bar{V})$ has the state-space realisation $\big(\mathbf{A}_p, \mathbf{B}_p, \mathbf{C}_p, 0\big)$. $\mathbf{A}_p$ (5.32) has the nonlinear terms $f_{\omega_r}/(J_r + J_p)$ and $f_\beta/(J_r + J_p)$, which depend on $\bar{V} \in \Theta$ as shown in Figure 5.7. $f_{\omega_r}(\bar{V})$ is derived in the similar way as that for the calculation of f_{ω_r} at $\bar{V} = 9$ m/s in Section 5.3. The difference is that now for FAST linearisations, the desired pump torque is 4.18e6 N·m (for all $\bar{V} \in \Theta$) which is calculated from (5.8) with $\tau_g = \tau_{gr} = 43,093.55$ N·m. The steady value of the blade pitch angle $\bar{\beta}$ varies with $\bar{V}$ as shown in Figure 5.8 [7]. $f_\beta(\bar{V})$ is derived according to $f_\beta(\bar{V}) = \left(\frac{\partial \tau_{aero}}{\partial \beta}\right)(\bar{V}) = \frac{1}{\omega_{rr}}\left(\frac{\partial p_r}{\partial \beta}\right)(\bar{V})$ where $\left(\frac{\partial p_r}{\partial \beta}\right)(\bar{V})$ is given in Table 7-1 of the report [7]. Clearly from Figure 5.7, the nonlinear terms in $\mathbf{A}_p$ can be approximated by two affine functions with $\bar{V} \in \Theta$ as the independent variable. Hence, $G_p(\bar{V})$ is affinely dependent on $\bar{V} \in \Theta$. Note that the controller output is $\hat{\beta}_d = \beta_d - \bar{\beta}$ where $\bar{\beta}$ is a function of $\bar{V}$ (see Figure 5.8). Therefore, the actual pitch angle command is $\beta_d = \hat{\beta}_d + \bar{\beta}(\bar{V})$. $\hat{\beta}_d$ is the output of the controller $K_p(\bar{V})$ as shown in Figure 5.6. $\bar{\beta}(\bar{V})$ is obtained by integrating the pitch

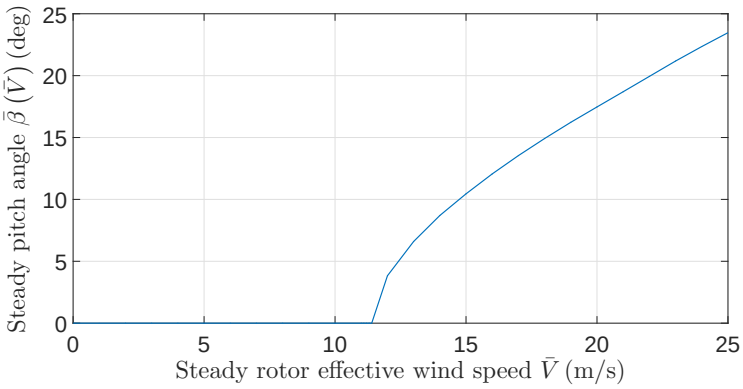

Figure 5.8: Steady pitch angle $\bar{\beta}(\bar{V})$ ($\bar{V}$ is the steady rotor effective wind speed) [7].

rate $\dot{\bar{\beta}}(\bar{V}) = \dot{\bar{V}}\frac{\mathrm{d}\bar{\beta}}{\mathrm{d}\bar{V}}(\bar{V})$ [9]. Such a mechanism can avoid the high pitch rate near the rated wind speed 11.4 m/s as indicated in Figure 5.8 (which will induce significant tower loads during the transition between Region 2 and 3), through limiting $\mathrm{d}\bar{\beta}/\mathrm{d}\bar{V}$ to 2.5°s/m.

Following the control structure shown in Figure 5.6, an augmented open-loop LPV system P_Σ is obtained:

$$\dot{\mathbf{x}} = \mathbf{A}(\bar{V})\mathbf{x} + \mathbf{B}_1(\bar{V})w + \mathbf{B}_2(\bar{V})\hat{\beta}_d, \tag{5.36}$$

$$\mathbf{z} = \mathbf{C}_1(\bar{V})\mathbf{x} + \mathbf{D}_{11}(\bar{V})w + \mathbf{D}_{12}(\bar{V})\hat{\beta}_d, \tag{5.37}$$

$$\hat{\omega}_r = \mathbf{C}_2(\bar{V})\mathbf{x} + \mathbf{D}_{21}(\bar{V})w. \tag{5.38}$$

Now determine a stabilising LPV controller $K_p(\bar{V})$ to satisfy (5.34). Recall that $G_p(\bar{V})$ depends affinely on $\bar{V} \in \Theta$, so does its augmented system P_Σ. Hence, according to the literature [127], first solve an optimisation problem offline: minimising $\gamma\left(\mathbf{X}, \mathbf{Y}, \hat{\mathbf{A}}_{K_j}, \hat{\mathbf{B}}_{K_j}, \hat{\mathbf{C}}_{K_j}\right)$ $(j = 1, 2)$ subject to (5.39) with $\star$ induced by symmetry.

$$\begin{bmatrix} \mathbf{X}\mathbf{A}(\theta_j) + \hat{\mathbf{B}}_{K_j}\mathbf{C}_2(\theta_j) + (\star) & \star & \star & \star \\ \hat{\mathbf{A}}_{K_j}^T + \mathbf{A}(\theta_j) & \mathbf{A}(\theta_j)\mathbf{Y} + \mathbf{B}_2(\theta_j)\hat{\mathbf{C}}_{K_j} + (\star) & \star & \star \\ \left[\mathbf{X}\mathbf{B}_1(\theta_j) + \hat{\mathbf{B}}_{K_j}\mathbf{D}_{21}(\theta_j)\right]^T & \mathbf{B}_1(\theta_j)^T & -\gamma\mathbf{I} & \star \\ \mathbf{C}_1(\theta_j) & \mathbf{C}_1(\theta_j)\mathbf{Y} + \mathbf{D}_{12}(\theta_j)\hat{\mathbf{C}}_{K_j} & \mathbf{D}_{11}(\theta_j) & -\gamma\mathbf{I} \end{bmatrix} < 0,$$

$$\begin{bmatrix} \mathbf{X} & \mathbf{I} \\ \mathbf{I} & \mathbf{Y} \end{bmatrix} > 0, \mathbf{X} = \mathbf{X}^T > 0, \mathbf{Y} = \mathbf{Y}^T > 0. \tag{5.39}$$

Then the controller K_j is derived at the vertex θ_j with the state-space realisation

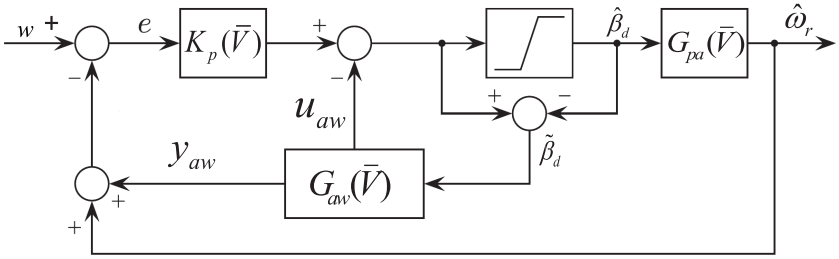

Figure 5.9: Anti-windup compensation scheme for the LPV pitch controller.

$\left(\mathbf{A}_{K_j}, \mathbf{B}_{K_j}, \mathbf{C}_{K_j}, 0\right)$ in which

$$\mathbf{A}_{K_j} = \mathbf{N}_p^{-1}\left(\hat{\mathbf{A}}_{K_j} - \mathbf{X}\mathbf{A}(\theta_j)\mathbf{Y} - \hat{\mathbf{B}}_{K_j}\mathbf{C}_2(\theta_j)\mathbf{Y} - \mathbf{X}\mathbf{B}_2(\theta_j)\hat{\mathbf{C}}_{K_j}\right)\mathbf{M}_p^{-T}, \tag{5.40}$$

$$\mathbf{B}_{K_j} = \mathbf{N}_p^{-1}\hat{\mathbf{B}}_{K_j}, \mathbf{C}_{K_j} = \hat{\mathbf{C}}_{K_j}\mathbf{M}_p^{-T}, \tag{5.41}$$

where $\mathbf{N}_p$ and $\mathbf{M}_p$ are the solutions of the factorisation problem $\mathbf{I} - \mathbf{X}\mathbf{Y} = \mathbf{N}_p\mathbf{M}_p^T$. For the online implementation, $\bar{V}$ is measured to obtain the LPV pitch controller $K_p(\bar{V})$ with the state-space realisation $(\mathbf{A}_K, \mathbf{B}_K, \mathbf{C}_K, 0)$ where

$$\begin{bmatrix} \mathbf{A}_K & \mathbf{B}_K \\ \mathbf{C}_K & 0 \end{bmatrix}(\bar{V}) = \sum_{j=1}^{2} \alpha_j \begin{bmatrix} \mathbf{A}_{K_j} & \mathbf{B}_{K_j} \\ \mathbf{C}_{K_j} & 0 \end{bmatrix} \tag{5.42}$$

in which $\alpha_1 = \frac{25-\bar{V}}{13.6}$ and $\alpha_2 = \frac{\bar{V}-11.4}{13.6}$. Note that α_1 and α_2 can be any continuous functions of $\bar{V}$ satisfying (5.35).

5.4.2 AW Compensator

The AW compensation scheme proposed in the paper [128] is employed for the LPV pitch controller (see Figure 5.9). Note that this AW setup can be incorporated with other pitch controllers because it is designed independently. This AW scheme is applicable only when the open-loop LPV plant is exponentially stable. However, due to the negative damping introduced by torque control (indicated by the term $p_r/\bar{\omega}_r^2$ in (5.32)), the LPV model $G_p(\bar{V})$ used for pitch control design is unstable when $\bar{V}$ is above and near the rated value 11.4 m/s. In order to obtain an exponentially stable LPV plant for the AW design, this negative damping is neglected. Such a treatment (also used in the reports [129, 7]) means that in (5.30) the rotor reaction

torque p_r/ω_r is assumed to remain at its constant steady value in Region 2. As a result, the LPV model $G_{pa}(\bar{V})$ used for the AW design is the same as $G_p(\bar{V})$ with $\mathbf{A}_p$ in (5.32) replaced with

$$\mathbf{A}_{pa} = \begin{bmatrix} \frac{f_{\omega_r}}{J_r+J_p} & \frac{f_\beta}{J_r+J_p} \\ 0 & -\frac{1}{T_\beta} \end{bmatrix}. \tag{5.43}$$

As shown in Figure 5.9, the AW compensator provides two compensation terms u_{aw} and y_{aw} to the controller output and input, respectively. The transfer function matrix $\mathbf{G}_{aw}(\bar{V})$ of the compensator is defined as $\mathbf{G}_{aw}(\bar{V}) = \begin{bmatrix} M(\bar{V}) - 1 & N(\bar{V}) \end{bmatrix}^T$ where $N(\bar{V})$ and $M(\bar{V})$ are the stable proper coprime transfer functions satisfying $G_{pa}(\bar{V}) = N(\bar{V})M(\bar{V})^{-1}$. Then its state-space realisation is

$$\mathbf{G}_{aw}(\bar{V}) \stackrel{s}{=} \left[\begin{array}{c|c} \mathbf{A}_{pa}(\bar{V}) + \mathbf{B}_p\mathbf{F}(\bar{V}) & \mathbf{B}_p \\ \hline \mathbf{F}(\bar{V}) & 0 \\ \mathbf{C}_p & 0 \end{array}\right] \tag{5.44}$$

where $\mathbf{F}(\bar{V})$ is a state-feedback gain. To ensure quadratic stability of the closed-loop system during saturation and to minimise the effect of y_{aw} on the controller input e, the following condition is required:

$$\left\|M(\bar{V}) - 1\right\|_{\mathcal{L}_2} < 1, \left\|N(\bar{V})\right\|_{\mathcal{L}_2} < \mu, \tag{5.45}$$

which is satisfied if $\|\mathbf{G}_{aw}\|_{\mathcal{L}_2} < \mu$ with $\mu \leq 1$. To fulfil this condition, first solve an optimisation problem offline: minimising $\mu\left(\mathbf{Q}, \mathbf{H}_j\right)$ $(j = 1, 2)$ subject to

$$\begin{bmatrix} \mathbf{A}_{pa}(\theta_j)\mathbf{Q} + \mathbf{B}_p\mathbf{H}_j + (\star) & \star & \star & \star \\ \mathbf{B}_p^T & -\mu & \star & \star \\ \mathbf{H}_j & 0 & -\mu & \star \\ \mathbf{C}_p\mathbf{Q} & 0 & 0 & -\mu \end{bmatrix} < 0,$$
$$\mathbf{Q} = \mathbf{Q}^T > 0, \mu \leq 1. \tag{5.46}$$

Then $\mathbf{F}(\bar{V})$ is obtained at the vertex θ_j: $\mathbf{F}(\theta_j) = \mathbf{H}_j\mathbf{Q}^{-1}$. $\bar{V}(t)$ is measured online to derive the AW compensator as

$$\mathbf{G}_{aw}(\bar{V}) \stackrel{s}{=} \sum_{j=1}^{2} \alpha_j \left[\begin{array}{c|c} \mathbf{A}_{pa}(\theta_j) + \mathbf{B}_p\mathbf{F}(\theta_j) & \mathbf{B}_p \\ \hline \mathbf{F}(\theta_j) & 0 \\ \mathbf{C}_p & 0 \end{array}\right]. \tag{5.47}$$

The optimisation tools Sedumi [130] and YALMIP [131] are used to solve the optimisation problems. Then the LPV pitch controller and its AW compensator are derived. Although they are designed for the case that the scheduling parameter $\bar{V}$ varies in Region 2, they actually work effectively in the entire operating range of the HWT. When $\bar{V}$ falls outside Region 2, they choose the state-space data at either the vertex θ_1 or θ_2 whichever is closer to $\bar{V}$. $\bar{V}$ is estimated by a nacelle-based pulsed LIDAR simulator developed below.

5.4.3 LIDAR Wind Preview

There are a few technologies offering remote fluid measurement, including LIDAR, SODAR (SOnic Detection And Ranging), Laser Doppler Anemometry (LDA) or Laser Doppler Velocimetry (LDV), and Particle Imaging Velocimetry (PIV). Having said that, LIDAR is the only deployable method on wind turbines for wind speed measurement [132].

An atmospheric LIDAR transmits a laser beam into the atmosphere and receives the light backscattered by aerosols transported by the wind. Since the wind moves towards the LIDAR, there exists a change between the frequencies of the transmitted laser and the received light. This effect is the so-called Doppler shift described by

$$|\delta f| = \frac{2v_{los}}{c_{li}} f_{li} = \frac{2v_{los}}{\lambda_{li}} \tag{5.48}$$

where c_{li} is the speed of light (3e8 m/s), f_{li} is the transmitted laser frequency, and λ_{li} is the transmitted laser wavelength. The LIDAR photodetector superimposes the received signal on a portion of the original laser beam. $|\delta f|$ is the absolute value of the beat frequency extracted from the derived superimposition. According to (5.48), through observing $|\delta f|$, the LIDAR measures the line-of-sight (LOS) wind speed v_{los} which is the component of the wind speed vector in the laser beam direction.

LIDAR systems can be either continuous wave (CW) or pulsed. A CW LIDAR determines v_{los} at a specific point ahead of it through focusing its transmitted laser beam at that point. A pulsed LIDAR cyclically emits a laser pulse which passes several range gates (the distances measured by the LIDAR sensor), so it simultaneously takes samples at multiple points along the laser beam [133]. Taking advantage of this feature, Schipf et al. [9] optimised the scan trajectory of a nacelle-mounted pulsed LIDAR for the NREL offshore 5-MW baseline turbine model, as illustrated in Figure 5.10. The LIDAR scans a circle in 1.6 seconds, with 8 points at each of the 5 measurement distances $x_{i,\Upsilon}$ $(i = 1, 2, \ldots, 5)$ distributing equally between $x_{1,\Upsilon} = 63$ m and $x_{5,\Upsilon} = 189$ m. The half-opening angle of the laser beam is $\alpha_l = 16.7°$.

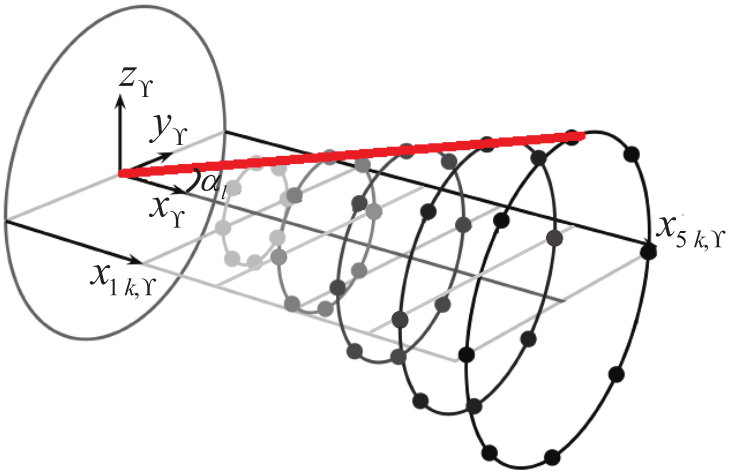

Figure 5.10: Circular pulsed LIDAR scan trajectory optimised by Schipf et al. [9] for the NREL offshore 5-MW baseline turbine model. The thick red line represents the laser beam.

Now a nacelle-mounted pulsed LIDAR simulator is developed employing the scan trajectory shown in Figure 5.10 to scan the turbulent three-dimensional wind field generated by NREL TurbSim (see Section 2.1) for the acquisition of the LOS wind speed during the FAST simulation. In Section 2.2, the coordinate systems $\mathcal{I}$ and $\mathcal{N}$ used by FAST are presented. The position of the LIDAR COM (centre of mass) is $\begin{bmatrix} 0\,m & 0\,m & 92.1\,m \end{bmatrix}^T$ in $\mathcal{I}$. The LIDAR coordinate system is denoted by Υ which is fixed on the nacelle so that it moves with the nacelle. It has the origin at the LIDAR COM and the set of orthogonal axes $\mathbf{x}_\Upsilon, \mathbf{y}_\Upsilon, \mathbf{z}_\Upsilon$ parallel with $\mathbf{x}_\mathcal{N}, \mathbf{y}_\mathcal{N}, \mathbf{z}_\mathcal{N}$. The nacelle IMU in FAST is specified to be at the LIDAR COM, and thus the nacelle IMU motion data outputted by FAST are equivalent to the LIDAR motion data with respect to $\mathcal{I}$ represented by $\begin{bmatrix} dx_{\Upsilon,\mathcal{I}} & dy_{\Upsilon,\mathcal{I}} & dz_{\Upsilon,\mathcal{I}} \end{bmatrix}^T$ (three-dimensional LIDAR displacement) and $\begin{bmatrix} \dot{dx}_{\Upsilon,\mathcal{I}} & \dot{dy}_{\Upsilon,\mathcal{I}} & \dot{dz}_{\Upsilon,\mathcal{I}} \end{bmatrix}^T$ (three-dimensional LIDAR velocity). Then the real-time position of the LIDAR COM in $\mathcal{I}$ is derived:

$$\begin{bmatrix} x_{\Upsilon,\mathcal{I}} & y_{\Upsilon,\mathcal{I}} & z_{\Upsilon,\mathcal{I}} \end{bmatrix}^T = \begin{bmatrix} 0\,m & 0\,m & 92.1\,m \end{bmatrix}^T + \begin{bmatrix} dx_{\Upsilon,\mathcal{I}} & dy_{\Upsilon,\mathcal{I}} & dz_{\Upsilon,\mathcal{I}} \end{bmatrix}^T. \quad (5.49)$$

The position of each measurement point in Figure 5.10 is denoted by $\begin{bmatrix} x_{ik,\Upsilon} & y_{ik,\Upsilon} & z_{ik,\Upsilon} \end{bmatrix}^T$ $(k = 1, 2, \ldots, 8)$ in Υ, or by $\begin{bmatrix} x_{ik,\mathcal{I}} & y_{ik,\mathcal{I}} & z_{ik,\mathcal{I}} \end{bmatrix}^T$ in $\mathcal{I}$. The former is fixed once the LIDAR configuration and scan trajectory are defined, while the latter varies as the LIDAR moves with the nacelle. $\begin{bmatrix} x_{ik,\Upsilon} & y_{ik,\Upsilon} & z_{ik,\Upsilon} \end{bmatrix}^T$ can

be transformed from Υ to $\mathcal{I}$ via

$$\mathbf{a}_{ik} = \mathbf{T}_{lt} \begin{bmatrix} x_{ik,\Upsilon} & y_{ik,\Upsilon} & z_{ik,\Upsilon} \end{bmatrix}^T \tag{5.50}$$

where $\mathbf{a}_{ik}$ symbolises $\begin{bmatrix} x_{ik,\Upsilon} & y_{ik,\Upsilon} & z_{ik,\Upsilon} \end{bmatrix}^T$ in $\mathcal{I}$, and

$$\mathbf{T}_{lt} = \begin{bmatrix} \mathbf{x}_{\mathcal{I}}\mathbf{x}_{\mathcal{N}} & \mathbf{x}_{\mathcal{I}}\mathbf{y}_{\mathcal{N}} & \mathbf{x}_{\mathcal{I}}\mathbf{z}_{\mathcal{N}} \\ \mathbf{y}_{\mathcal{I}}\mathbf{x}_{\mathcal{N}} & \mathbf{y}_{\mathcal{I}}\mathbf{y}_{\mathcal{N}} & \mathbf{y}_{\mathcal{I}}\mathbf{z}_{\mathcal{N}} \\ \mathbf{z}_{\mathcal{I}}\mathbf{x}_{\mathcal{N}} & \mathbf{z}_{\mathcal{I}}\mathbf{y}_{\mathcal{N}} & \mathbf{z}_{\mathcal{I}}\mathbf{z}_{\mathcal{N}} \end{bmatrix}. \tag{5.51}$$

All the elements in $\mathbf{T}_{lt}$ can be outputted by FAST in real time. Then one acquires

$$\begin{bmatrix} x_{ik,\mathcal{I}} & y_{ik,\mathcal{I}} & z_{ik,\mathcal{I}} \end{bmatrix}^T = \begin{bmatrix} x_{\Upsilon,\mathcal{I}} & y_{\Upsilon,\mathcal{I}} & z_{\Upsilon,\mathcal{I}} \end{bmatrix}^T + \mathbf{a}_{ik}. \tag{5.52}$$

Besides, the normalised vector of $\mathbf{a}_{ik}$ (equal among the points along a same laser beam) is

$$\mathbf{a}_{n,k} = \begin{bmatrix} x_{n,ik} & y_{n,ik} & z_{n,ik} \end{bmatrix}^T = \frac{\mathbf{a}_{ik}}{|\mathbf{a}_{ik}|}. \tag{5.53}$$

Due to the pulse length, a pulsed LIDAR measures the LOS wind speed at a point relying on the LOS wind speeds along the entire laser beam that includes the point and on a range weighting function $f_{rw}(r)$ where r is the distance from the measurement point. Here a normalised Gaussian shape $f_{rw}(r)$ (see Figure 5.11) is used following Schipf et al. [9]:

$$f_{rw}(r) = \frac{1}{\sigma_a\sqrt{2\pi}} \exp\left(-\frac{r^2}{2\sigma_a^2}\right),\ \sigma_a = \frac{W_L}{2\sqrt{2\ln 2}}, \tag{5.54}$$

where $W_L = 30$ m is the full width at half maximum. Then the LOS wind speed at the kth point in the ith measurement distance $v_{los,ik}$ is calculated as

$$v_{los,ik} = \int_{-\infty}^{\infty} f_{rw}(r)\mathbf{a}_{n,k}^T \begin{bmatrix} u_{rik,\mathcal{I}} - \dot{d}x_{\Upsilon,\mathcal{I}} \\ v_{rik,\mathcal{I}} - \dot{d}y_{\Upsilon,\mathcal{I}} \\ w_{rik,\mathcal{I}} - \dot{d}z_{\Upsilon,\mathcal{I}} \end{bmatrix} \mathrm{d}r \tag{5.55}$$

in which $u_{rik,\mathcal{I}}$, $v_{rik,\mathcal{I}}$, and $w_{rik,\mathcal{I}}$ are the longitudinal, crosswise, and vertical wind components respectively, at the time instant t_s, the crosswise location $y_{rik,\mathcal{I}}$, and the vertical location $z_{rik,\mathcal{I}}$ in the wind field grid generated by TurbSim. It is evident from (5.55) that the LIDAR measures $v_{los,ik}$ with respect to Υ. Recall from Section 2.2 that FAST adopts Taylor's frozen turbulence hypothesis assuming that the turbulent

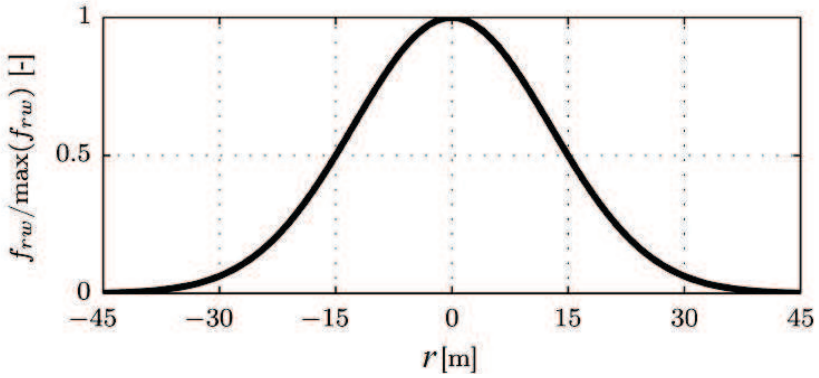

Figure 5.11: Normalised Gaussian shape range weighting function $f_{rw}(r)$ [9].

wind field moves with the mean hub-height wind speed $\bar{u}_{hub}$. Hence,

$$t_s = t_c + \frac{x_{ik,\mathcal{I}} + r x_{n,ik}}{\bar{u}_{hub}}, \tag{5.56}$$

$$y_{rik,\mathcal{I}} = y_{ik,\mathcal{I}} + r y_{n,ik}, \tag{5.57}$$

$$z_{rik,\mathcal{I}} = z_{ik,\mathcal{I}} + r z_{n,ik}, \tag{5.58}$$

where t_c is the current simulation time instant. With t_s, $y_{rik,\mathcal{I}}$ and $z_{rik,\mathcal{I}}$, $u_{rik,\mathcal{I}}$, $v_{rik,\mathcal{I}}$ and $w_{rik,\mathcal{I}}$ are derived through linear interpolation on the full-field gridded wind data from TurbSim.

To obtain the estimated steady rotor effective wind speed $\bar{V}$ for the LPV pitch controller and its AW compensator, $v_{los,ik}$ from the LIDAR needs processing. First the longitudinal wind component with respect to $\mathcal{I}$ at the kth point in the ith measurement distance (denoted by $u_{ik,\mathcal{I}}$) is calculated because the longitudinal wind component affects the rotor aerodynamics most [134]:

$$u_{ik,\mathcal{I}} = \frac{v_{los,ik} + x_{n,ik}\dot{x}_{\Upsilon,\mathcal{I}} + y_{n,ik}\dot{y}_{\Upsilon,\mathcal{I}} + z_{n,ik}\dot{z}_{\Upsilon,\mathcal{I}}}{x_{n,ik}}. \tag{5.59}$$

Then $u_{ik,\mathcal{I}}$ is averaged over the last circular scan:

$$u_{i,\mathcal{I}} = \frac{1}{8}\sum_{k=1}^{8} u_{ik,\mathcal{I}}. \tag{5.60}$$

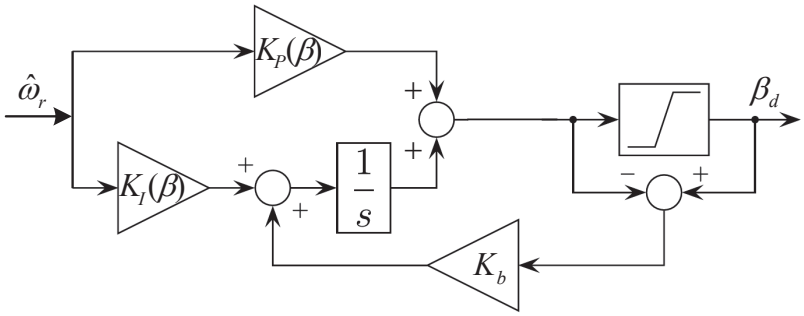

Figure 5.12: Configuration of the PI pitch controller with back-calculation AW compensation.

Subsequently, $u_{i,\mathcal{I}}$ is averaged after shifting them in time:

$$u_{\mathcal{I}} = \frac{1}{5}\sum_{i=1}^{5} u_{i,\mathcal{I}}\left(t_c - \frac{x_{i,\Upsilon}}{\bar{u}_{hub}}\right). \tag{5.61}$$

Finally, $\bar{V}$ is acquired by passing $u_{\mathcal{I}}$ through a second-order low-pass Butterworth filter to eliminate all uncorrelated frequencies. The cut-off frequency of the filter is 0.201 Hz which is the optimal value obtained by Schipf et al. [9] for the NREL offshore 5-MW baseline turbine model.

5.5 Simulation Study

In this section, performances of the $\mathcal{H}_\infty$ loop-shaping torque controller and LPV (with/without AW) pitch controller developed in Sections 5.3 and 5.4 are tested through simulation studies based on the transformed hydrostatic wind turbine (HWT) model (see Section 5.2) with the NREL OC3 monopile substructure. The performances of the LPV pitch controller are compared with a gain-scheduled PI pitch controller developed by Laguna [119] (tuned for a simplified HWT using the rotor of the NREL offshore 5-MW baseline wind turbine model) whose proportional and integral terms K_P and K_I are derived by substituting $N_g = 1$, $J_g = J_p = 3,680$ kg·m^2, $f_p = 0.6$ rad/s, and $\zeta_p = 0.7$ into (2.25). A back-calculation AW compensator (see Figure 5.12) is also designed for the above PI controller. The back-calculation coefficient K_b is tuned to be 0.5.

Two IEC full-field turbulent wind inputs together with a same irregular wave input are used during the simulations. The wind inputs are generated by NREL

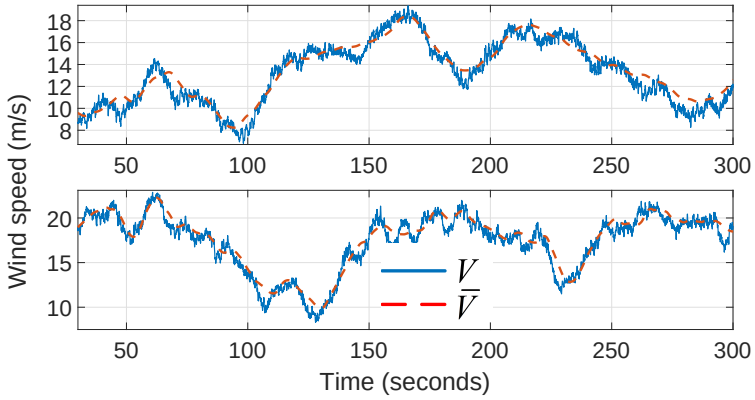

Figure 5.13: Actual and estimated (by LIDAR) rotor effective wind speeds (V and $\bar{V}$) under the turbulent wind input with a mean speed of 11.4 m/s (top) or 18 m/s (bottom) along with a wave input.

TurbSim using the IEC Kaimal spectral model with the Class 1 ETM (see Section 2.1.2). The mean hub-height longitudinal wind speeds are 11.4 m/s (rated speed) and 18 m/s for the two wind inputs respectively. The waves are irregularly generated based on the JONSWAP spectrum by FAST HydroDyn (see Section 2.2). The peak-spectral period and significant wave height of the incident waves are 10 seconds and 6 m, respectively.

Figure 5.13 shows the actual rotor effective wind speed V (computed by FAST AeroDyn) and its estimation $\bar{V}$ (by LIDAR). Clearly, the correlation between these two signals at low frequencies is good. This is very desirable since the low-frequency components contain the most wind power and affect the turbine most [135]. Besides, under either wind input, V covers both Regions 2 and 3 as shown in Figure 5.13. Figure 5.14 shows that the $\mathcal{H}_\infty$ loop-shaping torque controller tracks the pressure command P_{pd} (5.9) effectively. The LPV AW controller is used for pitch control here.

Tables 5.1 and 5.2 list the performances of 4 different pitch controllers under the two wind inputs respectively, along with the same wave input. The same $\mathcal{H}_\infty$ loop-shaping torque controller is used for these 4 cases. Here the standard deviation of the collective pitch rate is used to evaluate the damage on the blade bearings due to pitch activity [136]. The fore-aft and side-to-side damage equivalent loads (DEQLs) at the monopile base are computed using the NREL MLife code based on the time series of the fore-aft and side-to-side moments of the monopile base (see Section 2.3). As indicated in Tables 5.1 & 5.2, the PI AW controller and LPV controllers (with and without AW) attain much better overall performances than

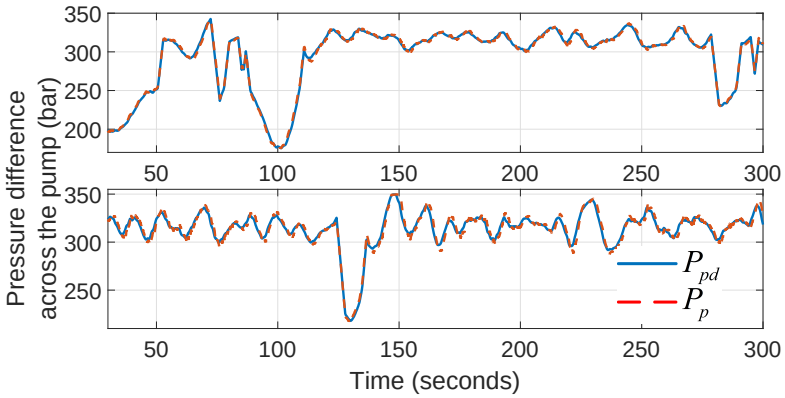

Figure 5.14: Pressure command P_{pd} and actual pressure difference across the pump P_p under the turbulent wind input with a mean speed of 11.4 m/s (top) or 18 m/s (bottom) along with a wave input.

Table 5.1: Performances of 4 pitch controllers under the turbulent wind input with a mean speed of 11.4 m/s along with a wave input. Changes w.r.t. the PI case are given in the brackets.

	PI	LPV	LPV AW	PI AW
Average power (kW)	4,309.8	4,398.0 (2.05%)	4,373.0 (1.47%)	4,331.8 (0.51%)
Standard deviation of power (kW)	750.34	697.93 (-6.98%)	695.45 (-7.32%)	724.94 (-3.39%)
Standard deviation of pitch rate (deg)	1.20	0.61 (-49.17%)	0.74 (-38.33%)	0.88 (-26.67%)
Fore-aft DEQL (kN·m)	20,614	7,854.0 (-59.11%)	6,197.7 (-69.93%)	7,772.6 (-62.29%)
Side-to-side DEQL (kN·m)	5,941.1	2,338.2 (-60.64%)	2,064.4 (-65.25%)	2,836.3 (-52.26%)

the PI controller developed by Laguna [119] under either wind input along with the wave input, including increased average power, improved regulation of the rotor speed & generator power, and considerably reduced damage on the blade bearings & monopile tower. Considering the two cases which have the AW compensator, the LPV AW controller is superior to the PI AW one especially in terms of mitigating the loads on the blade bearings & monopile tower. Figures 5.15 & 5.16 show the simulation results for the cases using three types of pitch controllers, which further

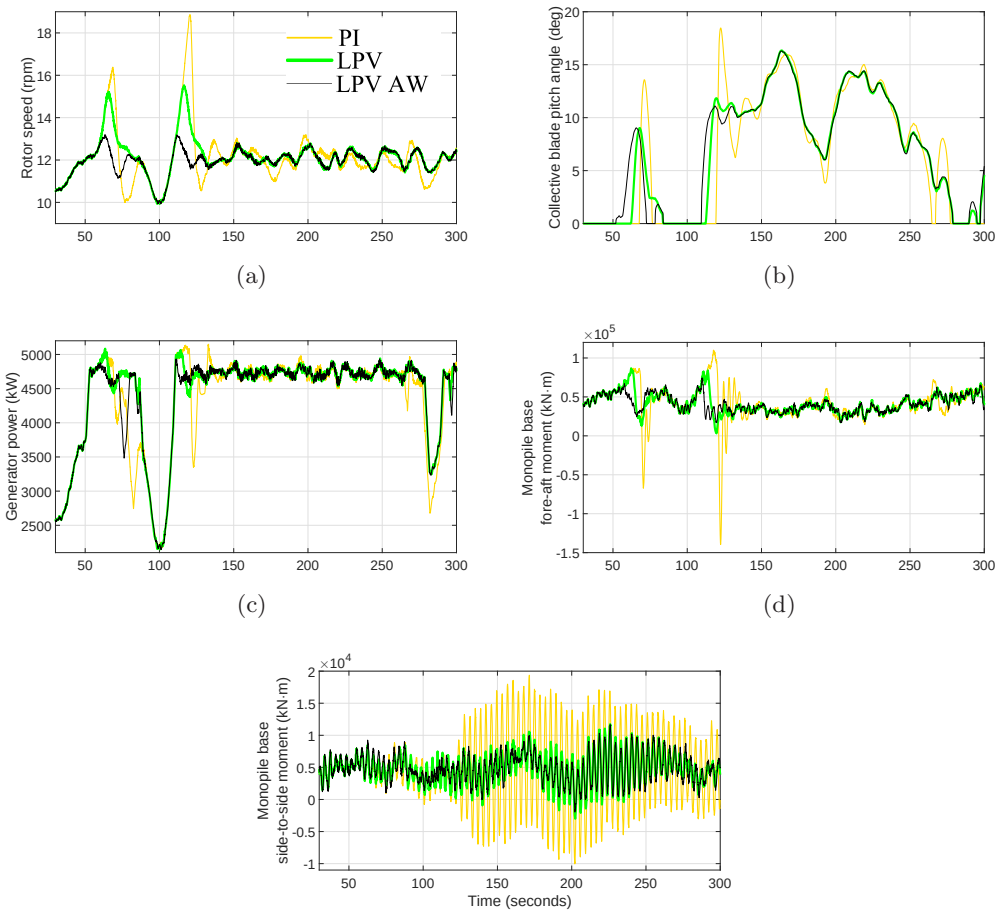

(a) (b) (c) (d) (e)

Figure 5.15: Simulation results under the turbulent wind input with a mean speed of 11.4 m/s along with a wave input. Figures 5.15a, 5.15b, 5.15c, 5.15d, and 5.15e depict the rotor speed, collective blade pitch angle, generator power, and monopile base fore-aft and side-to-side moments, respectively.

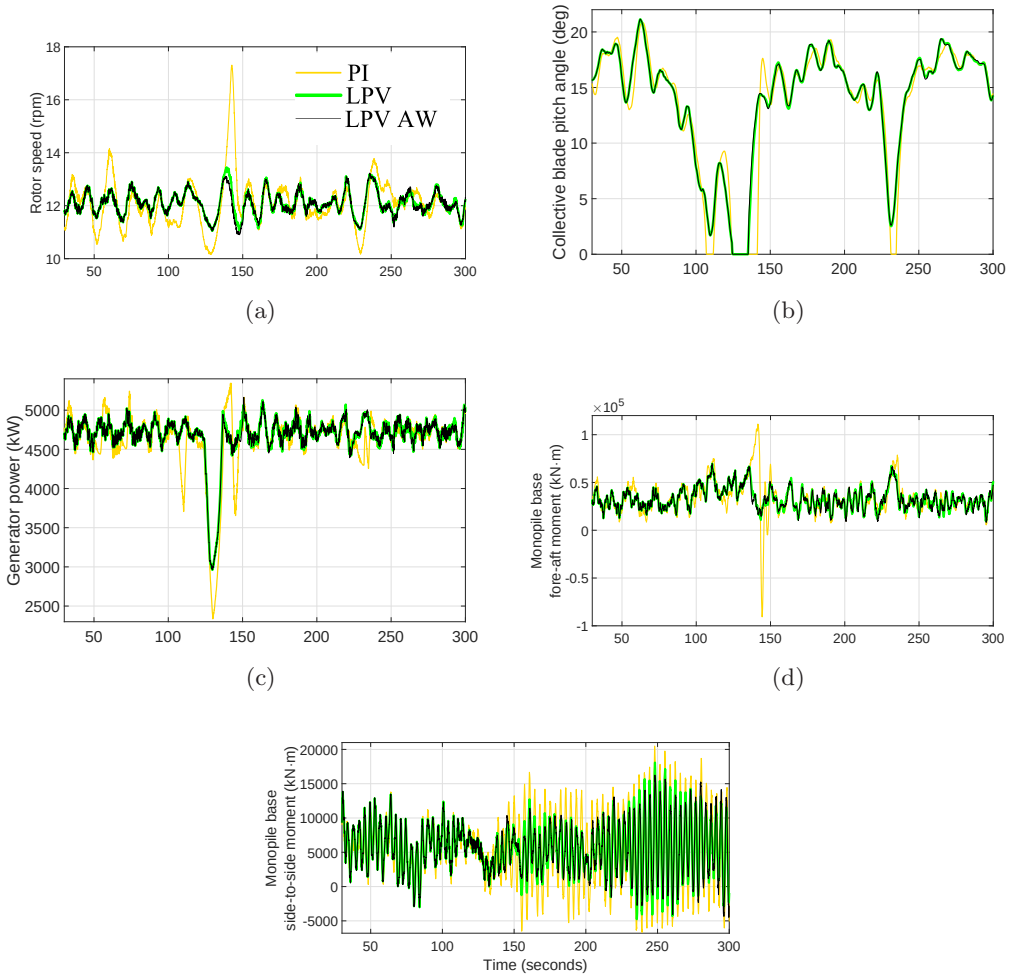

Figure 5.16: Simulation results under the turbulent wind input with a mean speed of 18 m/s along with a wave input. Figures 5.16a, 5.16b, 5.16c, 5.16d, and 5.16e depict the rotor speed, collective blade pitch angle, generator power, and monopile base fore-aft and side-to-side moments, respectively.

Table 5.2: Performances of 4 pitch controllers under the turbulent wind input with a mean speed of 18 m/s along with a wave input. Changes w.r.t. the PI case are given in the brackets.

	PI	LPV	LPV AW	PI AW
Average power (kW)	4,625.0	4,681.1 (1.21%)	4,679.8 (1.18%)	4,628.1 (0.067%)
Standard deviation of power (kW)	393.73	288.33 (-26.77%)	287.38 (-27.01%)	369.79 (-6.08%)
Standard deviation of pitch rate (deg)	1.11	0.79 (-28.83%)	0.81 (-27.03%)	0.99 (-10.81%)
Fore-aft DEQL (kN·m)	15,872	8,074.8 (-49.13%)	8,007.1 (-49.55%)	9,392.0 (-40.83%)
Side-to-side DEQL (kN·m)	5,764.0	4,336.1 (-24.77%)	4,173.7 (-27.59%)	5,748.7 (-0.27%)

verifies the conclusions from Tables 5.1 & 5.2. Besides, since the turbine generally works in Region 3 under the turbulent wind input with a mean speed of 18 m/s (see the bottom diagram of Figure 5.13), the superiority of the LPV controller (with/without AW) over the gain-scheduled PI controller in tracking the rated rotor speed and rated rotor power is more significant than that under the turbulent wind input with a mean speed of 11.4 m/s. In addition, it is noticeable from Figure 5.15 that significant rotor speed, generator power and tower loading variations occur due to pitch saturation during the transitions between Region 2 and 3 at about 55 second and 110 second (see the top diagram of Figure 5.13) for the cases using the PI and LPV (without AW) controllers, while the LPV AW pitch controller achieves much smoother responses. In Figure 5.16, during the transition at around 120 second (see the bottom diagram of Figure 5.13), much smoother responses of the rotor speed, generator power, and fore-aft moment of the monopile base are observed for both the LPV cases (with and without AW) compared with the gain-scheduled PI case. Furthermore, Figure 5.17 demonstrates that the LPV AW controller regulates the rotor speed much more tightly than its PI AW counterpart.

5.6 Conclusions

A novel power generation control design for a monopile hydrostatic wind turbine (HWT) was presented. The $\mathcal{H}_\infty$ loop-shaping torque control and LIDAR-based LPV

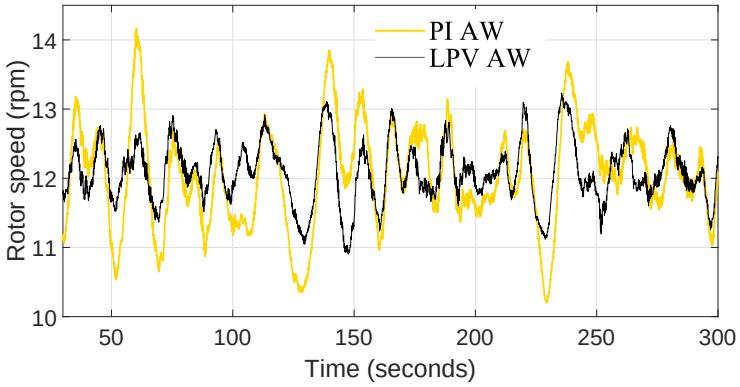

Figure 5.17: Rotor speed responses under the turbulent wind input with a mean speed of 18 m/s along with a wave input.

anti-windup (AW) pitch control mechanisms were proposed. For simulation studies, the NREL offshore 5-MW baseline turbine model (see Section 2.4) within FAST was transformed into a detailed aero-hydro-servo-elastic HWT simulation model. Then a torque controller and a blade pitch controller were designed for the transformed HWT with a monopile substructure. The simulation results showed that very good tracking behaviours have been achieved by the torque controller. Besides, the LPV (with or without AW) pitch control scheme attained much improved overall performances compared with the gain-scheduled PI pitch control system developed in [119], in terms of rotor speed regulation, power quality, and load reductions of the blade bearings & monopile tower. In addition, the LPV AW pitch controller had the smoothest responses during the transitions between Region 2 and 3 among the 3 controllers.

Chapter 6

Passive Vibration Control of An Offshore Floating Hydrostatic Wind Turbine

The hydraulic reservoir of a floating barge hydrostatic wind turbine (HWT) can be made use of to suppress pitch and roll motions of the barge. More specifically, the reservoir can be made into a shape of an annular rectangular to serve as a bidirectional tuned liquid column damper (BTLCD). This means a barge-motion damper is configured with negligible extra costs as an HWT needs a reservoir for fluid storage anyway. A barge HWT simulation model is developed through incorporating the coupled dynamics of the barge-reservoir system into the transformed HWT model (see Section 5.2) with the NREL ITI Energy barge substructure (see Section 2.4). Two simplified turbine-reservoir models are used to optimise parameters of the BTLCD reservoir, which describe the pitch and roll motions of the turbine-reservoir system respectively. The simulation results based on the barge HWT model show that the optimal BTLCD reservoir is very effective in mitigating the pitch and roll motions of the barge under realistic wind and wave excitations, which reduces the tower load and improves the power quality.

6.1 Introduction

There are several types of floating wind turbine substructures (e.g., the spar buoy, tension leg, and barge), among which the barge substructure (see Figure 1.2) is quite promising because of its simple design, fabrication, and installation [4]. However, barge rotational motions can not only cause large fluctuations in the rotor speed

and generator power, but also cause considerable load variations on the turbine, especially on the tower base [4]. Hence, it is of critical significance to develop control techniques to suppress these motions to improve energy capture, increase the tower's life expectancy, and enable the construction of lighter and cheaper wind turbine towers. As a spin-off application, the reservoir of the barge HWT can be made use of as a bidirectional tuned liquid column damper (BTLCD) to damp pitch and roll responses of the barge. The BTLCD reservoir is fixed on the floating barge.

A tuned liquid column damper (TLCD) is a U-shaped tube partially filled with liquid. Its vibration frequency is required to be tuned to a dominant modal frequency of the primary structure to suppress structural motions through the gravitational restoring force acting on the displaced liquid. Energy is dissipated through one or more orifices within the horizontal column of the TLCD [137]. The TLCD has been demonstrated to be effective in mitigating structural vibrations induced by winds, earthquakes, and waves [138, 139, 140, 141]. Explicit expressions of the optimal TLCD parameters were given in the literature [142, 143], but are only feasible for undamped primary structures with one degree of freedom (DOF) subject to white noise excitations. In other cases, numerical optimisation approaches were employed to optimise TLCDs to suppress structural translational motions [144, 143]. For structures in rotational motions, Xue et al. [145] validated that the TLCD can effectively damp structural pitch motions.

In terms of the TLCD's application in wind turbines, Colwell and Basu [146] placed a TLCD on top of a monopile wind turbine tower to demonstrate its feasibility for tower pitch suppression. Roderick [147] investigated to employ the TLCD to reduce the tower pitch vibrations of offshore wind turbines with three types of substructures, i.e., the fixed-bottom monopile, floating barge, and floating spar buoy. They optimised the TLCD parameters through a deterministic sweep which searched among a number of feasible combinations of parameter values to minimise the standard deviation of tower-top displacements. Their optimisation and simulation tests were both based on simplified turbine models consisting of TLCD dynamics, the first tower fore-aft bending DOF, and the substructure pitch displacement DOF (only for the cases of floating barge and spar buoy turbines). Coudurier et al. [148] designed a TLCD to damp the pitch motions of the MIT/NREL 5-MW barge wind turbine. They optimised the TLCD parameters through minimising the peak barge pitch response to harmonic wave excitations in a frequency range which was likely to excite the turbine pitch mode, by using the MATLAB optimisation function *fmincon*. Their optimisation was based on a simplified model containing TLCD dynamics and the barge pitch DOF. The simulation was based on a low-fidelity barge wind turbine

model containing the DOFs of the barge surge, heave, and pitch, and the TLCD dynamics. The results showed that the optimal TLCD performed well. Basu et al. [149] proposed a new type of TLCD for suppressing edgewise vibrations of offshore turbine blades.

Because the TLCD can only damp vibrations in one direction, bidirectional liquid dampers have been introduced in order to suppress structural vibrations in two perpendicular directions. Hitchcock et al. [150] designed a BTLCD comprising multiple TLCDs sharing a common horizontal liquid mass. Lee et al. [151] introduced a tuned liquid column and sloshing damper (TLCSD) which works as a TLCD and a tuned liquid sloshing damper (TLSD) in two perpendicular directions respectively. However, it is very difficult to tune TLSD parameters because the frequency and damping ratio of the TLSD increase non-linearly with the amplitude of the excitation. Rozas et al. [152] proposed a type of BTLCD which not only required less liquid but also had a simpler mathematical model which makes the parameter optimisation easier compared with the TLCSD. Here this type of BTLCD configuration is adapted for the reservoir to damp pitch and roll motions of the HWT barge in the fore-aft and side-to-side directions. Note that the BTLCD devised by Rozas et al. [152] was used to reduce vibrations in two perpendicular translational directions.

In order to conduct accurate simulation tests, the coupled dynamics of the barge-reservoir system are incorporated into the detailed aero-hydro-servo-elastic HWT model (developed in Section 5.2) with the NREL ITI Energy barge substructure. But the optimal BTLCD design is based on two simplified mathematical models which describe the fore-aft (pitch) and side-to-side (roll) motions of the turbine-reservoir system respectively. Since the fore-aft direction bears the largest loading from winds and waves, first the BTLCD reservoir parameters are optimised based on the model relevant to this direction. Then the remaining parameters are optimised based on the other model. The optimal parameters for the BTLCD reservoir are derived through multistart optimisation, i.e., running the MATLAB optimisation solver *fmincon* from multiple randomly selected starting points to obtain a minimum. The simulation results show that the optimal BTLCD reservoir achieves very good performances in mitigating barge pitch and roll motions of the barge HWT model, which reduces the tower-base damage load and improves the power quality.

The structure of the chapter is as follows. In Section 6.2, a barge HWT simulation model is developed through incorporating the coupled dynamics of the barge-reservoir system into the FAST code, based on the transformed HWT model

(see Section 5.2) with the NREL ITI Energy barge substructure. In Section 6.3, the parameters of the BTLCD reservoir are optimised based on two simplified mathematical models which describe the fore-aft and side-to-side motions of the turbine-reservoir system respectively. In Section 6.4, performances of the optimal BTLCD reservoir in suppressing barge pitch and roll motions are tested based on the barge HWT simulation model developed in Section 6.2.

6.2 Development of A Barge HWT Simulation Model with A BTLCD Reservoir

. In this section, a detailed aero-hydro-servo-elastic barge HWT simulation model is developed. In Section 5.2, the gearbox drivetrain of the NREL offshore 5-MW baseline turbine model is replaced with a typical HST drivetrain as shown in Figure 1.3. Now the coupled dynamics of the barge-reservoir system are incorporated into FAST. Note that here the same $\mathcal{H}_\infty$ loop-shaping design method is used for the torque controller to regulate the displacement of the hydraulic motor as the one proposed in Section 5.3. But a new pitch controller is designed, which is a gain-scheduled PI controller with the gains of the proportional and integral terms K_P and K_I derived by substituting $N_g = 1$, $J_g = J_p = 3,680$ kg·m^2, $f_p = 0.4$ rad/s, and $\zeta_p = 0.7$ into (2.25).

6.2.1 BTLCD Reservoir Configuration

The BTLCD reservoir on top of the HWT barge is illustrated in Figure 6.1. The BTLCD configuration proposed by Rozas et al. [152] is adopted for the reservoir. Recall from Section 2.2 that the barge has 6 motion DOFs in FAST containing 3 translational DOFs (surge, sway, and heave) and 3 rotational DOFs (roll, pitch, and yaw), as shown in Figure 6.1 where $\mathbf{x}_\mathcal{I}, \mathbf{y}_\mathcal{I}, \mathbf{z}_\mathcal{I}$ represents the set of orthogonal axes of the FAST inertial frame. The origin of $\mathbf{x}_\mathcal{I}, \mathbf{y}_\mathcal{I}, \mathbf{z}_\mathcal{I}$ is denoted as O which is the barge reference point defined in FAST. The BTLCD reservoir is composed of four vertical liquid columns (numbered 1, 3, 5, and 7) and four horizontal liquid columns (numbered 2, 4, 6, and 8). The columns numbered 1, 2, 3, 5, 6, and 7 form two TLCDs serving to damp barge pitch motions while the columns numbered 1, 7, 8, 3, 4, and 5 form two TLCDs to suppress barge roll motions.

α, β, and γ denote the rotational pitch, roll, and yaw displacements of the barge respectively. The set of orthogonal axes $\mathbf{l}, \mathbf{s}, \mathbf{h}$ of a coordinate system fixed on the barge translates and rotates with the barge, and coincides with $\mathbf{x}_\mathcal{I}, \mathbf{y}_\mathcal{I}, \mathbf{z}_\mathcal{I}$

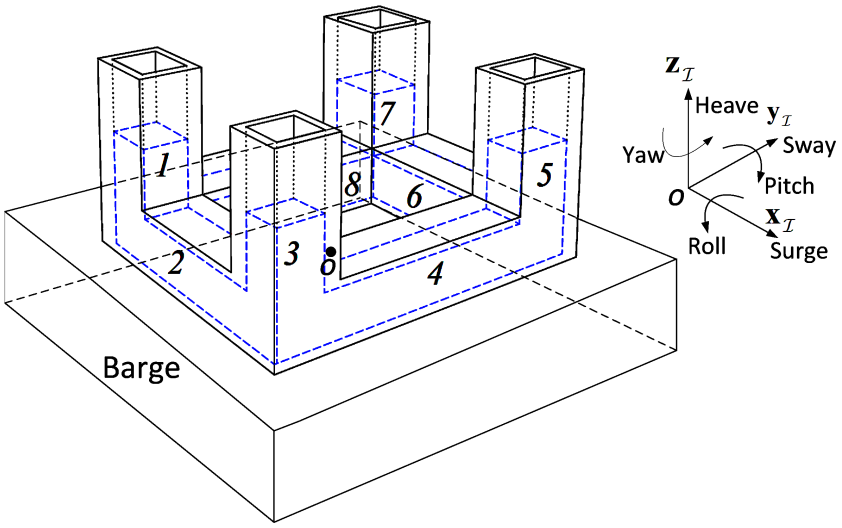

Figure 6.1: Barge with the BTLCD reservoir fixed on it.

when the barge is undisplaced. Jonkman [4] derived the transformation mapping from $\mathbf{x}_{\mathcal{I}}, \mathbf{y}_{\mathcal{I}}, \mathbf{z}_{\mathcal{I}}$ to $\mathbf{l}, \mathbf{s}, \mathbf{h}$:

$$\begin{bmatrix} \mathbf{l} & \mathbf{s} & \mathbf{h} \end{bmatrix}^T = \mathbf{T} \begin{bmatrix} \mathbf{x}_{\mathcal{I}} & \mathbf{y}_{\mathcal{I}} & \mathbf{z}_{\mathcal{I}} \end{bmatrix}^T \tag{6.1}$$

where

$$\mathbf{T} = \frac{1}{\Delta_3} \begin{bmatrix} \beta^2\Delta_2 + \alpha^2 + \gamma^2 & \gamma\Delta_1 + \beta\alpha\,(\Delta_2 - 1) & -\alpha\Delta_1 + \gamma\beta\,(\Delta_2 - 1) \\ -\gamma\Delta_1 + \alpha\beta\,(\Delta_2 - 1) & \beta^2 + \alpha^2\Delta_2 + \gamma^2 & \beta\Delta_1 + \alpha\gamma\,(\Delta_2 - 1) \\ \alpha\Delta_1 + \beta\gamma\,(\Delta_2 - 1) & -\beta\Delta_1 + \alpha\gamma\,(\Delta_2 - 1) & \alpha^2 + \beta^2 + \gamma^2\Delta_2 \end{bmatrix} \tag{6.2}$$

in which

$$\Delta_1 = \alpha^2 + \beta^2 + \gamma^2,\ \Delta_2 = \sqrt{1 + \Delta_1},\ \Delta_3 = \Delta_1\Delta_2. \tag{6.3}$$

The barge and BTLCD reservoir are symmetric with respect to the **lh**- and **sh**-planes.

Figure 6.2 is the three-view drawing of the BTLCD reservoir. A_x and L_x are the cross-section area and the length of the horizontal columns numbered 2 & 6, respectively. A_y and L_y are the cross-section area and the length of the horizontal columns numbered 4 & 8, respectively. A_v and L_v are the cross-section area and the length (when the liquid is undisplaced) of all the vertical columns. $u_k (k = 1, 2, \ldots, 8)$ is the liquid displacement in the column numbered k relative to the BTLCD reservoir. The liquid displacement in a vertical column can be related to

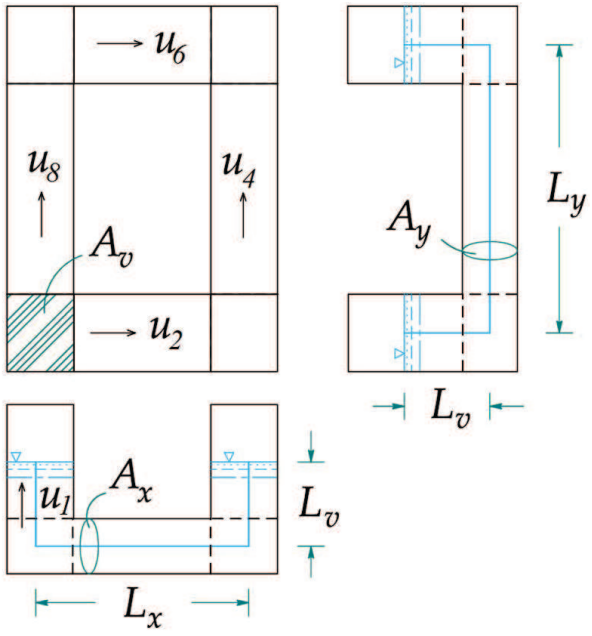

Figure 6.2: Three-view drawing of the BTLCD reservoir.

the liquid displacements in the adjacent horizontal columns, e.g.,

$$u_1 = -\left(r_x u_2 + r_y u_8\right) \tag{6.4}$$

where

$$r_x = A_x/A_v, \quad r_y = A_y/A_v \tag{6.5}$$

are the cross-section area ratios. There exists an orifice (generating a head loss) within each horizontal column of the BTLCD reservoir. The head loss coefficient in the columns numbered 2 and 6 is denoted by η_l. The head loss coefficient in the columns numbered 4 and 8 is denoted by η_s. The effective mass and natural frequency of the liquid in the columns numbered 1, 2, 3, 5, 6, and 7 which serves to damp barge pitch motions, are

$$M_{lp} = \rho_l A_v \left(4L_v + 2r_x L_x\right), \omega_{lp} = \sqrt{2g/L_{el}}, \tag{6.6}$$

respectively, where ρ_l is the liquid density, g is the acceleration of gravity, and $L_{el} = 2L_v + L_x/r_x$ is the equivalent length of the liquid for suppressing barge pitch motions. The effective mass and natural frequency of the liquid in the columns

numbered 1, 7, 8, 3, 4, and 5 (which serves to damp barge roll motions), are

$$M_{lr} = \rho_l A_v \left(4L_v + 2r_y L_y\right), \; \omega_{lr} = \sqrt{2g/L_{es}}, \tag{6.7}$$

respectively, where $L_{es} = 2L_v + L_y/r_y$ is the equivalent length of the liquid for mitigating barge roll motions. The total mass of the liquid in the BTLCD reservoir is

$$M_l = \rho_l A_v \left(4L_v + 2r_x L_x + 2r_y L_y\right). \tag{6.8}$$

6.2.2 Incorporating Coupled Dynamics of the Barge-reservoir System into the FAST Code

As described in Section 2.2, the FAST code uses Kane's dynamics (a direct result of Newton's law of motion) to obtain equations of motions (EOMs) for a wind turbine [4]. The time-domain EOMs of the whole baseline barge turbine are

$$M_{ij}\ddot{q}_j = f_i\left(\dot{\mathbf{q}}, \mathbf{q}\right), \tag{6.9}$$

where $\mathbf{q}$ is the set of turbine DOFs, q_j is the jth DOF, and M_{ij} is the (i, j)th component of the coefficient matrix for the accelerations of DOFs. f_i is the forcing function associated with q_i, and depends on $\mathbf{q}$ and $\dot{\mathbf{q}}$.

The dynamics of the BTLCD reservoir interact with the barge surge, sway, heave, pitch, roll, and yaw DOFs (denoted by $q_1, q_2, \ldots, q_6$, respectively). Thus, the extra forcing function f_m^r $(m = 1, 2, \ldots, 6)$ which depends on $u_1,\ u_2, \ldots,\ u_8$, $q_1,\ q_2, \ldots,\ q_6$ (along with their first and second derivatives) needs to be added to f_m in (6.9) when incorporating the BTLCD. A Simulink model of the BTLCD reservoir is created and coupled with the FAST code via the FAST/Simulink interface [65]. Using the input $\mathbf{U} = [q_1, q_2, \cdots, q_6, \dot{q}_1, \dot{q}_2, \cdots, \dot{q}_6, \ddot{q}_1, \ddot{q}_2, \cdots, \ddot{q}_6]$ from FAST, this Simulink model computes $u_1, u_2, \ldots, u_8$ along with their first and second derivatives, and $f_1^r, f_2^r, \ldots, f_6^r$. It also outputs the last six variables to FAST for the computation of $\mathbf{U}$.

The EOMs of the BTLCD reservoir (based on which the Simulink model of the BTLCD reservoir is created) and $f_1^r, f_2^r, \ldots, f_6^r$ are derived using Lagrange's equations which are the scalar equivalents of Newton's law of motion. The kinetic energy of the BTLCD reservoir is

$$T_l = \sum_{k=1}^{8} T_k \tag{6.10}$$

where T_k is the kinetic energy of the liquid column numbered k, and

$$T_1 = \frac{1}{2}\rho_l A_v \int_0^{L_v-\left(r_x u_2 + r_y u_8\right)} \mathbf{v}_1^2 \mathrm{d}h,\ T_2 = \frac{1}{2}\rho_l r_x A_v \int_{-Lx/2}^{Lx/2} \mathbf{v}_2^2 \mathrm{d}l, \tag{6.11}$$

in which h and l are respectively the coordinates of the liquid particle along the **h**- and **l**-axes. $\mathbf{v}_1$ and $\mathbf{v}_2$ are the velocities of any liquid particle in the columns numbered 1 and 2 relative to the inertial frame:

$$\begin{aligned}
&\mathbf{v}_1 = \dot{q}_1\mathbf{x}_\mathcal{I} + \dot{q}_2\mathbf{y}_\mathcal{I} + \dot{q}_3\mathbf{z}_\mathcal{I} + \dot{u}_1\mathbf{h} + \left(\dot{\alpha}\mathbf{y}_\mathcal{I} + \dot{\beta}\mathbf{x}_\mathcal{I} + \dot{\gamma}\mathbf{z}_\mathcal{I}\right) \times \left(-\tfrac{L_x}{2}\mathbf{l} - \tfrac{L_y}{2}\mathbf{s} + h\mathbf{h}\right)\\
&= \left[\dot{q}_1 + \dot{u}_1\mathbf{T}(3,1) + \dot{\alpha}\left(h\mathbf{T}(3,3) - \tfrac{L_x}{2}\mathbf{T}(1,3) - \tfrac{L_y}{2}\mathbf{T}(2,3)\right) +\right.\\
&\left.\dot{\gamma}\left(-h\mathbf{T}(3,2) + \tfrac{L_x}{2}\mathbf{T}(1,2) + \tfrac{L_y}{2}\mathbf{T}(2,2)\right)\right]\mathbf{x}_\mathcal{I} +\\
&\left[\dot{q}_2 + \dot{u}_1\mathbf{T}(3,2) + \dot{\beta}\left(-h\mathbf{T}(3,3) + \tfrac{L_x}{2}\mathbf{T}(1,3) + \tfrac{L_y}{2}\mathbf{T}(2,3)\right) +\right.\\
&\left.\dot{\gamma}\left(h\mathbf{T}(3,1) - \tfrac{L_x}{2}\mathbf{T}(1,1) - \tfrac{L_y}{2}\mathbf{T}(2,1)\right)\right]\mathbf{y}_\mathcal{I} +\\
&\left[\dot{q}_3 + \dot{u}_1\mathbf{T}(3,3) + \dot{\alpha}\left(-h\mathbf{T}(3,1) + \tfrac{L_x}{2}\mathbf{T}(1,1) + \tfrac{L_y}{2}\mathbf{T}(2,1)\right) +\right.\\
&\left.\dot{\beta}\left(h\mathbf{T}(3,2) - \tfrac{L_x}{2}\mathbf{T}(1,2) - \tfrac{L_y}{2}\mathbf{T}(2,2)\right)\right]\mathbf{z}_\mathcal{I},\\
&\mathbf{v}_2 = \dot{q}_1\mathbf{x}_\mathcal{I} + \dot{q}_2\mathbf{y}_\mathcal{I} + \dot{q}_3\mathbf{z}_\mathcal{I} + u_2\mathbf{l} + \left(\dot{\alpha}\mathbf{y}_\mathcal{I} + \dot{\beta}\mathbf{x}_\mathcal{I} + \dot{\gamma}\mathbf{z}_\mathcal{I}\right) \times \left(l\mathbf{l} - \tfrac{L_y}{2}\mathbf{s}\right)\\
&= \left[\dot{q}_1 + \dot{u}_2\mathbf{T}(1,1) + \dot{\alpha}\left(l\mathbf{T}(1,3) - \tfrac{L_y}{2}\mathbf{T}(2,3)\right) + \dot{\gamma}\left(-l\mathbf{T}(1,2) + \tfrac{L_y}{2}\mathbf{T}(2,2)\right)\right]\mathbf{x}_\mathcal{I} +\\
&\left[\dot{q}_2 + \dot{u}_2\mathbf{T}(1,2) + \dot{\beta}\left(-l\mathbf{T}(1,3) + \tfrac{L_y}{2}\mathbf{T}(2,3)\right) + \dot{\gamma}\left(l\mathbf{T}(1,1) - \tfrac{L_y}{2}\mathbf{T}(2,1)\right)\right]\mathbf{y}_\mathcal{I} +\\
&\left[\dot{q}_3 + \dot{u}_2\mathbf{T}(1,3) + \dot{\alpha}\left(-l\mathbf{T}(1,1) + \tfrac{L_y}{2}\mathbf{T}(2,1)\right) + \dot{\beta}\left(l\mathbf{T}(1,2) - \tfrac{L_y}{2}\mathbf{T}(2,2)\right)\right]\mathbf{z}_\mathcal{I},
\end{aligned} \tag{6.12}$$

where $\mathbf{T}$ is given in (6.2). $T_3, T_4, \ldots, T_8$ are derived in the similar way.

The point of zero potential energy is chosen to be the barge reference point O as shown in Figure 6.1. The potential energy of the BTLCD reservoir is

$$V_l = M_l g q_3 + \sum_{k=1}^{8} V_k \tag{6.13}$$

where V_k is the potential energy of the liquid column numbered k relative to O, and

$$\begin{aligned}
&V_1 = \rho_l A_v g\left(L_v + u_1\right)\left[-\tfrac{L_x}{2}\mathbf{l} - \tfrac{L_y}{2}\mathbf{s} + \tfrac{L_v+u_1}{2}\mathbf{h}\right]\mathbf{z}_\mathcal{I}\\
&= \rho_l A_v g\left(L_v + u_1\right)\left[-\tfrac{L_x}{2}\mathbf{T}(1,3) - \tfrac{L_y}{2}\mathbf{T}(2,3) + \tfrac{L_v+u_1}{2}\mathbf{T}(3,3)\right],\\
&V_2 = V_4 = V_6 = V_8 = 0.
\end{aligned} \tag{6.14}$$

V_3, V_5 and V_7 are derived in the similar way.

The total kinetic and potential energies of the HWT are respectively

$$T_t = T_l + T_b,\ V_t = V_l + V_b, \tag{6.15}$$

where T_b and V_b are the kinetic and potential energies of the HWT (excluding the BTLCD reservoir) respectively. Using Lagrange's equations, the EOMs of the whole HWT are

$$\frac{\mathrm{d}}{\mathrm{d}t}\left(\frac{\partial \mathcal{L}}{\partial \dot{q}_i}\right) - \frac{\partial \mathcal{L}}{\partial q_i} = f_{L,i},\ \mathcal{L} = T_t - V_t, \tag{6.16}$$

where $f_{L,i}$ is the non-conservative force acting on the DOF q_i where $i = 1, 2, \ldots, n+4$ (n is the number of turbine DOFs without the BTLCD reservoir). The extra DOFs q_{n+1}–q_{n+4} are equivalent to u_2, u_4, u_6, and u_8, respectively. They represent the liquid displacements in the four horizontal columns relative to the reservoir. Note that the dynamics associated with the terms $\frac{\mathrm{d}}{\mathrm{d}t}\left(\frac{\partial T_b}{\partial \dot{q}_j}\right)$, $\frac{\mathrm{d}}{\mathrm{d}t}\left(\frac{\partial V_b}{\partial \dot{q}_j}\right)$, $\frac{\partial T_b}{\partial q_j}$, $\frac{\partial Vb}{\partial q_j}$ and $f_{L1}, f_{L2}, \ldots, f_{Ln}$ have already been contained in the FAST code. Hence,

$$f_m^r = \frac{\partial\left(T_l - V_l\right)}{\partial q_m} - \frac{\mathrm{d}}{\mathrm{d}t}\left(\frac{\partial\left(T_l - V_l\right)}{\partial \dot{q}_m}\right). \tag{6.17}$$

The non-conservative forces $f_{L,n+1}$–$f_{L,n+4}$ acting on the DOFs q_{n+1}–q_{n+4} are the damping forces induced by the head loss of flow generated by the orifice within the four horizontal columns of the BTLCD reservoir:

$$\begin{aligned}
f_{L,n+1} &= -\tfrac{1}{2}\rho_l A_v r_x \eta_l \dot{q}_{n+1}\left|\dot{q}_{n+1}\right|, \\
f_{L,n+2} &= -\tfrac{1}{2}\rho_l A_v r_y \eta_s \dot{q}_{n+2}\left|\dot{q}_{n+2}\right|, \\
f_{L,n+3} &= -\tfrac{1}{2}\rho_l A_v r_x \eta_l \dot{q}_{n+3}\left|\dot{q}_{n+3}\right|, \\
f_{L,n+4} &= -\tfrac{1}{2}\rho_l A_v r_y \eta_s \dot{q}_{n+4}\left|\dot{q}_{n+4}\right|.
\end{aligned} \tag{6.18}$$

Then the EOMs of the BTLCD reservoir are derived as

$$\frac{\mathrm{d}}{\mathrm{d}t}\left(\frac{\partial\left(T_l - V_l\right)}{\partial \dot{q}_{n+w}}\right) - \frac{\partial\left(T_l - V_l\right)}{\partial q_{n+w}} = f_{L,n+w}, \tag{6.19}$$

where $w = 1, 2, 3, 4$.

6.3 Optimising the Parameters of the BTLCD Reservoir for Mitigating Barge Pitch and Roll Motions

The BTLCD reservoir is designed to suppress barge pitch and roll motions. Since the fore-aft direction suffers the largest loading from winds and waves, first the

reservoir parameters are optimised based on a simplified mathematical model Σ_p describing fore-aft (pitch) motions of the turbine-reservoir system. Then the remaining reservoir parameters are optimised based on a simplified model Σ_r describing side-to-side (roll) motions. Because the first tower fore-aft and side-to-side bending modes dominate the dynamic responses of the barge wind turbine tower, and the largest deflections for both modes occur at the tower top, either Σ_p or Σ_r can be treated as an inverted pendulum on a barge.

Σ_p is created by taking into account 3 DOFs: the liquid displacement q_{n+1}/q_{n+3} (u_2/u_6 in Figure 6.2) in the horizontal column numbered 2/6 relative to the reservoir (note that $q_{n+1} = q_{n+3}$ when only considering pitch motions of the turbine-reservoir system), the rotational pitch displacement of the pendulum tower from the $\mathbf{z}_{\mathcal{I}}$-axis denoted as q_7, and the barge pitch displacement DOF q_4. The kinetic and potential energies of Σ_p are respectively

$$\begin{aligned} &T_{op} = \tfrac{1}{2} I_{tp} \dot{q}_7^2 + \tfrac{1}{2} I_{bp} \dot{q}_4^2 + T_{lp}, \\ &V_{op} = \tfrac{1}{2} k_{tp} \left(q_7 - q_4\right)^2 + \tfrac{1}{2} \left(C_{hs} + C_{ml}\right) q_4^2 \\ &+ m_t g L_t \cos q_7 - m_p g L_p \cos q_4 + V_{lp}, \end{aligned} \tag{6.20}$$

where I_{tp} is the pitch inertia of the tower & RNA (rotor nacelle assembly), and I_{bp} is the barge pitch inertia. Both of them are about the barge reference point O. C_{hs} is the hydrostatic pitch restoring coefficient, and C_{ml} is the linearised pitch restoring coefficient from the mooring lines. m_t and k_{tp} are the total mass and equivalent pitch restoring coefficient of the tower & RNA, respectively. m_p is the barge mass, L_t is the distance from the mass centre of the tower & RNA to O, and L_p is the distance from the mass centre of the barge to O. T_{lp} and V_{lp} are T_l in (6.10) and V_l in (6.13) respectively, when setting $q_1, q_2, q_3, q_5, q_6, u_4\left(q_{n+2}\right), u_8\left(q_{n+4}\right)$ and their first derivatives to be zero, and substituting u_6 & $\dot{u}_6$ with u_2 & $\dot{u}_2$. Applying the Lagrange's equation approach, Σ_p is derived as

$$\frac{\mathrm{d}}{\mathrm{d}t}\left(\frac{\partial \mathcal{L}_{op}}{\partial \dot{q}_r}\right) - \frac{\partial \mathcal{L}_{op}}{\partial q_r} = f_{L,r},\ \mathcal{L}_{op} = T_{op} - V_{op}, \tag{6.21}$$

where $r = 4, 7, n+1$. $f_{L,n+1}$ is given in (6.18), and

$$\begin{aligned} f_{L,4} &= -A_{rad}\ddot{q}_4 - \left(B_{rad} + B_{vis}\right)\dot{q}_4 + d_{tp}\left(\dot{q}_7 - \dot{q}_4\right) + M_w, \\ f_{L,7} &= -d_{tp}\left(\dot{q}_7 - \dot{q}_4\right) + F_{aero} L_{hh}, \end{aligned} \tag{6.22}$$

where A_{rad} and B_{rad} are the added pitch inertia and pitch damping coefficient associated with the hydrodynamic radiation, respectively. B_{vis} is the linearised

Table 6.1: Values of some parameters in (6.20) and (6.22).

I_{tp}	3.55e9 kg·m^2
k_{tp}	1.47e10 N/m
C_{hs}	2.12e9 N/m
C_{ml}	2.62e7 N/m
A_{rad}	1.58e9 kg
B_{rad}	7.98e7 N·s/m
B_{vis}	5.43e4 N·s/m
d_{tp}	5e7 N·s/m
I_{tb}	4.28e9 kg·m^2
L_{tb}	7.01 m

pitch damping coefficient associated with the hydrodynamic viscous drag. M_w is the total wave-excitation pitch moment applied at O. d_{tp} is the equivalent pitch damping coefficient of the tower & RNA. L_{hh} is the hub height above the MSL, and F_{aero} is the aerodynamic rotor thrust acting on the hub. Assuming that the rotational pitch velocity of the pendulum tower $\dot{q}_7$ is low, F_{aero} can be described by a first-order Taylor series expansion at an operating point $V = \bar{V}$:

$$F_{aero} = \bar{F}_{aero} - \left(\frac{\partial F_{aero}}{\partial V}\right)_{\bar{V}} L_{hh}\dot{q}_7 \tag{6.23}$$

where $\bar{F}_{aero}$ is the steady aerodynamic rotor thrust at $V = \bar{V}$ [4].

In (6.20) and (6.22), the values of I_{bp}, m_t, m_p, L_t, L_p, and L_{hh} can be derived from Tables 2.1 and 2.4, while the values of other parameters are listed in Table 6.1. I_{tp} is obtained using the Aggregate Mass tool in ADAMS based on the ADAMS wind turbine dataset generated by the FAST-to-ADAMS preprocessor. C_{hs}, A_{rad}, and B_{rad} are respectively derived from the hydrostatic restoring, hydrodynamic-added-mass, and hydrodynamic-damping matrices created by WAMIT. k_{tp} and d_{tp} are computed based on two equivalent HWT models considering only the first tower fore-aft bending DOF and neglecting wind & wave effects:

$$\begin{aligned} \ddot{q}_7 &= -1.407\text{e}{-2}\dot{q}_7 - 4.001 q_7, \\ \ddot{q}_7 &= -\tfrac{d_{tp}}{I_{tp}}\dot{q}_7 + \tfrac{m_t g L_t - k_{tp}}{I_{tp}} q_7, \end{aligned} \tag{6.24}$$

which are derived from a FAST linearisation analysis and from Σ_p (6.21) respectively.

Then k_{tp} and d_{tp} are derived from

$$1.407\text{e}{-2} = \frac{d_{tp}}{I_{tp}},\ -4.001 = \frac{m_t g L_t - k_{tp}}{I_{tp}}. \tag{6.25}$$

B_{vis} and C_{ml} are calculated from the following HWT model which is obtained from a FAST linearisation analysis by considering only the barge pitch displacement DOF and neglecting wind & wave effects:

$$\ddot{q}_4 = -9.257\text{e}{-6}\dot{q}_4 - 0.2938 q_4 \tag{6.26}$$

where

$$-9.257\text{e}{-6} = -\frac{B_{vis}}{I_{tb} + A_{rad}},\ -0.2938 = \frac{(m_t + m_p) g L_{tb} - C_{hs} - C_{ml}}{I_{tb} + A_{rad}}. \tag{6.27}$$

I_{tb} is the pitch inertia of the whole turbine, and L_{tb} is the distance from the mass centre of the whole turbine to O. They are obtained using the Aggregate Mass tool in ADAMS and given in Table 6.1.

Now verify Σ_p (6.21) against the transformed 5-MW barge HWT model through structural simulations. Let both models oscillate freely from an initial barge pitch angle of 5°. Set F_{aero} and M_w in (6.22) to be 0, and employ an ODE (ordinary differential equation) solver in Matlab to simulate dynamics of Σ_p. Equivalently for the transformed barge HWT model, enable only its barge pitch displacement DOF and the first tower fore-aft bending DOF, and disable wind & wave effects. Figure 6.3 shows the simulation results of the barge pitch displacement q_4, tower-top displacement (TTD), and liquid displacement q_{n+1}/q_{n+3} using both models. Clearly they agree very well.

Now optimise the BTLCD reservoir parameters based on Σ_p. From (6.6) and (6.7), one gets

$$\rho_l A_v = \frac{M_{lp}}{4L_v + 2r_x L_x} = \frac{M_{lr}}{4L_v + 2r_y L_y}. \tag{6.28}$$

Introduce two mass ratios

$$\mu_p = \frac{M_{lp}}{M_{tb}},\ \mu_r = \frac{M_{lr}}{M_{tb}}, \tag{6.29}$$

where M_{tb} is the total mass of the HWT (excluding the reservoir). Combining (6.28) and (6.29), one obtains

$$r_y L_y = \frac{2L_v\left(\mu_r - \mu_p\right) + \mu_r r_x L_x}{\mu_p}. \tag{6.30}$$

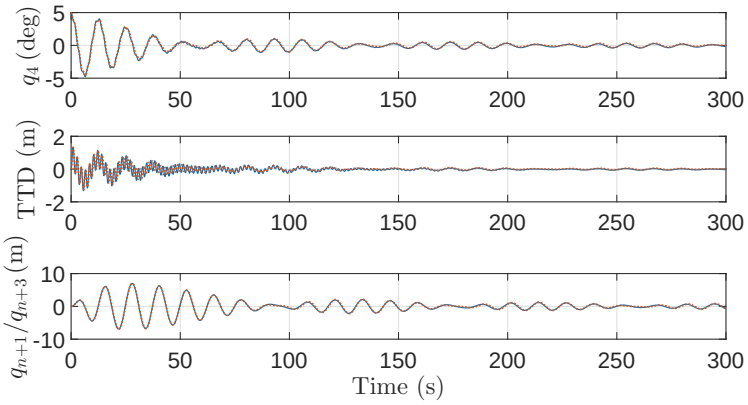

Figure 6.3: Barge pitch displacement q_4, tower-top displacement (TTD), and liquid displacement q_{n+1}/q_{n+3} obtained from simulations using the transformed 5-MW barge HWT model within FAST (blue solid lines) and the simplified turbine-reservoir model Σ_p (6.21) (red dotted lines).

Since large values of the mass ratios μ_p and μ_r are practically infeasible [153], $\mu_p = 6\%$ and $\mu_r = 4\%$ are set. $\mu_p > \mu_r$ is specified to provide more damping in the fore-aft direction than in the side-to-side direction. The BTLCD parameters to be optimised are

$$\mathbf{x}_{op} = \begin{bmatrix} L_x & L_v & r_x & \eta_l \end{bmatrix}. \tag{6.31}$$

The barge pitch mode has a natural frequency of about 0.0863 Hz (0.542 rad/s) [4]. Thus, the waves with peak spectral periods between 10 s and 15 s are most likely to excite that mode, causing large barge pitch motions. Besides, barge pitch motions grow as the wind speed increases. Therefore, the optimisation problem is to find an optimal $\mathbf{x}_{op}$ to minimise the maximal barge pitch displacement q_4 under specific loading conditions. The excitation loadings for Σ_p are extracted from the output data generated by simulations using the transformed barge HWT model within FAST. The value of $\bar{F}_{aero}$ in (6.23) is set to be 3.77e5 N which is the average aerodynamic rotor thrust on the transformed barge HWT under a steady hub-height longitudinal wind speed of 24 m/s (recall from Table 2.1 that the cut-out wind speed is 25 m/s) with all the tower and barge DOFs disabled. From Table 7-1 of the report [4], one gets $\left(\frac{\partial F_{aero}}{\partial V}\right)_{\bar{V}=24 \text{ m/s}} = 85.22\text{e}3$ N·s/m. Eleven 100-second time series are generated for M_w in (6.22), through FAST simulations using the transformed barge HWT model under the excitations of 11 irregular waves. The waves are modelled based on the JONSWAP spectrum, with the peak-spectral periods ranging from 10 s to 15 s in steps of 0.5 s. All the eleven waves have a same significant wave height of 5.5 m. Next 11 simulations are conducted on Σ_p using these M_w and $\bar{F}_{aero}$,

among which the maximal barge pitch displacement q_4 is obtained. Multistart optimisation is utilised to search for the optimal $\mathbf{x}_{op}$ (6.31). More specifically, the MATLAB sequential quadratic programming (SQP) algorithm *fmincon* is run from 40 randomly selected starting points within the bounds on the design parameters to obtain a local minimum. To ensure that the liquid remains in the four vertical columns of the BTLCD reservoir, a constraint is enforced:

$$r_x \cdot \max |q_{n+1}| \leq S_F L_v \tag{6.32}$$

where $r_x \cdot \max |q_{n+1}|$ is the maximal liquid displacement occurring in the vertical columns during all the eleven simulations. $S_F = 0.8$ is set to leave a margin in the vertical column, which may be used for damping barge roll motions. Besides, 1 m$\leq L_x \leq$ 40 m, 1 m$\leq L_v \leq$ 7 m, $0.1 \leq r_x \leq 10$, and $0 \leq \eta_l \leq 10$. The first two constraints are set to take into account the fact that the length of the horizontal columns should not exceed the barge length (40 m) and that the height of the reservoir should not be too large. Finally the optimal $\mathbf{x}_{op}$ is obtained:

$$\mathbf{x}_{op} = \begin{bmatrix} 30.15\,\text{m} & 7\,\text{m} & 0.51 & 2.24 \end{bmatrix}. \tag{6.33}$$

So the natural frequency of the liquid serving to damp barge pitch motions is 0.5166 rad/s (according to (6.6)) which is 95.31% of the barge pitch modal frequency of 0.542 rad/s.

Similarly, the following optimal values for the remaining parameters of the BTLCD reservoir are derived based on the simple model Σ_r which describes side-to-side (roll) motions of the turbine-reservoir system:

$$\mathbf{x}_{or} = \begin{bmatrix} L_y & r_y & \eta_s \end{bmatrix} = \begin{bmatrix} 18.43\,\text{m} & 0.3 & 1.46 \end{bmatrix}. \tag{6.34}$$

Note that $r_y L_y$ is a constant after $\mathbf{x}_{op}$ (6.31) is determined, according to (6.30). Therefore, actually the last two parameters have been optimised. And for the optimisation, $r_y \max |q_{n+2}| \leq 0.2 L_v$, 1 m$\leq L_y \leq$ 40 m, and $0 \leq \eta_s \leq 10$ are specified, where q_{n+2} (u_4) is the liquid displacement in the horizontal column numbered 4 relative to the BTLCD reservoir. From the parameters in (6.34), the natural frequency of the liquid serving to damp barge roll motions is derived as 0.5098 rad/s (according to (6.7)) which is 94.05% of the barge roll modal frequency (0.542 rad/s). Using (6.5), (6.28), (6.29), (6.33), and (6.34), the optimal BTLCD dimensions are given as follows. The cross-section area and length of the horizontal columns numbered 2 and 6 (see Figures 6.1 and 6.2) are $A_x = 3.49$ m^2 and $L_x = 30.15$ m. The cross-section

area and length of the horizontal columns numbered 4 and 8 are $A_y = 2.05$ m^2 and $L_y = 18.43$ m. The cross-section area and length (when the liquid is undisplaced) of all the vertical columns are $A_v = 6.85$ m^2 and $L_v = 7$ m. The optimal head loss coefficient in columns numbered 2 and 6 is $\eta_l = 2.24$ while the optimal head loss coefficient in columns numbered 4 and 8 is $\eta_s = 1.46$. Following (6.8), the total mass of the liquid in the BTLCD reservoir is 438,552 kg which is 6.66% of the HWT mass.

6.4 Simulation Study

FAST simulations are carried out based on the transformed 5-MW barge HWT model in both cases without and with the BTLCD configuration whose optimal parameters are given in (6.33) and (6.34). Here the simulations are conducted under two types of extreme events and two types of normal events. The two extreme events are for the tower-base fore-aft bending moment (Event E.1) and the side-to-side bending moment (Event E.2) respectively, which were recorded in the report [4]. The wind conditions in all the events are generated based on the IEC Kaimal Spectral Model with NTM in TurbSim (see Section 2.1.2). For Events E.1 and E.2, the mean hub-height longitudinal wind speeds are 22 m/s and 24 m/s respectively, and the turbulence intensity is category B. For the two normal events (Event N.1 and Event N.2), the mean hub-height longitudinal wind speeds are 9 m/s (below-rated) and 18 m/s (above-rated) respectively, and the turbulence intensity is category A. The wave conditions in all the events are generated by the HydroDyn module which is integrated into FAST based on the JONSWAP spectrum (see Section 2.2). For Events E.1 and E.2, the peak-spectral periods of the incident waves are 13.4 s and 15.5 s respectively, with the significant wave heights being 4.7 m and 5.5 m. For Events N.1 and N.2, the peak-spectral periods of the incident waves are 12 s and 11 s respectively, with the significant wave heights being 2 m and 4.5 m.

Figures 6.4 and 6.7 show the hub-height longitudinal wind speeds and the wave elevations in the two extreme events (Events E.1 and E.2). As shown in Figures 6.5 and 6.8, in both events, the barge pitch and roll displacements of the HWT with the BTLCD configuration are much smaller than the cases without the BTLCD configuration, which results in less fluctuations in the rotor speed and generator power. Due to the BTLCD configuration, the standard deviations (SDs) of the barge pitch and roll displacements reduce by 21.36% and 42.42% respectively in Event E.1, and decrease by 22.61% and 30.51% respectively in Event E.2. The absolute peaks of the barge pitch and roll displacements reduce by 11.25% and 39.34% respectively in

Table 6.2: Tower-base fore-aft and side-to-side DEQLs of the transformed NREL 5-MW barge HWT model in the cases without and with the BTLCD configuration under two extreme events for the tower-base fore-aft bending moment (Event E.1) and the side-to-side bending moment (Event E.2), as well as the load reduction ratios (in the brackets) by the BTLCD.

	Event E.1		Event E.2	
	Fore-aft DEQL (kN)	Side-to-side DEQL (kN)	Fore-aft DEQL (kN)	Side-to-side DEQL (kN)
Without BTLCD	83,435	25,131	121,910	32,045
With BTLCD	73,324 (12.11%)	18,195 (27.6%)	104,300 (14.45%)	25,756 (19.63%)

Event E.1, and decrease by 14.66% and 26.95% respectively in Event E.2. Besides, the SDs of the rotor speed and the generator power decrease by 12.05% and 14.98% respectively in Event E.1, and decrease by 14.45% and 12.38% respectively in Event E.2. It is clear from Figures 6.6 and 6.9 that the liquid remains in the BTLCD reservoir during these simulations.

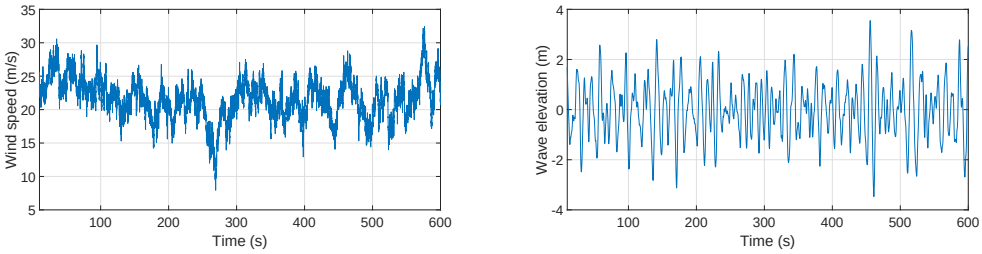

(a) (b)

Figure 6.4: The hub-height longitudinal wind speed and wave elevation in the extreme event for the tower-base fore-aft bending moment.

Table 6.2 summarises the fore-aft and side-to-side damage equivalent loads (DEQLs) at the tower base in both cases with and without the BTLCD configuration, during the above simulations for the two extreme events. MLife [67] is employed to calculate these DEQLs using the time-series of tower-base bending moments based on a rainflow counting algorithm. The tower-base DEQL reduction ratios due to the BTLCD configuration in Table 6.2 demonstrates that the optimal BTLCD reservoir can effectively reduce the tower loads.

Figures 6.10 and 6.13 show the hub-height longitudinal wind speeds and the

Table 6.3: Tower-base fore-aft and side-to-side DEQLs of the transformed NREL 5-MW barge HWT model in the cases without and with the BTLCD configuration under two normal events where the mean hub-height longitudinal wind speeds are 9 m/s (Event N.1) and 18 m/s (Event N.2) respectively, as well as the load reduction ratios (in the brackets) by the BTLCD.

	Event N.1		Event N.2	
	Fore-aft DEQL (kN)	Side-to-side DEQL (kN)	Fore-aft DEQL (kN)	Side-to-side DEQL (kN)
Without BTLCD	48,968	9,385.3	105,920	26,423
With BTLCD	43,894 (10.36%)	7,121.9 (24.12%)	91,703 (13.42%)	20,122 (23.85%)

wave elevations in the two normal events (Events N.1 and N.2). As illustrated in Figures 6.11 and 6.14, in both events, the barge pitch and roll displacements of the HWT with the BTLCD configuration are much smaller than the cases without the BTLCD configuration, which results in less fluctuations in the rotor speed and generator power. Due to the BTLCD configuration, the SDs of the barge pitch and roll displacements reduce by 18.78% and 36.14% respectively in Event N.1 where the mean hub-height longitudinal wind speed is 9 m/s, and decrease by 22.95% and 34.86% respectively in Event N.2 where the mean hub-height longitudinal wind speed is 18 m/s. The absolute peaks of the barge pitch and roll displacements reduce by 13.22% and 28.85% respectively in Event N.1, and decrease by 19.32% and 25.16% respectively in Event N.2. In addition, the SDs of the rotor speed and the generator power decrease by 13.30% and 14.71% respectively in Event N.2. The BTLCD reservoir does not change the SDs of the rotor speed and generator power very much in Event N.1 because in this event the wind speed is below-rated during most of the simulation period (see Figure 6.10a) and therefore the turbine is controlled to capture maximum power rather than track a fixed rotor speed and a fixed rotor power. It is clear from Figures 6.12 and 6.15 that the liquid remains in the BTLCD reservoir during these simulations.

Table 6.3 summarises the fore-aft and side-to-side DEQLs at the tower base in both cases with and without the BTLCD configuration, during the above simulations for the two normal events. The tower-base DEQL reduction ratios due to the BTLCD configuration in Table 6.3 demonstrates that the optimal BTLCD reservoir can effectively reduce the tower loads.

6.5 Conclusions

The reservoir of a barge HWT was used as a BTLCD to damp pitch and roll responses of the barge substructure. To test performances of this spin-off application of the reservoir, a detailed aero-hydro-servo-elastic barge HWT simulation model with a BTLCD reservoir was developed. For this purpose, the FAST code was modified to incorporate the coupled dynamics of the barge-reservoir system into the transformed HWT model (obtained in Section 5.2) with the NREL ITI Energy barge substructure (see Section 2.4) by using the Lagrange's equation approach. Multi-start optimisation was applied to derive the optimal parameters of the BTLCD reservoir based on two simplified mathematical models which describe pitch and roll motions of the turbine-reservoir system respectively. Through simulation studies under two types of extreme events and two types of normal events, the BTLCD reservoir was shown to effectively suppress the barge pitch and roll motions, which mitigated the damage loads of the tower, and reduced the fluctuations of the rotor speed and generator power.

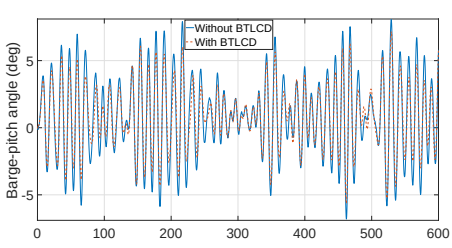

(a)

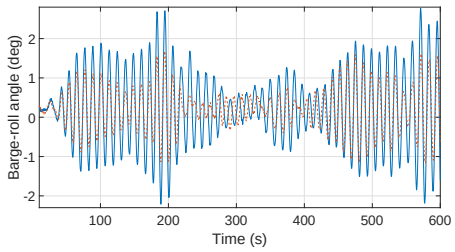

(b)

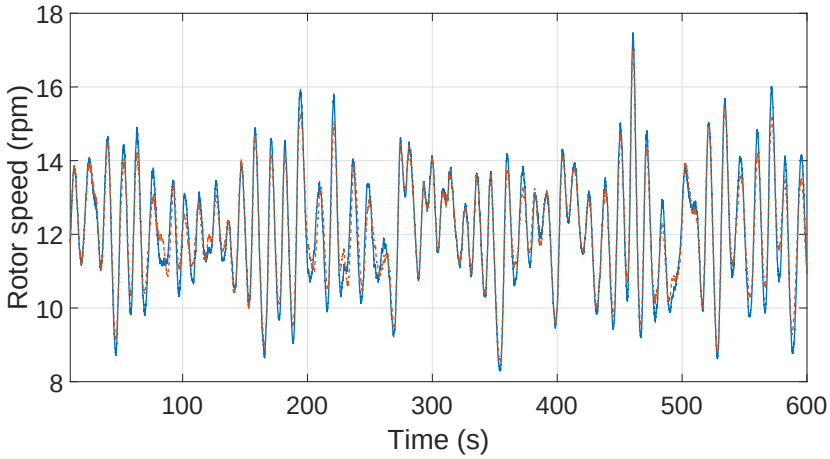

(c)

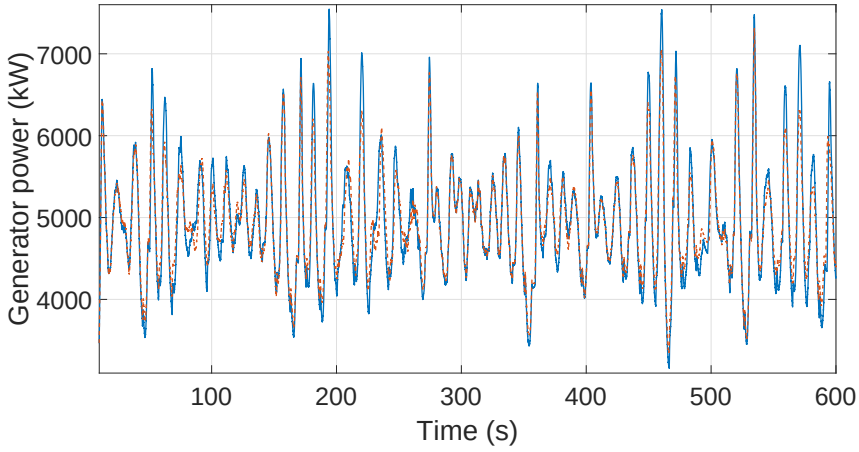

(d)

Figure 6.5: Simulations results for the transformed NREL 5-MW barge HWT model in the cases without (blue solid lines) and with (red dash lines) the BTLCD configuration, in the extreme event for the tower-base fore-aft bending moment. Figure 6.5a, 6.5b, 6.5c and 6.5d depict the barge pitch and roll displacements, the rotor speed and the generator power,respectively.

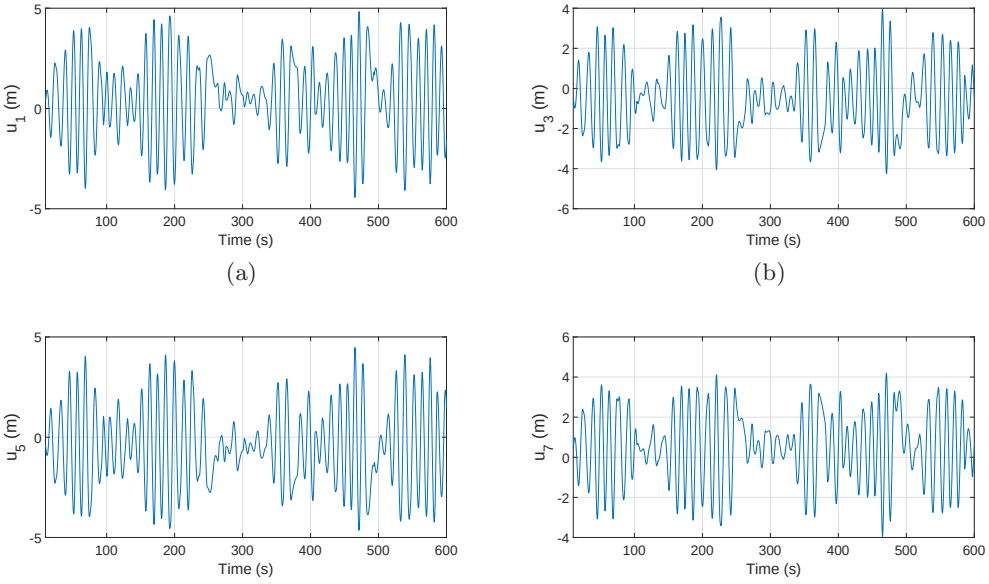

Figure 6.6: Liquid displacements u_1, u_3, u_5 and u_7 in the four vertical columns numbered 1, 3, 5 and 7 of the BTLCD reservoir for the transformed NREL 5-MW barge HWT model with the BTLCD configuration, in the extreme event for the tower-base fore-aft bending moment.

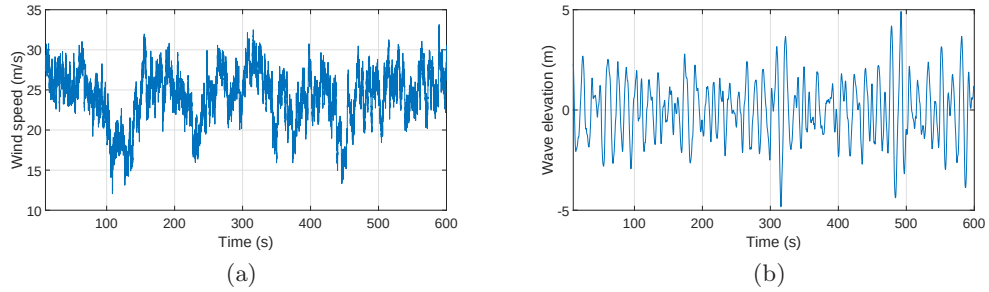

Figure 6.7: The hub-height longitudinal wind speed and wave elevation in the extreme event for the tower-base side-to-side bending moment.

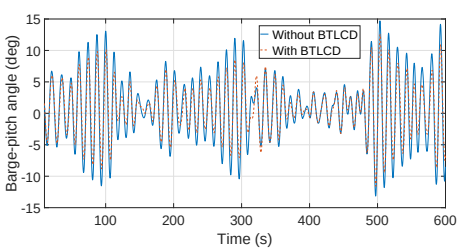

(a)

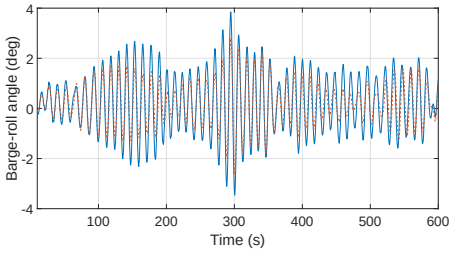

(b)

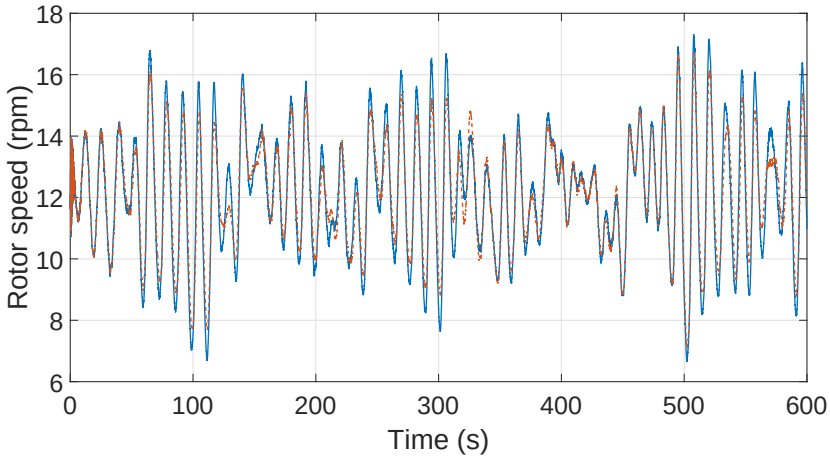

(c)

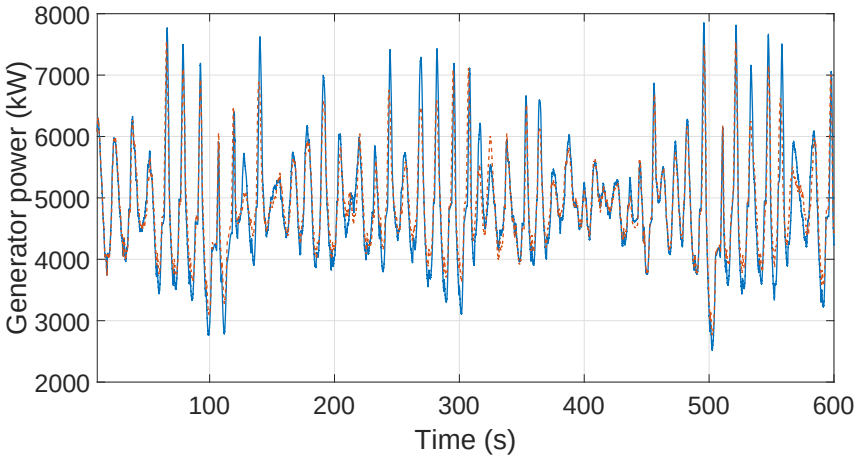

(d)

Figure 6.8: Simulations results for the transformed NREL 5-MW barge HWT model in the cases without (blue solid lines) and with (red dash lines) the BTLCD configuration, in the extreme event for the tower-base side-to-side bending moment. Figure 6.8a, 6.8b, 6.8c and 6.8d depict the barge pitch and roll displacements, the rotor speed and the generator power,respectively.

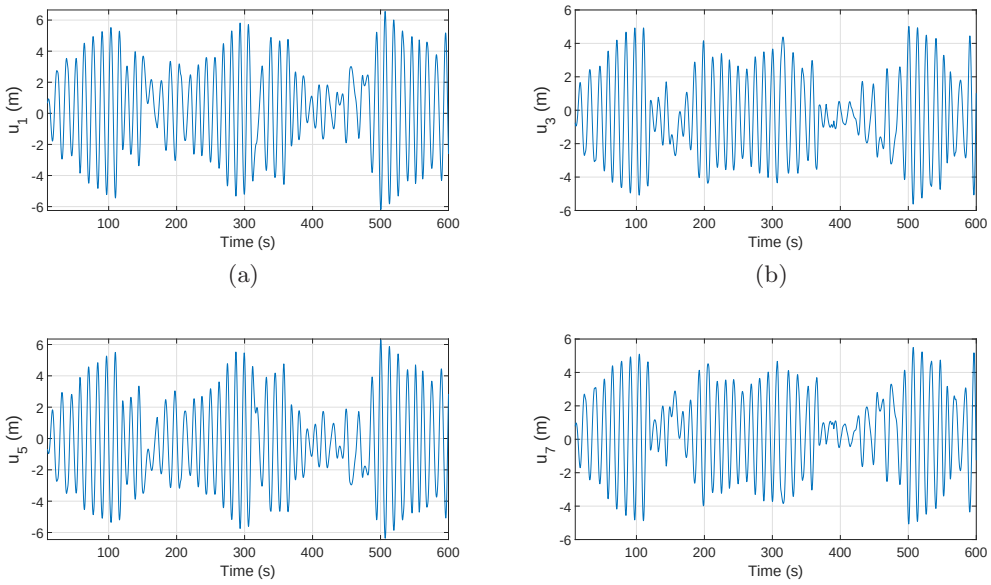

Figure 6.9: Liquid displacements u_1, u_3, u_5 and u_7 in the four vertical columns numbered 1, 3, 5 and 7 of the BTLCD reservoir for the transformed NREL 5-MW barge HWT model with the BTLCD configuration, in the extreme event for the tower-base side-to-side bending moment.

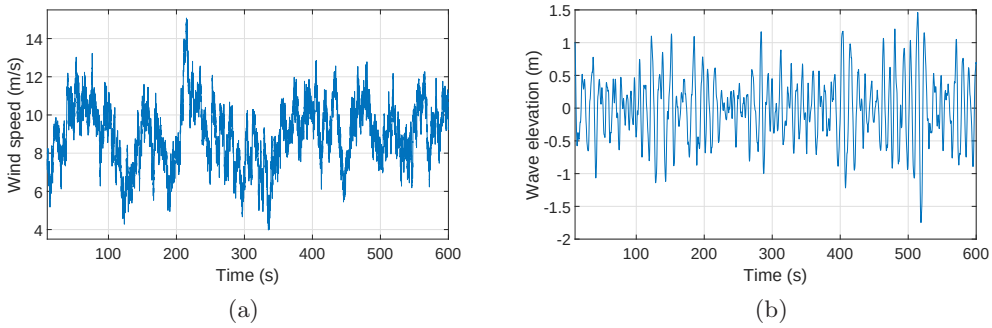

Figure 6.10: The hub-height longitudinal wind speed and wave elevation in the normal event where the mean hub-height longitudinal wind speed is 9 m/s.

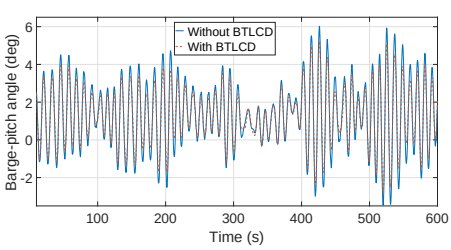

(a)

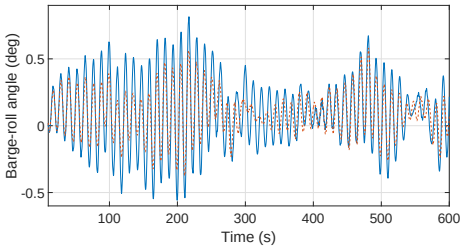

(b)

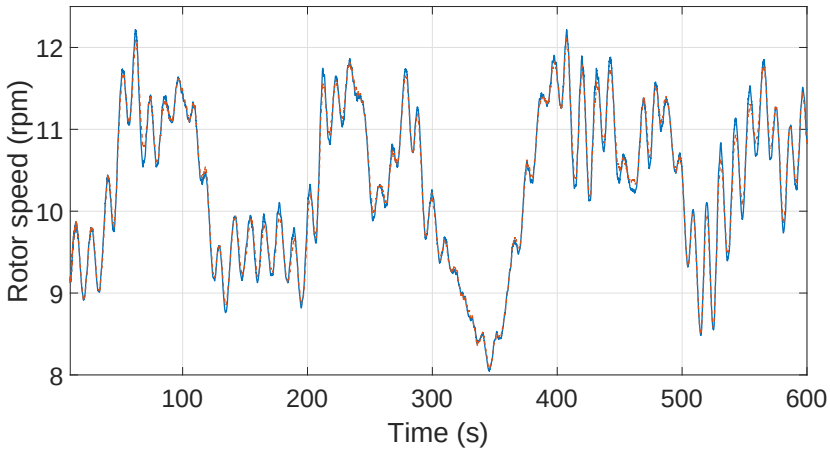

(c)

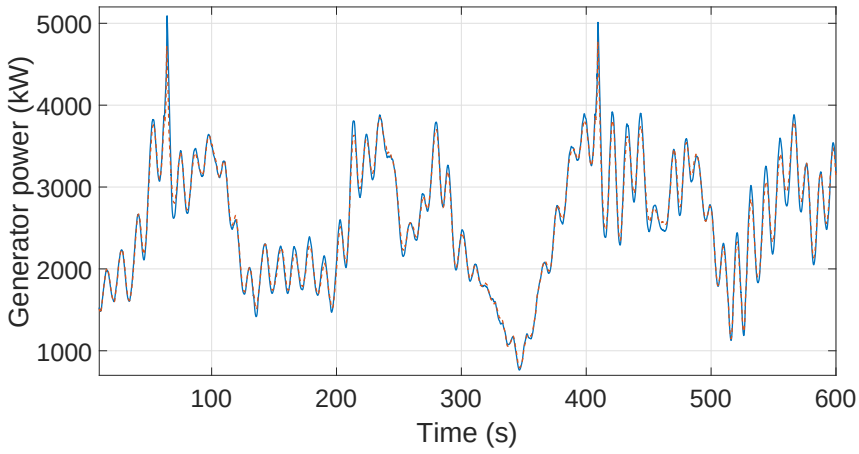

(d)

Figure 6.11: Simulations results for the transformed NREL 5-MW barge HWT model in the normal event where the mean hub-height longitudinal wind speed is 9 m/s. Figures 6.11a, 6.11b, 6.11c and 6.11d depict the barge pitch and roll displacements, the rotor speed, and the generator power, respectively.

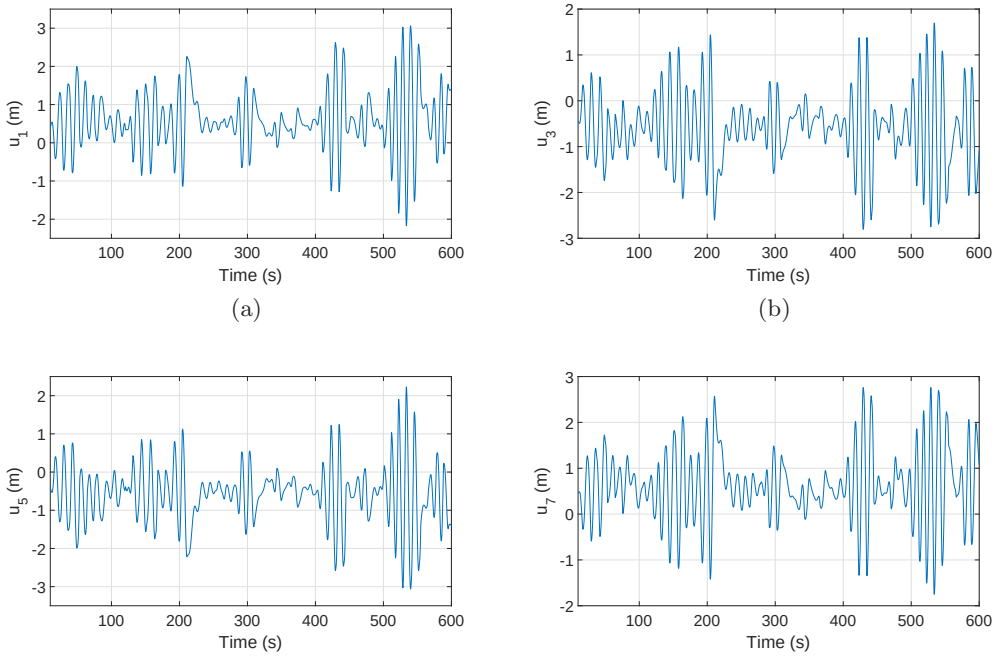

Figure 6.12: Liquid displacements u_1, u_3, u_5 and u_7 in the four vertical columns numbered 1, 3, 5 and 7 of the BTLCD reservoir for the transformed NREL 5-MW barge HWT model with the BTLCD configuration, in the normal event where the mean hub-height longitudinal wind speed is 9 m/s.

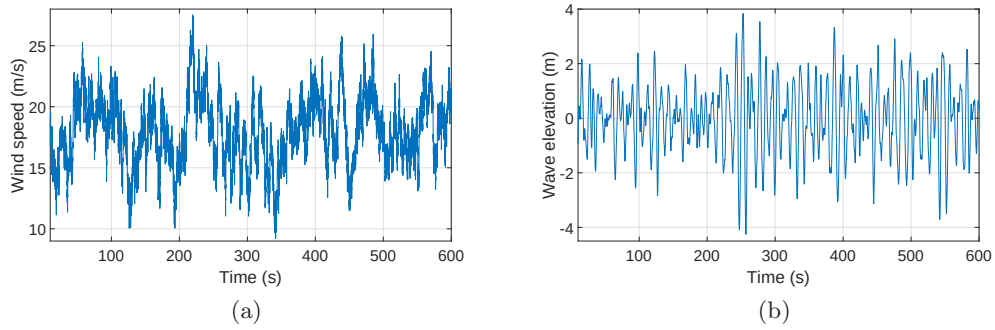

Figure 6.13: The hub-height longitudinal wind speed and wave elevation in the normal event where the mean hub-height longitudinal wind speed is 18 m/s.

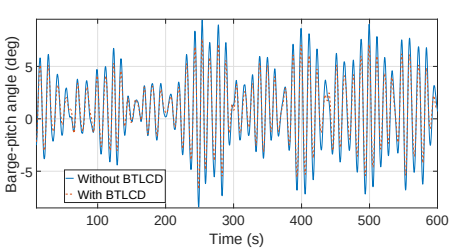

(a)

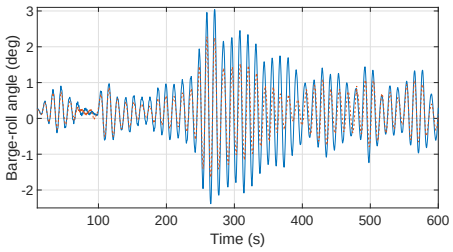

(b)

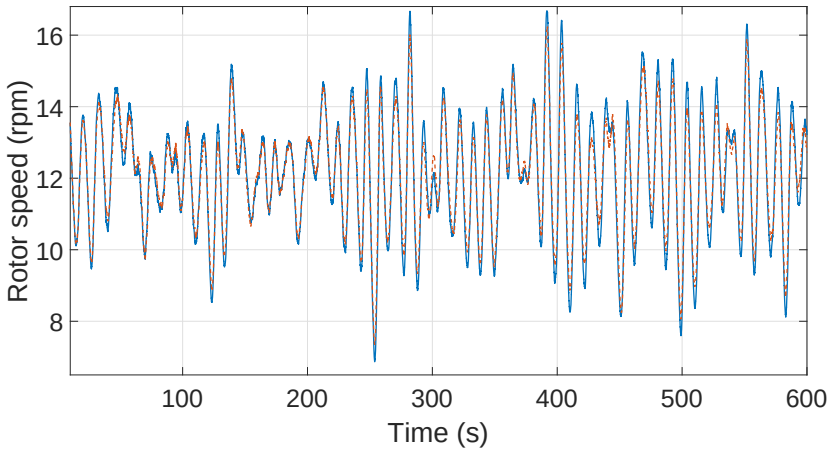

(c)

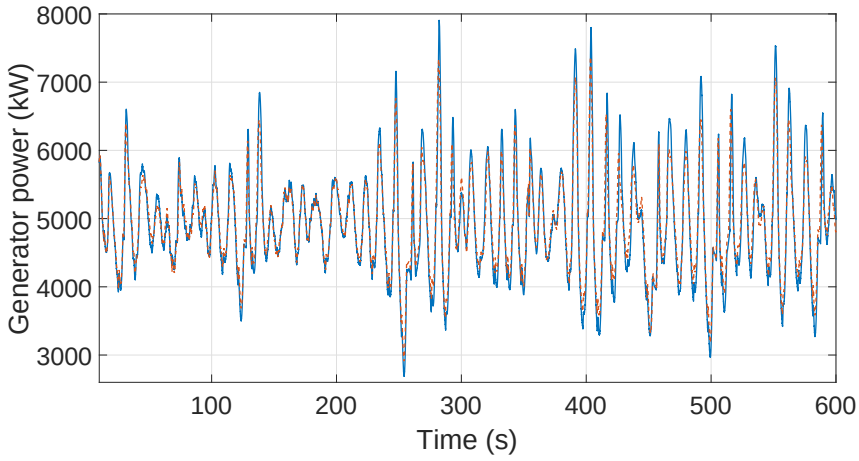

(d)

Figure 6.14: Simulations results for the transformed NREL 5-MW barge HWT model in the normal event where the mean hub-height longitudinal wind speed is 18 m/s. Figures 6.14a, 6.14b, 6.14c and 6.14d depict the barge pitch and roll displacements, the rotor speed, and the generator power, respectively.

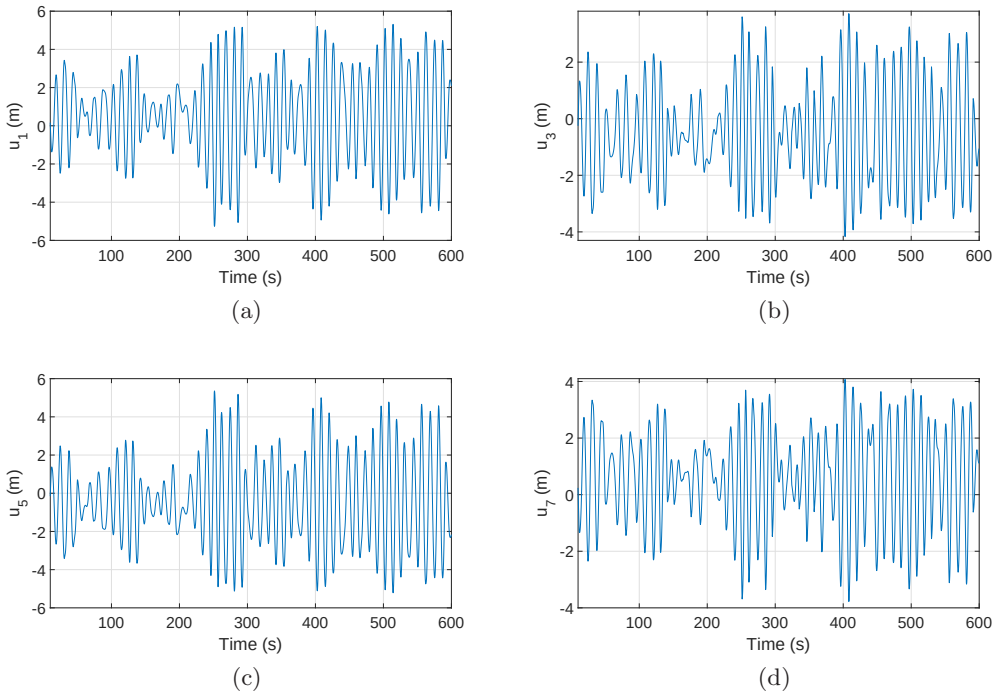

Figure 6.15: Liquid displacements u_1, u_3, u_5 and u_7 in the four vertical columns numbered 1, 3, 5 and 7 of the BTLCD reservoir for the transformed NREL 5-MW barge HWT model with the BTLCD configuration, in the normal event where the mean hub-height longitudinal wind speed is 18 m/s.

Chapter 7

Conclusions and Future Work

Several control strategies were proposed and demonstrated to greatly improve the performances of conventional (geared equipped) and hydrostatic offshore wind turbines in terms of power generation and structural vibration reduction. Note that power generation and structural vibration are coupled with each other, e.g., Figures 6.5 and 6.8 show that the mitigation of barge pitch and roll motions was accompanied by the improvement of power quality. Chapters 3 and 4 conducted research on conventional turbines, while Chapters 5 and 6 investigated hydrostatic turbines. All the four chapters are summarised below.

Chapter 3 dealt with maximum power capture of a conventional (geared equipped) wind turbine. The SESC scheme was proposed for torque control through simplifying the conventional ESC algorithm presented in [75], and the MSESC scheme was developed through further simplifying the SESC loop. Both algorithms can find the optimal torque gain (where the power coefficient is optimal, and thus the wind power extraction is maximised) without requiring the turbine properties. Through simulations, SESC and MSESC were shown to be almost as effective as conventional ESC in seeking out the optimal torque gain, but with simpler control setups. Besides, the torque controllers using ESC significantly enhanced the rotor power over the standard torque controller. However, it was seen that the MSESC scheme converged more slowly than the other two ESC methods, which tallied with the analyses at the end of Section 3.2.

Chapter 4 successfully used a TMD system configured in the nacelle to suppress the vibrations of a monopile wind turbine tower. For the optimisation of the TMD system, first the turbine tower-TMD system Σ (4.1)–(4.5) was modelled based on the infinite-dimensional NASA SCOLE model [40, 41]. Then the spectral element method was employed to discretise Σ along the tower's span and obtain its finite-

dimensional version Σ_d (4.48)–(4.49). Based on Σ_d, the transfer function matrix $\mathbf{H}$ (4.48)–(4.49) was derived, using which the frequency-limited $\mathcal{H}_2$ optimisation was performed to acquire the optimal spring and damping constants for the TMD. The simulation studies showed that the optimal TMD system achieved up to 69.7% tower fatigue load reduction. As an extension of the above research, a method was then presented for the design of multiple TMDs to suppress vibrations of the non-uniform SCOLE model with multiple dominant vibration modes (representing the monopile wind turbine tower with multiple modes needed to be controlled). More specifically, multiple TMDs were optimised for mitigating vibrations under harmonic and random excitations based on the frequency-limited $\mathcal{H}_\infty$ and $\mathcal{H}_2$ optimisations, respectively. Note that the actual optimisation scheme ($\mathcal{H}_\infty$ or $\mathcal{H}_2$) should be chosen based on the spectra of external excitations. The proposed optimisation scheme was able to suppress several dominant vibration modes simultaneously and meanwhile improve the robustness of the TMD system against mistuning effects (by adjusting the trade-off constraint in the optimisation problem).

Chapter 5 addressed power generation control of a monopile HWT. An $\mathcal{H}_\infty$ loop-shaping torque controller and an LPV pitch controller were developed. The torque controller regulates the motor displacement to make the pressure difference across the pump track its command. This enables maximum power capture in Region 2 and constant turbine output power in Region 3. The pitch controller saturates the pitch angle at its lower limit in Region 2 and functions in Region 3 to regulate the rotor speed around its rated value. For system recovery after pitch saturation during the transition between Region 2 and 3, an anti-windup (AW) compensator was designed for the pitch controller. The scheduling parameter of the LPV pitch controller and AW compensator is the steady rotor effective wind speed which is estimated by a developed LIDAR simulator. To demonstrate the proposed control schemes, the NREL offshore 5-MW baseline turbine model (see Section 2.4) within FAST was transformed into a detailed aero-hydro-servo-elastic monopile HWT simulation model. Through the tests using the transformed HWT, the torque controller achieved very good tracking performances. Besides, compared with the gain-scheduled PI pitch control system developed in [119], the LPV (with or without AW) pitch controller delivered tighter rotor speed regulation, better power quality, and reduced loads of the blade bearings & tower. Furthermore, during the region transitions, the LPV AW pitch controller markedly improved the performances compared with the PI or LPV (without AW) pitch controller.

Chapter 6 presented a spin-off application of the reservoir in the HST system to damp pitch and roll responses of the floating barge substructure for a barge HWT.

More specifically, the reservoir was made into the shape of the BTLCD presented in [152]. To demonstrate this application, an accurate barge HWT simulation model was developed through incorporating the coupled dynamics of the barge-reservoir system into the transformed HWT model within FAST (obtained in Section 5.2) by using the Lagrange's equation approach. Via multistart optimisations, the optimal parameters of the BTLCD reservoir were derived based on two simplified mathematical models which describe pitch and roll motions of the turbine-reservoir system respectively. The BTLCD reservoir were assessed through conducting the simulations using the transformed barge HWT. Due to the BTLCD configuration, significantly decreased barge pitch and roll motions were observed, resulting in reduced damage loads on the tower, and less fluctuations of the rotor speed and generator power.

The recommendations for future studies are as follows:

a. Apply SESC and MSESC algorithms proposed in Chapter 3 to torque control of the HWT to maximise its power capture.
b. Decrease the tower's thickness for the BTLCD-stabilised HWT, and determine the optimal tower configuration which has the lowest cost and meets prescribed design criteria.
c. Further improve HWT performances, particularly in generated power quality and utilisation of wind energy by employing energy storage techniques.

Bibliography

[1] J. Jonkman, "Manuscript document of NREL's baseline wind turbine aeroelastic model for use in various offshore analysis concept studies," June 2006. [Online]. Available: http://www.ieawind.org/AnnexXXIIISecure/Subtask_2S_docs/OC3Files/BaselineTurbine/NRELOffshrBsline5MW.pdf

[2] G. Stewart and M. A. Lackner, "Offshore wind turbine load reduction employing optimal passive tuned mass damping systems," *IEEE Transactions on Control Systems Technology*, vol. 21, no. 4, pp. 1090–1104, 2013.

[3] K. E. Johnson, L. Y. Pao, M. J. Balas, and L. J. Fingersh, "Control of variable-speed wind turbines: Standard and adaptive techniques for maximizing energy capture," *IEEE Control Systems Magazine*, vol. 26, no. 3, pp. 70–81, 2006.

[4] J. M. Jonkman, "Dynamics modeling and loads analysis of an offshore floating wind turbine," National Renewable Energy Laboratory, CO, USA, Tech. Rep., 2007.

[5] R. Dutta, "Modeling and analysis of short term energy storage for mid-size hydrostatic wind turbine," Master's thesis, University of Minnesota, 2012.

[6] B. Jonkman and J. Jonkman, *FAST v8.16.00a-bjj*, National Renewable Energy Laboratory, CO, USA, 2016.

[7] J. Jonkman, S. Butterfield, W. Musial, and G. Scott, "Definition of a 5-MW reference wind turbine for offshore system development," National Renewable Energy Laboratory, CO, USA, Tech. Rep., 2009.

[8] J. J. Connor, *Introduction to Structural Motion Control*. New Jersey: Prentice Hall, 2002.

[9] D. Schipf, E. Simley, F. Lemmer, L. Y. Pao, and P. W. Cheng, "Collective pitch feedforward control of floating wind turbines using lidar," *Journal of Ocean and Wind Energy*, vol. 2, no. 4, pp. 223–230, 2015.

[10] L. Fried, L. Qiao, S. Sawyer, and S. Shukla, "Global wind report 2015—annual market update," Global Wind Energy Council, Brussels, Belgium, Tech. Rep., 2016.

[11] A. Pullen and M. G. Eneland, "Global wind 2006 report," Global Wind Energy Council, Brussels, Belgium, Tech. Rep., 2007.

[12] THE EUROPEAN WIND ENERGY ASSOCIATION, "Wind energy statistics and targets." [Online]. Available: http://www.ewea.org/uploads/pics/EWEA_Wind_energy_factsheet.png

[13] BTM Consult, "International wind energy development: World market update 2010," October 2011. [Online]. Available: http://www.altenergymag.com/content.php?post_type=1713

[14] M. Rock and L. Parsons, "Offshore wind energy," Environmental and Energy Study Institute, NW, USA, Tech. Rep., 2010.

[15] "UK offshore wind: Opportunities for trade and investment," UK Trade & Investment, London, UK, Tech. Rep., 2015.

[16] S. Wyatt, A. Govindji, R. James, N. Duan, B. Xie, M. Liu, and G. Yi, "Detailed appraisal of the offshore wind industry in China," Carbon Trust, London, UK, Tech. Rep., 2014.

[17] L. Small, S. Beirne, and O. Gutin, "Offshore wind: Can the United States catch up with Europe?" Environmental and Energy Study Institute, NW, USA, Tech. Rep., 2016.

[18] P. Krogsgaard and B. T. Madsen, "Offshore wind power 2010," BTM Consult ApS, Ringkoebing, Denmark, Tech. Rep., 2010.

[19] S. Cavazzi and A. Dutton, "An Offshore Wind Energy Geographic Information System (OWE-GIS) for assessment of the UK's offshore wind energy potential," *Renewable Energy*, vol. 87, pp. 212–228, 2016.

[20] "How does the wind make electricity?" Energy Center of Wisconsin, WI, USA, Tech. Rep., 2000.

[21] W. Musial and S. Butterfield, "Future for offshore wind energy in the United States," in *EnergyOcean 2004*, FL, USA, June 2004.

[22] W. Musial, P. Beiter, S. Tegen, and A. Smith, "Potential offshore wind energy areas in California: An assessment of locations, technology, and costs," National Renewable Energy Laboratory, CO, USA, Tech. Rep. NREL/TP-5000-67414, 2016.

[23] "Offshore wind energy—wind energy fact sheet 1," Renewable Energy Enquiries Bureau, ETSU, Harwell, UK, Tech. Rep., 2001.

[24] J.-C. Ossyra, "Reliable, lightweight transmissions for off-shore, utility scale wind turbines," Eaton Corporation, WI, USA, Tech. Rep., 2012.

[25] J. Carroll, A. McDonald, and D. McMillan, "Failure rate, repair time and unscheduled O&M cost analysis of offshore wind turbines," *Wind Energy*, vol. 19, pp. 1107–1119, 2015.

[26] Y. Feng, Y. Qiu, C. J. Crabtree, H. Long, and P. J. Tavner, "Monitoring wind turbine gearboxes," *Wind Energy*, vol. 16, no. 5, pp. 728–740, 2013.

[27] P. Tavner, J. Xiang, and F. Spinato, "Reliability analysis for wind turbines," *Wind Energy*, vol. 10, no. 1, pp. 1–18, 2007.

[28] F. Spinato, P. J. Tavner, G. Van Bussel, and E. Koutoulakos, "Reliability of wind turbine subassemblies," *IET Renewable Power Generation*, vol. 3, no. 4, pp. 387–401, 2009.

[29] S. Sheng, "Report on wind turbine subsystem reliability—a survey of various databases," National Renewable Energy Laboratory, CO, USA, Tech. Rep., 2013.

[30] L. Ran, P. A. Mawby, P. McKeever, and S. Konaklieva, "Condition monitoring of power electronics for offshore wind," *Engineering & Technology Reference*, pp. 1–10, 2012, DOI: 10.1049/etr.2014.0004.

[31] B. Backwell and N. Medic, "Offshore wind energy powering the UK since 2000: Owners' workshop manual," 2016. [Online]. Available: http://mhivestasoffshore.com/manuals/offshore_haynes_manual_2016.pdf

[32] J. Carroll, A. McDonald, I. Dinwoodie, D. McMillan, M. Revie, and I. Lazakis, "Availability, operation and maintenance costs of offshore wind turbines with different drive train configurations," *Wind Energy*, vol. 20, no. 2, pp. 361–378, 2017.

[33] J. Carroll, A. McDonald, and D. McMillan, "Reliability comparison of wind turbines with DFIG and PMG drive trains," *IEEE Transactions on Energy Conversion*, vol. 30, no. 2, pp. 663–670, 2015.

[34] J. Rapp and J. Turesson, "Hydrostatic transmission in wind turbines: Development of test platform," Master's thesis, Linköping University, 2015.

[35] J. M. Jonkman, "Assessing the potential of a mechanical continuously variable transmission for wind turbines," National Renewable Energy Laboratory, CO, USA, Tech. Rep. NREL/CP-500-38212, 2005.

[36] N. Diepeveen, "On the application of fluid power transmission in offshore wind turbines," Ph.D. dissertation, Delft University of Technology, 2013.

[37] J. Taylor, W. Rampen, A. Robertson, and N. Caldwell, "Digital Displacement hydraulic hybrids," in *JSAE Annual Congress*, Yokohama, Japan, May 2011.

[38] M. K. OBE, "Bringing electronic controls to hydraulics," *Ingenia*, vol. 64, pp. 24–28, 2015.

[39] T. T. Soong and B. Spencer, "Supplemental energy dissipation: state-of-the-art and state-of-the-practice," *Engineering Structures*, vol. 24, no. 3, pp. 243–259, March 2002.

[40] X. Zhao and G. Weiss, "Suppression of the vibrations of wind turbine towers," *IMA Journal of Mathematical Control and Information*, vol. 28, no. 3, pp. 377–389, 2011.

[41] X. Zhao and G. Weiss, "Well-posedness and controllability of a wind turbine tower model," *IMA Journal of Mathematical Control and Information*, vol. 28, pp. 103–119, 2011.

[42] V.-N. Dinh, B. Basu, and S. Nagarajaiah, "Semi-active control of vibrations of spar type floating offshore wind turbines," *Smart Structures and Systems*, vol. 18, no. 4, pp. 683–705, 2016.

[43] V.-N. Dinh and B. Basu, "Passive control of floating offshore wind turbine nacelle and spar vibrations by multiple tuned mass dampers," *Structural Control and Health Monitoring*, vol. 22, no. 1, pp. 152–176, 2015.

[44] A. Staino, B. Basu, and S. R. Nielsen, "Actuator control of edgewise vibrations in wind turbine blades," *Journal of Sound and Vibration*, vol. 331, no. 6, pp. 1233–1256, 2012.

[45] B. Fitzgerald, B. Basu, and S. R. Nielsen, "Active tuned mass dampers for control of in-plane vibrations of wind turbine blades," *Structural Control and Health Monitoring*, vol. 20, no. 12, pp. 1377–1396, 2013.

[46] B. Spencer and S. Nagarajaiah, "State of the art of structural control," *Journal of Structural Engineering*, vol. 129, no. 7, pp. 845–856, July 2003.

[47] M. D. Symans and M. C. Constantinou, "Semi-active control systems for seismic protection of structures: a state-of-the-art review," *Engineering structures*, vol. 21, no. 6, pp. 469–487, 1999.

[48] M. A. Lackner and M. A. Rotea, "Passive structural control of offshore wind turbines," *Wind Energy*, vol. 14, no. 3, pp. 373–388, 2011.

[49] X. Tong, X. Zhao, and S. Zhao, "Passive structural vibration control of a monopile wind turbine tower," in *54th IEEE Conference on Decision and Control*, Osaka, Japan, December 2015.

[50] X. Tong, X. Zhao, and S. Zhao, "Load reduction of a monopile wind turbine tower using optimal tuned mass dampers," *International Journal of Control*, vol. 90, no. 7, pp. 1283–1298, 2017.

[51] O. S. Thomassen, "Sensitivity analysis of large rotor diameter on offshore wind turbines with suction foundation," Master's thesis, Norwegian University of Science and Technology, 2014.

[52] W. Weijtjens, N. Noppe, A. Iliopoulos, and C. Devriendt, "Monitoring the consumed fatigue life on three offshore wind turbines," in *Structural Health Monitoring 2015: System Reliability for Verification and Implementation*, CA, USA, September 2015.

[53] M. B. Zaaijer, "Foundation modelling to assess dynamic behaviour of offshore wind turbines," *Applied Ocean Research*, vol. 28, pp. 45–57, 2006.

[54] T. Verbelen, G. D. Sitter, and C. Devriendt, "Design verification of offshore wind turbines on monopile foundations," March 2015. [Online]. Available: http://www.ewea.org/offshore2015/conference/allposters/PO104.pdf

[55] X. Tong and X. Zhao, "Vibration suppression of the finite-dimensional approximation of the non-uniform SCOLE model using multiple tuned mass dampers," in *55th IEEE Conference on Decision and Control*, NV, USA, December 2016.

[56] X. Tong and X. Zhao, "Passive vibration control of the scole beam system," *Structural Control and Health Monitoring*, accepted subject to revision.

[57] X. Tong and X. Zhao, "LPV pitch control of a hydrostatic wind turbine based on LIDAR preview," in *2017 American Control Conference*, WA, USA, May 2017.

[58] X. Tong and X. Zhao, "Power generation control of a monopile hydrostatic wind turbine using an $\mathcal{H}_\infty$ loop-shaping torque controller and an LPV pitch controller," *IEEE Transactions on control systems technology*, 2017, DOI: 10.1109/TCST.2017.2749562.

[59] X. Tong and X. Zhao, "Platform-pitch response mitigation of a floating hydrostatic wind turbine," submitted.

[60] X. Tong, X. Zhao, and A. Karcanias, "Passive vibration control of an offshore floating hydrostatic wind turbine model," *Wind Energy*, accepted subject to revision.

[61] B. J. Jonkman, "TurbSim user's guide: Version 1.50," National Renewable Energy Laboratory, CO, USA, Tech. Rep., 2009.

[62] *Wind Turbines—Part 1: Design Requirements*, 3rd ed., International Electrotechnical Commission, Geneva, Switzerland, 2005.

[63] A. Platt, B. Jonkman, and J. Jonkman, "InflowWind user's guide," National Wind Technology Center, CO, USA, Tech. Rep., 2016.

[64] J. Jonkman, A. Robertson, and G. Hayman, "HydroDyn user's guide and theory manual," National Renewable Energy Laboratory, CO, USA, Tech. Rep., 2014.

[65] J. M. Jonkman and M. L. Buhl Jr, "FAST user's guide," National Renewable Energy Laboratory, CO, USA, Tech. Rep., 2005.

[66] *Building Models in ADAMS/View*, MSC Software Corporation, CA, USA, 2000.

[67] G. J. Hayman, "MLife theory manual for version 1.00," National Renewable Energy Laboratory, CO, USA, Tech. Rep., 2012.

[68] A. Halfpenny, "A frequency domain approach for fatigue life estimation from finite element analysis," *Key Engineering Materials*, vol. 167–168, pp. 401–410, 1999.

[69] D. Matha, "Model development and loads analysis of an offshore wind turbine on a tension leg platform, with a comparison to other floating turbine concepts," National Renewable Energy Laboratory, CO, USA, Tech. Rep., 2010.

[70] H. Sutherland, "On the fatigue analysis of wind turbines," Sandia National Laboratories, NM, USA, Tech. Rep., 1999.

[71] L. Y. Pao and K. E. Johnson, "A tutorial on the dynamics and control of wind turbines and wind farms," in *2009 American Control Conference*, MO, USA, June 2009.

[72] K. Johnson, L. J. Fingersh, M. Balas, and L. Pao, "Methods for increasing region 2 power capture on a variable-speed wind turbine," *Journal of Solar Energy Engineering*, vol. 126, pp. 1092–1100, 2004.

[73] N. A. Cutululis, E. Ceanga, A. D. Hansen, and P. Sorensen, "Robust multi-model control of an autonomous wind power system," *Wind Energy*, vol. 9, pp. 399–419, 2006.

[74] J. Creaby, Y. Y. Li, and J. E. Seem, "Maximizing wind turbine energy capture using multivariable extremum seeking control," *Wind Engineering*, vol. 33, pp. 361–388, 2009.

[75] M. Krstić and H.-H. Wang, "Stability of extremum seeking feedback for general nonlinear dynamic systems," *Automatica*, vol. 36, pp. 595–601, 2000.

[76] E. Bossanyi, "Wind turbine control for load reduction," *Wind energy*, vol. 6, no. 3, pp. 229–244, 2003.

[77] P. J. Darrow, "Wind turbine control design to reduce capital costs," National Renewable Energy Laboratory, CO, USA, Tech. Rep., 2010.

[78] M. Soltani, R. Wisniewski, P. Brath, and S. Boyd, "Load reduction of wind turbines using receding horizon control," in *IEEE Multi-Conference on Systems and Control*, CO, USA, September 2011, pp. 852–857.

[79] X. Zhao and G. Weiss, "Stabilization of a wind turbine tower model in the plane of the turbine blades," *International Journal of Control*, vol. 87, pp. 2027–2034, 2014.

[80] Z. Zhang, S. R. K. Neilsen, F. Blaabjerg, and D. Zhou, "Dynamics and control of lateral tower vibrations in offshore wind turbines by means of active generator torque," *Energies*, vol. 7, pp. 7746–7772, 2014.

[81] F. Sadek, B. Mohraz, A. W. Taylor, and R. M. Chung, "A method of estimating the parameters of tuned mass dampers for seismic applications," *Earthquake Engineering and Structural Dynamics*, vol. 26, pp. 617–635, 1997.

[82] Date of access: 21/04/2017. [Online]. Available: http://www.amusingplanet.com/2014/08/the-728-ton-tuned-mass-damper-of-taipei.html

[83] J. P. D. Hartog, *Mechanical Vibration*, 4th ed. New York: McGraw-Hill, 1956.

[84] P. H. Wirsching and G. C. Campbell, "Minimal structural response under random excitation using the vibration absorber," *Earthquake Engineering and Structural Dynamics*, vol. 2, no. 4, pp. 303–312, 1974.

[85] R. J. McNamara, "Tuned mass dampers for buildings," *Journal of the Structural Division*, vol. 103, no. 9, pp. 1785–1798, 1977.

[86] G. B. Warburton, "Optimum absorber parameters for various combinations of response and excitation parameters," *Earthquake Engineering and Structural Dynamics*, vol. 10, no. 3, pp. 381–401, 1982.

[87] D. Younesian, E. Esmailzadeh, and R. Sedaghati, "Passive vibration control of beams subjected to random excitations with peaked PSD," *Journal of Vibration and Control*, vol. 12, no. 9, pp. 941–953, 2006.

[88] A. Y. T. Leung, H. Zhang, C. C. Cheng, and Y. Y. Lee, "Particle swarm optimization of TMD by non-stationary base excitation during earthquake," *Earthquake Engineering and Structural Dynamics*, vol. 37, pp. 1223–1246, 2008.

[89] K. Xu and T. Igusa, "Dynamic characteristics of multiple substructures with closely spaced frequencies," *Earthquake Engineering and Structural Dynamics*, vol. 21, pp. 1059–1070, 1992.

[90] H. Yamaguchi, "Fundamental characteristics of multiple tuned mass dampers for suppressing harmonically forced oscillations," *Earthquake Engineering and Structural Dynamics*, vol. 22, pp. 51–62, 1993.

[91] M. Abé, "Dynamic characterization of multiple tuned mass dampers and some design formulas," *Earthquake Engineering and Structural Dynamics*, vol. 23, pp. 813–835, 1994.

[92] T. Igusa and K. Xu, "Vibration control using multiple tuned mass dampers," *Journal of Sound and Vibration*, vol. 175, no. 4, pp. 491–503, 1994.

[93] M. Luu, V. Zabel, and C. Könke, "An optimization method of multi-resonant response of high-speed train bridges using TMDs," *Finite Elements in Analysis and Design*, vol. 53, pp. 13–23, 2012.

[94] A. Kareem and S. Kline, "Performance of multiple mass dampers under random loading," *Journal of Structural Engineering*, vol. 121, no. 2, pp. 348–361, 1995.

[95] A. J. Clark, "Multiple passive tuned mass dampers for reducing earthquake induced building motion," in *Ninth World Conference on Earthquake Engineering*, Tokyo-Kyoto, Japan, August 1988.

[96] L. Bergman, D. McFarland, J. Hall, E. Johnson, and A. Kareem, "Optimal distribution of tuned mass dampers in wind-sensitive structures," in *5th International Conference on Structural Safety and Reliability*, CA, USA, August 1989, pp. 95–102.

[97] R. Lewandowski and J. Grzymisawska, "Dynamic analysis of structures with multiple tuned mass dampers," *Journal of Civil Engineering and Management*, vol. 15, no. 1, pp. 77–86, 2009.

[98] W. Littman and L. Markus, "Stabilization of a hybrid system of elasticity by feedback boundary damping," *Annali di Matematica Pura ed Applicata*, vol. 152, no. 1, pp. 281–330, 1988.

[99] W. Littman and L. Markus, "Exact boundary controllability of a hybrid system of elasticity," *Archive for Rational Mechanics and Analysis*, vol. 103, pp. 193–235, 1988.

[100] X. Zhao and G. Weiss, "Strong stabilization of a non-uniform SCOLE model," in *17th World Congress of the International Federation of Automatic Control*, Seoul, Korea, July 2008.

[101] X. Zhao and G. Weiss, "Well-posedness, regularity and exact controllability of the SCOLE model," *Mathematics of Control, Signals, and Systems (MCSS)*, vol. 22, no. 2, pp. 91–127, 2010.

[102] X. Zhao and G. Weiss, "Strong stabilization of the SCOLE model using a tuned mass damper," in *SIAM Conference on Control and Its Applications*, Paris, France, July 2015.

[103] X. Zhao and G. Weiss, "Stability properties of coupled impedance passive LTI systems," *IEEE Transactions on Automatic Control*, 2017, DOI: 10.1109/TAC.2017.2694558.

[104] J. P. Boyd, *Chebyshev and Fourier Spectral Methods*, 2nd ed. New York: Dover Publications, 2001.

[105] L. Zuo and S. Nayfeh, "Design of passive mechanical systems via decentralized control techniques," in *43rd AIAA/ASME/ASCE/AHS/ASC Structures, Structural Dynamics, and Materials Conference*, CO, USA, April 2002.

[106] L. Zuo, "Effective and robust vibration control using series multiple tuned-mass dampers," *Journal of Vibration and Acoustics*, vol. 131, no. 3, 2009, DOI: 10.1115/1.3085879.

[107] P. Vuillemin, C. Poussot-Vassal, and D. Alazard, "Poles residues descent algorithm for optimal frequency-limited $\mathcal{H}_2$ model approximation," in *2014 European Control Conference (ECC)*, Strasbourg, France, June 2014, pp. 1080–1085.

[108] W. K. Gawronski, *Advanced structural dynamics and active control of structures*, 1st ed. New York: Springer, 2004.

[109] P. Passon, M. Kuhn, S. Butterfield, J. Jonkman, T. Camp, and T. J. Larsen, "OC3—benchmark exercise of aero-elastic offshore wind turbine codes," in *The Science of Making Torque from Wind*, Lyngby, Denmark, August 2007.

[110] D. Chen, K. Huang, V. Bretel, and L. Hou, "Comparison of structural properties between monopile and tripod offshore wind-turbine support structures," *Advances in Mechanical Engineering*, vol. 5, 2013, DOI: 10.1155/2013/175684.

[111] T. Fitzpatrick, P. Dallard, S. L. Bourva, A. Low, R. R. Smith, and M. Willford, *Linking London: The Millennium Bridge*. London: The Royal Academy of Engineering, 2001.

[112] C. C. Lin, J. F. Wang, and B. L. Chen, "Train-induced vibration control of high-speed railway bridges equipped with multiple tuned mass dampers," *Journal of Bridge Engineering*, vol. 10, no. 4, pp. 398–414, 2005.

[113] K. S. Moon, "Vertically distributed multiple tuned mass dampers in tall buildings: performance analysis and preliminary design," *The Structural Design of Tall and Special Buildings*, vol. 19, no. 3, pp. 347–366, 2010.

[114] M. Abé and T. Igusa, "Tuned mass dampers for structures with closely spaced natural frequencies," *Earthquake Engineering and Structural Dynamics*, vol. 243, pp. 247–261, 1995.

[115] I. H. Shames and C. L. Dym, *Energy and finite element methods in structural mechanics*. New York: Taylor & Francis, 1985.

[116] G. Falsone and D. Sattineri, "An Euler-Bernoulli-like finite element method for Timoshenko beams," *Mechanics Research Communications*, vol. 38, no. 1, pp. 12–16, 2011.

[117] F. Wang and K. A. Stelson, "Model predictive control for power optimization in a hydrostatic wind turbine," in *13th Scandinavian International Conference on Fluid Power*, Linköping, Sweden, June 2013.

[118] B. Skaare, B. Hörnsten, and F. G. Nielsen, "Modeling, simulation and control of a wind turbine with a hydraulic transmission system," *Wind Energy*, vol. 16, no. 8, pp. 1259–1276, 2013.

[119] A. J. Laguna, "Modeling and analysis of an offshore wind turbine with fluid power transmission for centralized electricity generation," *Journal of Computational and Nonlinear Dynamics*, vol. 10, p. 041002, 2015.

[120] W. Yang and W. Tobler, "Dissipative modal approximation of fluid transmission lines using linear friction model," *Journal of dynamic systems, measurement, and control*, vol. 113, no. 1, pp. 152–162, 1991.

[121] J. Makinen, R. Piche, and A. Ellman, "Fluid transmission line modeling using a variational method," *Journal of dynamic systems, measurement, and control*, vol. 122, no. 1, pp. 153–162, 2000.

[122] Y. Liu and B. D. Anderson, "Singular perturbation approximation of balanced systems," *International Journal of Control*, vol. 50, no. 4, pp. 1379–1405, 1989.

[123] A. Varga, "Balancing free square-root algorithm for computing singular perturbation approximations," in *30th IEEE Conference on Decision and Control*, Brighton, UK, December 1991.

[124] K. Glover and D. McFarlane, "Robust stabilization of normalized coprime factor plant descriptions with $\mathcal{H}_\infty$-bounded uncertainty," *IEEE Transactions on Automatic Control*, vol. 34, no. 8, pp. 821–830, 1989.

[125] J. Doyle, "Advances in multivariable control," Lecture Notes at ONR/Honeywell Workshop, MN, USA, October 1984.

[126] D. McFarlane and K. Glover, "A loop-shaping design procedure using $\mathcal{H}_\infty$ synthesis," *IEEE Transactions on Automatic Control*, vol. 37, no. 6, pp. 759–769, 1992.

[127] P. Apkarian and R. J. Adams, "Advanced gain-scheduling techniques for uncertain systems," *IEEE Transactions on control systems technology*, vol. 6, no. 1, pp. 21–32, 1998.

[128] M. C. Turner and I. Postlethwaite, "A new perspective on static and low order anti-windup synthesis," *International Journal of Control*, vol. 77, no. 1, pp. 27–44, 2004.

[129] M. H. Hansen, A. D. Hansen, T. J. Larsen, S. Øye, P. Sørensen, and P. Fuglsang, "Control design for a pitch-regulated, variable speed wind turbine," Risø National Laboratory, Denmark, Tech. Rep., 2005.

[130] J. F. Sturm, "Using SeDuMi 1.02, a MATLAB toolbox for optimization over symmetric cones," *Optimization methods and software*, vol. 11, no. 1-4, pp. 625–653, 1999.

[131] J. Lofberg, "YALMIP: A toolbox for modeling and optimization in MATLAB," in *13th IEEE International Symposium on Computer Aided Control System Design*, Taipei, Taiwan, September 2004, pp. 284–289.

[132] M. Harris, M. Hand, and A. Wright, "Lidar for turbine control," National Renewable Energy Laboratory, CO, USA, Tech. Rep., 2006.

[133] F. Dunne, D. Schlipf, L. Pao, A. Wright, B. Jonkman, N. Kelley, and E. Simley, "Comparison of two independent lidar-based pitch control designs," National Renewable Energy Laboratory, CO, USA, Tech. Rep., 2012.

[134] E. Simley, L. Y. Pao, P. Gebraad, and M. Churchfield, "Investigation of the impact of the upstream induction zone on LIDAR measurement accuracy for wind turbine control applications using large-eddy simulation," in *The Science of Making Torque from Wind 2014*, Roskilde, Denmark, June 2014.

[135] F. Dunne, L. Y. Pao, D. Schlipf, and A. K. Scholbrock, "Importance of lidar measurement timing accuracy for wind turbine control," in *2014 American Control Conference*, OR, USA, June 2014.

[136] K. Z. Østergaard, J. Stoustrup, and P. Brath, "Linear parameter varying control of wind turbines covering both partial load and full load conditions," *International Journal of Robust and Nonlinear Control*, vol. 19, no. 1, pp. 92–116, 2009.

[137] S. Colwell and B. Basu, "Experimental and theoretical investigations of equivalent viscous damping of structures with TLCD for different fluids," *Journal of structural engineering*, vol. 134, no. 1, pp. 154–163, 2008.

[138] T. Balendra, C. Wang, and H. Cheong, "Effectiveness of tuned liquid column dampers for vibration control of towers," *Engineering Structures*, vol. 17, no. 9, pp. 668–675, 1995.

[139] F. Sadek, B. Mohraz, and H. Lew, "Single- and multiple-tuned liquid column dampers for seismic applications," *Earthquake Engineering and Structural Dynamics*, vol. 27, no. 5, pp. 439–464, 1998.

[140] J.-C. Wu, C.-H. Chang, and Y.-Y. Lin, "Optimal designs for non-uniform tuned liquid column dampers in horizontal motion," *Journal of Sound and Vibration*, vol. 326, no. 1, pp. 104–122, 2009.

[141] T. Chatterjee and S. Chakraborty, "Vibration mitigation of structures subjected to random wave forces by liquid column dampers," *Ocean Engineering*, vol. 87, pp. 151–161, 2014.

[142] C. Chang, C. Hsu, and S. Swei, "Control of buildings using single and multiple tuned liquid column dampers," *Structural Engineering and Mechanics*, vol. 6, no. 1, pp. 77–93, 1998.

[143] S. K. Yalla and A. Kareem, "Optimum absorber parameters for tuned liquid column dampers," *Journal of Structural Engineering*, vol. 126, no. 8, pp. 906–915, 2000.

[144] H. Gao, K. Kwok, and B. Samali, "Optimization of tuned liquid column dampers," *Engineering structures*, vol. 19, no. 6, pp. 476–486, 1997.

[145] S. Xue, J. Ko, and Y. Xu, "Tuned liquid column damper for suppressing pitching motion of structures," *Engineering Structures*, vol. 22, no. 11, pp. 1538–1551, 2000.

[146] S. Colwell and B. Basu, "Tuned liquid column dampers in offshore wind turbines for structural control," *Engineering Structures*, vol. 31, no. 2, pp. 358–368, 2009.

[147] C. Roderick, "Vibration reduction of offshore wind turbines using tuned liquid column dampers," Master's thesis, University of Massachusetts Amherst, 2012.

[148] C. Coudurier, O. Lepreux, and N. Petit, "Passive and semi-active control of an offshore floating wind turbine using a tuned liquid column damper," in *10th IFAC Conference on Manoeuvring and Control of Marine Craft*, Copenhagen, Denmark, August 2015.

[149] B. Basu, Z. Zhang, and S. R. Nielsen, "Damping of edgewise vibration in wind turbine blades by means of circular liquid dampers," *Wind Energy*, vol. 19, no. 2, pp. 213–226, 2016.

[150] P. Hitchcock, K. Kwok, R. Watkins, and B. Samali, "Characteristics of liquid column vibration absorbers (LCVA)—II," *Engineering Structures*, vol. 19, no. 2, pp. 135–144, 1997.

[151] S.-K. Lee, K.-W. Min, and H.-R. Lee, "Parameter identification of new bidirectional tuned liquid column and sloshing dampers," *Journal of Sound and Vibration*, vol. 330, no. 7, pp. 1312–1327, 2011.

[152] L. Rozas, R. L. Boroschek, A. Tamburrino, and M. Rojas, "A bidirectional tuned liquid column damper for reducing the seismic response of buildings," *Structural Control and Health Monitoring*, vol. 23, no. 4, pp. 621–640, 2016.

[153] A. Ghosh and B. Basu, "A closed-form optimal tuning criterion for TMD in damped structures," *Structural Control and Health Monitoring*, vol. 14, no. 4, pp. 681–692, 2007.